



POSITRONIUM ANNIHILATION SPECTROSCOPY

Characterization of Novel Nano-porous
Materials with Advanced Functionalities

Lars Frieder **GERCHOW**
DISS ETH NO. 26855

DISS. ETH NO. 26855

**Positronium Annihilation
Spectroscopy
Characterization of Novel
Nano-porous Materials with
Advanced Functionalities**

A thesis submitted to attain the degree of
Doctor of Sciences of ETH Zurich

(Dr. sc. ETH Zurich)

presented by

Lars Frieder Gerchow

MSc. ETH Zurich, Switzerland

born on 30th Januar, 1989

citizen of Germany

accepted on the recommendation of

Prof. Dr. André Rubbia, examiner

Prof. Dr. Paolo Crivelli, co-examiner

Dr. Thomas Prokscha, co-examiner

Prof. Dr. Hans-Arno Synal, co-examiner

2020

‘There is a great satisfaction in building
good tools for other people to use.’

Freeman John DYSON

Acknowledgements

My absolute biggest thanks goes to Paolo, as a friend and the best supervisor one could imagine. His passion for a beautiful approach to science and life is truly inspiring and simply incomparable.

I am also in great debt to Carlos for more things that I could possibly list here. Thanks mate, the time with you has been a blast!

Thanks also goes to André for supporting the endeavours of applied positron studies, his profound inputs on long term plans and his dedication for this thesis.

Another great encounter was to work with Dave. The plentiful advice, discussion and the remarkable approaches to solving the many problems in the lab taught me the nuts and bolts of the lab life.

Big gratitude goes to all the other group members, i.e. Adamo, Artem, Alex, Balint, Ben, Emilio, Di, Gianluca, Henry, Johannes, Laura, Max, Michael, Rich and Zak. I think you'd all agree, we can be especially lucky that we form such a pleasant squad.

Furthermore, I'd like to thank the whole staff of the Institute, Bruno and Patrick in the mechanical workshop, Ulf and Diogo for their support and fun times, and especially Bettina, Jennifer, Rosa, Gaby and Caroline from the administration, without them, science would be a nuisance.

Thanks also goes to our collaboration partners Nick and Etienne from PSI and now Los Alamos, Robbie, Sharon and Bego from the ACE group, Maksym and Vanessa from the MADE group.

I would also like to thank all the students I had the chance to meet during their studies, Alessandro, Hevjin, Sebastian, Prapti, Mark, Nicola, Jonas, Umberto, Nikola, Sven, Matthias, Gustav, Manuel, Mirald, Jesse, Philipp, Paul, Lucas, Max, Devesh and more. Another shout-out to the physics lab assistant apprentices who visited our group, Andras, Nicola, Simon and Damian. It was a pleasure to work with you.

Moreover, I'd like to thank Thomas and Arno for examining this thesis and the many great encounters.

A big hug goes to the best allies one can imagine, Luca and Jan, keep on rocking! Only the combination of all these people allowed me to enjoy this project as deeply as I did.

Last but not least I thank all my friends in the many beautiful places on this wonderful earth, my unique family with all the aunts and uncles, cousins, grandparents, my brother and all the related kin, especially to emphasize are my parents Peter and Susanne for their unlimited support and love. Without them, I wouldn't have achieved this.

Finally, I'd like to deeply thank my love - Fiona - words are not enough to describe how lucky I am to have her in my life.

If you want to go fast, go alone. If you want to go far, go together.
(African Proverb)

Abstract

Positron, the anti-particle of the electron, and its bound state with an electron, positronium, have found many applications in physics and chemistry. Due to the unique sensitivity to a materials local electron density, positrons can be used to investigate complex voids structures. As such, the development and characterization of materials with precisely engineered porous networks is a vibrant area of research. Applied studies with positron have found relevance in catalysis, opto-, nano- and microelectronics, gas sorption, separation, and sensors, among others. The technique relies on the rapid annihilation of the positrons with the electrons of the material under study. In contrary to scattering, transmission or equilibrium techniques, the positron is a truly local probe of its surroundings. The methods studying the annihilation in time, energy and position are grouped under the term Positron annihilation spectroscopy (PAS). Studies have shown sensitivity to the amount, distribution, and connectivity of single site defects, micro- and mesoporosity levels. Control over these parameters are essential to guide the design for future materials.

The objective of this thesis was to expand the scope of PAS for the characterization of novel nanoporous materials with advanced functionalities. One aspect of this work was increasing the availability of positron beams. Different production schemes exploiting the recent advances and availability of cyclotrons were investigated. With the development of new kinds of radioactive thin-film sources, a step towards small lab scale positron beams was made.

The field of possible applications was expanded with studies on state-of-the-art materials with the ETH slow positron beam. A study on the pore evolution of ZSM-5 zeolite emphasizes the unique sensitivity of PAS to the presence of guest species within the micropore network. This opens new doors to study the impact of targeted inclusion of pendant molecules on the textural properties of other porous materials. Another study focused on the distinct impact of chemical properties, e.g. acidity, on the positron annihilation characteristics. The ability to evaluate both porosity and acidity in functional materials will widen the scope of the technique for the analysis of functional materials.

Moreover, proof of concept studies on different type of nanocrystals, surface-anchored metal-organic frameworks, defect engineered copper films and carbon nanotubes were made. For more wide-spread usage of PAS in the general scientific community, also a strong fundamental understanding and the development of a solid theoretical framework for data analysis is essential. An automated analysis to derive the desired structural information without requiring an involved knowledge of the technique is a particular challenge. Therefore, another core activity of the thesis was the development of improved numerical tools and models to account for the complexity in the pore architecture of functional materials.

Concluding, the work presented in this thesis expanded the number of successful application of PAS. Furthermore, it highlighted a set of problems which need to be tackled towards a more wide-spread use and proposed solution approaches.

Zusammenfassung

Positronen und der gebundene Zustand mit einem Elektron, Positronium, haben viele Anwendungen in der Physik und Chemie. Aufgrund der einzigartigen Sensitivität von Positronen, ist die Anzahl neuer Anwendungen in den letzten Jahren stetig gestiegen. Ein Fokus ist die Untersuchung von neuartigen Materialien mit funktionellen Eigenschaften und komplexen Strukturen mit Anwendungen in den Materialwissenschaften, der Nanotechnologie, der Festkörperphysik oder der Medizin. Mit der Positronenvernichtungsspektroskopie (PAS) lassen sich besonders gut Aussagen über die Menge, Verteilung und Konnektivität von Porosität über verschiedene Grossskalen die für das Design wesentlich sind, treffen. Trotz dieses vielversprechenden Potenzials sind sich die meisten Wissenschaftler der Möglichkeiten dieser Anwendung in den verschiedensten Bereichen nicht bewusst. Folglich ist die Technik eher unverbreitet.

Ziel dieser Arbeit war es, den Anwendungsbereich von PAS zur Charakterisierung neuartiger nanoporöser Materialien zu erweitern. Ein Aspekt dieser Arbeit war, die relevanten Bereiche für eine erhöhte Verfügbarkeit von Positronenstrahlen zu untersuchen. Dafür wurden verschiedene Quellentypen untersucht und die jüngsten Fortschritte bezüglich der Verfügbarkeit von Protonen Zyklotrons bewertet. Mit der Entwicklung neuer Arten radioaktiver Dünnschichtquellen wurde ein wichtiger Schritt in Richtung kompakter Positronenstrahlen für den Laborgebrauch gemacht.

Das Anwendungsfeld vom PAS wurde mit Studien an modernsten Materialien mit dem Positronenstrahl der ETH vergrössert. Eine Studie zur Porenentwicklung von ZSM-5 Zeolith verdeutlicht die einzigartige Empfindlichkeit von PAS gegenüber dem Vorhandensein von Gastspezies im Mikroporen-Netzwerken. Eine andere Studie konzentrierte sich auf den Einfluss chemischer Eigenschaften, z.B. den Säuregehalt, auf die Positronenvernichtungseigenschaften. Die Fähigkeit, sowohl die Porosität als auch die Azidität in funktionellen Materialien zu verstehen, bestärkt den Umfang der Technik zur Analyse von funktionellen Materialien. Darüber hinaus wurden Machbarkeitsstudien zu verschiedenen Arten von Nanokristallen, oberflächenverankerten metallorganischen Gerüsten, Kupferfilmen mit gezielter Defektentwicklung und Kohlenstoffnanoröhren durchgeführt. Eine weitere Kernaktivität der Arbeit war die Entwicklung verbesserter numerischer Werkzeuge und Modelle, um die Komplexität der Porenarchitektur funktioneller Materialien gezielter berücksichtigen zu können.

Zusammenfassend hat die in diesem Werk vorgestellte Arbeit weitere erfolgreichen Anwendungen von PAS aufgezeigt. Darüber hinaus wurde eine Reihe von Problemen erläutert die im Hinblick auf eine breitere Nutzung angegangen werden müssen und Lösungsvorschläge derer vorgeschlagen.

Contents

1	Introduction	1
1.1	Positron Annihilation Spectroscopy	1
1.2	Limitations and Potential	4
2	Positron(ium) Annihilation Spectroscopy	7
2.1	Interaction of Positrons with Matter	7
2.1.1	Secondaries	9
2.1.2	Scattering	10
2.1.3	para-Positronium Annihilation	11
2.1.4	Direct Annihilation	12
2.1.5	ortho-Positronium Annihilation	12
2.2	Positron Annihilation Spectroscopy Methods	13
2.2.1	Positron Annihilation Lifetime Spectroscopy	13
2.2.2	Time-of-Flight	17
2.2.3	Doppler Broadening Spectroscopy	17
2.2.4	Angular Correlation of Positron Annihilation Radiation	19
2.2.5	Age Momentum Correlation	20
2.2.6	Others	20
3	Instrumentation	23
3.1	Experimental Techniques	23
3.1.1	Positron sources	24
3.1.2	Bulk Setup	26
3.1.3	Beam Setups	27
3.1.4	Detectors	31
3.2	ETH Zürich Continuous Slow Positron Beam	32
3.3	Operando Cell	35
3.4	Beam Development	42
3.4.1	Bunching Simulations	42
3.4.2	Buffer gas trap secondary beamline	47
3.4.3	Test beam	52
3.5	Detector Development	53
3.5.1	Micro Channel Plate Detectors	53
3.6	Cyclotron Driven Isotope Production Sources	57
4	High Efficiency Cyclotron Trap Assisted Moderator	65
4.1	The Cyclotron Trap	65

4.1.1	The Principles of a Cyclotron Trap	65
4.1.2	The idea	68
4.1.3	Similarities and differences to other CT moderation setups	69
4.2	A proof of principle	71
4.3	Simulation	72
4.3.1	Implementation	72
4.3.2	Figure of merit	74
4.3.3	The positron source	74
4.3.4	The magnetic field	76
4.3.5	Trajectories	78
4.3.6	The moderator	81
4.3.7	The vacuum chamber	82
4.3.8	Extraction, blocking and guiding	83
4.3.9	Detection	83
4.4	Experimental setup	84
4.4.1	The coils	85
4.4.2	Thin film positron sources	87
4.4.3	The tungsten moderator	91
4.4.4	Extraction and blocking system	91
4.4.5	Detection systems	92
4.5	Discussion	93
4.6	Conclusions and Outlook	96
5	Positron(ium) Modelling	97
5.1	Positron Implantation Profiles	98
5.2	Quantum Mechanical Confinement of Positronium	100
5.2.1	Calibration Material - Metal-Organic Frameworks	100
5.2.2	Modelling of Open Pore Geometries	102
6	Studies on Zeolites	109
6.1	The material class of zeolites	109
6.2	Zeolite Detemplation	110
6.3	Acidity in Zeolites	125
7	Other Material Studies	145
7.1	Surface Anchored Metal-Organic Frameworks	146
7.2	Nanocrystals	148
7.2.1	Cu-Zn-In-Se Nanocrystals	148
7.2.2	Pb-S Nanocrystals	150
7.2.3	Ge-Te Nanocrystals	152
7.3	Defect Engineered Thin Copper Films	153
7.4	Carbon Nanotubes	154
8	Conclusion	159
9	Outlook	165
	Acronyms	167

Bibliography

169

List of Figures

1.1	Positron physical processes	2
1.2	Zeolite lifetime under reaction	4
1.3	Comparison of defect characterization methods	5
2.1	Schematics of decay channel kinematics	8
2.2	Overview of positron lifetimes in porous media	9
2.3	Reprint of Figure 1.1	10
2.4	Makhovian Profile	11
2.5	Schematic of a positron annihilation lifetime spectrometer.	14
2.6	Example positron annihilation lifetime spectrum	14
2.7	Principle of the Tao Eldrup Model	15
2.8	Time of flight scheme	18
2.9	PAS methods	19
3.1	^{22}Na source β^+ energy spectrum	25
3.2	γ Attenuation coefficient for W	27
3.3	Beam Scheme	28
3.4	Positron tagging scheme with a Micro-Channel Plate	30
3.5	Schemes of single particle detectors	32
3.6	Picture and schematic of ETH slow positron beam	33
3.7	Overview of the PALS spectrometer	35
3.8	Time spectra of the PALS scintillators	36
3.9	Energy spectra of the PAS detectors	36
3.10	Schematic of AIST in-situ cell.	38
3.11	ETH operando cell overview	40
3.12	Microscopy picture of SiN membrane	40
3.13	Picture of the new operando SiN window	42
3.14	Initial bunching energy distribution	43
3.15	Initial phase space for bunching simulations	46
3.16	Phase space after applying a bunching potential	46
3.17	Phase space after evolving a positron bunch	47
3.18	Phase space after applying a 2nd bunching potential	48
3.19	Phase space for bunched positron pulse on target	48
3.20	Bunching pulse and the time distributions of positrons at different positions	49
3.21	Buffer gas pulse beam bunching simulation	51
3.22	Energy and time density of the buffer gas trap positron bunch	51

3.23	Switch yard	52
3.24	Low flux positron beam	53
3.25	CF63 compatible MCP assembly	54
3.26	Central hole 1S2S MCP	56
3.27	Map of IBA proton cyclotrons	58
4.1	Schematic of a magnetic mirror	66
4.2	Principle of a cyclotron trap	67
4.3	Scheme of the high efficiency cyclotron assisted moderator principle	69
4.4	Sketch of the muon moderation cyclotron trap	70
4.5	Scheme of the positron (pre-)moderation scheme of Waeber et al.	71
4.6	Simulated ^{58}Co e^+ energy spectrum	74
4.7	Simulated initial momentum ratio	75
4.8	Simulated magnetic field $B_z(z)$ at $r = 0$ of the cyclotron trap	76
4.9	Surface plot of a simulated magnetic field $B(z, r)$ of the cyclotron trap	77
4.10	Simulated positron trajectories	78
4.11	z -positions of mirroring	79
4.12	Energy E of the positrons when they are mirrored	80
4.13	Energy deposited in the moderator foil in one passage	81
4.14	Energy deposited in the moderator foil during one passage versus the energy with which they imping	82
4.15	Passlength λ of the positrons in the moderator foil	83
4.16	Number of mirroring events n of 10^6 positrons versus their initial energy	84
4.17	Number of passages through the foils n of 10^6 positrons versus their initial energy	85
4.18	Simulated moderation efficiencies of a positron energy spectrum from ^{48}V	86
4.19	Simulated stopping position of positrons from ^{48}V decay inside a $1\ \mu\text{m}$ W foil	86
4.20	Maximum radius $r(E, z)$ positrons of given energy E as a function of z .	87
4.21	Model and picture of the final setup	88
4.22	Picture of the coils creating the magnetic bottle	89
4.23	Measurement of the magnetic field $B(z)$ of the coils	90
4.24	Picture of thin Ti foil TANDEM proton irradiation mount	91
4.25	The standalone W foil annealing station	92
4.26	Model and picture of the sample, moderator and extraction grid mount	93
4.27	Picture of the BGO detection setup	94
4.28	Picture of the single particle detection setup	95
5.1	Three-dimensional positron implantation profiles	99
5.2	Overview over IRMOF frameworks	101
5.3	Kronig-Penney potential	103
5.4	Detailed structure of IRMOF-1 and 3D square linker model	104
5.5	Example electron densities in IRMOF-1	105

5.6	Ps potentials from electron density.	106
5.7	Discretisation artefacts from VESTA in electron density export . .	107
5.8	Isosurface square potential model results for IRMOF frameworks .	108
6.1	MFI type zeolite pore network	111
6.2	Zeolite hierarchy overview	111
6.3	Template agent in MFI zeolite framework	112
6.4	Positron annihilation lifetime spectra of zeolite detemplation samples	116
6.5	PAS response of MFI zeolite detemplation	116
6.6	Schematic of detemplation percolation models	119
6.7	Illustration of the observed mechanism of SDA removal in ZSM-5 zeolites and the effect on oPs diffusion	121
6.8	list of figures caption	121
6.9	Variation of Ps micropore response with detemplation of ZN-x zeolites.	123
6.10	Comparison of the calculated intensity of out-diffusion with PALS data	124
6.11	Illustration of the observed mechanism of SDA removal in ZSM-5 zeolites and the effect on oPs diffusion	124
6.12	Effect of Brønsted acidity on oPs formation	129
6.13	oPs lifetimes and intensities in relation to Brønsted acidity of large zeolite samples	129
6.14	oPs lifetimes and intensities in Brønsted acidic commercial zeolite samples	132
6.15	Scanning electron micrographs of selected zeolites and acidity char- acterization	133
6.16	PALS spectra of large acidity study zeolite samples	135
6.17	Effect of implantation energy on PALS response in acidic zeolites	138
6.18	Schematic representation of positronium formation and annihila- tion paths in acidic zeolites	140
6.19	Numerical model estimating Brønsted and Lewis acidity on PALS response.	142
6.20	Numerical model estimating Brønsted and Lewis acidity on PALS response at high energy.	143
7.1	Ball and stick model of MOF HKUST-1	146
7.2	SEM images of SURMOF	147
7.3	Cu-Zn-In-Se NC DBS and PALS results	149
7.4	Sketch of nanocrystals linker exchange.	151
7.5	DBS spectrum of Cu IBAD	154
7.6	Schematic of carbon nanotube and a micrograph of a carbon nan- otube forest	155
7.7	CNT HPGc gamma spectrum.	156
7.8	CNT 511 peak to spectrum ratio.	158

List of Tables

3.1	Thin film positron source isotope properties.	26
3.2	Comparison of PAS detectors	35
3.3	Typical proton energies and currents for commercial proton cyclotrons	58
3.4	Alternative radioactive positron beam sources.	62
4.1	Endpoint energies T_{\max} and maximum cyclotron radii a_{\max} for $B =$ 500 G of different beta emitters.	76
5.1	IRMOF properties	102
6.1	Fitting results of detemplation study ZM zeolite PALS spectra . .	115
6.2	Fitting results of detemplation study ZN zeolite PALS spectra . .	122
6.3	Composition, porosity, and acidity of the samples in the acidity study	128
6.4	PALS results of acidity study Sil zeolite	130
6.5	PALS results of acidity study Z80 zeolite	130
6.6	PALS results of acidity study Z50 zeolite	131
6.7	PALS results of acidity study on commercial and ion exchanged zeolites	134
6.8	PALS results of acidity study Sn-MFI zeolite	136
6.9	PALS results of acidity study ZC-Sn zeolites	137
6.10	PALS results of acidity study Z50-Na zeolite	138
7.1	Fitting results of Cu-Zn-In-Se NC PALS spectra	150
7.2	Fitting results of Pb-S NC PALS spectra	152
7.3	Fitting results of Ge-Te NC PALS spectra	153
7.4	Copper thin film pilot study summary	154
7.5	Carbon nanotube measurement summary	157
8.1	Summary of the results of applied material PAS studies	161

Chapter 1

Introduction

Breakthroughs in the development of novel materials and devices are often prompted by advances in characterization methods and vice versa. The design of functional solids by precise engineering of small defects, voids, porous structure and the amount, distribution and connectivity of such is a vibrant field of research. The increasing complexity is in demand of improved descriptors to successfully discriminate during the development. Especially in the design of hierarchical nano-porous materials commonly applied tools like electron microscopy or sorption techniques do not provide access to the manifold structure information and their impact on the materials properties.

1.1 Positron Annihilation Spectroscopy

Positrons, the anti-particles of an electron predicted by Dirac in 1928 [1], and first discovered by Anderson in 1933 [2], readily annihilate when interacting with matter. The energy of the annihilation is carried away by two or more gamma rays. Before annihilating, the positron and electron may form a hydrogen-like atom called Positronium (Ps). Depending on the relative spin orientation of the electron and positron being parallel or anti-parallel, Ps is differentiated into the triplet Ortho-Positronium (oPs) and singlet Para-Positronium (pPs), respectively.

The term Positron Annihilation Spectroscopy (PAS) is grouping methods employing the unique sensitivity of the annihilation characteristics of positrons and Ps to study materials. Acting as a dynamic local probe, positrons can resolve the smallest structural features in various depth and concentrations. The dependence to the immediate electronic environment on the nanometer scale yields complementary insight to established techniques on e.g. defect sizes and pore architecture. These properties have led to the development of different techniques and applications in many laboratories around the world over the years [3]. The handful of these methods grouped under PAS are applied to study defects and porosity by measuring the precise energy, angular correlation of the annihilation photons, the annihilation position in space, and the time difference between the

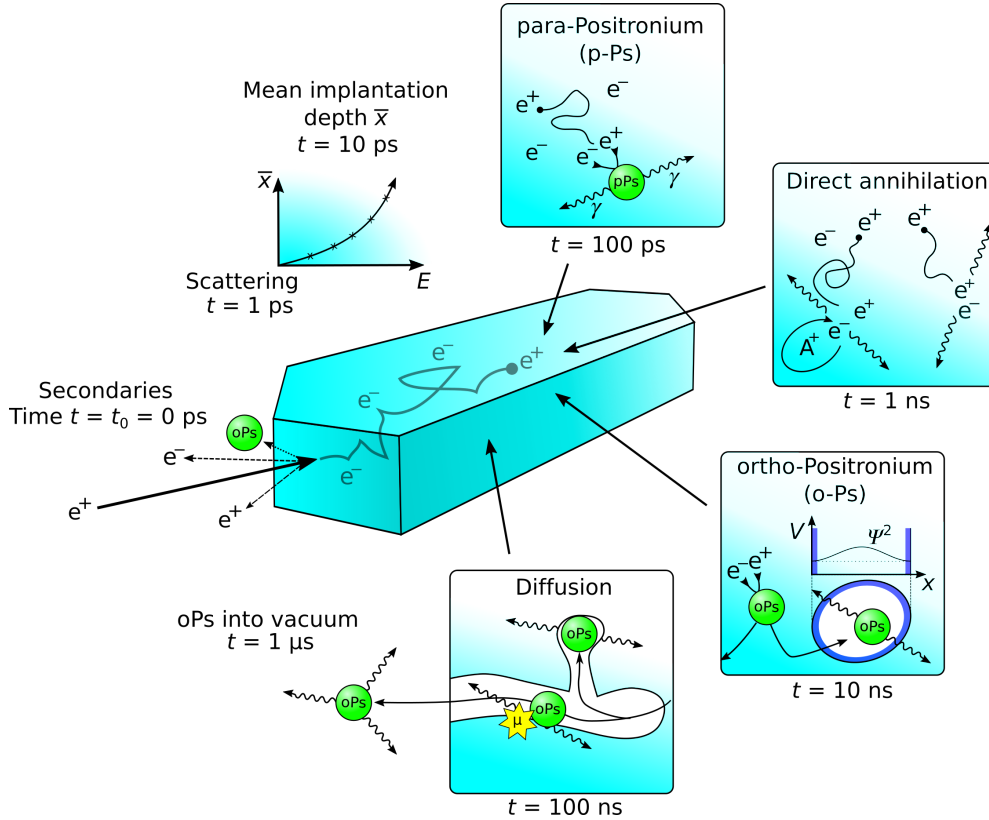


Figure 1.1: Schematic overview depicting the physical processes, and their timescales, which are of importance for PAS.

positron's first interaction with the object under study, until its annihilation. A deeper explanation of the most common techniques is given in Section 2.1.5.

The interplay of all aspects leading to the annihilation and the subsequent emission of gamma rays enables the unique perception on voids in materials. Figure 1.1 shows an overview of the physical processes which need to be considered for the application of PAS.

Secondary particles created on impact can provide information about surface characteristics. Changing the implantation energy results in depth profiling [4], allowing to probe the homogeneity or the interconnection length of pores [5, 6], or porosity hidden beneath dense layers or diffusion barriers not accessible by other techniques [7, 8], e.g. gas adsorption [9]. The direct annihilation of positrons is influenced by positron binding defects and the electron momentum distribution. A thermalised positron may form the hydrogen-like atom positronium with an electron. The rapidly decaying singlet called pPs with a lifetime in vacuum of $\tau_{\text{pPs}} = 125$ ps and the longer lived oPs $\tau_{\text{oPs}} = 142$ ns. The long lived oPs can be quantum mechanically confined in pores on the nm to um scale. Depending to what electron density the oPs is exposed to, its lifetime will be shortened down to 1 ns.

Practically all parameters from the annihilation, the ratio of the distinct annihilation channels, pPs, direct annihilation (also called in-flight, positron or e^+ annihilation), Ps in pores or vacuum, as the attributed lifetimes, gamma ray

energy and collinearity can be used for the assessment. When studying a set of samples, the change in the annihilation response can be used to disseminate differences in the pore network in terms of interconnectivity, pore topologies, distribution, accessibility and sizes, as chemical active sites like acidity.

So far, however, PAS has only been largely applied in academics. Direct (positron) annihilation used for defect assessment in metals and semiconductors has been the focus of many research projects in the past [4, 10, 11]. This sub-field focusses on the changes in the lifetime in the sub ns scale of direct annihilation of positrons and Doppler shifts of the annihilation photons. A defect can quantum mechanically confine a positron and reduce the probability of annihilation with the electrons resulting in a longer lifetime. The two 511 keV photons emitted on annihilation can carry Doppler shifts of the participating electron momentum. A change of electron momentum can often be related to defects and their type [4].

On the other hand, the research related to the longer lifetime region accompanying Ps is not as established. Early work was done for the characterization of porous silica which led to the first theoretical models of positronium lifetimes in materials [12, 13]. These models were later refined [14] and successfully applied in porous low-k dielectrics [5, 6] and polymers [15].

Proof-of-concept work done in collaboration with the group of Advanced Catalysis Engineering (ACE) from the Institute for Chemistry and Bioengineering, D-CHAB, ETH, has shown a particular interesting correlation about the effect of oPs created inside the material and diffusing back out into vacuum for the material class of hierarchical porous zeolites. The investigated zeolite structure MFI has an intrinsic pore structure of long channels with a diameter 0.55 nm and artificial added larger pores in the nm range. It is used as a catalyst in the chemical industry for the cracking of larger carbon molecules into smaller ones. These processes heavily rely on the interconnectivity [16].

Figure 1.2 shows the assessment of the pore network of a set of differently treated materials with two techniques related to a performance parameter, the lifetime of a material under reaction. The two techniques are the most commonly applied technique for pore characterization, gas sorption, and PAS. In gas sorption the material of investigation is subjected to gas of high pressures at a constant temperature and the uptake and release of gas is measured as isotherms. These isotherms provide information of pore volumes in different size regimes. However, as the Figure 1.2 shows, gas sorption parameters do not show a correlation to the zeolite performance. In contrast, the PAS parameters of oPs out-diffusion, which can be understood as the level of interconnectivity, shows a clear correlation. Up to now, PAS is the only method that conveys such a relationship [17].

These findings kicked off the material characterization with positrons at ETH and the work of this thesis was dedicated to establish and advance it further.

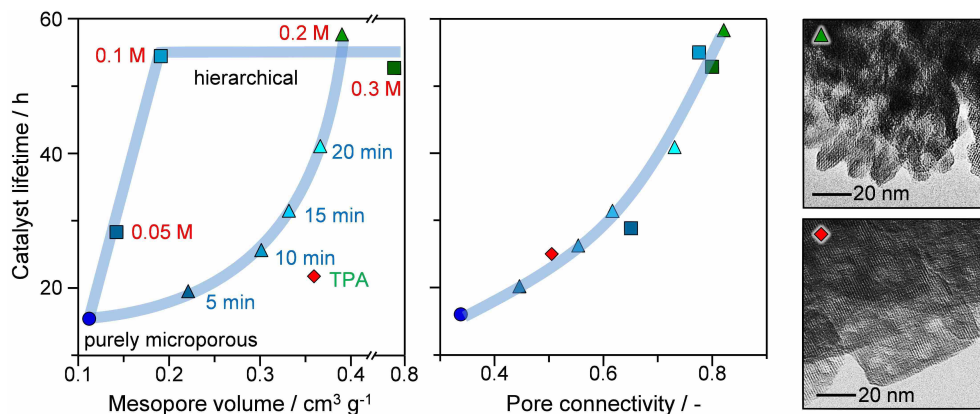


Figure 1.2: Lifetime of hierarchical MFI zeolite for the conversion of methanol to olefins. (left) mesopore volume by gas sorption. (right) PAS pore connectivity. (small) TEM micrographs. Reproduced with permission from [17]. Copyright 2019, John Wiley and Sons.

1.2 Limitations and Potential

With the current trend of downscaling functional architectures small scale features like defects or pores, engineered or unwanted, the importance of PAS is expected to increase given its unique sensitivity compared to other techniques as shown in Figure 1.3. It was shown that complementary information compared to well-established methods can be gained [3, 11, 15]. Specifically, the positron acting as a dynamic local probe enables this different viewpoint.

For a successful widespread usage of this technique, there are still a few key points that should be addressed [3, 4, 10, 11, 15, 18–20].

First of all the community is comparatively small with only a few dozen positron beams worldwide. Moreover, most laboratories utilizing positrons do not solely focus on the material characterization. This limits the accessibility for potential users and discoveries pushing the boundaries of existing techniques.

Secondly, the sparse material research is mostly focused on the scientific side. An increase in the study of industrially relevant materials would increase the awareness, therefore the demand and ultimately boost the availability.

Furthermore, some fields of the underlying physics are not fully understood yet. For example, the formation of Ps in a material is still a mostly qualitative model. There is no ab-initio physical understanding to successfully predict the quantitative amount of positronium formation.

Also, the modelling of the correlation between lifetimes and pore sizes has its limits within basic geometries. The Tao Eldrup model presented in Section 2.2.1 works well for spheres, cubes and channels with closed walls and localized Ps. Geometries of higher symmetries which allow delocalised Ps Bloch states and open pore structures which large openings like cages require more advanced models where only a little or very specific effort has been made so far. Moreover, highly

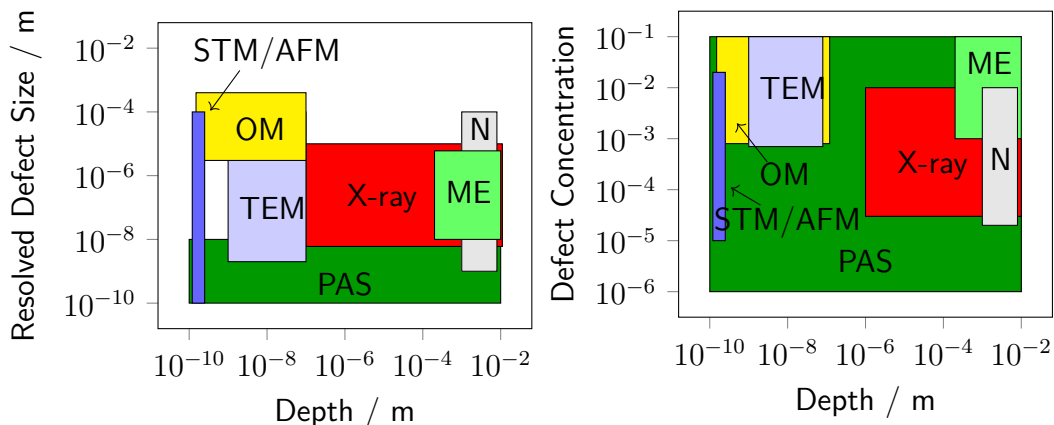


Figure 1.3: Overview of PAS sensitivity for defect sizes and concentration compared to other techniques, optical Microscopy (OM), Transmission Electron Microscopy (TEM), Scanning Tunneling Microscopy (STM), Atomic Force Microscopy (AFM), Neutron scattering (N), and MEchanical techniques (ME). Adapted from [15].

connected systems with pore of various sizes have only been started to be studied.

Last but not least, also instrumentation and data analysis itself can still undergo improvements. A sophisticated analysis would include all annihilation parameters to draw encompassing conclusions. Unfortunately, many studies nowadays do not go to the necessary depth regarding the correlation of the parameters which panders to jump to erroneous interpretations. This is partially due to detectors optimized for the different PAS methods presented in Section 3.1.

Another reason is that the data analysis tools are not robust enough yet for the inexperienced user. The current solutions used in the community are often susceptible to input bias in the data fitting procedures.

In regard of the kick-off studies [16, 17] on the particular class of zeolites which motivated this thesis PAS has shown a novel complementary insight. On the other hand, for a more quantitative comparison across a multitude of materials it was shown that paramets like the acidity could play an important role. Moreover, zeolites can exhibit pores spanning over whole crystals as localised ones of different sizes. The effect of such geometries on the PAS response has not been investigated in detail [10]

Therefore, the work conducted in this thesis can be separated into three sectors, work on the instrumentation (Chapter 3 and Chapter 4) for higher availability, exploring new possibilities for descriptive models (Chapter 5), and applied material characterizations, the continued investigation of zeolites and proof-of-concept studies of other nano-porous materials with advanced functionalities (Chapter 7) by means of positronium diffusion and annihilation.

Chapter 2

Positron(ium) Annihilation Spectroscopy

This chapter introduces the background knowledge for the techniques associated with PAS. All quantities related from the start of interaction of positrons with material up to the annihilation and the detection of the annihilation photons can yield valuable information about the underlying processes. After an introduction to the interaction of positrons with matter an overview of the most common PAS methods is given.

2.1 Interaction of Positrons with Matter

Positrons, the anti-particles of an electron predicted by Dirac in 1928 [1], and first discovered by Anderson in 1933 [2], readily annihilate when interacting with matter. Before annihilating, the positron and electron may form a hydrogen-like atom called Ps. Depending on the relative spin orientation of the electron and positron being parallel or anti-parallel, Ps is differentiated into the triplet oPs and singlet pPs, respectively. During the annihilation, the available energy, mainly consisting of the rest masses of the involved positron and electron (1022 keV), is emitted via gamma rays. Because of charge conjugation conservation in Quantum Electrodynamics (QED), the triplet will decay into an odd, and the singlet into an even number of photons [21]. Since the emission of a single photon is forbidden by momentum conservation, oPs mainly decays into three photons within a plane to conserve momentum. The photon energies fulfil three-body decay kinematics as first calculated by Ore and Powell [22] and depicted in the overview of the kinematics in Figure 2.1

$$E_{\gamma,i} \leq 511 \text{ keV} , \sum_i^3 E_{\gamma,i} = 1022 \text{ keV} . \quad (2.1)$$

The singlets (pPs) main annihilation channel in the centre of mass frame is into

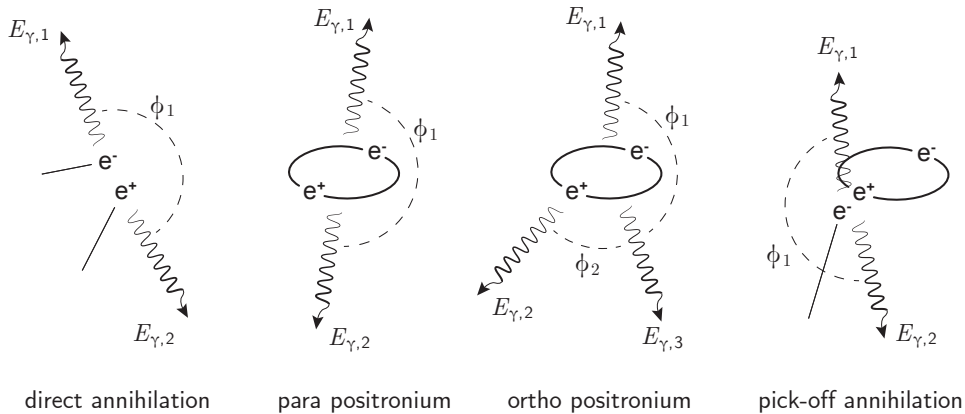


Figure 2.1: Schematic of the different positron decay channels and their kinematics. The energies of the emitted photons from the annihilation have to conserve the energy and momentum the respective positron and electron had before.

two back-to-back photons with

$$E_{\gamma,1} = E_{\gamma,2} = 511 \text{ keV} . \quad (2.2)$$

While higher orders decays into 5, 7,... or 4, 6,... are possible, they are greatly suppressed by multiples of the fine structure constant α . Other rare decays predicted by the Standard Model (SM) or by physics beyond the standard model [23–27], are even less probable and not of concern for material characterization with positrons. The most precise theoretically calculated decay rates in vacuum for pPs [28] and oPs [29–33] are

$$\Gamma_{\text{pPs,exp}} = 7989.7168(2) \mu\text{s}^{-1} \quad (2.3)$$

$$\Gamma_{\text{oPs,exp}} = 7.039\,929(10) \mu\text{s}^{-1} . \quad (2.4)$$

The leading factor for the three order of magnitude smaller decay rate of oPs is the suppression by the additional photon. The measured values $\Gamma_{\text{pPs}} = 7990.0(17) \mu\text{s}^{-1}$ [34] and $\Gamma_{\text{oPs}} = 7.0404(10) \mu\text{s}^{-1}$ [35] agree well with the predicted ones. With Ps being a purely leptonic system free of finite-size effects and mostly annihilating through the electromagnetic force, measurements of these decay rates have been of fundamental interest in the past for the verification and development of bound state QED [36].

Since the discovery of positronium by Deutsch in 1951 [37] it was realized that both positrons and positronium are highly sensitive to their immediate electronic surroundings in an astonishing fashion. It was found that depending on the kind of gas and the concentration, i.e., pressure, the decay rate will increase due to a process called pick-off annihilation [38].

The positron has a finite probability to annihilate with an electron other than its bound partner effectively reducing the lifetime. In denser mediums like liquids or solids the electron densities, their chemical potentials and the variation of

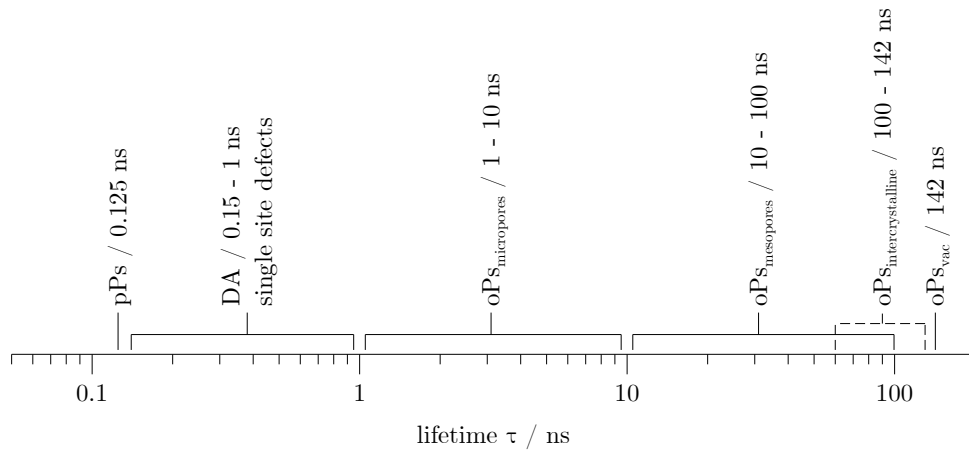


Figure 2.2: Overview of lifetime intervals and the corresponding confining elements using the porosity terminology of the IUPAC definitions: pore diameter < 2 nm for micropores, between 2 and 50 nm for mesopores, above 50 nm for macropores [39].

such can give rise to multiple pick-off decay channels, each being a characteristic of its physical nature e.g. material-dependent electronic configurations, band structures, defects and voids. While the effect on the annihilation characteristics can be manifold, as will be discussed in the following sections, one parameter, the lifetime, stands out. Spanning over three orders of magnitude from the pPs annihilation with 125 ps to the oPs vacuum lifetime of 142 ns, it maps single site defects (a single missing atom $\sim \text{\AA}$) up to open voids with sizes of 100 nm. An overview of lifetimes and the corresponding environment is shown in Figure 2.2.

However, to be able to fully understand observations, one has to account for the most dominant physical processes from the moment the positron firstly interacted with matter until it annihilates, see Figure 2.3. Moreover, even the emission and propagation of the gamma rays, their detection and the whole data acquisition can be of relevance.

2.1.1 Secondaries

When a positron impinges on a surface with keV energy, multiple electrons, called secondary electrons, can be knocked out of the material [40]. In case of a head-on collision with a nucleus, the positron may leave the material again and is usually called a backscattered positron. While exiting the material, a backscattered positron has a non-vanishing probability to capture an electron to form positronium. With energies of eV and more the Ps is often called fast, hot, or backscattered positronium [41]. The momentum, direction and ratio of these secondaries yield valuable information about the surface of the material [42], but in the assessment of the interior of a sample, it is only the secondary electrons which can be used to tag the impact of the positron defining the time $t_0 = 0$ ns for PAS measurements [43].

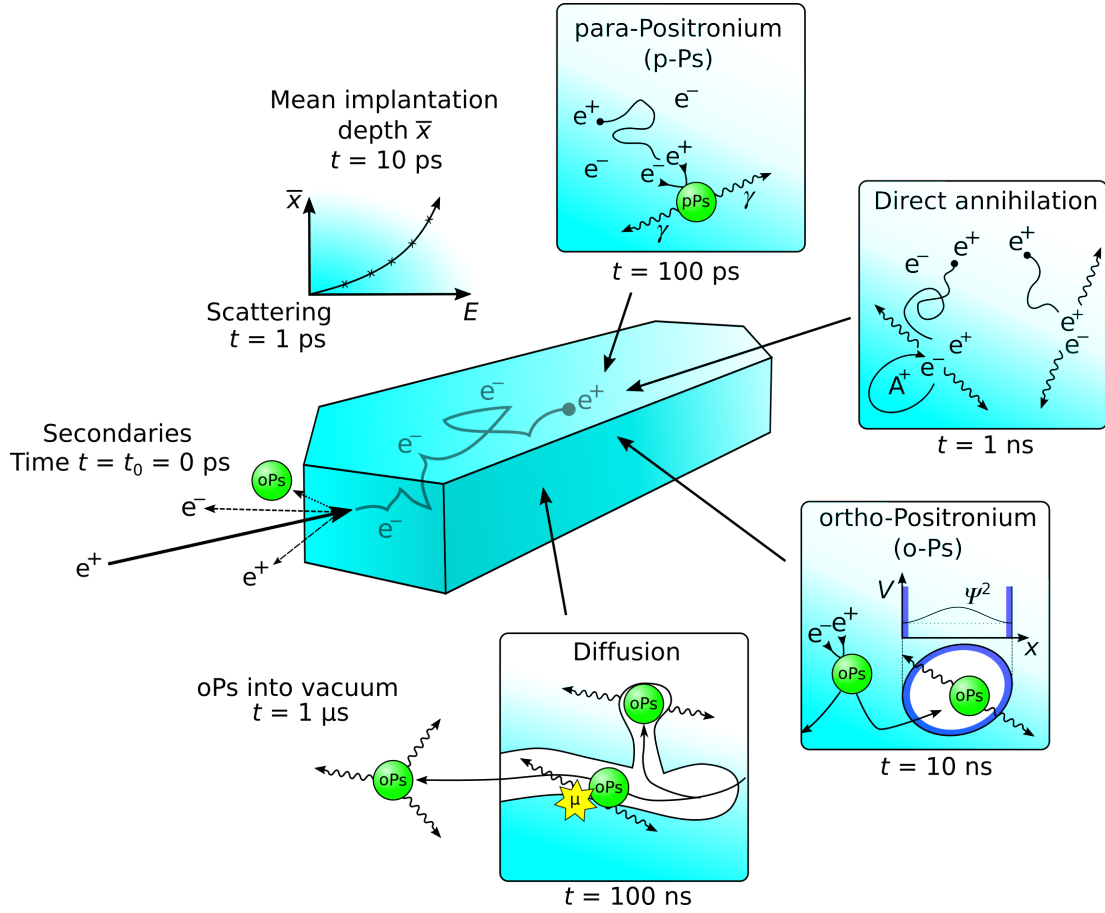


Figure 2.3: Schematic overview depicting the physical processes, and their timescales, which are of importance for PAS. Reprint of Figure 1.1 for readability.

2.1.2 Scattering

After implantation, the positrons undergo multiple collisions inside the bulk material reaching thermal energies in a matter of tenths of picoseconds. The main loss mechanism is the ionization of electrons, which form the so-called ‘spur’. The implantation depth depends on the positrons initial energy E . The obtained distribution in 1D depicted in Figure 2.4 is called Makhovian implantation profile [44] which can be parametrized as

$$P(x) = \frac{d}{dx} \mu_T(x) = \frac{mx^{m-1}}{x_0^m} \exp \left[- \left(\frac{x}{x_0} \right)^m \right], \quad (2.5)$$

where m is a material-dependent dimensionless parameter and x_0 is related to the mean penetration depth \bar{x} by

$$x_0 = \frac{\bar{x}}{\Gamma[m^{-1} + 1]}, \quad (2.6)$$

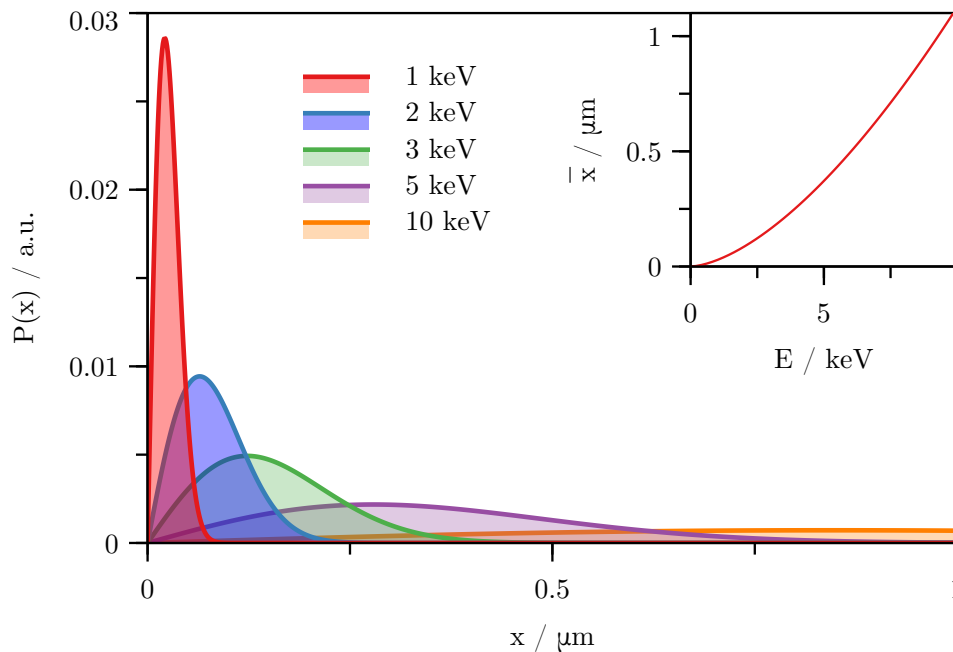


Figure 2.4: One dimensional positron implantation profiles $P(x)$ for different energies E_{e^+} and the relation to the mean implantation depth \bar{x} (in the inset).

with Γ being the Gamma function. Depending on the implantation energy E (in keV) the mean penetration depth is

$$\bar{x} = \frac{\alpha}{\rho} E^n, \quad (2.7)$$

with the density ρ [g/cm^3]. The exponent $n = 1.6$ and $\alpha = \frac{40}{\sqrt{2}} \mu\text{g cm}^{-2} \text{keV}^{-n}$ are material dependent fitting parameters, which can be obtained by transmission/absorption experiments with samples of different thickness. The values 1.6 and 40 were found empirically with techniques where positron impinge perpendicular on the surface of the material. The denominator $\sqrt{2}$ was introduced to account for grainy samples where the mean incident angle is 45° [45–47]. Considering a finite 2D or 3D object of the size comparable to \bar{x} , a convolution of the 1D case becomes inevitable when the implantation profile is of relevance to assess non-uniform properties or volumes as will be shown in Section 5.1.

2.1.3 para-Positronium Annihilation

A thermalized positron may pick an ionized electron from the spur (spur model [48, 49]) or capture a bound valence electron (Ore Model [50]) and form positronium. In the case of anti-parallel spins, it is the singlet pPs which decays with a lifetime of 125 ps by intrinsic annihilation emitting two back-to-back 511 keV photons.

2.1.4 Direct Annihilation

Positrons do not necessarily need to form positronium prior to the annihilation. The direct annihilation is a competing process of positrons annihilating with an electron in the sample. Any electron, ionized from the spur and bulk (valence as core) electrons will result in the emission of two gamma rays. Because of the smaller overlap of the positron and electron wave function compared to the pPs, the lifetime is slightly larger, material dependent, and usually below 1 ns.

2.1.5 ortho-Positronium Annihilation

While understanding and considering all the processes is important for the analysis of porous materials with positrons, oPs annihilation has the highest sensitivity in the porosity assessment. oPs, formed as pPs but having parallel spins, has lifetimes depending on its surroundings ranging from a couple of ns up to a maximum of 142 ns. The upper limit is the vacuum value predicted by QED, a shortening of the lifetime of oPs inside a material arises due to the so-called *pick-off* effect, the annihilation of the positron with another electron from the bulk rather than the one it is bound to.

This process leads to a direct correlation between the lifetime of oPs to the surrounding electron density, i.e., pore topology of a material. Since the de-Broglie wavelength is in the same order of magnitude as the characteristic sizes of typical voids in bulk material, atomic defects, micro-, or mesopores, etc., these mimic a finite potential well where oPs can be quantum mechanically confined in a lower energy state than in the bulk. The size and geometry of a void will dictate the wave-function and probability distribution of such confined positronium. As expected, the trapped oPs is more likely to be found in the centre of the void because of the repulsive force of the electrons on the pore surface through the Pauli exclusion principle against the positronium's electron.

Nevertheless, there is a non-vanishing overlap of the positronium wave function with the electron layer at the surface of the void leading to pick-off annihilation into two photons with a lifetime characteristic to the void's topology. An approximation of such confinement and its correlation to the lifetime was initially described by the Tao-Eldrup model [12, 13], and subsequently refined [14, 51]. Moreover, if the material has a porous network, oPs lives long enough to diffuse through it.

The propagation process is geometry dependent, i.e., more classical in channels or based on quantum mechanical tunnelling from pore to pore in closed voids [52–54]. During the diffusion process, the interconnectivity throughout the network and to the object's surface, as chemically active sites, are probed. This may be observed by measuring lifetimes associated to large voids, lower oPs formation due to the oxidation of oPs or the emission into vacuum with a kinetic energy equal to the confinement energy in the pore. The escape from the bulk material is followed by the self-annihilation in vacuum into three gamma rays with the very distinct lifetime of 142 ns and can be well separated from micro- and mesopore decays.

Studies employing these relation are presented in Section 6.2 and 6.3. Additional information can be gained from gamma ray energy, making the probed electron momentum distribution visible in Doppler shifts of the photons as detailed in Section 2.2.3 and 2.2.4.

There exist a multitude of experimental techniques which are sometimes published under different names and abbreviations as there is no overall agreement on a nomenclature. Nevertheless, the most common techniques can still be grouped under PAS as all methods are recording spectra of the annihilation in one or another dimension, time, energy, collinearity, etc.

2.2 Positron Annihilation Spectroscopy Methods

While all methods are relying on the fact that a positron will annihilate with an electron at some point different techniques may focus on different processes and quantities of the interaction of positrons with matter. This is partially because there might be a specific interest in a particular processes but also because the quantities often require different detectors and a thorough detection has not yet been developed.

2.2.1 Positron Annihilation Lifetime Spectroscopy

Positron annihilation lifetime spectroscopy (PALS) is a method to investigate the structure of a bulk sample on a nm scale. A schematic of the experimental setup of the spectrometer is shown in Figure 2.5. It is based on acquiring a lifetime spectrum S by recording millions of start (t_0) and stop (annihilation) events as shown in Figure 2.6. This spectrum $S(t)$ is a sum of exponentials convoluted with the detector's time resolution $R(t)$. The individual components are corresponding to the different annihilation channels i with lifetimes τ_i and intensities I_i presented in Section 2.1.

$$S(t) = \sum_i I_i/\tau_i \exp(-t/\tau_i) \otimes R(t) \quad (2.8)$$

The ratios and lifetimes of these can be extracted with sophisticated fitting procedures involving Markov Chain Monte Carlo, Simulated Annealing and Bayesian Inference methods, and provide quantitative information in terms of interconnectivity, pore sizes and distribution of a porous network [5, 14]. Prior calibration and/or simulation of the setup to compensate different two gamma/three gamma detection efficiencies which can distort such relations might be important.

Studying the evolution of these parameters for different sample sets, or a single sample which underwent treatments, gives insight into the relative porosity or defect parameters. When using a positron beam different implantation energies can be used to do a depth profiling. This gives access to study distributions,

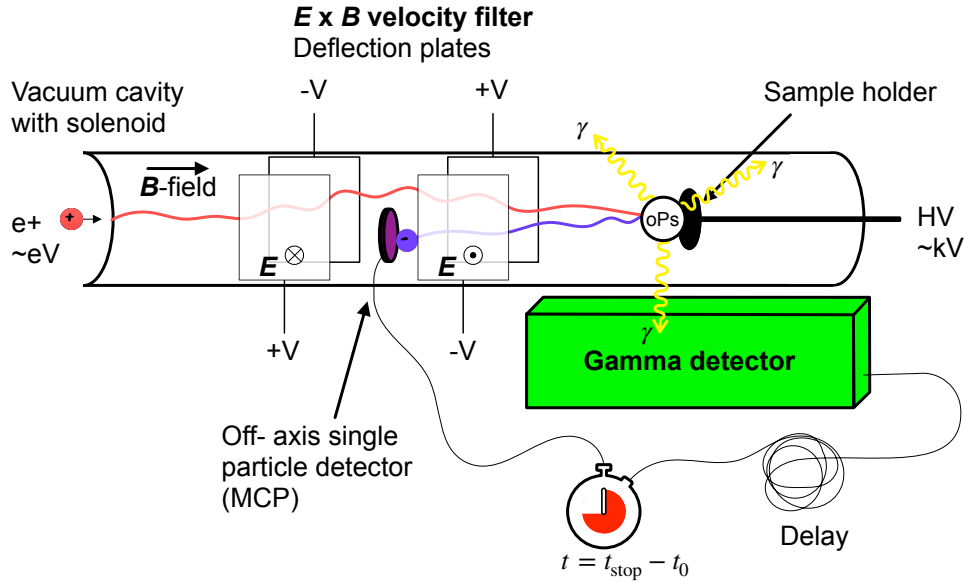


Figure 2.5: Schematic of a positron annihilation lifetime spectrometer. Positrons coming from the left (red) pass a time tagging system like shown in Figure 3.4. Secondary electrons (red) created on positron impact on the target are transported back to the time tagging detector MicroChannel Plate (MCP) .

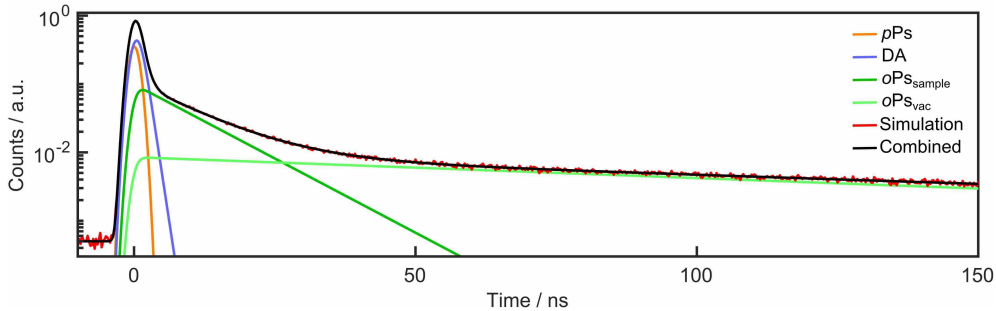


Figure 2.6: Example of a typical positron annihilation lifetime spectrum. Reproduced with permission.

buried layers, or interfaces. For the interpretation of these values beyond relative changes from one measurement to the other one has to rely on models.

Tao-Eldrup Models

The correlation between positronium lifetime and void size already indicated in Figure 2.2 has been explained at first by Tao-Eldrup model (TE). Tao and Eldrup could validate it with experimental data on $r \leq 1$ nm sized pores in bulk polymers [12, 13]. It assumes the positronium being a single particle of twice the electron mass confined in the ground state of an infinite spherical potential well. In the centre an infinite lifetime is assumed, in an empirically determined distance $\Delta R = 0.16$ nm to the walls the spin-averaged Ps lifetime of 0.5 ns. The overall annihilation rate is an average of the annihilation rate in the whole volume

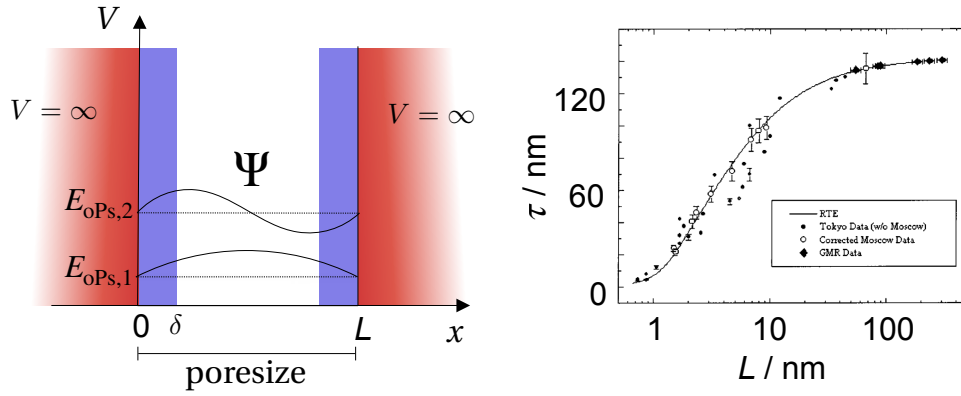


Figure 2.7: The principle of the Rectangular extension of the Tao El-drup model (RTE) and its experimental confirmation [14]. Reproduced with permission. Copyright 2001 American Chemical Society.

of a pore weighted by the absolute value of the oPs wave function. The TE annihilation rate of confined oPs in a pore with a radius of $R + \Delta R$ is

$$\Gamma_{\text{TE}}(R) = \Gamma_{\text{A}} \left[1 - \frac{R}{R + \Delta R} + \frac{1}{2\pi} \sin \left(\frac{2\pi R}{R + \Delta R} \right) \right], \quad (2.9)$$

with the spin-averaged vacuum annihilation rate $\Gamma_{\text{A}} = (\Gamma_{\text{pPs}} + 3\Gamma_{\text{oPs}})/4$, the singlet Γ_{pPs} and triplet Γ_{oPs} vacuum annihilation rates. However, the TE model has its limitation, it only works well for pore sizes with $R < 1$ nm.

An approach to overcome this restriction was to include excited states in the model [55]. Acknowledging temperature is important because in larger pores excited states can be more easily populated as the energy difference gets smaller. Even if this model was in agreement with the data of well-known materials, it failed in practice because to get an accurate result the calculation of several high order Bessel functions and its zeros was needed [55]. A more practical solution was implemented by Gidley et al. [5]. They implemented rectangular pores in the TE model, called the RTE model, and included excited states which were necessary to model larger pores with diameters up to 100 nm and temperatures above 0 K as shown in Figure 2.7.

The approximation is of advantage as the calculation of excited states can be simply done by separation of variables. Moreover, it has been shown in [56], that the annihilation rate is quite geometry independent and more defined by the classical mean free path, $l = 4V/S$, where V is the volume and S the surface area of the pore. The results of the RTE can, therefore, be scaled to represent other (closed) pore geometries.

For calculation of the annihilation rate in the RTE model the positronium wave function $\Psi(x, y, z)$ is approximated as the single-particle solution of an infinite square well with side lengths a, b, c ,

$$\Psi(\mathbf{x}) = \sqrt{\frac{8}{abc}} \sin \left(\frac{n_x \pi x}{a} \right) \sin \left(\frac{n_y \pi y}{b} \right) \sin \left(\frac{n_z \pi z}{c} \right), \quad (2.10)$$

In the center of the pore, the annihilation rate is assumed to be Γ_T . In the region near the walls, within a distance δ , the spin-averaged rate Γ_A is taken. The overall annihilation rate is expressed as

$$\Gamma(x, y, z) = \Gamma_A - \Lambda(x, y, z) ,$$

$$\text{with } \Lambda(x, y, z) = \begin{cases} \frac{\Gamma_{\text{pPs}} - \Gamma_{\text{oPs}}}{4}, & \begin{pmatrix} \delta \\ \delta \\ \delta \end{pmatrix} \leq \begin{pmatrix} x \\ y \\ z \end{pmatrix} \leq \begin{pmatrix} a - \delta \\ b - \delta \\ c - \delta \end{pmatrix}, \\ 0, & \text{otherwise,} \end{cases} \quad (2.11)$$

The expectation value of the annihilation rate can be expressed as the trace of the density matrix times the annihilation rate matrix [14]. For an oPs atom in thermal equilibrium with the pore, the Boltzmann equation describes the population of the excited states. Therefore the non zero elements of the density matrix are

$$\rho_{ijk,ijk} = \frac{\exp(-E_{ijk}/k_B T)}{\sum_{i,j,k=1}^{\infty} \exp\{-E_{ijk}/k_B T\}}, \quad (2.12)$$

with the energies from the three-dimensional infinite potential well,

$$E_{\text{tot}} = E_i + E_j + E_k = \frac{h^2}{8m} \left(\frac{n_x^2}{L_x^2} + \frac{n_y^2}{L_y^2} + \frac{n_z^2}{L_z^2} \right), \quad \text{with } n_x, n_y, n_z \in \mathbb{N}^+ \quad (2.13)$$

the equation becomes,

$$\rho_{ijk,ijk} = \frac{\exp\left[-\frac{h^2}{16k_B T m_e} \left(\frac{i^2}{a^2} + \frac{j^2}{b^2} + \frac{k^2}{c^2}\right)\right]}{\sum_{i,j,k=1}^{\infty} \exp\left[-\frac{h^2}{16k_B T m_e} \left(\frac{i^2}{a^2} + \frac{j^2}{b^2} + \frac{k^2}{c^2}\right)\right]}. \quad (2.14)$$

Since the density matrix is diagonal for a system in thermal equilibrium, its only needed to evaluate the diagonal entries of the annihilation rate matrix

$$\begin{aligned} \Gamma_{ijk,ijk} &= \langle ijk | \Gamma_A - \Lambda(x, y, z) | ijk \rangle \\ &= \Gamma_A - \frac{\Gamma_{\text{pPs}} - \Gamma_{\text{oPs}}}{4} \int_{\delta}^{a-\delta} dx \int_{\delta}^{b-\delta} dy \int_{\delta}^{c-\delta} dz \Psi^2(x, y, z) \\ &= \Gamma_A - \frac{\Gamma_{\text{pPs}} - \Gamma_{\text{oPs}}}{4} f_i(a) f_j(b) f_k(c), \\ &\quad \text{with } f_p(q) = 1 - \frac{2\delta}{q} + \frac{1}{p\pi} \sin\left(\frac{2p\pi\delta}{q}\right). \end{aligned} \quad (2.15)$$

The expected annihilation rate in the RTE model thus is

$$\begin{aligned}
 \Gamma_{\text{RTE}} &= \text{Tr}\{\rho\delta\} = \sum_{i,j,k=1}^{\infty} \rho_{ijk,ijk} \delta_{ijk,ijk} \\
 &= \Gamma_{\text{A}} - \frac{\Gamma_{\text{pPs}} - \Gamma_{\text{oPs}}}{4} F(a, T)F(b, T)F(c, T) , \\
 \text{with } F(q, T) &= \frac{\sum_{i=1}^{\infty} f_i(q) \exp\left(-\frac{\hbar^2 i^2}{16q^2 k_{\text{B}} T m}\right)}{\sum_{i=1}^{\infty} \exp\left(-\frac{\hbar^2 i^2}{16q^2 k_{\text{B}} T m}\right)} \\
 &= 1 - \frac{2\delta}{q} + \frac{\sum_{i=1}^{\infty} \frac{1}{i\pi} \sin\left(\frac{2i\pi\delta}{q}\right) \exp\left(-\frac{\hbar^2 i^2}{16q^2 k_{\text{B}} T m}\right)}{\sum_{i=1}^{\infty} \exp\left(-\frac{\hbar^2 i^2}{16q^2 k_{\text{B}} T m}\right)} .
 \end{aligned} \tag{2.16}$$

The constant δ was determined by comparison to the TE-model's ΔR to be 0.18 nm. Overall it is the most spread model used in the literature and was successfully used to predict the lifetime of simple pore structures like 3D spheres, cubes, 3D rectangles, 2D channels and 1D sheets [5, 6, 8, 16, 17, 51, 56–65].

To study other changes in the PAS parameters suitable models need to be developed on a case by case basis.

For example, out-diffusion from porous thin films was successfully described by Gidley et al. [5]. Adaptations from there for a study zeolites, a materials with a more complex hierarchical organization, is described in Section 6.2.

2.2.2 Time-of-Flight

Measuring the velocity distribution of the oPs emitted into vacuum by recording the spatial annihilation points outside of the sample or measuring the time spectrum of oPs flying a pre-defined distance like shown in Figure 2.8. A subsequent analysis with Monte Carlo simulations allow determining what underlying velocity distribution would create the measured time or spatial distributions. The velocity is directly linked to the confinement energy of the pore oPs was emitted from and holds information about the quantum-mechanical state of oPs in the pore network [52, 53, 66].

2.2.3 Doppler Broadening Spectroscopy

If the positron and electron would be at rest when they annihilate the 511 keV line would have the width of the detector resolution. While this assumption is true for positronium, in fact mostly any positron just before annihilation, an electron can have various energies and momentum from being bound as a core electron, over valence to conduction electrons. This electron momentum p will introduce a Doppler shift of the two thought to be $E_{\gamma,1} = E_{\gamma,2} = 511$ keV photons γ_1 and γ_2 by the part of the momentum perpendicular to the detector surface p_{\perp} [67].

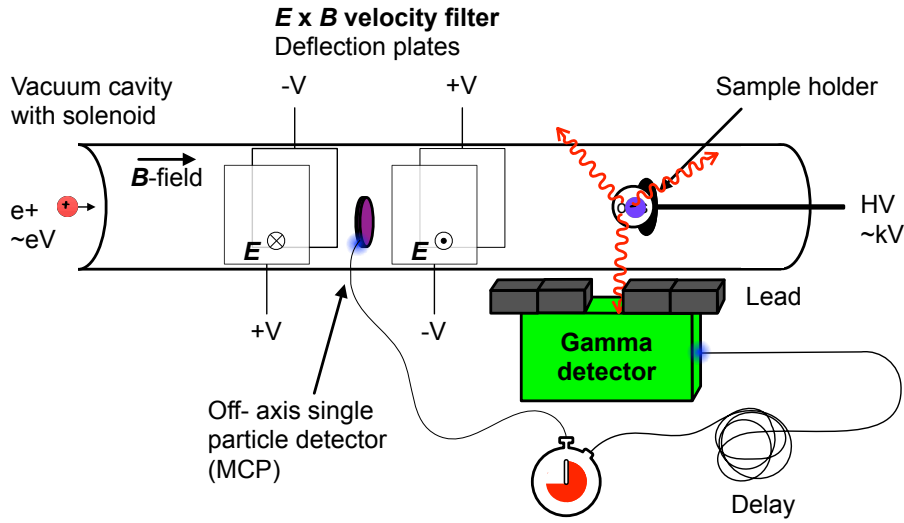


Figure 2.8: Sketch of the Time-Of-Flight (TOF) spectrometer. Positron coming from the left (red) pass a time tagging system like shown in Figure 3.4. Secondary electrons (blue) created on positron impact on the target are transported back to the time tagging detector MCP. Reproduced with permission. Copyright 2019, American Physical Society.

Assuming without loss of generality the electron momentum pointing to the plane of detector 2 (measuring $E_{\gamma,2}$) the shifted photon energies are

$$E_{\gamma,1} = m_e c^2 - \frac{1}{2} p_{\perp} c, E_{\gamma,2} = m_e c^2 + \frac{1}{2} p_{\perp} c. \quad (2.17)$$

The collection of a spectrum composed of many photons smears the individual shifts to a broadening of the original 511 line.

Recording the energy spectrum of the annihilation photons as shown in Figure 2.9a using a High Purity Germanium (HPGe) detector which has an excellent energy resolution (~ 1 keV) and therefore is sensitive to the broadening is called Doppler Broadening Spectroscopy (DBS). Analyzing the line shape lets one deduce information about the momentum distribution of the electrons the positrons annihilated within the bulk.

In the analysis of the DBS spectrum usually, the ratio of different areas to the total peak area are compared, i.e., the S-parameter is the central S-area ("S" for shape) over the total area as a parameter for low momentum electrons and the similar W-parameter ("W" for wings) for large momentum electrons as shown in Figure 2.9c. This way e.g. the concentration of crystallographic point defects, as they typically bind low momentum electrons or chemically active sites, can be studied because these alter the for the positron visible electron momentum distribution [4].

An advanced way of DBS is CDBS which is based on the same principle but makes use of the greatly improved Signal to Noise Ratio (SNR), see Figure 2.9c, by using two HPGe detectors in coincidence and back-to-back geometry. The

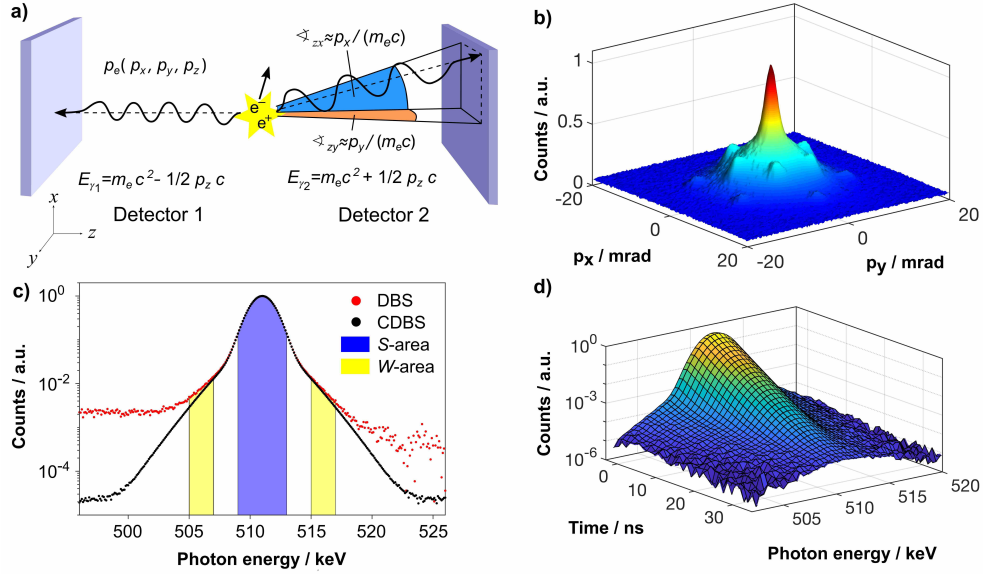


Figure 2.9: a) The properties of the two photon annihilation of a positron at rest with an electron having a finite momentum $p_e = (p_x, p_y, p_z)$ that fulfills momentum and energy conservation. b) A simulated 2D ACAR spectrum of the distribution of p_x and p_y momenta of crystalline quartz. c) Typical spectra of DBS (red dots) and Coincidence Doppler Broadening Spectroscopy (CDBS) (black dots) of $E_{\gamma,1}$. d) An AMOC plot, the relief of a DBS spectrum in time. Reproduced with permission. Copyright 2019, John Wiley and Sons.

higher sensitivity allows to study the full line shape rather than comparing areas as done in DBS. When comparing full sample sets it is also common to compare all samples to a reference by looking at the ratio of the full line shapes [68].

2.2.4 Angular Correlation of Positron Annihilation Radiation

Like in DBS the momentum of the electrons induces not only Doppler shifts but also deviations from the momentum conservation thought to be back-to-back annihilation angle of the two 511 keV photons. With two detectors in coincidence one measures the Angular Correlation of positron Annihilation Radiation (ACAR), i.e., the 511 keV photons, which deviate slightly from 180° as shown in Figure 2.9b. Considering the case of annihilation at rest with $p_{\text{tot}} = 0$ where the photons would impinge perpendicular on two detectors would have 0° between them. If now the annihilating electron has a momentum $p = p_{\parallel} + p_{\perp}$ with p_{\perp} perpendicular to the

detector surface the measured angle becomes

$$\angle = \arctan \left(\frac{p_{\parallel}}{m_e c + p_{\perp}} \right) \quad (2.18)$$

$$\approx \frac{p_{\parallel}}{m_e c} , \quad (2.19)$$

$$\text{with } p_{\perp} \ll m_e c \text{ and } p_{\parallel} \ll m_e c . \quad (2.20)$$

With scanning or position sensitive detectors this correlation can be extended to two dimensions (2DACAR). Compared to CDBS an even better SNR leads to not only assessing the concentration of crystallographic point defects or chemically active sites but can also yield information about their type. In the case of defect-free samples, it was also employed to measure the Fermi surface of the material [69].

2.2.5 Age Momentum Correlation

Combining a DBS spectrum taken with a HPGe detector with a scintillation detector with good time resolution one can study the evolution of the 511 line within the positron lifetime as depicted in Figure 2.9d. This additional information of the time domain allows to observe variation in the positron-electron momentum distribution depending on the positron state, e.g. slowing down, trapping, chemical reactions and positronium pick-off annihilation [70].

An only recently developed advanced implementation of this technique, Four-dimensional Age MOmentum Correlation (4DAMOC), a position-sensitive HPGe combined with a position-sensitive detector with a good timing resolution allows to measure the lifetime of the positron and the full 3D momentum of the electron $p_e = (p_x, p_y, p_z)$ at the same time. It can be understood as combining AMOC with 2DACAR [71].

2.2.6 Others

While these are the most common techniques the list of possible methods is long and growing. Worth to mention is the development of Positron induced Auger Electron Spectroscopy (PAES) [72], a surface analysis tool making use of the potentially very shallow annihilation of an electron to induce Auger transitions without using damaging and more penetrating high energetic electrons.

Furthermore, the in Section 3.1.3 presented the development of the buffer gas positron trap by Surko [73, 74], accumulating thousands of positrons over long periods, implanting them all at once opens the path to observe kinematic effects by taking 'snapshot Positronium Annihilation Lifetime Spectroscopy (PALS) spectra'. This method called Single Shot Positron Annihilation Lifetime Spectroscopy (SSPALS) is a completely new field with many more possible applications [75], e.g. shooting light from pulsed lasers onto the sample at times of the positron implantation or positronium emission [76, 77].

Moreover, a lot of effort was not only put in developing these methods but also a considerable amount of work lies in the proper data analysis of the methods. For now, the interested reader is invited to peruse the given references for a higher level of detail.

Chapter 3

Instrumentation

The heart of any applied research is the experimental apparatus. Having a setup creating *good* data in terms of the quantities of interest is the prerequisite for a successful analysis. This chapter introduces the instrumentations related to PAS and the work conducted in this sector. Section 3.2 describes the continuous slow positron beam at ETH used for most of the studies presented in this thesis. The interdisciplinary project of the development of an in-operando cell, PAS measurements of chemicals under reaction at up to 1 bar and 500 °C, is presented in Section 3.3. Furthermore, development of additional positron beam access at ETH (Section 3.4) and tailored detector arrangements (Section 3.5) are presented. Finally, a novel approach to radioactive source production schemes utilizing the increased availability of medical proton cyclotrons is discussed in Chapter 3.6.

3.1 Experimental Techniques

The basis of any positron experiment is the source. From a strictly instrumental point of view, one can separate PAS devices into two groups, bulk- and beam-based, distinct in the way the sample is probed. The different energy spectra of the positrons lead to different penetration depths as will be discussed in Section 3.1.2 and 3.1.3. While Beam PAS is superior in the structural analysis by its variable implantation profile and spot size, also requiring less sample material, it is more expensive in acquisition and maintaining.

In contrast, bulk PAS does not necessarily need to be operated under vacuum and can, therefore, be performed in gas atmospheres more easily. The source is in contact with the sample and is directly penetrated by the keV positrons. In a beam, the positrons have to travel up to several meters at lower energies (\sim eV). Since any residual gas will readily annihilate the positrons the formation and transport has to be in Ultra High Vacuum (UHV). A more complete overview about implementation can be found here [20].

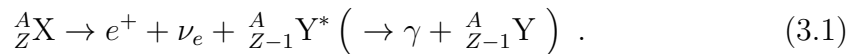
3.1.1 Positron sources

In contrary to electrons positrons are not abundant in nature. One has to rely on sources which are most often man-made to deliver sufficient rates (MHz - GHz). In general, there are two physical processes which are exploited for the generation of positrons, β^+ decay and pair-production. The radioactive sources are more commonly seen in laboratory scale experiments while techniques involving pair-production usually involve heavier machinery like accelerators or reactors which only exist in large scale facilities.

Overall, the activity of positron sources has intrinsic limits. The positron emission from radioactive sources is capped by self-absorption. After a certain activity, i.e., large amounts of necessary material, the probability of positrons stopping in the source becomes significant. This limit is reached for ^{22}Na at around 5 GBq [78, 79]. For the case of pair production, it is the intensity of the primary beam and also the amount of power that one can deliver to the converter without damaging it [80]. The highest rate of fast positron rates for electron LINAC based pair production sources is $10^{13} \text{ e}^+/\text{s}$ at the EPOS facility in Halle, Germany [79]. The strongest fast positron source used for a slow positron beam creation worldwide is at the NEutron induced POsitrone source at MUniCh (NEPOMUC) [78]. The positrons generated by pair production from absorption of high-energy prompt gamma-rays reach an intensity of $10^{14} \text{ e}^+/\text{s}$.

Radioactive

The most commonly used sources on a laboratory scale are radioactive β^+ emitters. During the decay, a proton in a nucleus with mass number A and atomic number Z disintegrates into a neutron, positron and electron neutrino, leaving behind a daughter nucleus. Depending on the available energy, this process is followed by further decays. E.g. if the nucleus is in an excited state, with the emission of photons,



The kinetic energy the positron carries away is determined by the three-body decay and ranges from 0 keV up to the endpoint energy T_{max} , see Figure 3.1. While there exists plenty of different β^+ sources, they have vastly different properties which led to the use of only a few for PAS [20].

The main criteria is the half-life $t_{1/2}$. A long half-life guarantees a similar positron flux over a given period. This makes comparisons between different experiments easier as one can work under similar initial conditions. Moreover, a long-lasting source does not need frequent replacement which with current infrastructure results in less downtime and eventually operational costs. Other source properties of interest are the exact decay scheme, possible ways of production, i.e., reactions and their cross-sections, the β^+ branching $\Gamma(\beta^+)$ as a measure of positron emission relative to the overall activity of a source which might have other competing decay

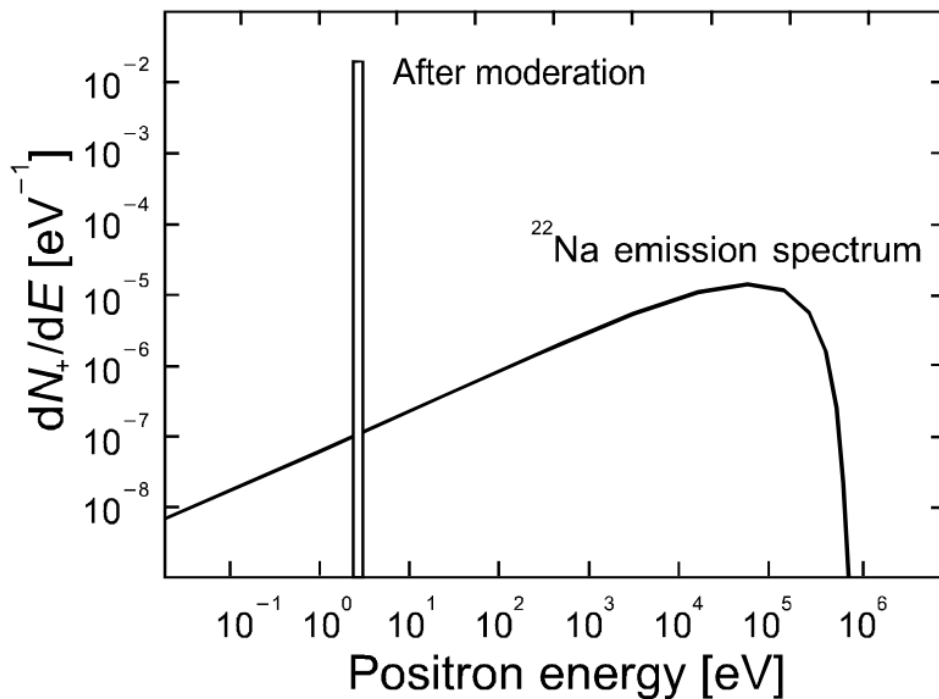


Figure 3.1: Scheme of the energy spectrum of positrons emitted from a ^{22}Na source and after moderation in a (110) tungsten foil.

channels as e.g. electron capture, and the already named endpoint energy T_{max} . Last but not least, also the safety during handling and usage, e.g. phase at room temperature or vacuum compatibility, is important for laboratory purposes.

A list of common sources and their properties is presented in Table 3.1. In the past, ^{58}Co was the most often used emitter as it was easily produced in high activities from Ni being exposed to fast neutrons in the flourishing days of fast nuclear reactors. Nowadays it is more convenient to use ^{22}Na as it offers a much larger β^+ branching and a vastly longer half-life of 2.6 years with a similar endpoint energy. This is only possible due to the advance in particle accelerators technology which increased their abundance in industry. Isotopes requiring high fluxes at high energies are even produced under profitable business concept like being done by iThemba Labs¹ in South Africa.

Pair Production

Rather than from decay, one can also get positrons by pair-production from energetic photons. A photon with sufficient energy ($E_\gamma \geq 2m_{\text{particle}}$) can convert into a pair of particle anti-particle conserving energy and quantum numbers like charge, strangeness, lepton number, etc. As also momentum needs to be conserved, this process is only possible if another object carries away the recoil. Practically, this is achieved by irradiating a solid with hard gamma rays where either single nuclei or electrons will interact with the photon [82]. The necessary photons

¹<http://www.tlabs.ac.za/>

Table 3.1: Endpoint energy T_{\max} of the β^+ , half-life $t_{1/2}$, β^+ branching $\text{Br}(\beta^+)$, production target and reaction, maximum cross-section $\sigma_{\max}(E_\sigma)$, corresponding projectile energy E_σ , EOB activity A_{EOB} for 1 μm foil sources of ^{58}Co , ^{22}Na and ^{48}V [81].

Isotope	^{58}Co	^{22}Na	^{48}V
T_{\max} (keV)	475	545	695
$t_{1/2}$ (d)	70.85	950	15.97
$\text{Br}(\beta^+)$ (%)	14.9	90.6	50
Reaction	$^{58}\text{Ni}(\text{n}_{\text{fast}},\text{p})$	$^{27}\text{Al}(\text{p},\text{X})$	$^{48}\text{Ti}(\text{p},\text{n})$
$\sigma_{\max}(E_\sigma)$ (mb)	600	44	382
E_σ (MeV)	10	44	12
ρ_{target} (g/cm^3)	8.9	2.7	4.5
A_{EOB} ($\text{kBq}/10^{16}$ neutrons)	47.5	-	-
A_{EOB} ($\text{kBq}/\mu\text{A h}$)	-	0.05	24

can be created by multiple methods, accelerator-based bremsstrahlung [83–86], nuclear reactor neutron-induced bremsstrahlung [87–89] or from intense laser pulses either via Compton scattering with a high energetic electron beam or again bremsstrahlung from laser-accelerated electrons in solid targets [90–92].

The cross section σ_{N} for positron electron production from a photon interacting with a nucleus has a threshold energy of $E_\gamma = 2m_e = 1.022 \text{ MeV}$ and depends on the target’s material atomic number Z as $\sigma \propto Z^2$. The creation can also occur in the field of an atomic electron, called *triplet production* due to the emission of a third particle, the electron struck from the recoil. The kinematics result in a higher threshold of $E_\gamma = 4m_e = 2.044 \text{ MeV}$ and the cross section is only linear with Z $\sigma_e \propto Z$. Standard targets are Au, Pt or W. Tungsten is preferred because of its higher melting point and lower costs. Both pair production channels have a strong energy dependence early on, and quickly become the dominant photon matter interaction and plateau at about 100 MeV. A plot of the attenuation coefficient of tungsten versus photon energy is shown in Figure 3.2.

3.1.2 Bulk Setup

In Bulk PAS one uses a thin radioactive β^+ emitter which is sandwiched between sample material. The positrons of the β^+ spectrum with energies ranging from 0 keV to e.g. 543 keV for ^{22}Na uniformly probe several hundreds of μm . The sample chamber is surrounded by gamma detectors to observe the annihilation photons. If interested in the correlation of the time of annihilation with the moment of implantation one has to work with a positron source where it is possible to trigger on a nuclear transition gamma-ray as the t_0 which is in coincidence with the emission of a positron from the β^+ source. This necessity and its long lifetime makes ^{22}Na to the most commonly used source in Bulk PAS.

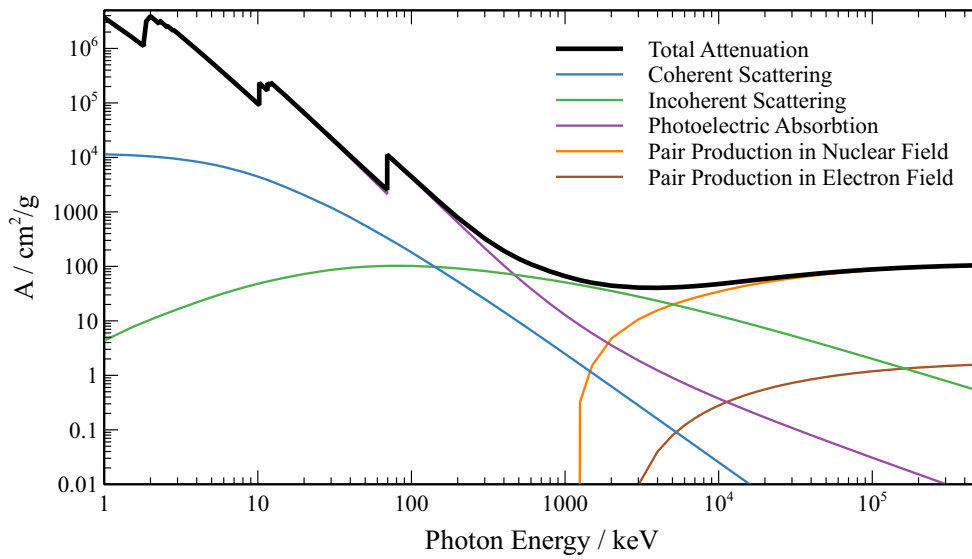


Figure 3.2: Gamma attenuation coefficient of the different physical processes and the total attenuation for tungsten [93].

3.1.3 Beam Setups

A schematic of the parts of a positron beams is shown in Figure 3.3. For almost all experiments with positrons, having a source of monoenergetic e^+ is of great advantage or even crucial because a narrow energy spectrum leads to the ability to distinguish and investigate underlying physics where the energy is an important parameter. Since all available sources emit positrons with an energy spectrum up to several MeV via pair production or radioactive decay, the method of converting positrons of variable energies to a more or less constant energy called *moderation* is of great interest. Starting from a narrow energy distribution of these slow positrons after moderation on the eV scale, they can then be guided electrostatically or magnetically, accelerated with the mean energy between some eV up to tens of keV and impinged on a sample.

In contrast to the one from the Bulk PAS, this allows a narrow implantation profile which enables to study surface, surface near, bulk and depth-dependent effects. While the operation of a bulk setup can be done at atmospheric pressure, the high cross-section of slow positrons with gas requires an ultra-high vacuum (UHV) environment. The time-tagging of positrons necessary to study the annihilation in the time domain can be done in two ways. The first is time bunching the positrons relative to a global clock to define the moment of arrival by beam manipulation. The second is by detection of secondary particles produced by the positrons on impact.

Positron Moderation

Ever since its first discovery in 1950 [94] moderation efficiency has been a vibrant field of research. The conversion from fast (keV) to slow positrons (\sim eV) occurs

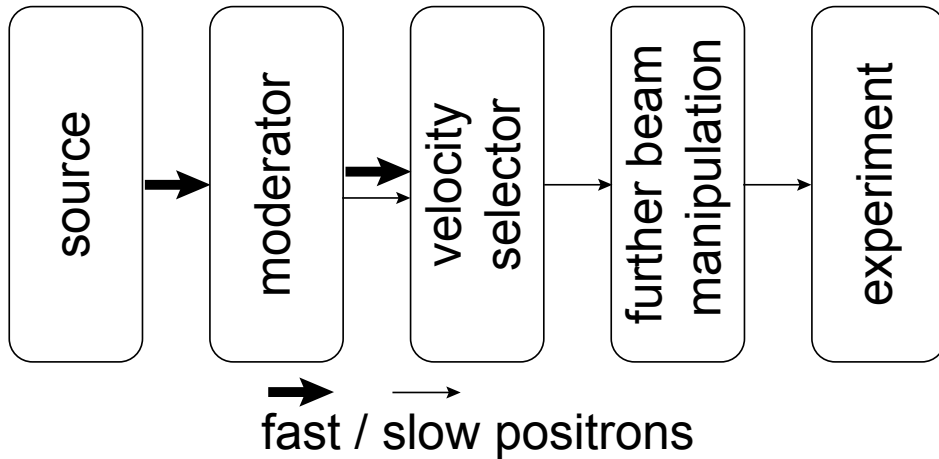


Figure 3.3: Schematic parts of a slow positron beam.

in a range of specific solids and moderation itself is even in them a subsidiary process [95, 96]. Two classes of materials with specific properties allow a small fraction of the positrons which have stopped in the material to be re-emitted from the surface before they annihilate. One type is metals with a negative work function [97], the other is materials with very long diffusion lengths for positrons [96]. Because the positron flux is one of the main performance parameters of a positron beam, a high efficiency is of special interest. This is valid for both standard radioactive source laboratory beams as for intense beams. Especially because the production rate of fast positrons for both methods has the upper limits discussed in Section 3.1.1.

Different moderators are compared by a quantity called *moderation efficiency* ε . In the literature, one finds different definitions of ε . A commonly used one is a) to use the number of moderated positrons N_{mod} divided by the number of fast positrons impinging on the moderator. Another is b) to divide N_{mod} by the total number of positrons emitted by the source or c) in the case of a radioactive source the overall activity. Each definition serves as an assessment of various aspects. When using a) one focuses on the performance of the material, b) weights in the geometric design and c) is a more general approach, e.g. useful when the source has different decay channels, having a higher overall decay rate than actual positron activity (positrons emitted per second) and radiation safety is of interest. When not stated differently, from now on definition b) is used for the moderation efficiency ε .

The standard work function based moderators are thin single crystalline tungsten foils or tungsten meshes with efficiencies of the order of 10^{-4} [98]. The most efficient commonly used moderators rely on the long diffusion length of positrons in frozen rare gases, e.g. neon has a typical efficiency of $\varepsilon = 7 \times 10^{-3}$ [96]. A novel class of moderator developed at ETH, the cyclotron trap assisted moderator, outperformed these with an efficiency of 1% in an proof-of-principle experiment [99]. Moreover, preliminary simulations suggest a potential of up to 10%. The moderation method and the work towards dedicated positron sources to deliver rates

similar to standard radioactive base beams is presented in Chapter 4.

Continuous Beam

A slow positron beam in *continuous* mode is using the low energy positrons directly from the moderator without further modifying the time domain. The rate is therefore based on the stochastic emission of positrons from the source and follows a Poisson distribution. Continuous operation provides the highest average positron rate for a given source. Typical rates are 10^6 e⁺/s for radioactive sources but go up to 10^9 e⁺/s for reactor based beams.

A high rate seems to be beneficial to gather the needed statistics faster but depending on the application it can also lead to unwanted pile-up background. Measurements like TOF and PALS, which rely on detecting the annihilation photons up to hundreds of ns after the arrival of the corresponding positron, will suffer if there is a high chance of having two annihilation events in the same time window. The times of arrival will not have distinctive stops but can be paired with uncorrelated signals which results in distortions of the data. A way to overcome this, is to compress the random arrivals by bunching them to short pulses which is presented in the next section.

The time tagging is usually achieved by detecting secondaries emitted on positron impact shown in Figure 3.4 for the case of a magnetically guided slow positron beams. With the target at a negative potential U , Secondary Electrons (SE) created at the target will be accelerated upstream. A charged particle detector, such as a MCP facing downstream, can then detect them and serve as a t_0 tagging. The time resolution hereby depends on the MCP resolution, which is usually sub ns, and in most cases on the more significant differences in \sim ns transit times of the electrons [43]. For enhanced efficiencies, one can combine the detector positioned slightly off-axis with an $E \times B$ deflection system which steers the positrons going downstream around the detector and deflects the upstream moving electrons in the opposite direction directly on the detector.

Bunched Beam

Time bunching is a technique where a continuous beam is manipulated by time-varying electric fields in order to have predefined time periods where positrons can arrive on the target and when not. One can imagine the potential set on the source to vary in time in a manner that creates a velocity distribution linear in time. Later positrons will start to catch up to earlier ones until at one point in time all positrons are in the same spot. Obviously, it is not possible to increase the potential indefinitely. Therefore it needs to be ramped down in regular intervals. The resulting velocity distribution will resemble a sawtooth wave. The positrons will travel in compressing *bunches* with a repetition rate of the sawtooth signal. The term bunch, usually understood as a multiple number of particles arriving in a short time followed by a time of no arrivals, has to be loosened for the technically achievable positron rates and bunch frequencies (kHz-MHz). Depending on the

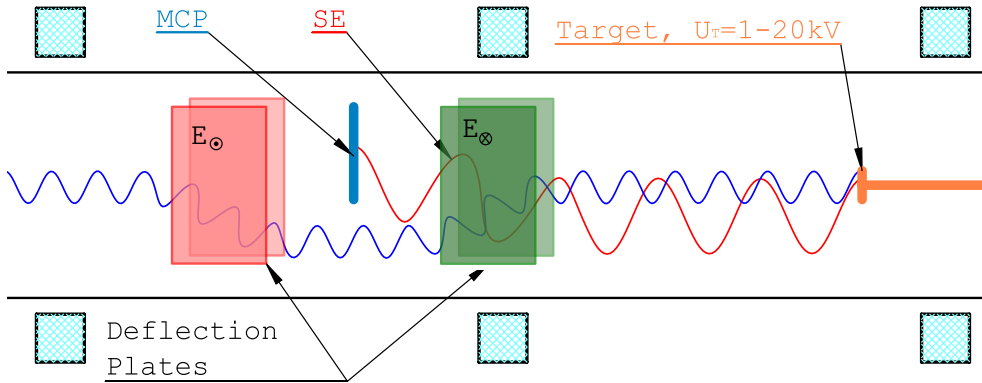


Figure 3.4: Scheme of a time tagging setup used for continuous positron beams. Positrons are coming from the left (blue) and are guided around the MCP tagging detector which faces the target, secondary electrons (SE, red) created by the impact of positrons on the target at a given potential U are transported back to the MCP. Taken from [100]

positron flux after moderation and the repetition rate, a bunch can have no positrons, one positron or multiple ones.

The time of arrival will be defined by a transit time offset relative to the signal triggering the bunching spread out from a time jitter due to the energy distribution of the positrons. In specific configurations, it can be of interest to combine the bunching with a secondary detection scheme. Either when the bunching time of arrival distribution is worse than the time resolution of the secondary particle detector or when one requires the rejection of possibly ‘empty’ bunches.

Buffer Gas Trap

A beam utilizing the principle of a buffer gas trap is also a bunched beam but works with an accumulating technique rather than accelerating positrons to different velocities [73]. Positrons emitted from the moderator enter a multistage Penning-Malmberg trap with a stepwise increasing depth. To be trapped, the positrons need to dissipate energy such that they fall below the entry potential. This is achieved by having nitrogen as a first buffer gas at residual pressures.

A collision of a e^+ with an N_2 can excite the nitrogen molecule and catch the positron in the first stage of the trap. Subsequent collisions will cause the positrons to be eventually trapped in the last stage with leftover energy of a few eV. To reduce the annihilation losses during the trapping, the buffer gas pressure is reduced towards the last stage by differential pumping. In the last stage another gas, CF_4 , is used to further cool down the positrons to a thermal energy spread. The different molecular structure is more susceptible for low energetic excitations and has a lower annihilation cross-section.

With this technique, positrons can be accumulated for up to a few seconds before saturation is reached. To keep the positron plasma better confined, the last stage’s

electrode is segmented into four quarter shell cylinders. On these electrodes, an alternating electric potential is set on top of a constant one. The time-dependent potential is a sine function with $\pi/2$ phase shifts between the 4 electrodes to create a rotating electric field. This method is called the *rotating wall technique* and is proven to compress the plasma efficiently [74, 101].

Sudden release of the stored positrons allows intense bunches of up to 10^5 e^+ /bunch. The repetition rate is correlated with the number of e^+ per bunch and the energy spread, as the accumulation and cooling time is reduced. Useful frequencies are therefore lying in \sim Hz – 10 kHz.

3.1.4 Detectors

The detectors necessary for PAS include gamma-ray detectors and single charged particle detectors. Single-particle detectors are required for tagging and the assessment of the beam quality. Important characteristics are the time resolution, dark count rates, detection efficiency and depending on the application, possibly the position resolution. Given the low currents of particles, all single-particle detectors follow an electron multiplication scheme to create a readable electric signal. The incoming particle, called the primary, will impinge on a cathode where it releases secondary electrons on impact. These electrons are then further multiplied by accelerating them onto dynodes. By repeating this process, 10^5 to 10^8 electrons are finally collected on an anode which can be read out by electronics. Depending on the dynode structure one differentiates between discrete dynode multiplication as found in standard electron multipliers and photomultipliers (PMT), and continuous dynodes as in channeltrons or MCP, see Figure 3.5.

The MCP is the most utilized. An early review of the technology can be found here [102]. For similar detection efficiencies, it is the most compact and the only method in which the multiplication preserves the position information. Specific anode configurations exploiting this, offer sub-mm position resolution. Moreover, MCPs offer the best time resolutions due to the low spread of the electron shower from the short transit times.

The other single particles detectors can offer better detection efficiencies because of higher open area ratios (active to dead area ratio) and enjoy exceptionally low accidentals from having less dynode surface. These accidentals, also called dark counts, mostly originate from thermal emission of electrons from the dynode surface which produces signals indistinguishable from real events. The gamma-ray detectors, mostly scintillators, are used to study the annihilation photons.

An incoming high-energy photon can excite or ionize the scintillators material. With the energy of the particle transferred to the scintillator. The energy is then re-emitted by *scintillation*, the emission in the form of light mostly in the visible to UV spectrum. With electric light sensors such as photomultipliers, which exploit the photoelectric effect to transform the photons into electrons and then multiply these in the schemes as the single-particle detectors, the initial particle becomes measurable. While the list of performance parameters is similar to the one of

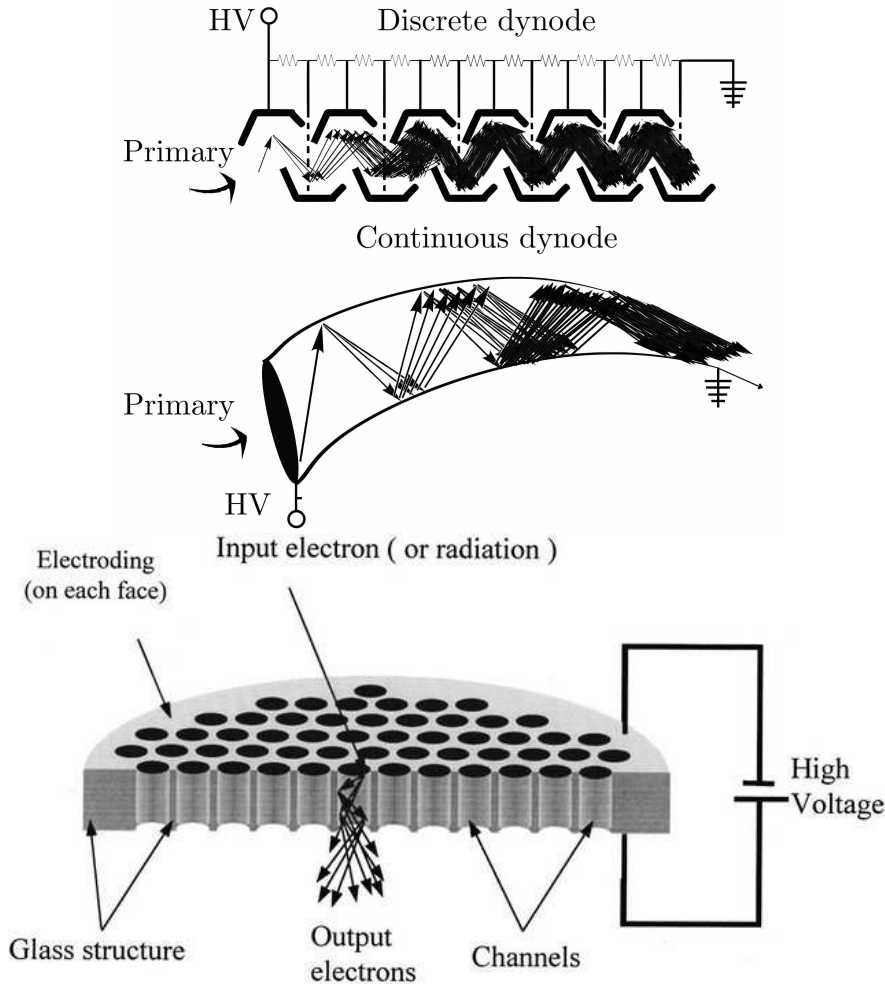


Figure 3.5: Multiplication schemes of different single particle detectors [103, 104].

single-particle detectors, time resolution, detection efficiency, etc., scintillator assemblies are also assessed by the energy resolution of the energy of the primary particle. The characteristics are dependent on multiple material parameters as geometrical configurations.

3.2 ETH Zürich Continuous Slow Positron Beam

Most of the PALS work presented in this thesis evolves around the magnetically guided ETHZ Slow Positron Beam located at ETH Zurich Höggerberg. With the groundwork being started at CERN in 2002. The setup was build and designed for a study of exotic decays of oPs in vacuum as described by Alberola et al. in 2006 [24]. After being moved to Zurich in 2010 a new goal to measure the oPs 1S-2S transition was set [105, 106].

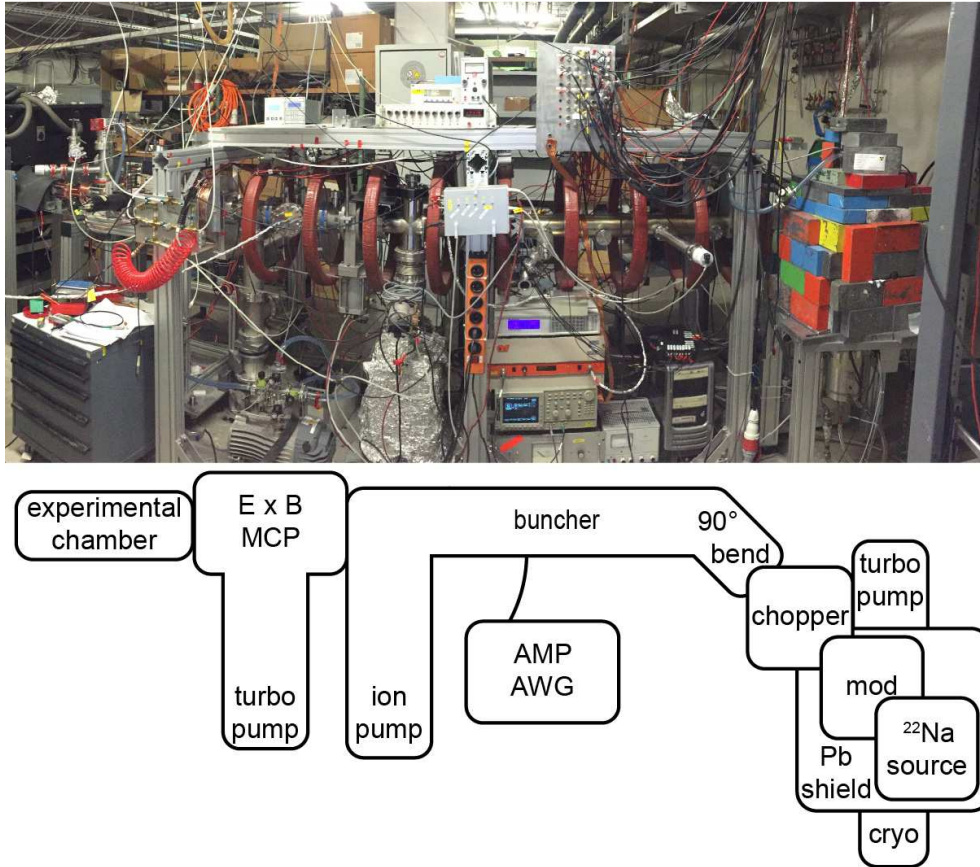


Figure 3.6: Picture and schematic of ETH slow positron beam.

It was during that period, that the search for efficient positron to positronium into vacuum converters for fundamental studies sparked the material characterization activities. Since then, some parts like detector setup and the source have undergone multiple upgrades but the overall concept stayed the same. A picture and a scheme are shown in Figure 3.6.

The power train is a ^{22}Na Source, with the current one inherited from the ALPHA experiment². It had an initial activity of 417 MBq (19.06.2014). In the early years in Zurich, it was coupled to a cryogenic solid neon moderator. Later in 2015, it got replaced by a tungsten mesh moderator as the rare gas moderator was moved to the second positron beam which is based on a buffer gas trap [107]. Only to go via an intermediate frozen argon moderator upgrade in early 2018 back to a more efficient neon version in late 2019. Depending on the model the source potential was set to be between 100 V and 200 V. After the moderator, a couple of beam shaping components follow before the positrons are guided to the experimental setup.

The first element is the chopper. A combination of drift tubes and a high transmission mesh allows blocking the beam by applying a potential. With in-house developed electronics allowing to switch up to $\Delta V = 200$ V on top of a DC offset V_0 with rise and fall times of $\tau \sim 20$ ns at frequencies of up to $f \leq 500$ MHz

²<http://alpha.web.cern.ch>

and duty cycles D between $3\tau/f \leq D \leq (1 - 3\tau/f)$ the beam can be effectively *chopped* into bunches of positrons.

After the chopper, the beam is magnetically guided along a 90° bend. A small fraction of fast positrons penetrated the moderator material. Because they contaminate the beam quality, they get separated from the slow ones. While the moderated positrons follow the magnetic field lines adiabatically, the unmoderated ones with keV energies go straight and annihilate in the vacuum chamber wall. The bend therefore effectively acts as a crude velocity selector.

Between this energy filter and the experimental sector lies a long straight vacuum pipe with approximately an 1 m long drift tube which serves as a buncher, see Section 3.1.3. A set of coils in a Helmholtz configuration creates a uniform magnetic field up to the experimental section. The tube was specifically designed to have a 50Ω wave impedance mimicking a RF cable to perfectly accept alternating potentials. When coupled to an arbitrary waveform generator (AWG) and an amplifier (AMP) a time-dependent voltage $V(t) \sim t^2$ can be applied. This will accelerate positrons arriving at the entry at later times. The squared dependence will lead to linear velocity distribution. On exit, the same trick can be applied to increase the overall energy amplitude. With the correct slope and travel distance, all accelerated positrons will arrive at the same time (smeared only by the effect of the energy spread).

A set of steering coils complements the beam manipulation to correct for any drift introduced by the curve or offset from prior misalignments. Afterwards, a $E \times B$ deflection system like shown in Figure 3.4 guides the beam around the positron tagging system.

The beam is then coupled into a magnetic guiding field of the sample chamber created by a long solenoid. It has the advantage over larger coils that a solenoid has very little external stray field which could disturb detector operation. The sample stage consists of a long arm reaching inside the solenoid with an insulated holder at the end. With an electric feed through (SHV20) it is possible to set the sample to potentials up to 20 kV. This will accelerate the positrons onto target once they reach the proximity and define the implantation energy E_{e^+} . Moreover, it also defines the energy of the secondary electrons which are guided back up-stream to the tagging system.

Outside of the vacuum chamber multiple gamma-ray detectors were incorporated to around the beam forming the PAS spectrometer. A Bismuth Germanium Oxide (BGO) and Barium Fluoride (BaF_2) scintillator for PALS are shown in Figure 3.7. The large solid angle of the BGO with its size of $20 \text{ cm} \times 8 \text{ cm}$ makes the BGO ideal to measure oPs escaped into vacuum. It's high Z and density provide a high detection efficiency. In comparison, the BaF_2 is much smaller ($2.5 \text{ cm} \times 2 \text{ cm}$) but its intrinsic fluorescent decay is a lot faster, 0.7 ns versus the 300 ns of BGO. A comparison of the time spectra is shown in Figure 3.8. Therefore, the BaF_2 is important for resolving oPs components with $\tau \sim \text{ns}$ lifetimes. The High Purity Germanium (HPGe) detector with its good energy resolution is needed for DBS measurements. It is connected to a liquid nitrogen cryostat to be cooled down to 77 K. This is important as the HPGe is a semiconductor which would otherwise

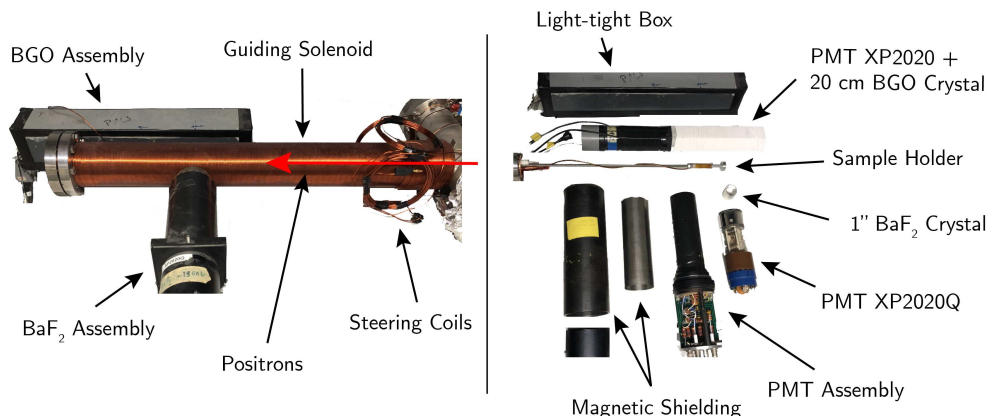


Figure 3.7: Overview of the PALS spectrometer. (left) The guiding solenoid, steering coils, the BaF₂ and BGO detectors. (right) Details of the detectors and the sample holder which is inside the guiding solenoid vacuum tube.

Table 3.2: Comparison of PAS detectors in terms of energy resolution $\Delta E = \sigma_{511}/511$ keV and time resolution σ_t

Material	ΔE (%)	σ_t (ns)
BGO	16	5
BaF ₂	18	0.9
Ge	0.3	³

suffer from high intrinsic current/background at room temperature. The energy spectra of the HPGe and the BaF₂ (very similar to the BGO one) are shown in Figure 3.9. Table 3.2 summarizes the different characteristic time and energy resolutions.

3.3 Operando Cell

The ETH operando cell is a project initiated in as a continuation of the zeolite performance study [16, 17]. Zeolites are a porous material used as catalysts in chemical engineering applications. The reactions require temperatures of several hundred °C and gas pressures of around 1 bar to have a sufficient rate. A standard application is the cracking of olefins. Adding zeolite Z to the cracking of a reactant ABC into products A and B will speed up the reaction rate k



In principle the catalyst in a reaction is not consumed by the reaction. However, in reality, unwanted product or containment C can deactivate the zeolite rendering

³Integrated electronics of detector does not allow a timing readout.

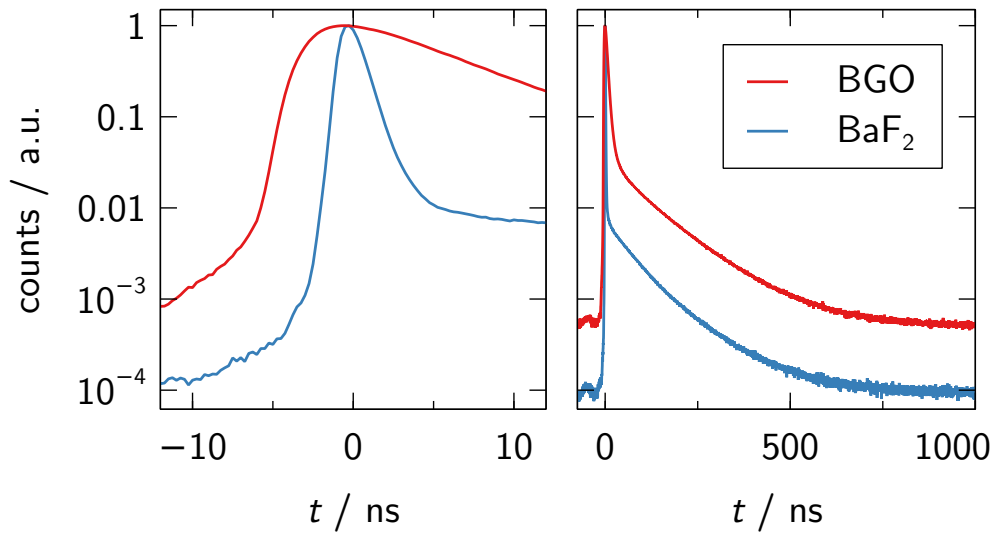


Figure 3.8: Time spectra of the PALS detection system of the BaF₂ and BGO scintillator normalized to the prompt peak. A zoom on the peak is shown on the *left* to emphasize the different time resolutions.

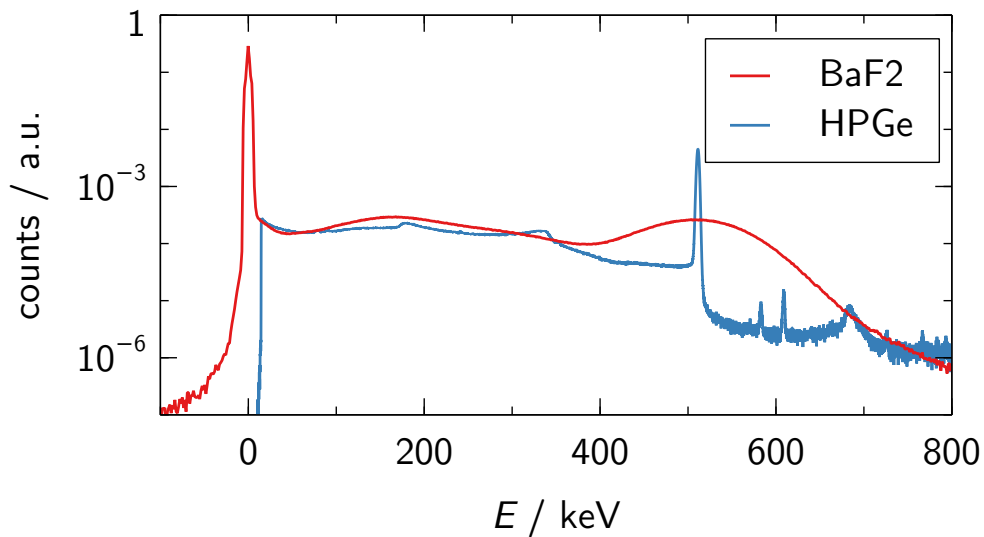
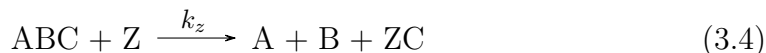


Figure 3.9: PAS energy spectrum of the HPGe and BaF₂ detectors normalized to the area.

it useless.



This process is quantified as the lifetime of the catalyst. For the design of zeolites for industrial applications it is therefore of interest to have not only a high reaction rate $k_z \gg k$ but also a sufficient lifetime.

In the mentioned study [17], differently performing zeolite types were measured through PALS. A clear relation between the lifetime under reaction and a PALS response was striking. To further investigate this effect on a microscopic level it is of interest to study the evolution of the porous framework of the zeolites.

A simple approach would be to iteratively characterize samples with different durations under reaction. It is however anticipated that the time it takes for the transfer from the reaction oven to the positron beam and the different conditions in temperature and gaseous atmosphere will have an impact on the precise structure of the coke deposition. Therefore, the ideal case is to perform a measurement under *in-operando* conditions, i.e., while the use-case reaction is running.

This challenging task of combining an olefin cracking reactor cell with a positron beam was started together with the Advanced Catalysis Engineering group of ETH in late 2016. The main criteria are:

- positron beam
 - vacuum for positron transport up to interface
 - positron tagging capabilities for PALS
 - annihilation detectors shielded from high temperature
 - magnetic field for positron transportation in proximity of cell
- reactor cell
 - controllable stable operation of up to 600 °C
 - controlled flow of 1 bar of gas through sample (ethanol - nitrogen mixture)
 - sample close to interface - limiting e^+ annihilations in gas
- interface
 - acceptable transmission for positrons
 - withstand 1 bar differential pressure
 - sustain the high temperature

A setup for the characterization of polymers under controlled humidity at atmospheric pressure was already implemented by Zhou et al. at AIST, Japan [108]. The schematic is shown in Figure 3.10. A pulsed positron beam with a narrow phase space and a beam spot of 200 μm originating from an intense electron

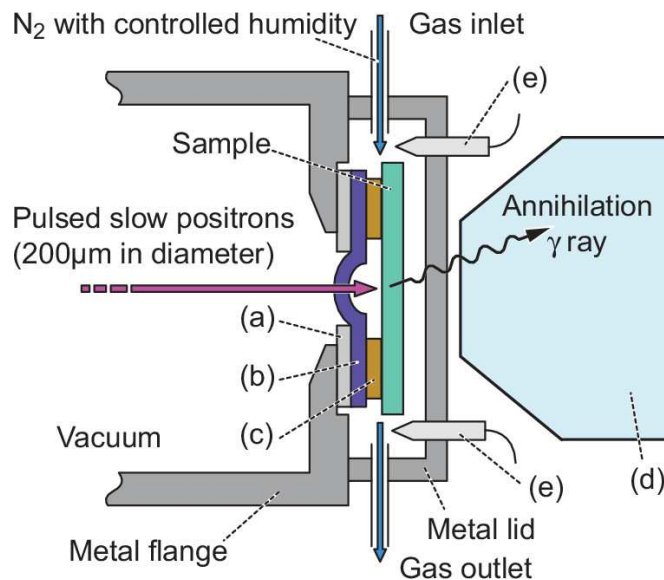


Figure 3.10: Schematic of the in-situ humidity controlled PAS cell at AIST, Japan (not to scale). (a) Silicon frame, (b) SiN film window, (c) Kapton foil spacer, (d) BaF₂ scintillator, and (e) temperature-humidity probes. Reprinted with permission from [108]. Copyright 2012 by AIP Publishing.

LINAC pair production source is shot through a 30 nm thick 0.5 mm × 0.5 mm SiN window onto the sample mounted in an enclosed humidity-controlled chamber.

For the design of the ETH operando cell, two differences exist, the higher temperature and the worse beam spot size. Theoretically, the pulsed buffer gas trap beam would be the more suitable candidate as the driving positron source. Because the secondary beamline, see Section 3.4.2, was only in the early planning stage and the positronium spectroscopy experiment was installed for long term measurements, the cell was drafted for the continuous beam. This imposed additional requirements on the design. The cell would need to be floated at a high voltage of around 10 keV to ensure the positrons penetrate the interface and still have sufficient implantation energy. Furthermore, the interface would need to act as the positron tagging surface for the secondary electron emission on positron impact. On the same time, it should produce as little uncorrelated spontaneous electrons, a main source of background, as possible.

The principle and first test prototype shown in Figure 3.11 was designed, built and tested in close collaboration with the members of the ACE group of the Institute for Chemical and Bioengineering (ICB), DCHAB, ETH. An austenitic stainless steel cap and body form the housing. With a copper o-ring gasket inspired by CF sealing, the two parts enable to load the sample, and seal for UHV tightness afterwards. The gas lines are fed from the back and flush the whole interior space in which the sample sits.

A resistive heater wire mounted as a spiral in a ceramic housing enables to deliver the necessary power to heat the cell. The temperature is measured either by the resistivity curve of the heater itself or by an additional thermocouple introduced

axially from the back into the ceramic. Electrically isolated with a PEEK or ceramic cylinder the whole cell is mounted on a stick and can be placed and floated at HV in the beam UHV chamber in the same fashion as sketched for the standard targets in Figure 3.4. This also ensures the shielding of the detectors from the high temperature by the external vacuum vessel as enables the usage of the existing solenoid for the magnetic guiding field. The power cables for the heater not shown here are also floated at the same HV and electrically isolated by an inductive transformer from the PID controller power supply outside of the vacuum system.

The interface is a SiN window from Silson Ltd.⁴ similar to the one used in the AIST approach. A square substrate of SiN $14\text{ mm} \times 14\text{ mm} \times 0.4\text{ mm}$ hosts membranes of $350\text{ }\mu\text{m} \times 350\text{ }\mu\text{m} \times 30\text{ nm}$ in a rectangular pattern with a pitch of 0.75 mm within a 10 mm circular boundary. This arrangement offers the technical maximum possible optical transmission or *open area ratio* of $T = (0.35\text{ mm})^2 / (0.75\text{ mm})^2 = 0.218$. The transmission probability for 5 keV positrons through a 30 nm SiN is around 95% [109]. Larger membrane sizes or a smaller pitch would reduce the stability below the critical 1 bar requirement. The window substrates were glued to the cell cap right after production from Silson Ltd. To reduce potential charging effects of the SiN from positron beam exposure a 3 nm Au deposition was added with the help of the deposition service from Paul Scherrer Institute (PSI).

The prototype shown in Figure 3.11 was used for the first tests just under vacuum, without heating and gas. A previously well-characterised zeolite powder with an oPs vacuum fraction was mounted by acetone solution evaporation. To study the effect of the cap and window the following sequence was measured

1. w/o a cap
2. w/ a cap but w/o a window
3. w/ a cap and w/ a window

The first part of the study showed the expected PALS response. During the second part of the measurements first problems became eminent. An unexpectedly high number of uncorrelated spontaneous electrons were emitted from the cap under HV. This issue could be resolved by additional surface polishing. Afterwards, the results were also in line with the data from 2. The third part of the investigation showed a severe problem. It yielded no oPs production. From original fraction of about $f_{\text{oPs,vac}} = 0.3$ is expected to be attenuated by the open area ratio and the physical positron transmission to $f_{\text{oPs,vac}}^{\text{SiN}} = 0.3 \cdot 0.218 \cdot 0.95 = 0.06$. An investigation by mounting the window in front of an MCP confirmed the problem of little to no transmission. A precise analysis with an optical microscope performed by Begoña Puértolas shown in Figure 3.12 revealed what one might already expect when looking at the optical transmission from a light source presented in Figure 3.11. The windows were manufactured too small. With the measured side length of $131\text{ }\mu\text{m}$ the open area is only 0.03 . This explains why no $f_{\text{oPs,vac}}^{\text{SiN}} = 0.009$ was found.

⁴<http://silson.com/>

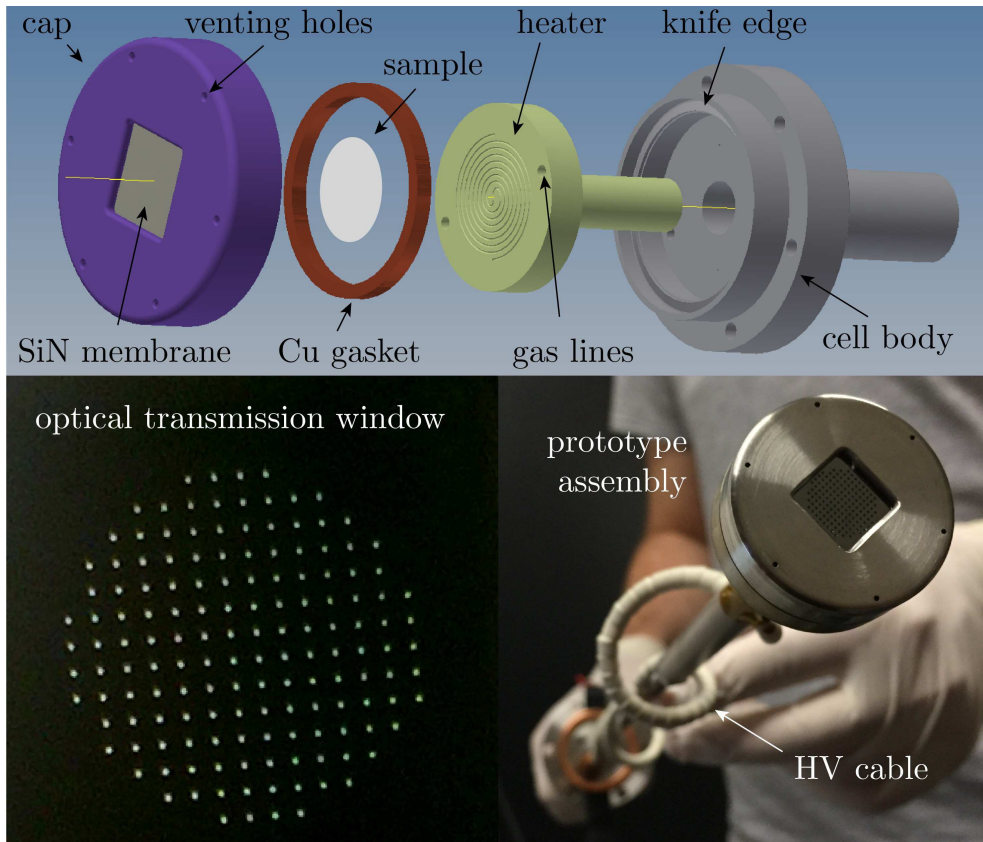


Figure 3.11: Schematic and pictures of the operando cell.

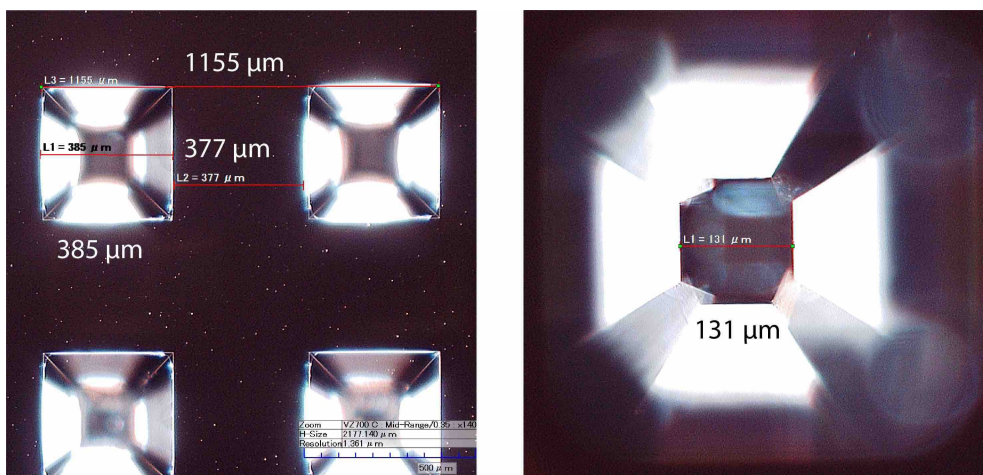


Figure 3.12: Optical microscopy size measurement of the SiN membrane

During the downtime, because of several month lead time for the new windows, several other tests were performed. To distinguish between potential error sources a blank cap without any SiN window was used to study the design approach.

1. heating tests
2. chemical reaction rate
3. vacuum tightness w/ & w/o heating
4. heating w/ HV
5. vacuum tightness w/ heating w/ old window

The chemical reaction study lead to an improved gas design which guarantees a better saturation for the sample by introducing an axial offset between the inlet and outlet. Reproducible vacuum tightness was achieved after several glueing iterations. The joints of the different materials under temperature cycling required specific care, i.e., several layers of glue, to deal with the different expansion rates. Several heating cycles with the cell under vacuum and HV were also performed successfully.

The vacuum heating test performed with the old window assemblies to test membrane stability under heat strain revealed a severe mistake from the SiN window supplier. During the heating, major leaks would appear. Further warming up would let the window fall off the cap. After consultation with the company, it was found that the glue used to mount the SiN in the cap is not specified for the required temperature in contrary to what was communicated during the design phase. With a resistance of up to 180 °C the utilised two-component epoxy Loctite 9492 is not suitable for the needed 600 °C.

Several other in-house tested epoxies which are rated for the necessary temperature, on the other hand, failed to meet the UHV sealing requirement. Pictures of the new, recently received, SiN windows are shown in Figure 3.13. The proper open area ratio is visible.

Currently, a supposedly last resort of special welding techniques to seal the SiN wafer via an intermediate material to the cap is explored with the help of the mechanical workshop of PSI. While a proper vacuum seal is strictly necessary, the project of utilizing the second positron beam of the laboratory, the buffer-gas trap based bunched beam, for PAS measurements (see Section 3.4.2) could already ease the requirements. The beam offers a much better energy spread (\sim thermal) and a smaller beam spot, thus the membrane arrangement could be switched from an array to a single one. In regard of the space limitations, one single 1 mm² window is considerably more stable and will be a lot easier to handle. Moreover, the cell would not need to be floated at 10 keV to guarantee sufficient positron implantation energies because the pulsed positron bunches can be accelerated beforehand.

On success, this would revolutionize the understanding of catalytic materials and other functional solids by enabling the time-resolved monitoring of pore network evolution under reaction conditions as also studying the details of gas sorption in

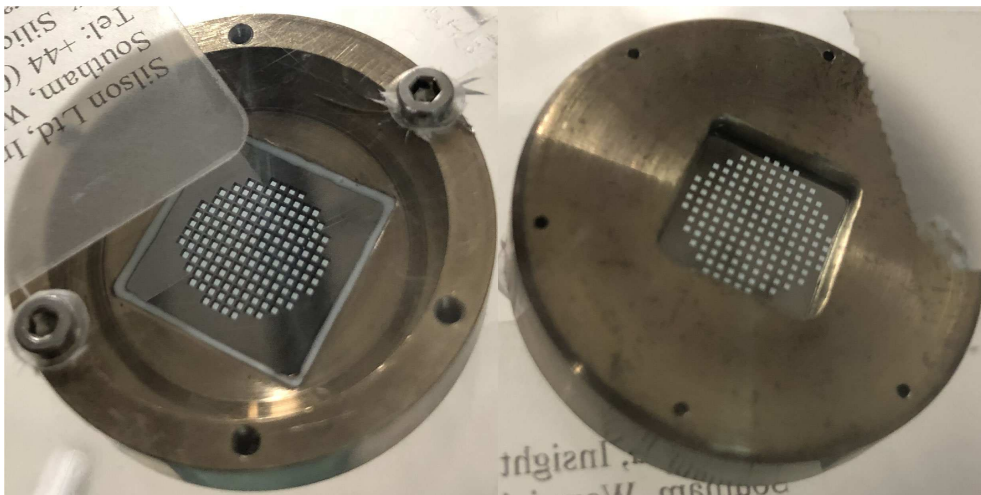


Figure 3.13: Picture of new operando window with an open area ratio of 21.8%.

porous materials.

3.4 Beam Development

Improving the properties of an experimental setup, a higher availability or tailoring towards specific applications goes hand in hand with any research. One part was to study the performance of the buffer gas trap based beam for material characterization. In Section 3.4.1 a simulation developed to model the bunching process is presented. The results applied to the characteristics of the buffer gas trap beam are shown in Section 3.4.2.

3.4.1 Bunching Simulations

One important figure of merit of a positron beam for material characterization is the time resolution of the positron arrival on a target. A good time resolution allows the differentiation of decay components with short lifetimes. As presented in Section 3.1.3, there exist two ways of tagging a positron arrival. The direct way, by defining the arrival by e.g. detection of secondary particles generated on impact, or the indirect way by pulsing the positrons to pre-define the possible time of arrivals.

The time resolution of the direct methods, i.e. the detection of SE, is limited to $\sigma_t \sim 1$ ns because of the spread of the electron transit time, detector and DAQ time jitter [43]. The spread of the time of arrival in the indirect way is related to the energy spread of the positrons. A difference in energy leads to different transit times covering the same distance in the beam. For example a typical transportation energy of a positron beam is 100 eV. The cw-beam has an overall beam length of around 3 m. Considering an energy difference of 1 eV between two

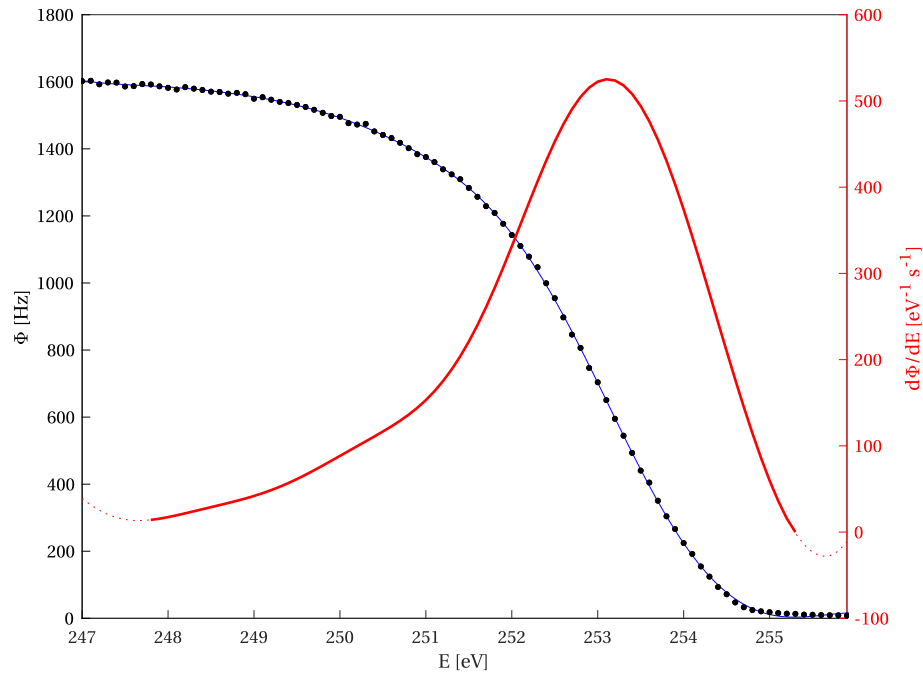


Figure 3.14: Measured positron energy distribution of the cw-beam used as an input for the bunching simulations.

positrons, the difference in transit would be 2.5 ns. Under such circumstances a direct tagging would give better results.

As a matter of fact, the positrons exiting a buffer gas trapped beam have an energy spread of only ~ 25 meV [74] since the positrons thermalise at the temperature of the cooling gas. Running the numbers gives a time difference of 0.06 ns.

While this estimation gives an impression of the importance of a low energy spread for a good time resolution for an indirect method, it is not directly applicable. The examples are based on knowing the start t_0 , e.g. the emission of the positron. This is in practice even harder to achieve than measuring the time of arrival.

The solution comes with the process of bunching. Let's take two hypothetical positrons which are starting with a time difference of 50 ns. One can now impose the same time of arrival by accelerating the later one. Again, assuming 3 m distance and 100 eV energy for the first positron its transit time would be 505.5 ns. The second positron, starting 50 ns later, needs to be accelerated such that it *catches up*, i.e. its transit time needs to be reduced to $505.5 \text{ ns} - 50 \text{ ns} = 455.5 \text{ ns}$. This implies, that its energy should be 126 eV instead of 100 eV. Since the voltage goes like $V \propto t^2$, this scheme cannot be continued forever, e.g. for a positron starting 350 ns later the energy already needs to be on the keV level.

To overcome this limitation one can periodically return to the starting energy of 100 eV. The result are positrons arriving as pulses with a frequency of this re-start. Practically, this can be achieved by applying a time varying potential on an electrode which accelerates (and/or decelerates) positrons either when

they are created and/or while they pass through [110]. The time dependent potential is usually applied by amplifying the output of an Arbitrary Waveform Generator (AWG). Because the amplitude an amplifier can output is limited, some bunching schemes rely on applying a varying potential twice [24] to reach sufficient compression.

To calculate the needed waveform for bunching positrons with a realistic energy distributions, e.g. a Gaussian spread with $\sigma_E = 1$ eV around a mean energy of 100 eV, numerical solutions from simulations become indispensable. While there exist simulation suites like SIMION [111] which can work with varying potential and magnetic fields, the Monte Carlo particle tracing methods are rather time-consuming. For example, the simulation of bunching 10^4 positrons starting at various times in an 300 ns interval takes several hours to compute.

To increase the iterative optimization a MATLAB code was developed to simulate a simplified case. The simulation neglects fringe fields, i.e. makes the assumption that the acceleration or deceleration process has a negligible duration compared to the overall time-of-flight. It is also reduced to one dimension, the beam axis. For magnetically transported beams this approximation is justified as long as the magnetic field strength does not vary significantly, i.e. no momentum is transferred from the axial to the radial component or vice versa. The numerical code, based on matrix operations, uses a linearly sampled phase space density matrix representation and runs considerably faster. The simulation of similar parameters is achieved in tenth of seconds. Moreover, not only the calculated ideal pulse shape, but also a real measured one can be easily incorporated into the simulation to model the measured data.

The starting point are three matrices of size $m \times n$, representing the energy values \mathbf{E} , the time \mathbf{T} , and the density \mathbf{P} of the phase space. The initial energy matrix holds the energy distribution of the beam in the m -dimension and is padded to match the n -dimension which holds the starting time information in the time matrix. In contrary to the common approach of looking at the variables with respect to time, the matrices can be understood as recordings with respect to a given point in space.

$$\mathbf{E}_{m,n} = \begin{pmatrix} E_1 & E_1 & \cdots & E_1 \\ E_2 & E_2 & \cdots & E_2 \\ \vdots & \vdots & \ddots & \vdots \\ E_m & E_m & \cdots & E_m \end{pmatrix}, \quad (3.5)$$

$$\mathbf{T}_{m,n} = \begin{pmatrix} t_1 & t_2 & \cdots & t_n \\ t_1 & t_2 & \cdots & t_n \\ \vdots & \vdots & \ddots & \vdots \\ t_1 & t_2 & \cdots & t_n \end{pmatrix}, \quad (3.6)$$

$$\mathbf{P}_{m,n} = \begin{pmatrix} \rho_{1,1} & \rho_{1,2} & \cdots & \rho_{1,n} \\ \rho_{2,1} & \rho_{2,2} & \cdots & \rho_{2,n} \\ \vdots & \vdots & \ddots & \vdots \\ \rho_{m,1} & \rho_{m,2} & \cdots & \rho_{m,n} \end{pmatrix}. \quad (3.7)$$

The times are linearly spaced over the region of interest, e.g. $t_1 = 0$ and $t_n = 1/f_B$ with f_B being the frequency at which the buncher operates (*re-starts* the ramping up). The energies E_j are a linearly spaced samples of the energies of interest, e.g. ranging from $\pm 3\sigma$ for a Gaussian energy spread. The densities $\mathbf{P}_{i,j}$ represent the normalized probability ($\sum_{i,j} \mathbf{P}_{i,j} = 1$) of the phase space sample $(\mathbf{E}_{i,j}, \mathbf{T}_{i,j})$. Figure 3.14 shows a measured positron energy profile of the cw-beam. Padding it to the starting times of interest results in the initial phase space representation shown in Figure 3.15.

If the positrons now travel for a given distance s_1 the matrices are evolved like

$$\mathbf{E}' = \mathbf{E}, \quad (3.8)$$

$$\mathbf{T}'_{i,j} = \mathbf{T}_{i,j} + s_1 \sqrt{\frac{m}{2\mathbf{E}_{i,j}}}, \quad (3.9)$$

$$\mathbf{P}' = \mathbf{P} \quad (3.10)$$

to represent the variables in regard to this new position.

If there is a change in energy, e.g. all positrons are accelerated from the same electrode potential V_1 it is simply added to the energy matrix

$$\mathbf{E}'_{i,j} = \mathbf{E}_{i,j} + V_1. \quad (3.11)$$

A time varying potential $V(t)$ applied at s_1 would be incorporated as

$$\mathbf{E}'_{i,j} = \mathbf{E}_{i,j} + V(\mathbf{T}'_{i,j}). \quad (3.12)$$

An example of the application of a $V \propto t^2$ potential is shown in Figure 3.16. The evolution of the phase space of Figure 3.15 for a distance of 1 m is shown in Figure 3.17.

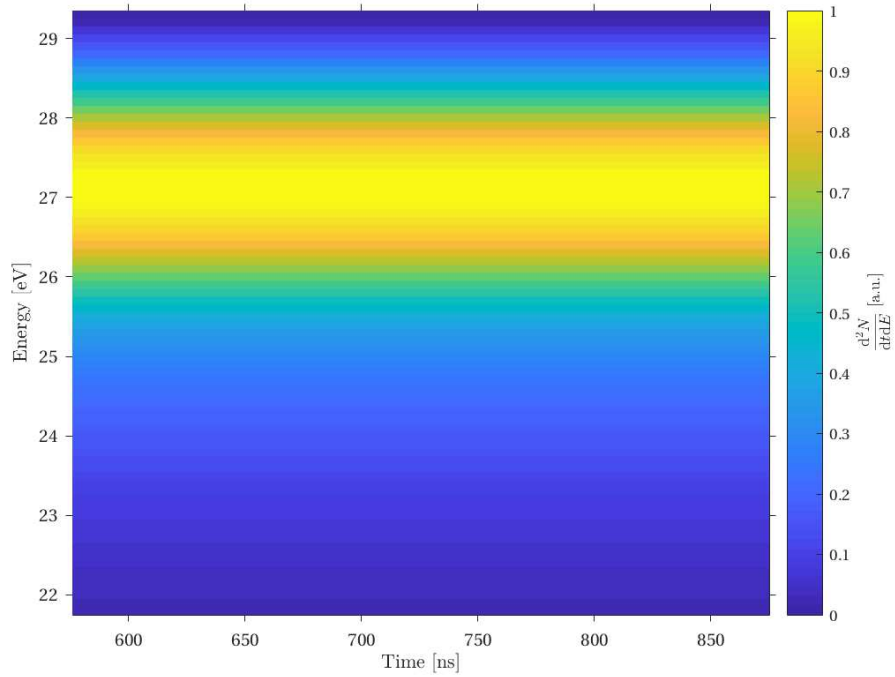


Figure 3.15: The initial phase space in terms of energy, time and density for the bunching simulation.

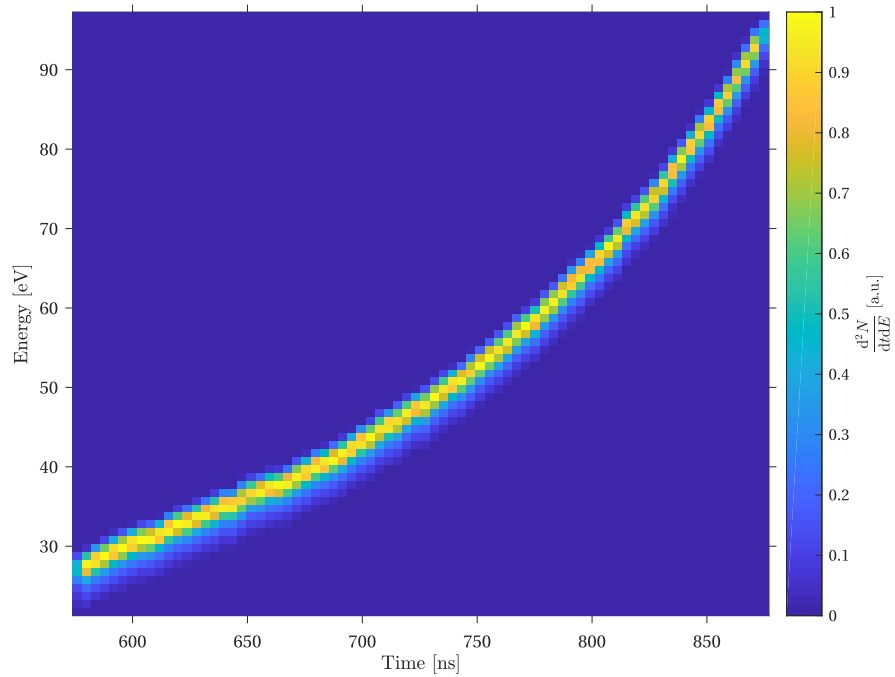


Figure 3.16: The phase space in terms of energy, time and density of a bunch of positrons after the application of a time varying bunching potential.

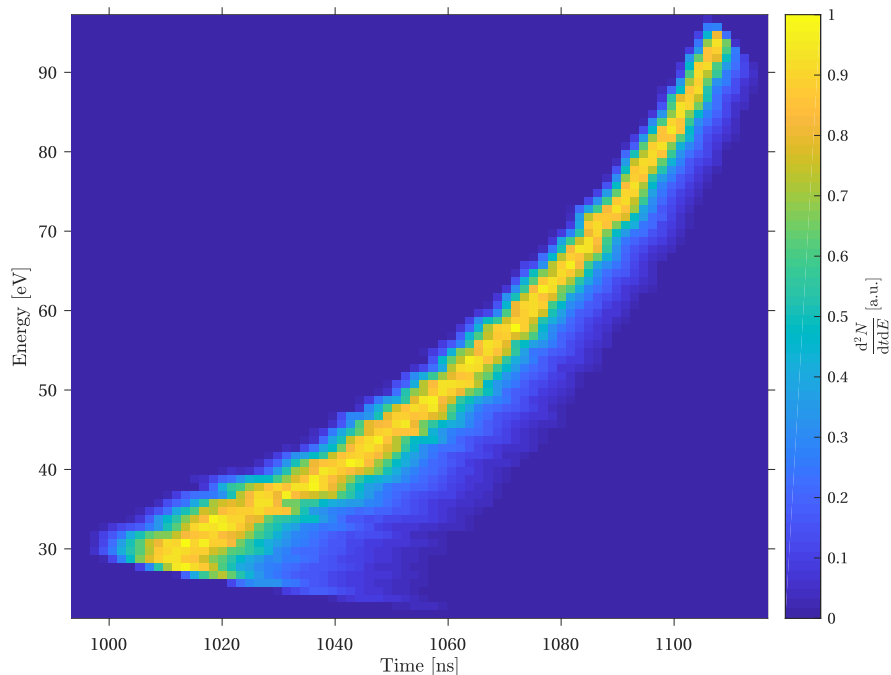


Figure 3.17: The phase space in terms of energy, time and density for a bunch of positrons after evolution over a distance.

If an optimal compression after another distance s_2 is of interest it can be found by adjusting $V(t)$ to minimizing the spread of the time of arrivals \mathbf{T}'' weighted with the density and the boundary condition of a monotonously increasing $V(t)$. The search is implemented via the *quasi-newton algorithm* [112] already embedded in MATLAB.

The simulation was used for the optimization of the bunching process of the cw-beam for the EPIC experiment as then was validated by recreating measured time of arrival spectra from a *real* waveform acquired with a digitizer connected to the bunching electrode [27]. Figure 3.18 shows the application of a second time varying potential and Figure 3.19 the final evolution over a distance of 3 m representing the phase space for the arrival on the target. The applied pulse shape with the corresponding positron bunch time distributions to which it is applied are shown in Figure 3.20.

3.4.2 Buffer gas trap secondary beamline

The second positron beam in the laboratory, described in detail in [107], is a buffer gas trap beam used for positronium spectroscopy. The intense pulses within a short time, very low energy spread (thermal) and the possibility to operate with field-free regions makes it an interesting setup for material characterization experiments with specific requirements. Reactions which happen in very short time scales $\leq 1 \mu\text{s}$ might be analysed with the Single-Shot Positron Annihilation Lifetimes Spectroscopy (SSPALS) technique. A full positron annihilation spectrum can be

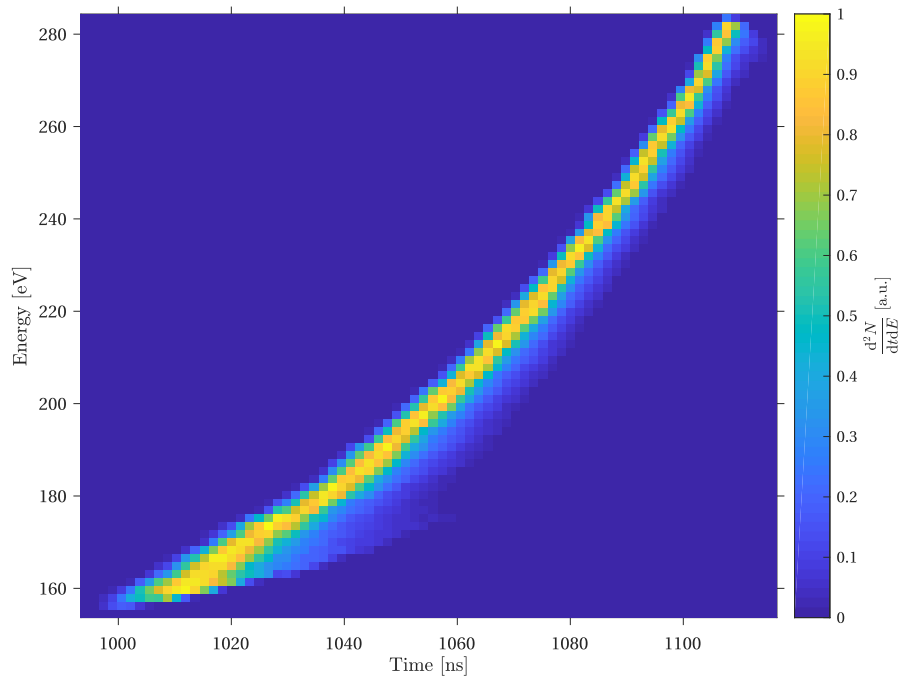


Figure 3.18: The phase space in terms of energy, time and density of a bunch of positrons after the application of a second time varying bunching potential.

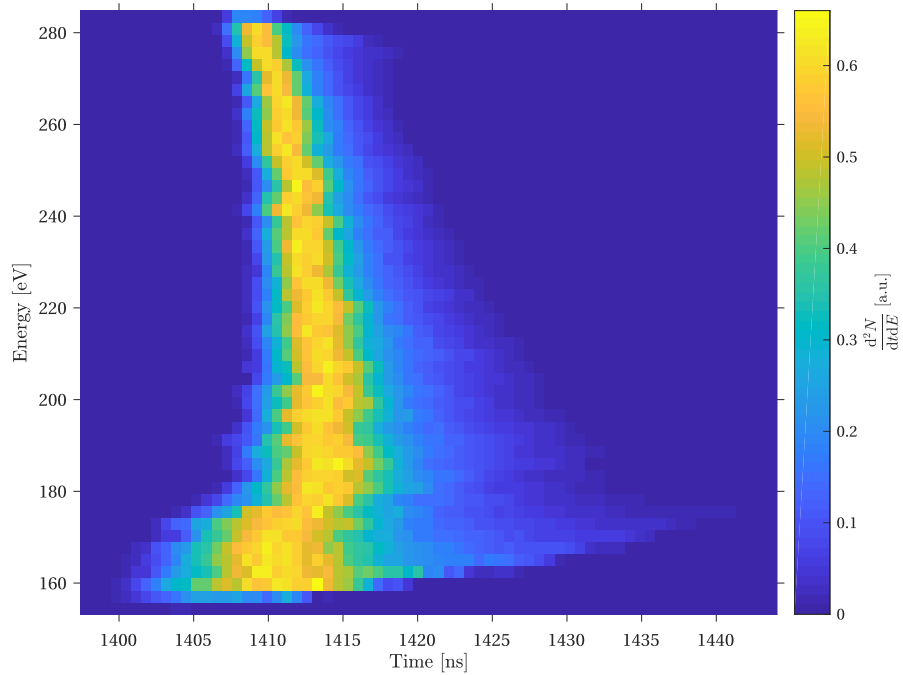


Figure 3.19: The phase space in terms of energy, time and density of a bunch of positrons arriving at the target.

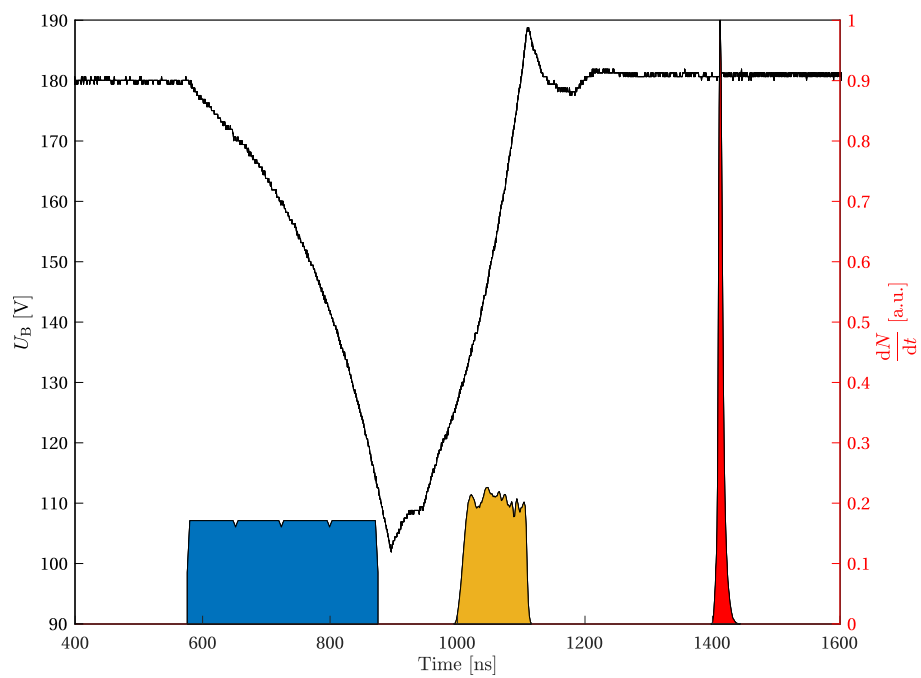


Figure 3.20: A measured bunching pulse (black line) is applied to an initial 300 ns long positron pulse twice (blue & orange). After evolution of the phase space the time distribution on target becomes the red curve.

recorded with a single bunch of positrons creating a snapshot of the properties of the sample in time. Other samples, which can not be set on potential because they would get damaged, could be characterized thoroughly. Furthermore, the low energy spread of the positrons would allow studying interesting resonances in the positronium formation like predicted for fullerenes by Hervieux et al. in [113].

Because the laser system for the positronium spectroscopy and the experimental chamber regularly undergoes upgrades and maintenance, the utilization of the beamline is far from 100%. Therefore the possibility to use the otherwise lost positrons for material characterization or other tests would be of great advantage. A change of the experimental setup on the end of the beam is not realistic as the effort would outmatch the profit. In that perspective, the installation of a switchyard with two ports was developed. The feasibility of a Y-switch was simulated with Simion 8.1⁵ in late 2016. The setup was later designed, constructed and tested for vacuum performance in 2018, see Figure 3.23.

The time resolution of the system was estimated with the simulation described in Section 3.4.1.

With the energy distribution stated in the literature for this kind of beam of 25 meV [73] time resolutions of sub ns are achievable. Taking a realistic configuration of an initial positron energy exiting the trap of 100 eV, a buncher electrode length of 30 cm, a positron pulse width of 60 ns and another distance of 30 cm to the target results in a time spread of 30 ps. The necessary pulse amplitude is less than 50 V is very well within the specification of simple commercial amplifier systems. The plots of the compression and phase space on target are shown in Figure 3.21 & 3.22.

Increasing the energy distribution of the initial bunch to 0.25 eV to account for non-perfect bunching process, e.g. timing miss alignment, noise on the electronics, etc., still results in a time spread of only 0.24 ns. Compared to the current PAS spectrometer (see Table 3.2), this is an improvement by a factor of three for the pessimistic case and more than a factor of ten for the ideal case. A spectrometer with this time resolution will allow to separate even the fastest decaying oPs components from the direct annihilation channels.

Moreover, the short positron bunches can be accelerated to the keV implantation energies by a pulsed electrode without having to float the target holder at a high potential. Not only does this simplify the mechanical design of the sample mount, but also allows for uncomplicated additional features like e.g. heating or cooling. Last but not least, also samples which would get damaged when subjected to high voltage, e.g. Carbon NanoTube (CNT) samples like presented in Section 7.4, could be measured.

The final installation was done during a spectroscopy measurement downtime in 2019. The whole project was realized over the cause of three physics laboratory assistant apprentices visits. This did not only open the possibility for a second beam port but also allowed relocation of the spectroscopy setup into the dedicated

⁵<https://simion.com>

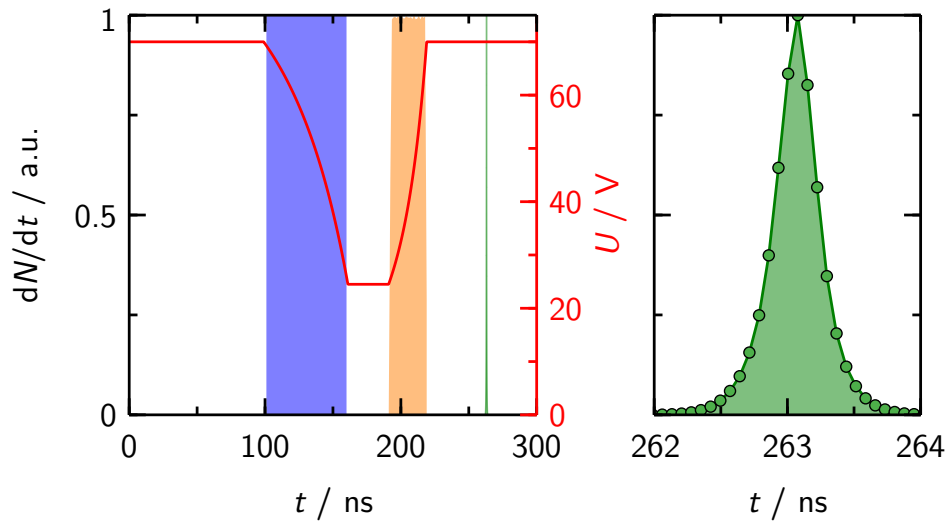


Figure 3.21: The ideal bunching pulse to compress the positron pulse from the buffer gas beam and the corresponding time distributions.

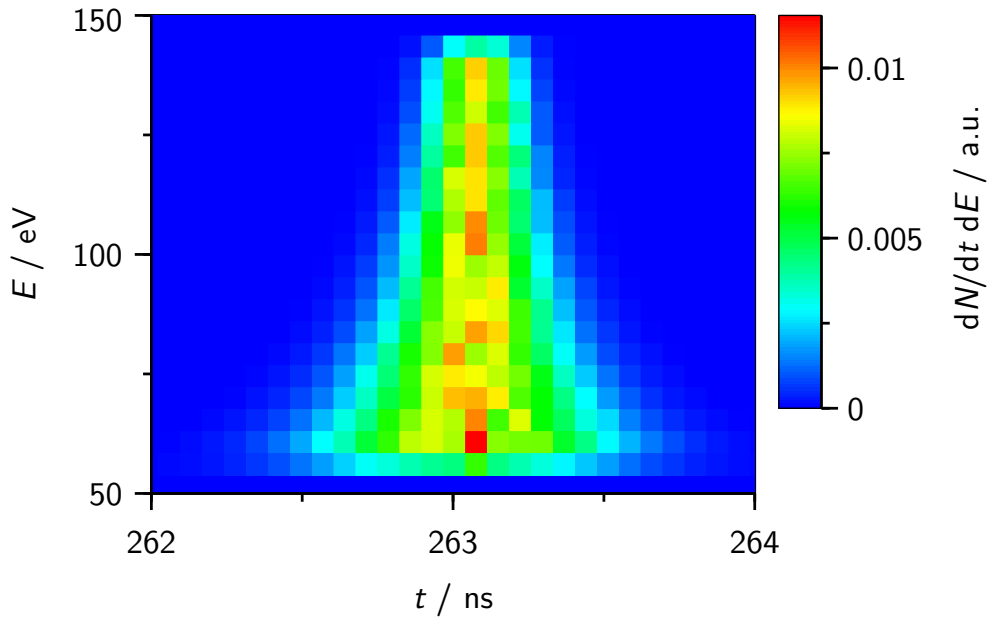


Figure 3.22: A representation of the energy and time distribution of the buffer gas trap positron bunch arriving on target.

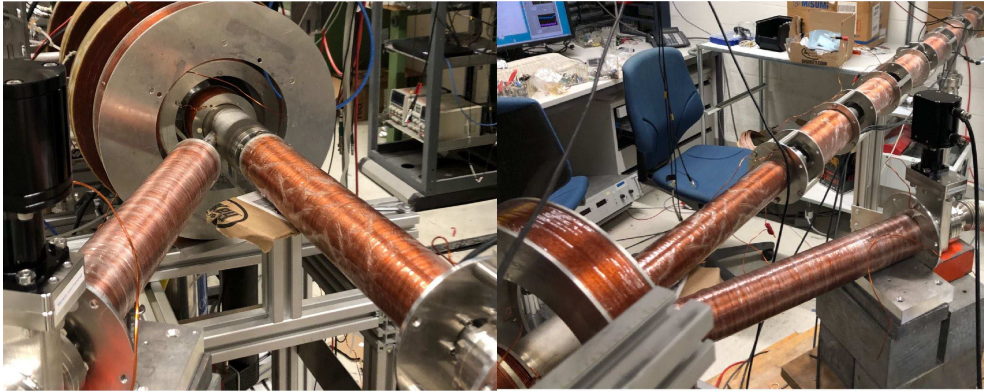


Figure 3.23: A picture of the Y section installed at the buffer gas trap beam. The CF16 port at 30° and the rotatable coil enable a second beam line.

laser room by rather transporting the positrons to the laser system than the other way around.

3.4.3 Test beam

The small slow positron beam shown in Figure 3.4.3 was constructed. The idea stems from a similar standpoint as the switchyard. Often some equipment or parts of other experiments need to be tested. An interruption of operation of the larger positron beam is unwanted, often cumbersome and time-consuming. A small setup which offers a constant flux of positrons, even at low rates, is often enough to do a proof of concept and efficiency studies.

Therefore a system with a tungsten mesh moderator and a weak ^{22}Na source (130 MBq on 01.01.2012) was designed, constructed and tested. In the search for an optimal moderation efficiency with multiple tungsten meshes with 92.2% transmission and a wire diameter of $25\ \mu\text{m}$ ⁶ up to 16 layers were stacked. The best moderation efficiency of $\epsilon = 8 \times 10^{-4}\ \text{e}^+\ \text{s}^{-1}$ was achieved with 14 layers of mesh resulting in a slow positron flux of about 1000 Hz.

To measure the number positrons per second BGO and BaF_2 scintillators were calibrated with a positron emitter of known and similar activity. It was also found that the annealing of the tungsten meshes plays an important role. Otherwise, the highly oxidised surface will trap any positron before it would get fully emitted from the surface via the negative work function principle.

Not annealed meshes exhibited no measurable slow positron flux. For the annealing process of solid single-crystal tungsten moderators a RHEED electron gun⁷ was used to bombard the thin foil with $\sim 1\ \text{mA}$ of 10 keV electrons. This procedure proofed to not work on stacked meshes since even at 16 meshes the transmission is still too high with $T = 0.922^{16} = 0.27$ to absorb enough power and the large

⁶UNIQUE Wire Weaving Co., Inc., www.uniquewire.com

⁷RHEED-20, STAIB Instruments, www.staibinstruments.com

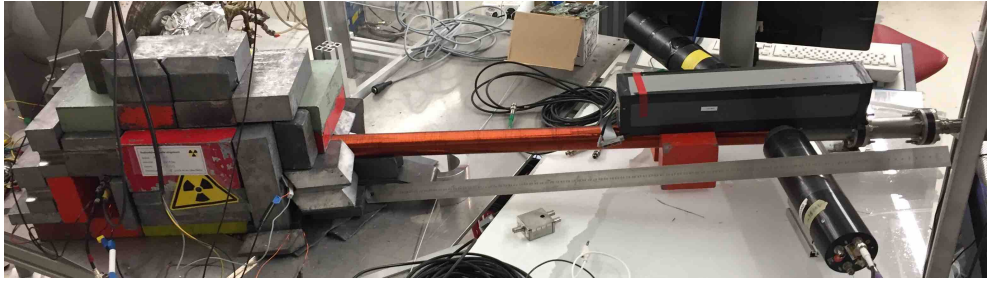


Figure 3.24: A picture of the low flux positron beam for equipment tests. The source and the moderator are in the lead castle on the left. The long solenoid ensures only little fast positron contamination. The detectors on the right (BGO - rectangular box, 2x BaF₂ - cylinders) and an electron multiplier inside the vacuum chamber serve for beam characterization.

surface emitted too much heat. A solution was found by sandwiching the meshes between 50 μm thin sheets of tungsten which absorb all transmitted electrons and also limits the loss from the thermal radiation of the meshes.

3.5 Detector Development

A proper detector (and DAQ) setup is as crucial as good beam qualities are to conduct a successful PAS. While some integrated solutions can be purchased off the shelf, others are only available in parts, but most of the time an experimental one-of-a-kind specific setup is required. In the particular case of the two most prominent detector types, single charged particle detectors and gamma-ray detectors, see Section 3.1.4, the necessity for unique designs for positron beams is most prominent. This includes simple geometrical aspects as mounts, electrodes, etc., as readout schemes and acquisition tools.

3.5.1 Micro Channel Plate Detectors

Most commercially available MCP detectors have outstanding properties regarding their individual purpose. Unfortunately in the design others properties important in research regularly fall a bit behind. The universality or re-usability is often not guaranteed. It might be electrical connections which are not built for repetitive dis- and re-connecting, unhandy mounts, often bulkier than necessary, no redundant parts for versatility and especially service ability. As any electric part degrades with time, the heart of the detector, the microchannel plates, need to be replaced from time to time. Some mounts are simply glued together intended for single-use, others were just not made with this task in mind.

Most commercial designs rely on stacking cylinders of conducting and insulating materials on top of each other. The sandwich is then held by at least three insulating pillars. Resulting from this design choice the electrical connections

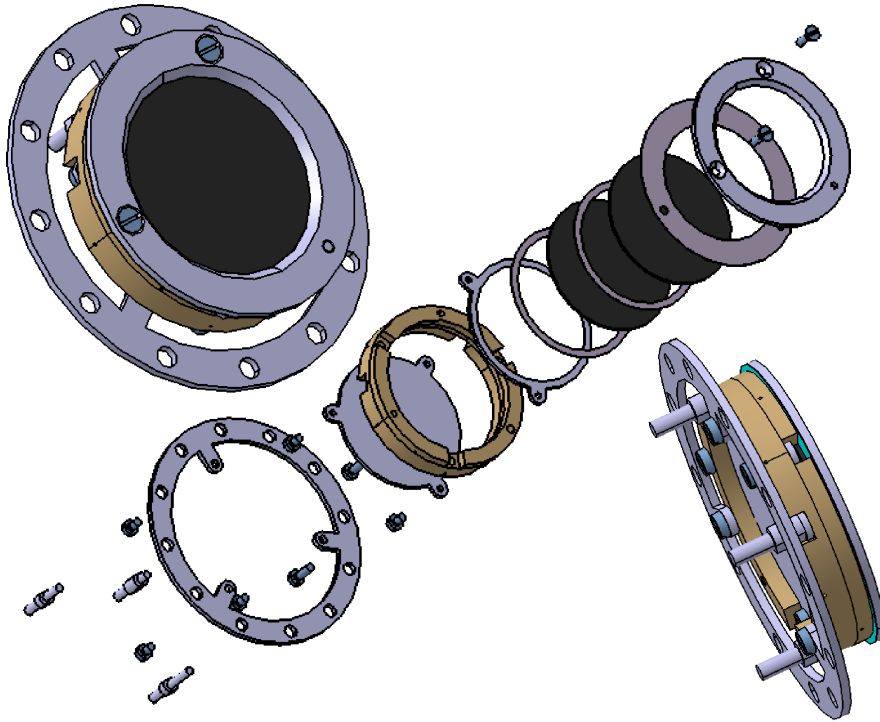


Figure 3.25: CAD model of the CF 63 compatible MCP assembly. The explosion view shows from left to right, the electrical connectors, mounting screws, mounting pad, anode screws, anode, insulating peek cylinder, backplate holder, nickel contact ring, back plate, nickel contact ring, front plate, nickel contact ring, front plate holder and insulator cover, and the front plate cover mounting screws.

necessary on the top and bottom of the plates as for the readout anode are arranged radially. This method limits the usability in confined spaces. Also, assemblies for standard-sized plates of e.g. 40 mm have outer diameters of 50 mm and high voltage connections extending out up to an enclosing diameter of 76 mm. While these plates would be ideal to cover a large area inside a CF63 (I.D. 58 mm) vacuum pipe, the assemblies are practically not usable for such application.

For this purpose the multi-purpose compact mount shown in Figure 3.25 suitable for positron beam applications was designed. The criteria were vacuum part size Con-Flat (CF) standard compatibility, in house production, easy of handling, low cost and versatility. An enclosing peek cylinder which confines and insulates the assembly radially serves as the base. Rings with arms screwed to this cylinder hold the microchannel plates in place. For the assembly, the plates can be simply dropped into the cylinder and clamped down by a front ring. The electrical connections are designed for standard vacuum plugs and directly screw into the respective parts. Furthermore, they are decoupling the mechanical stress generating on connecting. The MCP housing has an outer diameter of 42 mm, the mounting pad which can hold additional equipment like rejection electrodes etc. via M3 through holes has an outer diameter of 56.5 mm.

Central Hole

For the related project of the 1S-2S spectroscopy of positronium in a field-free region [114] setup an MCP with special requirements was designed. A dedicated low background detection scheme was thought of. The speciality is, that Ps is usually formed in reflection geometry. A positron beam impinges on a target from where Ps is emitted into vacuum backwards, upstream. Lasers and detectors for the excitation and measurement are therefore now arranged in a linear scheme but rather occupy the same space as last beam shaping elements.

The detection scheme of the experiment is the detection of the Ps substituents. After emission into vacuum, a two-photon excitation brings a small fraction of 1S Ps to the 2S state. A second laser brings 2S atoms to highly excited Rydberg states. As excited states have longer self-annihilation lifetimes than the previously discussed 142 ns because the positron and electron wave functions have less overlap the Rydberg atoms can travel longer distances than ground state Ps. This allows for background suppression simply by putting space between detectors and source. Additionally, a measurement of the time of flight and a known distance allows approximating the velocity which can be fed into the data analysis to correct for Doppler effects which shift and distort the measured transition line in frequency. Moreover, being so close to the continuum, the ionization threshold is substantially lower for a Rydberg Ps. In fact, so low that by simple electric fields with strengths of $\sim \text{kV mm}^{-1}$ the atom can be field ionized and electron and or positron can be detected as charged particles and remnants of the excitation.

This gave rise to the necessity of an MPC with a central hole with a defined field ionizing region and severe potential shielding. The opening needed to be large enough not to clip the positron beam while shielding the beam from the kV potentials on the MCP plates. On the other hand, the hole is in the maximum of the direction of Ps emission, the bigger the hole the more signal is lost. The design is shown in Figure 3.26 balances these requirements.

Position Sensitive (Segmented, Resistive Anode, Phosphor Screen)

As an important tool for beam quality (spot size, shape, etc.) and alignment single-particle, position-sensitive detectors are very useful. While there is a multitude of possible detectors for higher energetic particles, charged particles on the eV scale are mostly characterised by MCP detectors. The design principle of the MCP retains the position, see Figure 3.5. For the position-sensitive anode collecting the charge, multiple designs with different pros and cons can be found in the literature [102]. The most commonly used one is a phosphor screen [115].

Electrons from the MCP plates get accelerated to 4 keV to have enough energy to excite the micron sized phosphor grains of the screen. The subsequent light emission via fluorescence can be detected with CCD cameras and such to get a two-dimensional digital image. A simple but limited approach is to segment the anode in one or two dimensions. While this is mechanically easy a high number of readouts is necessary for a decent position resolution.

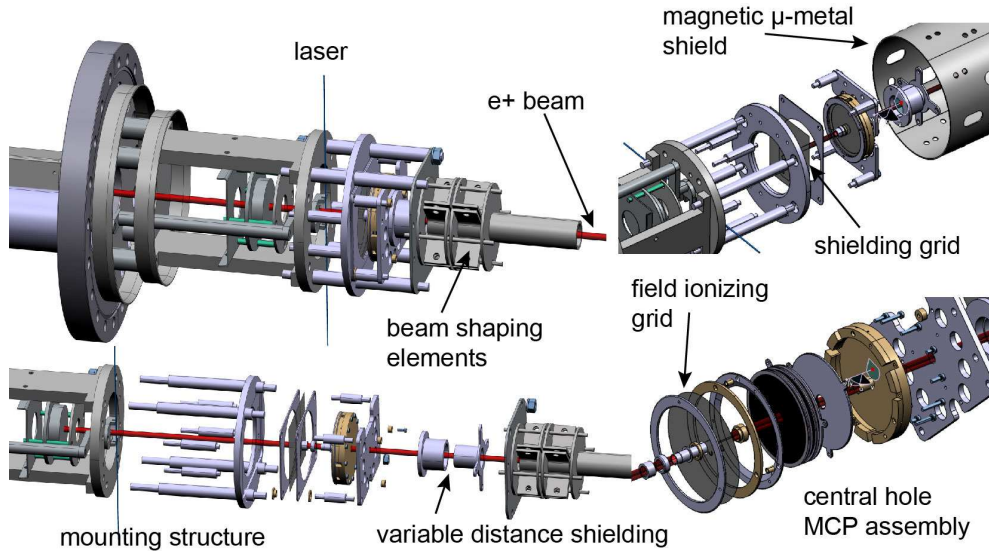


Figure 3.26: CAD model of the central hole positronium 1S2S spectroscopy.

Other anode types are based on charge division. Either directly distributing the charge depending on the position or by measuring the transit times. One implementation is the delay line anode which is based on at least two wires [116]. When the electron cloud emitted from the back of the MCP stack hits the wire it creates an electrical signal which travels to both ends. By slowing down the pulse measuring the time difference at both ends becomes feasible and one can determine on which wire segment the signal was induced and therefore derive the pitch or position. With two such wires arranged perpendicular two-dimensional information can be reconstructed.

Another approach is to use an anode pattern which has electrodes with periodic patterns changing some characteristic size in one direction. The most common design is the wedge strip arrangement [117]. The emerging electron cloud is then physically split and can be quantified with charge integrators.

Yet another technique is to use a highly resistive layer as the anode and measure the charge at multiple points on the border [118]. The charge is divided depending on the position it hit the anode as the resistance towards the measurement points varies. With charge integration or more advanced pulse shape analysis, the signals of all read-out points can be combined via triangulation to reconstruct the impact position. While this approach has the least requirement in terms of read-out electronics the detector design is rather bulky. The reason for this is to limit the distortion originating from the finite size of the resistive layer [118]. With the layer shaped in circular arcs covering the MCP active area, a linear position feedback is regained.

Simulations have shown that rectangular anodes with a boundary layer of lower resistivity for correcting the distortions can provide a similar performance [119]. Since the footprint of such anode is still considerably bigger than the MCP itself it would not be feasible to be coupled to e.g. the MCP mount shown in Figure 3.25. In

fact, none of the position-sensitive anode designs, except a phosphor screen, are of comparable size as the MCP plate. As discussed before, the phosphor screen does not offer acceptable single particle position and time determination and requires either optical access or a directly in vacuum mounted CCD camera.

These points lead to designing and testing a resistive layer anode of polygonal shape of a higher order than a rectangle to cover the MCP active area but offer a smaller footprint. A hexagon was found to be the optimal shape. Similar considerations of distortion compensation boundary layers like done by Ju et al. [119] were made. The resistive layer was formed by 100 nm carbon sputtering done at PSI on an insulating aluminium oxide plate. While the principle, design and production were promising a flaw of missing terminating resistors on the readout points became eminent. Charge clouds impacting close to one readout could cause currents in the mA because of the limited resistance which effectively damage the carbon layer.

3.6 Cyclotron Driven Isotope Production Sources

In the wake of the thin film source research, the question arose if it would be viable to use short-lived β^+ emitters for intense slow positron beams as well. The usual problem of the fast decay and therefore reduction in flux requires frequent source exchange.

While the usual turnover of e.g. ^{22}Na is 4-5 years (~ 2 half-lives) one would require depending on the isotope monthly, daily or even hourly source exchanges or top-ups. The recent increase in the number of accessible particle beams energetic enough to create synthetic isotopes motivates to revise the common perception in the positron community that only ^{22}Na and to some extent ^{58}Co are practical radioactive isotopes. Moreover, the usual opinion is that for intense beams it is necessary to follow the path of pair production schemes described in Section 3.1.1.

Good candidates for the necessary frequent source productions are proton cyclotrons designed for the medical application of positron emission tomography (PET) isotope productions. New developments of target stations enable high current irradiations with small beam spots [120]. Furthermore, the energy range necessary for typical PET isotopes like ^{18}F overlaps with many threshold energies for the creation of other β^+ emitters. An overview of the properties of proton cyclotron from the market-leading companies is presented in Table 3.3. Given by the scheduling of PET scans in hospitals the cyclotrons are also not utilized to 100%. An example of the coverage of cyclotrons of IBA Radio Pharma Solutions in Europe is shown in Figure 3.27.

Primary criteria for the potential positron sources are the half-life, β^+ branching, endpoint energy, phase or solidity at ambient temperature, production process, threshold energy E_{thres} , cross-section σ , yield Y , abundance of target material, melting or boiling point of target material and potentially competing (follow-up)

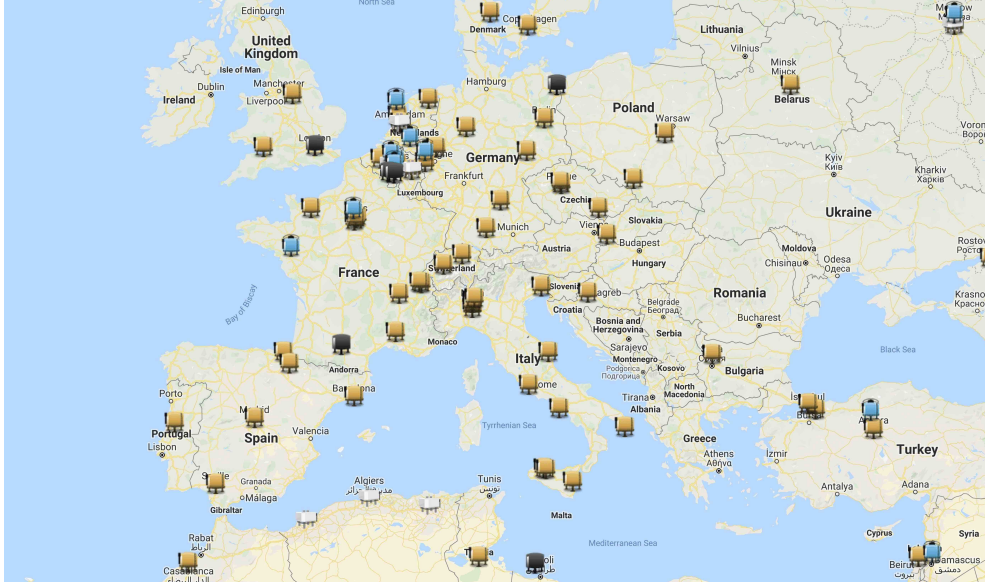


Figure 3.27: A map showing the IBA proton cyclotrons (black 11 MeV, yellow 18 MeV, blue 30 MeV version) mainly used for positron emission tomography isotope production distribution in Europe [121].

Table 3.3: Typical proton energies E_p and maximal currents I_{\max} for commercial cyclotrons of the industry leaders IBA Radio Pharma Solutions (IBA), General Electric Health Care (GE) and Advanced Cyclotron Systems Inc. (ACSI)

E_p (MeV)	7.8	9.6	16.5	18	19	24	30	30	30-70
I_{\max} (μA)	25	50	160	300	300	300	500	1500	750
Company	GE	GE	GE	IBA	ACSI	ACSI	ACSI	IBA	IBA

reactions. Of secondary importance would be overall radiation which needs to be considered for shielding purposes, re-usability of the source as a future target, etc. An overview of positron sources is given in Table 3.4. For the case of low Z targets, the cross-section distributions for low production threshold energies are usually a lot broader. Therefore, the physical yield Y at the highest cross-section is underestimating what is technically feasible.

The number of product atoms N produced per second P_N is given by the target 2D number density n , the projectiles per second Φ , and the process cross-section $\sigma(E_p)$ (cm^2), which depends on the projectile energy E_p

$$P_N = \sigma(E_p) n \Phi . \quad (3.13)$$

In case of protons and fixed solid targets this translates to

$$P_N = \sigma(E_p) \frac{dN_A I}{M e} , \quad (3.14)$$

with the area density d (g cm^{-2}), Avogadro's number N_A , molar mass M (g mol^{-1}), beam current I (A) and elementary charge e . Therefore, the activity production rate P_A (Bq s^{-1}) is

$$P_A = P_N \frac{\ln(2)}{t_{1/2}} . \quad (3.15)$$

It is also common to describe irradiations in terms of a physical activity yield Y_A ($\text{Bq}/\mu\text{Ah}$), after a hypothetical one hour irradiation with a current of $1 \mu\text{A}$,

$$Y_A = \frac{P_N}{I} \frac{3600 \text{ s } \mu\text{A}}{1 \text{ h } \mu\text{A}} = \sigma(E_p) \frac{dN_A}{M} \frac{1 \mu\text{A} 3600 \text{ s}}{e} \mu\text{A}^{-1} \text{ h}^{-1} . \quad (3.16)$$

While this is a quantity purely describing the production process under given conditions, a more practical descriptor is the end-of-bombardment activity A_{EOB} , the activity of a sample after irradiation for a given time t_{irr} . It includes the potential decay of the already produced radioisotopes with lifetime $\tau = t_{1/2}/\ln(2)$ and is therefore given by

$$A_{\text{EOB}} = P_N \left(1 - e^{-t_{\text{irr}}/\tau}\right) . \quad (3.17)$$

It is important to use this formula rather than the approximation $A_{\text{EOB}} \approx Y_A t_{\text{irr}} I$ when the irradiation duration t_{irr} is of similar magnitude as the lifetime τ (or even longer). The equation shows that the maximum activity for a given process and beam current P_N is already reached after an irradiation duration of a couple of lifetimes.

A typical scheme could either be having a positron beam facility on the same site as the cyclotron or in delivery distance of the radioisotopes like many hospitals with PET scanners. Assuming the ideal case of a fast transfer from irradiation to installation in the beam one can analyse what the average source activity would be.

Making the case for a $^{44}\text{Ca}(p,n)^{44}\text{Sc}$ production with the ETH IBA 18 MeV cyclotron, stationed in the Radiopharmaceutical Science group of Prof. R. Schibli.

Assuming a one hour irradiation with 300 μA on target, followed by an additional hour of transfer time, the immediate positron activity is $A(2\text{ h}) = 592\text{ GBq}$. The mean of the next 24 hours is $\bar{A}(1\text{ d}) = 70\text{ GBq}$, $\bar{A}(2\text{ d}) = 71\text{ GBq}$ for 48 hours. After these two days, it already decayed to $A(2\text{ d}) = 0.2\text{ GBq}$ which is a bit lower than commercially available ^{22}Na sources. A comparable advantage in terms of disposal is that already after a total of 3 days and 7 hours the activity is at a manageable level of 1 MBq while ^{22}Na discarded is usually still quite active for a long time.

Any isotope with even shorter lifetimes would preferentially be used in a literal on-line production scheme where the positron beam is directly attached or in ultimate proximity of the cyclotron. A more futuristic approach would be to store the resulting high positron fluxes for longer periods of times and extracting them in smaller amounts. Potential longer living sources would be $^{86}\text{Sr}(p,n)^{86}\text{Y}$ with 15 h half-life and a β^+ activity after irradiation and transfer of 60 GBq, $^{89}\text{Y}(p,n)^{89}\text{Zr}$ with 3.3 days and 7.5 GBq or $^{\text{nat}}\text{Ti}(p,n)^{48}\text{V}$ with 16 days and 3 GBq. While the A_{EOB} activities for longer living isotopes are naturally lower, the sources presented here could be potentially topped off with multiple irradiation at different times.

Another interesting candidate is ^{68}Ga which was already studied for its spin-polarized beam properties [122]. It is extensively used in PET but has a rather short lifetime of 1.1 h. While it can be directly produced via $^{68}\text{Zn}(p,n)^{68}\text{Ga}$ it is more common to use a so-called Ge/Ga-generator. The underlying process is $^{68}\text{Ge}(100\% \text{ EC})^{68}\text{Ga}$ with a life-time of 271 d. The germanium again can be produced with $^{\text{nat}}\text{Ga}(p,xn)^{68}\text{Ge}$. With this natural ‘delay’ in the decay scheme ^{68}Ge is created from irradiation, e.g. 3 GBq per 1 h with a 1500 μA 30 MeV cyclotron. The product is then shipped to PET facilities where the ^{68}Ga gets continuously produced under equilibrium which can then be chemically extracted. Since the high activities which are necessary for PET require equally active generators, the industry behind is already developed and capable of producing large amounts of ^{68}Ge .

Other possibilities might be the use of advanced charged particle traps and short-lived isotopes which deliver a high positron flux over time-scales of only minutes or hours. However, this would require a very good vacuum in the UHV or even XHV, will be necessary to store positrons for a prolonged period to limit the annihilation losses with the residual gas particles. With the possibility of effectively extracting a relatively small number of positrons per time from such trap it might be possible to form a constant flux. A potential schemes to generate such beam could be similar to the evaporative cooling concept used in the alpha experiment [123], but with the opposite interest, using the *evaporated* particles. An interesting figure of merit would be the total number of positrons, i.e., the integrated positron flux, which can be utilized in terms of e.g. a one-hour irradiation.

A general list of positron sources reachable by proton irradiation is shown in Table 3.4. The previous considerations for the activities have only been based on the easily calculable variables of fast positron flux. For a more detailed study, specifically the effect of the endpoint energy T_{max} on the positron moderation

needs to be considered to assess overall beam performances. In general, it is to be expected that higher energies result in lower efficiencies but, as the moderation process has never been modelled in detail, the magnitude is unclear. On the other hand, the spin polarization of a slow positron beam, originating from the parity non-conservation in the weak interaction on the decay, is increased for higher endpoint energies. The application for highly polarized beams is the study of magnetic materials like investigated by Gidley et al [\[124\]](#).

Table 3.4: Overview of bulk positron source properties accessible via proton irradiation: half-life $t_{1/2}$, endpoint energy T_{\max} or Q^+ values when the exact scheme is unknown (*), β^+ branching $\text{Br}(\beta^+)$, production target and reaction, energy at the highest cross section E_σ , physical yield Y_A at E_σ and natural target isotope abundance C [81, 125, 126].

Isotope	$t_{1/2}$	T_{\max} (keV)	$\text{Br}(\beta^+)$ (%)	Reaction	E_σ (MeV)	Y_A ($\frac{\text{MBq}}{\mu\text{A h}}$)	C (%)
^{44}Sc	4 h (^{44}Ti 59.1 a)	1474	94	$^{45}\text{Sc}(\text{p},2\text{n})^{44}\text{Ti}$ $^{44}\text{Ti}(100\% \text{ EC})^{44}\text{Sc}$	22	0.0011	100
^{22}Na	2.6 a	545	91	$^{27}\text{Al}(\text{p},\text{x})^{22}\text{Na}$	44	0.135	100
^{68}Ga	1.1 h (^{68}Ge 271 d)	1899	89	$^{\text{nat}}\text{Ga}(\text{p},\text{xn})^{68}\text{Ge}$ $^{68}\text{Ge}(100\% \text{ EC})^{68}\text{Ga}$	22	0.72	^{69}Ga 60 ^{71}Ga 40
^{65}Zn	244 d	325	1.5	$^{\text{nat}}\text{Cu}(\text{p},\text{x})^{65}\text{Zn}$	11	0.21	^{63}Cu 69, ^{65}Cu 31
^{58}Co	71 d	475	15	$^{\text{nat}}\text{Cu}(\text{p},\text{x})^{58}\text{Co}$	40	1	^{63}Cu 69, ^{65}Cu 31
^{82}Rb	1.3 min (^{82}Sr 25 d)	3378	50	$^{\text{nat}}\text{Rb}(\text{p},\text{x})^{82}\text{Sr}$ $^{82}\text{Sr}(100\% \text{ EC})^{82}\text{Rb}$	50	4.6	^{85}Rb 72, ^{87}Rb 28
^{48}V	16 d	695	50	$^{\text{nat}}\text{Ti}(\text{p},\text{n})^{48}\text{V}$	12	9.4	^{48}Ti 74
^{62}Cu	9.7 min ($^{62}\text{Zn}^{\text{b}}$ 9.2 d)	2926 604	98 8.2	$^{63}\text{Cu}(\text{p},2\text{n})^{62}\text{Zn}^{\text{b}}$ $^{62}\text{Zn}(100\% \text{ EC}+\beta^+)^{62}\text{Cu}$	24	174	69
^{72}As	1.1 d (^{72}Se 8.4 d)	3334*	88	$^{75}\text{As}(\text{p},4\text{n})^{72}\text{Se}$ $^{72}\text{Se}(100\% \text{ EC})^{72}\text{As}$	50	17	100
^{118}Sb	3.6 min (^{118}Te 6 d)	2634*	74	$^{\text{nat}}\text{Sb}(\text{p},\text{x})^{118}\text{Te}$ $^{118}\text{Te}(100\% \text{ EC})^{118}\text{Sb}$	45	41	^{121}Sb 57, ^{123}Sb 43,
^{52g}Mn	5.6 d	245	29	$^{52}\text{Cr}(\text{p},\text{n})^{52g}\text{Mn}(\text{m}+)$	15	10	84
^{140}Pr	3.3 min (^{140}Nd 3.4 d)	2366*	51	$^{141}\text{Pr}(\text{p},2\text{n})^{140}\text{Nd}$ $^{140}\text{Nd}(100\% \text{ EC})^{140}\text{Pr}$	23	128	100

Isotope	$t_{1/2}$	T_{\max} (keV)	Br(β^+) (%)	Reaction	E_{σ} (MeV)	Y_A ($\frac{\text{MBq}}{\mu\text{Ah}}$)	C (%)
^{89}Zr	3.3 d	902	23	$^{89}\text{Y}(\text{p},\text{n})^{89}\text{Zr}$	13	54	100
^{128}Cs	3.7 min (^{128}Ba 2.4 d)	2906*	69	$^{133}\text{Cs}(\text{p},6\text{n})^{128}\text{Ba}$ $^{128}\text{Ba}(100\% \text{ EC})^{128}\text{Cs}$	65	101	100
^{72}As	1.1 d	3334*	88	$^{\text{nat}}\text{Ge}(\text{p},\text{xn})^{72}\text{As}$	12	55	^{72}Ge 27, ^{73}Ge 8, ^{74}Ge 37
^{122}I	3.7 min (^{122}Xe 20 h)	3212	78	$^{124}\text{Xe}(\text{p},\text{x})^{122}\text{Xe}$ $^{127}\text{I}(\text{p},6\text{n})^{122}\text{Xe}$ $^{122}\text{Xe}(100\% \text{ EC})^{122}\text{I}$	40 80	458 641	0.1 100
^{55}Co	18 h	530	76	$^{58}\text{Ni}(\text{p},\alpha)^{55}\text{Co}$ $^{56}\text{Fe}(\text{p},2\text{n})^{55}\text{Co}$	17 25	19 71	58 92
^{86}Y	15 h	534	32	$^{86}\text{Sr}(\text{p},\text{n})^{86}\text{Y}$ $^{88}\text{Sr}(\text{p},3\text{n})^{86}\text{Y}$	15 40	455 1.1×10^3	10 83
^{90}Nb	15 h	1000*	51	$^{93}\text{Nb}(\text{p},\text{x})^{90}\text{Nb}$	50	803	100
^{66}Ga	9.5 h	4153, 924	50, 3.7	$^{66}\text{Zn}(\text{p},\text{n})^{66}\text{Ga}$	12	336	28
$^{52\text{m}}\text{Mn}$	21 min (^{52}Fe 8.3 h)	1179 807	97 56	$^{\text{nat}}\text{Ni}(\text{p},\text{x})^{52}\text{Fe}$ $^{55}\text{Mn}(\text{p},4\text{n})^{52}\text{Fe}$ $^{52}\text{Fe}(100\% \text{ EC}+\beta^+)^{52\text{m}}\text{Mn}$	65 55	14.3 8.8	^{58}Ni 68, ^{60}Ni 26 100
^{73}Se	7.2 h	1275	64	$^{75}\text{As}(\text{p},3\text{n})^{73}\text{Se}$	35	975	100
^{44}Sc	4 h	1474	94	$^{44}\text{Ca}(\text{p},\text{n})^{44}\text{Sc}$	11	1×10^3	2
$^{110\text{m}}\text{In}$	1.2 h (^{110}Sn 4 h)	2856*	61	$^{\text{nat}}\text{In}(\text{p},\text{xn})^{110}\text{Sn}$ $^{110}\text{Sn}(100\% \text{ EC})^{110\text{m}}\text{In}$	70	916	^{113}In 4, ^{115}In 96
^{61}Cu	3.3 h	1216, 932, 560	52, 5, 3	$^{61}\text{Ni}(\text{p},\text{n})^{61}\text{Cu}$ $^{64}\text{Zn}(\text{p},\alpha)^{61}\text{Cu}$	11 15	890 195	1 49

Isotope	$t_{1/2}$	T_{\max} (keV)	Br(β^+) (%)	Reaction	E_{σ} (MeV)	Y_A ($\frac{\text{MBq}}{\mu\text{A h}}$)	C (%)
^{18}F	1.8 h	634	97	$^{18}\text{O}(\text{p},\text{n})^{18}\text{F}$	5	440	0.2
^{57}Ni	1.5 h	862, 735, 482	35, 7, 1	$^{\text{nat}}\text{Ni}(\text{p},\text{x})^{57}\text{Ni}$	28	96	^{58}Ni 68, ^{60}Ni 26
^{120}I	1.4 h	4593*	68	$^{120}\text{Te}(\text{p},\text{n})^{120}\text{I}$	15	2.8×10^3	1
				$^{122}\text{Te}(\text{p},3\text{n})^{120}\text{I}$	36	8×10^3	3
$^{110\text{m}}\text{In}$	1.2 h	2856*	61	$^{110}\text{Cd}(\text{p},\text{n})^{110\text{m}}\text{In}$	13	297	13
^{68}Ga	1.1 h	1899	89	$^{68}\text{Zn}(\text{p},\text{n})^{68}\text{Ga}$	12	5.2×10^3	19
$^{94\text{m}}\text{Tc}$	52 min	2439	70	$^{94}\text{Mo}(\text{p},\text{n})^{94\text{m}}\text{Tc}$	12	2.5×10^3	9
^{63}Zn	39 min	2344, 1674, 1382	80, 7, 5	$^{\text{nat}}\text{Cu}(\text{p},\text{x})^{63}\text{Zn}$	12	3.7×10^3	^{63}Cu 69, ^{65}Cu 31
$^{52\text{m}}\text{Mn}$	21 min	1179	97	$^{52}\text{Cr}(\text{p},\text{n})^{52\text{m}}\text{Mn}$	10	4×10^3	84
^{11}C	20 min	960	99.8	$^{14}\text{N}(\text{p},\alpha)^{11}\text{C}$	7	2.4×10^3	100
^{13}N	10 min	1199	99.8	$^{16}\text{O}(\text{p},\alpha)^{13}\text{N}$	9	1.3×10^3	100
^{62}Cu	9.7 min	2926*	98	$^{62}\text{Ni}(\text{p},\text{n})^{62}\text{Cu}$	12	26×10^3	4
^{15}O	2 min	1732	99.9	$^{15}\text{N}(\text{p},\text{n})^{15}\text{O}$	8	35×10^3	0.4

Chapter 4

High Efficiency Cyclotron Trap Assisted Moderator

To form a slow positron beam, the positrons from the broad keV to a few MeV energy spectrum of the source have to be converted to a mono-energetic eV beam using moderators. Given the low moderation efficiencies, strong positron sources are needed to reach sufficient slow positron beam fluxes. The need for more efficient moderation schemes and readily available positron sources is therefore eminent.

The here presented cyclotron trap assisted moderation scheme developed in this thesis greatly improves the amount of positrons available for the moderation process resulting in a higher efficiency [99].

4.1 The Cyclotron Trap

A Cyclotron Trap (CT), also called magnetic bottle, consists of two coils separated by some distance along their coil axes. By running a current in the same direction through both coils a magnetic field arises which has two maxima at the center of each coil and a local minimum between them when going along their symmetry axis. This can lead to a confinement of charged particles with certain attributes. These particles then travel back and forth in a circular motion between the two coils, as being fixed on a spiral aligned with the trap.

4.1.1 The Principles of a Cyclotron Trap

In an inhomogeneous magnetic field of cylindrical symmetry in z direction with a small gradient parallel to the field lines the magnetic field has a small radial component. A particle moving parallel to the field lines, like approaching a coil, with the spiraling motion, will experience a net force anti parallel to the gradient during one cycle. With the integral definition of the abbreviated action one can show that the action is constant for slowly spatial varying fields where the

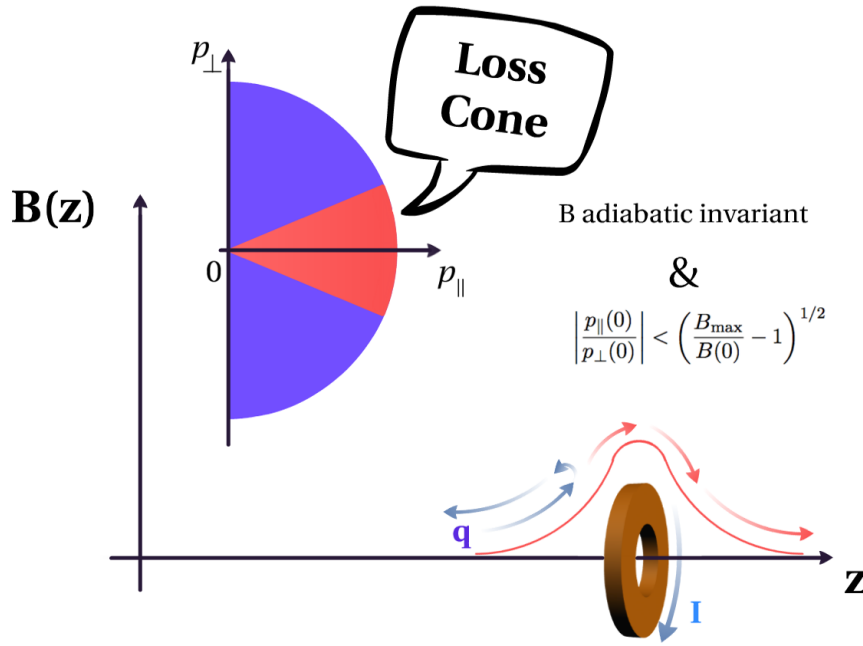


Figure 4.1: Schematic of a magnetic mirror. When a charge q approaches a coil (red cylinder) with an applied current I , p_{\parallel} will be transferred to p_{\perp} because of the rising magnetic field (solid red line). If the stated requirements of adiabatic invariance and the initial momentum ratio are fulfilled, the particle will be mirrored (blue). If the initial momentum ratio does not fulfill the stated equation it will pass the coil and escape (red). With a look on the phase space one can define the loss cone.

magnetic field value does not significantly change for one cyclotron cycle of the particle (see [127, Ch. 12.5] for a more complete derivation). The abbreviated action shows that the magnetic flux $\Phi_B = B \cdot \pi \cdot a^2$ through the orbit of the particle is an adiabatic invariant. This leads to the following equations

$$\left. \begin{array}{l} B \cdot a^2 \\ p_{\perp}/B \end{array} \right\} = \text{constant} . \quad (4.1)$$

One could say that the particle adjusts its movement such that the flux through its orbit stays constant. Together with the energy conservation

$$E_{\text{kin}} = \frac{p^2}{2m} = \text{constant} , \quad (4.2)$$

$$\text{with } p^2 = p_{\parallel}^2 + p_{\perp}^2 , \quad (4.3)$$

and the relation for p_{\perp} at different points in the magnetic field

$$\frac{p_{\perp}^2(z)}{B(z)} = \frac{p_{\perp 0}^2}{B_0} , \quad (4.4)$$

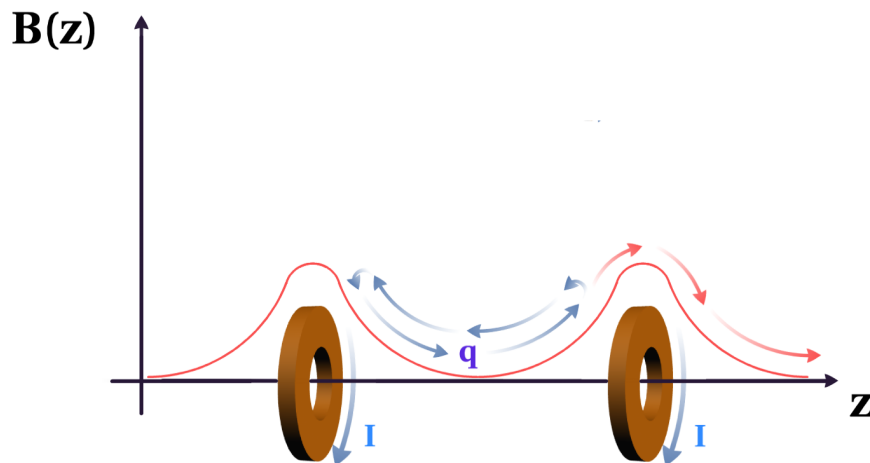


Figure 4.2: Principle of a cyclotron trap. A combination of two magnetic mirrors (see figure 4.1) is called magnetic bottle or cyclotron trap and can confine charged particles (blue arrows). Particles which do not fulfill the requirements of magnetic mirroring will escape this setup (red arrows).

with the subscript 0 denoting the initial values, one finds an expression for p_{\parallel} as

$$p_{\parallel}^2 = p_0^2 - p_{\perp 0}^2 \frac{B(z)}{B_0}. \quad (4.5)$$

This shows, that the adiabatic process of maintaining the same flux in the orbit leads to a faster spiraling and decreasing parallel momentum when moving in an increasing magnetic field. The opposite is true for decreasing magnetic field values. This ultimately means, that for magnetic field value ratios high enough particles will move slower and slower in z direction, stop and travel back. This is called magnetic mirroring. Reorganizing (4.5) gives the mirror condition for the momentum ratio of a particle for a given magnetic field configuration with its maximum value B_{\max} on the particles path and the value at the vertex of the particles creation B_0

$$\left| \frac{p_{\parallel 0}}{p_{\perp 0}} \right| \leq \sqrt{\frac{B_{\max}}{B_0} - 1}, \quad (4.6)$$

$$\theta = \arctan \left(\frac{p_{\perp 0}}{p_{\parallel 0}} \right) \quad (4.7)$$

$$\theta \leq \arctan \left(\left[\frac{B_{\max}}{B_0} - 1 \right]^{-\frac{1}{2}} \right) \quad (4.8)$$

This condition is independent of the absolute value of the total momentum $|p_0|$ but only the ratio is important. One can, thus, define a set of momenta in phase space which do not fulfil this condition as the *loss cone*, the 3D volume representation of that set which can be characterized by its aperture angle, as depicted in fig 4.1. Combining two identical magnetic mirrors, like aligning two coils on-axis as shown

in Figure 4.2, will create a confinement of a charged particle fulfilling the mirror condition (4.6), blue arrows in the figure, while those in the loss cone will escape, red arrows in the figure. Trapped particles will then perform their spiraling motion in the region between the $\pm z$ values where the corresponding magnetic field values $B(z) = B(-z) \leq B_{\max}$ define the point of return via eq. (4.5) = 0. This setup is called magnetic bottle or cyclotron trap (CT).

4.1.2 The idea

The first time a cyclotron trap was used for moderation of charged particles was done by L. M. Simons at the Paul Scherrer Institute (PSI) in the early nineties [128, 129]. The original idea was extended to work as a moderator for anti-protons, the antiparticle of the proton, and negative muons [130], an elementary particle with the same properties as the electron but heavier. A difference in this moderation compared to what was discussed before for positron moderation is that, for muons and antiprotons the process of moderation is more to be understood as slowing them down below a certain energy threshold than a thermalisation and re-emission as for positrons. Inspired by this W. B. Waeber et al. started to implement an approach for the slowing down of positrons which is based on the same principle [131] but unluckily did not manage to tune their complex experimental setup to reach their very promising theoretical predictions [132–134].

Because the muon moderation at PSI is working properly since 1993 [130] and its beauty in simplicity, it was a logical step to try to apply the principle of cyclotron trap assisted moderation on positrons. The difference however is the placement of the source and the scheme of moderation, which also differs from the setup from Waeber et al. as will be discussed in more detail in Section 4.1.3.

The pursued idea in this thesis we named the High Efficiency Cyclotron Trap Assisted Moderator (HECTAM⁺) also makes use of a cyclotron trap. In the center of the CT two very thin foils are placed, one containing radioactive material acting as the source, matched with a tungsten moderator foil. Without the trapping mechanism this would merely act as a thin film moderation geometry with a single passage of the positrons resulting in a low efficiency. The *revolution* comes by the recycling the otherwise lost positrons. A positron emitted from the source foil passing through the moderator foil but not stopping will be trapped if it fulfils the mirroring condition (4.6). Therefore, it will travel back and eventually pass through the moderator and source foil again.

Doing so they have multiple chances of being moderated or lose more energy due to inelastic scattering in the foils. In this way nearly the whole spectrum of positrons emitted from the source is available for moderation while with a simple thin film moderation geometry only less than 1% of all emitted positrons have a non-vanishing probability for getting moderated. Because moderated (slow) positrons are emitted in a cone of 60° from a well defined tungsten surface, the emitted slow positrons are very likely to be in the loss cone and are able to escape from the trap to form a slow positron beam.

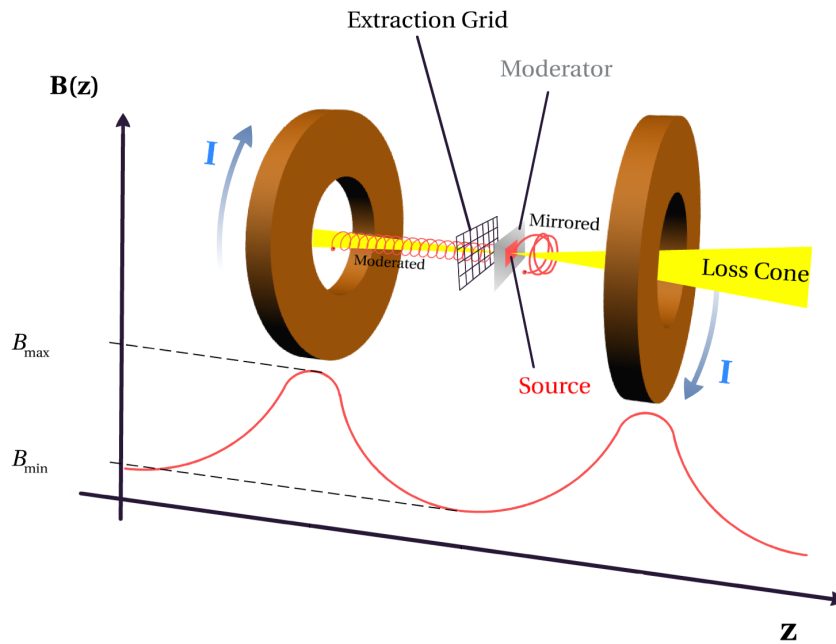


Figure 4.3: Scheme of the high efficiency cyclotron assisted moderator principle. Two coils (orange cylinders) aligned on-axis and fed with a current I create a magnetic field, sketched as the red line, forming a cyclotron trap with the on-axis magnetic field values B_{\max} and B_{\min} . In the center of the trap two thin foils, the source and the moderator, are placed. With the help of the extraction grid an electric field in $-z$ direction is added.

This extraction is of course depending on the magnetic field ratio B_{\max}/B_{\min} as explained in the previous section. To ensure a nearly perfect extraction a grid is added in front of the moderator to be able to create an electric field parallel to the trap axis which accelerates the moderated positrons into the loss cone.

4.1.3 Similarities and differences to other CT moderation setups

One CT moderation setup to compare is the one used for the slowing down of muons at PSI, cf. Figure 4.4. As mentioned earlier in this section, L. M. Simons developed the idea of slowing down muons inside a cyclotron trap placing a thin foil in the center plane of the trap [130]. The trap consists of two superconducting coils separated by 40 cm and cooled by liquid helium to create a magnetic field with values of 4 T at the coil centers and 2 T in the trap center. The muons are inserted by in-flight decay of a radially entering pion beam at energies of a few MeV.

Not all created muons are getting trapped because of their differing momentum ratios. The trapped ones will lose their energy by inelastic scattering with a 160 nm thick Formvar foil. The foil was chosen to be this thin to still have some

stopping power but small enough that the trajectory is not drastically affected and it does not absorb too many low energy muons. After passing on average several hundred times through the foil the muons will have an energy of 10-50 keV and are then extracted by an electric potential of -19 kV applied to the foil. The resulting beam of *slow* muons has an energy spectrum of 20-50 keV [135].

Compared to the energy spread of some eV of the proposed e^+ moderation setup the difference in the resulting beam quality is evident. This is caused by the additional physical process of positron moderation. While in this *muon moderation* the muons are (just) slowed down to some keV by passing through the thin Formvar foil, in the HECTAM⁺, the positrons are slowed down till they thermalise in the stopping foil which also acts as a positron moderator, re-emitting positrons with some eV. Furthermore the positron source is placed in the CT and also acts as a stopping foil. Last but not least to confine positrons with a CT much smaller magnetic fields are sufficient because of the momenta due to the smaller initial kinetic energy. This makes the use of superconducting coils and cryogenics unnecessary.

Waeber et al. tried to adapt the principle of slowing down charged particles by passing it through a foil placed in a cyclotron trap, as applied for the *muon moderation*, to slow down positrons, cf. Figure 4.5. Because they added high voltage electrostatic mirrors on the ends of the magnetic bottle to get a nearly perfect confinement, an axial extraction is not possible. Their extraction scheme is therefore somewhat more complex and consists of a complicated alignment of multiple electrodes and coils. They claimed that they can extract approximately 80% of the confined positrons once the kinetic energy dropped below 7 keV [131].

After this extraction, the keV positrons are guided to a neon moderator to form a slow positron beam. In the first publications they report about astonishing estimated and simulated moderation efficiencies of up to 40% [132–134]. Unfortunately, the complexity of the setup led to many unexpected losses and limited

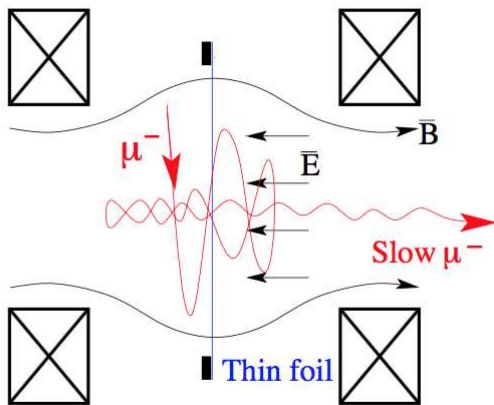


Figure 4.4: Sketch of the muon moderation cyclotron trap. The crossed rectangles are the cross section of the coils creating the magnetic field B (curved the black arrows). The blue line represents a thin carbon foil which creates the electric field E (straight black arrows). The red line shows a trajectory of a muon μ^- . Entering radially the muon is confined in the cyclotron trap. Figure reprinted with permission from [135].

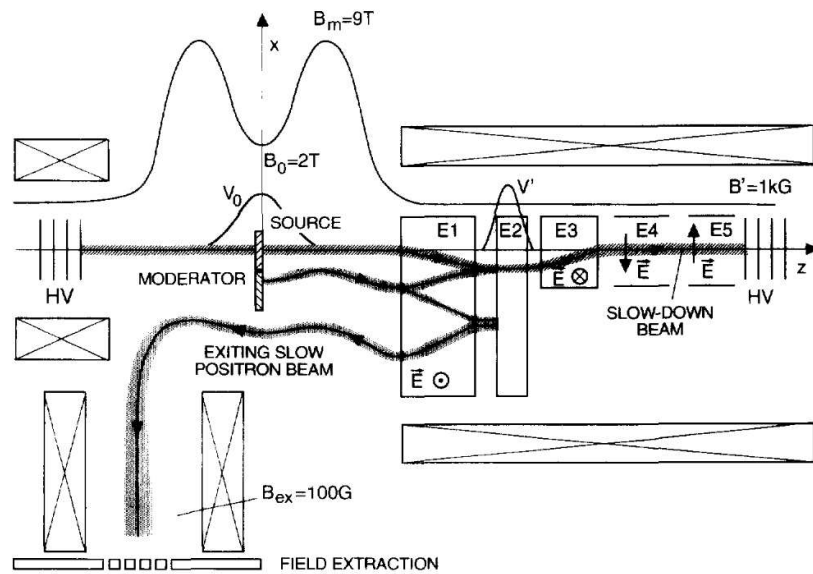


Figure 4.5: Scheme of the positron (pre-)moderation scheme of Waeber et al. The setup for slowing down positrons to some keV consists of several coils, grouped as the crossed rectangles, and multiple electrodes, solid lines. The positron trajectories are depicted by the shaded area around the solid black line with arrowheads for their direction. Reprinted with permission from [133]. Copyright 1995, Elsevier.

their experimental moderation efficiency to 10^{-3} [134] and the experiment was thus discontinued.

On the contrary to this design, in the HECTAM⁺ the moderation takes place inside the cyclotron trap and the extraction is axially. Furthermore the HECTAM⁺ does not make use of a neon moderator and is not thought to only work with superconducting coils and high voltage electrostatic mirrors. This provides the advantage that cryogenics are completely unnecessary therefore the overall setup can be held much more simple and user friendly.

4.2 A proof of principle

The idea of the HECTAM⁺ project was not to design and build a perfectly tuned moderation setup but to see if cyclotron assisted positron moderation can be really as highly efficient as assumed. Therefore the policy was to use available material and parts as much as possible. This gave some boundary conditions which led to the final, far from optimal, setup. The greatest influence in this perspective came from the coils used to create the magnetic bottle.

The two coils were recycled from the *WEB-Magnet*, a setup designed to create a very strong homogeneous magnetic field, provided by Prof. Klaus Kirch and Prof. Christoph Grab. As it revealed itself during the project, the production of

the positron source also had a larger impact than assumed. The facility at PSI used in the past does not perform this procedure anymore. This limitation will be addressed more precisely in section 4.3.3 and 4.5.

4.3 Simulation

To get the most out of the boundary conditions and to understand the qualitatively influence of different parameters in the setup a lot of simulations were performed. In a first step the magnetic field created by the two coils was analyzed. This determined the possible coil configurations which were simulated and exported as field maps first with COMSOL¹ and later with MATLAB².

These field maps were then used for particle tracing in Geant4³. The created simulation data was analyzed and evaluated via ROOT⁴. While Geant4 was mainly used for particle tracing in magnetic fields and matter interaction, SIMION⁵ gave a counterpart for particle tracing in electric fields of a little more complicated electrode arrangements. The purpose of SRIM⁶ is mainly to simulate ion implantation in solids, with this the production of the positron source was addressed.

At last the results of the simulations were put together to create a 3D assembly of the experiment in CATIA⁷. After the setup was built, the final magnetic field was measured with a probe LabVIEW⁸ and fed back into the simulations.

4.3.1 Implementation

After analyzing what magnetic fields the coils can produce and simulating them a great amount of time was spent to establish a Geant4 suite to simulate and observe the particle trajectories. This suite records various data sets at different times, positions and events to validate the simulations in term of the physics it should imitate and to get an estimation of the figure of merit. While COMSOL was a great tool to analyze and reproduce the coils and their magnetic field qualitatively, it had its limits in providing the magnetic field maps for the Geant4 simulations. When using the field maps, particles with initial momentum ratios which should cause mirroring, were hardly ever mirrored or experienced some strange trapping at the z values where they should change their direction.

This bug can be explained by how the magnetic field maps are calculated in COMSOL in combination with how Geant4 extrapolates the magnetic field values for its particles tracking from the field maps. COMSOL as a finite element analysis

¹<http://www.comsol.com/>

²<http://www.mathworks.com/products/matlab>

³<http://geant4.org/>

⁴<http://root.cern.ch/>

⁵<http://simion.com/>

⁶<http://srim.org/>

⁷<http://www.3ds.com/products-services/catia/>

⁸<http://www.ni.com/labview/>

program calculates the magnetic field for nodes of an user defined mesh. This mesh can be chosen in multiple shapes and sizes. To satisfy some boundary conditions the mesh should also extend way further than the region of interest to limit the occurrence of artifacts. The field calculated by COMSOL can then be extracted in a regular grid, e.g. as a text file. To extract the values from the calculated field to a regular grid which points are, without loss of generality, not in coincidence with the nodes of the mesh of arbitrary positions, some extrapolation have to be made.

When one would look close enough, the field maps will have some small local minima because of some unlucky combination of node positions and field values when extrapolating. Even when this is not evident, when looking at some plots of the fields, it will have an impact on the particle tracing. When Geant4 is simulating a particle trajectory it does this by calculating the force acting on the particle at its position and then performs a finite step and adjusts the velocity etc. accordingly. Once the field maps are read into Geant4, it will therefore extrapolate the values of the grid points to the current position of the particle since the particles trajectory will always lie in between some grid points because of the finite size of both the step size and the grid resolution.

As explained in section 4.1.1, particles propagating in a spatial increasing magnetic field will experience a net force pointing against their axial momentum, slowing them down and if they fulfill the mirroring condition *stop*, performing only a circular motion, and then gain axial momentum pointing backwards. When the field now has a local minimum in the region where the particle would perform this reversal in axial momentum, it will at some point face an increasing magnetic field, again, and be slowed down, even though its heading in the direction of the global minimum, the center of the cyclotron trap. If this minimum is deep enough, the particle will get trapped in this local well instead of the whole magnetic bottle. Once this effect was understood the necessity of a in $\pm z$ direction monotonically increasing magnetic field map became evident.

The available solutions would be to either reduce the grid resolution below the z step size or find a work-around for the extrapolation. Even though a higher resolution in the COMSOL field maps has shown an improvement, they also came along with an enormous increase in file size and computation duration and a different approach seemed to be necessary. The remedy came by switching to Matlab. Here the implementation of a grid is not problematic.

To calculate the magnetic field of a current loop for a given point one has to solve two elliptical integrals numerically [136], for which Matlab offers an included tool. While COMSOL simulates finite size coils within a reasonable time Matlab would suffer from serious computation overload when one tries to calculate the magnetic field for each winding of the coils individually. Therefore the coils were approximated by single current loops with the justification that the mirroring mainly depends on the magnetic field ratio than on the field values in the proximity of the coils. With the field maps created by Matlab the tracking in Geant4 now provided results consisting with the theory. With establishing a figure of merit different configurations of sources, moderators and magnetic fields were explored.

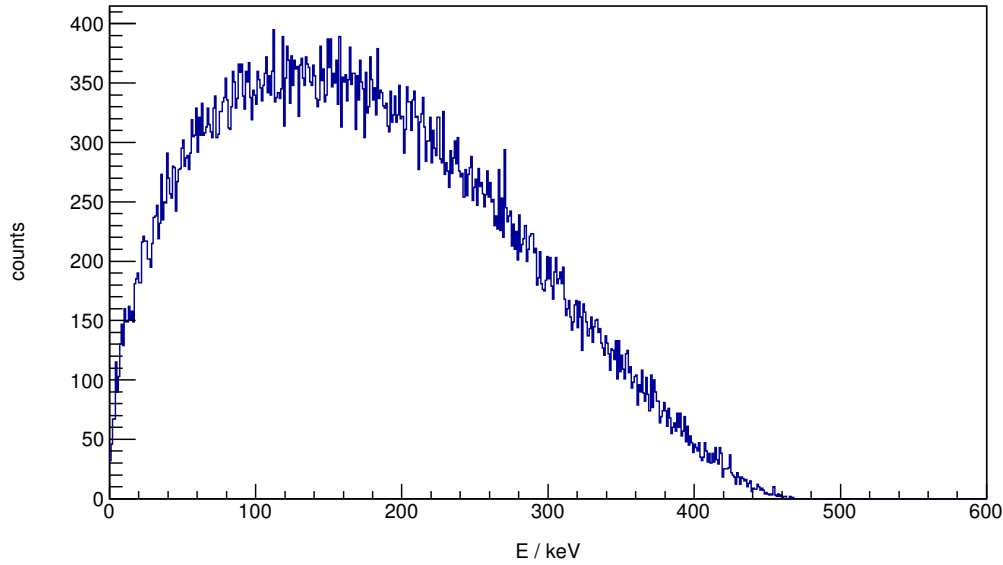


Figure 4.6: Simulated ^{58}Co e^+ energy spectrum of 10^6 events.

This lead to the results discussed in the following sections.

4.3.2 Figure of merit

Because neither the moderation process, nor the diffusion after thermalisation, of positrons is included in the physics implemented in Geant4, a different figure of merit had to be found. Since the positron implantation profiles simulated with Geant4 are validated with experimental data [137], the amount of positrons annihilating in the moderator was chosen to give a good estimate. To further address the issue, that not all positrons stopping in a moderator have the chance to moderate, only the ones annihilating within 100 nm near the surface were considered, because this is the distance positrons can diffuse in a metal before annihilating [138]. This was verified by simulation of a thin film geometry which gave a figure of merit of same order of magnitude as the values of real experiments reported in the literature. All parameters were thus chosen to maximize this figure of merit.

4.3.3 The positron source

There are three things to consider for the positron source, the position, the dimension and the radioactive isotope. The position and the dimension are important because the source is placed inside the trap and positrons will therefore have to pass through it and can annihilate within the source instead of thermalising in the moderator. Furthermore, the dimension will have an impact on the emission of the positrons. The used isotope is important for the simulation because each isotope has its characteristic energy spectrum, which does not directly have an

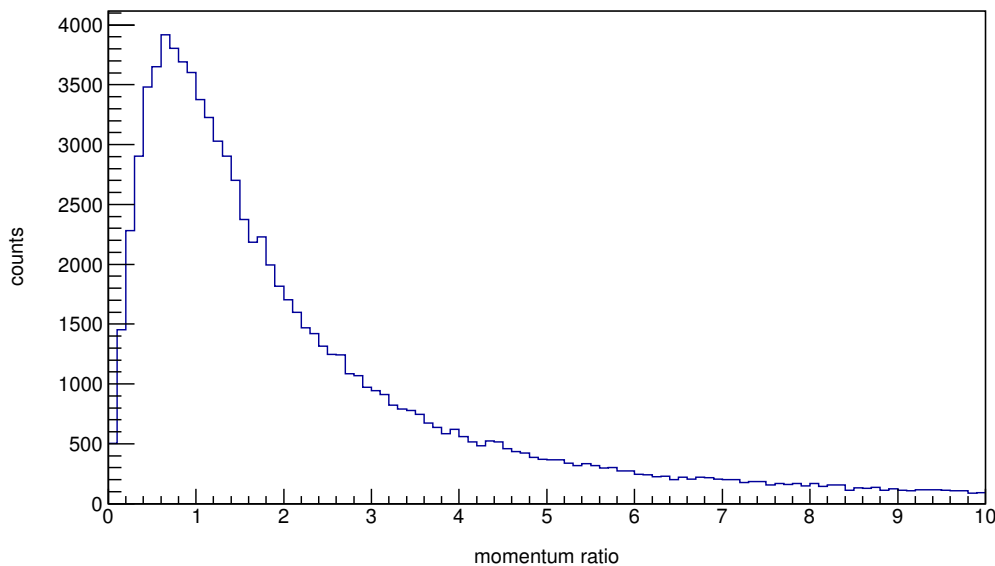


Figure 4.7: Simulated initial momentum ratio of an isotropic emission. The momentum ratio is defined by the division of p_{\parallel} by p_{\perp}

impact on the mirroring, but affects the mean cyclotron radius and with the assumption that the energy loss during each passage is more or less independent of the energy⁹, the number of passages till it can stop in the foils.

For the choice of the source material of course ultimately more characteristics, like lifetime, branching etc., have to be considered, but since those have no effect on the simulation they will be addressed later in section 4.4.2.

The probability $N(p)$ for the emission of a beta particle per unit time with a momentum p is described by the equation

$$N(p) = C \cdot p^2 \cdot (T_{\max} - T)^2, \quad (4.9)$$

with C a constant, T being the total energy of the beta particle

$$T = \sqrt{(p^2 + m_e^2)} - m_e \quad (4.10)$$

and T_{\max} the nuclei specific endpoint energy of the beta spectrum [139]. To simulate positrons which follow this probability distribution with a Monte Carlo method at least two random numbers are necessary. The first random number will probe the energy of the positron T_{rnd} between $T = 0$ and $T = T_{\max}$. Then, one shoots random numbers $0 \leq N_{\text{rnd}} \leq N_{\max}$ for this T value till the created random number fulfills

$$0 \leq N_{\text{rnd}} \leq N(T) = ((T_{\text{rnd}} + m_e)^2 - m_e^2) \cdot (T_{\max} - T_{\text{rnd}})^2. \quad (4.11)$$

⁹This issue will be discussed in more detail in section 4.3.5

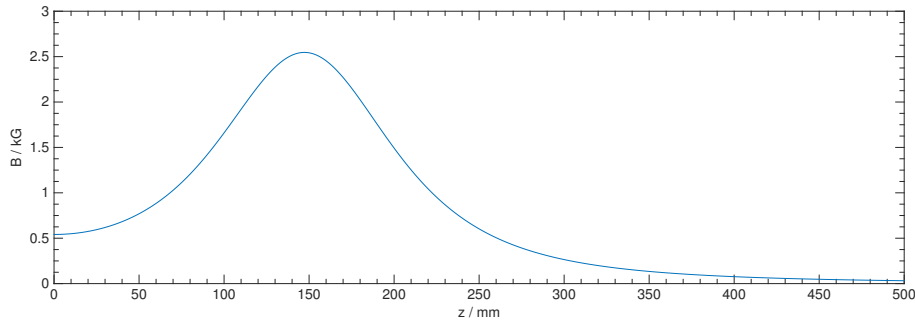


Figure 4.8: Simulated magnetic field $B_z(z)$ at $r = 0$ of the cyclotron trap. The origin is placed in the center of the trap. For simplicity the coils are approximated as current loops. The used program was Matlab.

The value for N_{\max} can be calculated via the derivative of $N(T)$,

$$0 = \left. \frac{dN(T_{\text{rnd}})}{dT} \right|_{T=T_1}, \quad (4.12)$$

$$T_1 = \frac{T_{\max} - 3 \cdot m_e}{4} + \sqrt{\frac{(T_{\max} - 3 \cdot m_e)^2}{16} + \frac{T_{\max} \cdot m_e}{2}}, \quad (4.13)$$

as $N_{\max} = N(T_1)$. A simulated spectrum of ^{58}Co is shown in Figure 4.6. The isotopes considered in this project are ^{58}Co , ^{22}Na and ^{48}V . Why the selection is limited to these three will also be explained in detail in section 4.4.2.

Table 4.1: Endpoint energies T_{\max} and maximum cyclotron radii a_{\max} for $B = 500$ G of different beta emitters.

Isotope	^{58}Co	^{22}Na	^{48}V
T_{\max} / keV	475	545	695
a_{\max} / cm	46.5	49.8	56.2

The emission was simulated as being isotropic originating from the whole source volume with the activity distributed with a Gaussian profile in the x and y direction. What became clear with the first simulations is, that the less source material is present in the setup, the more positrons will annihilate within the W moderator foil, giving a higher figure of merit. Whereby the thickness has a greater impact than the other dimensions. Testing different positions of the source showed that the placement in the center of the coils matched with the moderator is the most promising option.

4.3.4 The magnetic field

Two things are important for the choice of the magnetic field. The ratio of the minimum and maximum field values on the z -axis because it defines the performance of the trapping mechanism in axial direction and the overall strength,

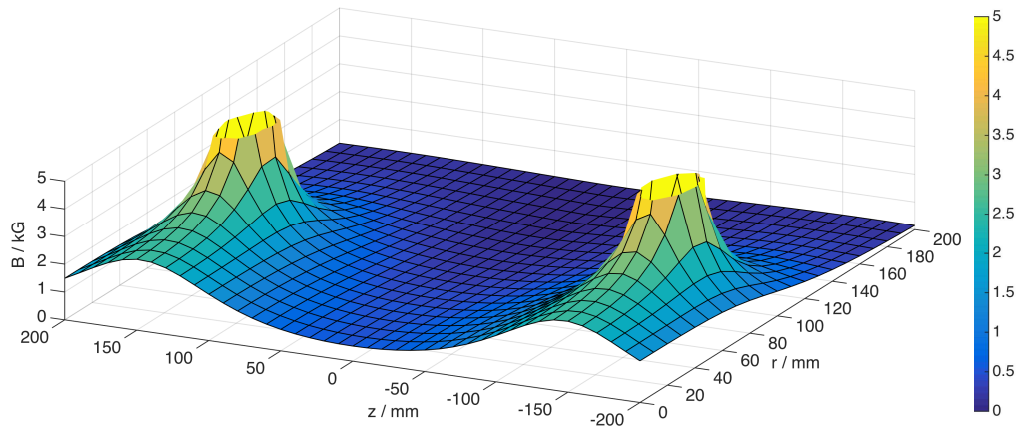


Figure 4.9: Surface plot of a simulated magnetic field $B(z, r)$ of the cyclotron trap consisting of two current loops made with Matlab. The z -axis is limited to 5 kG to get the general picture, the singularities at the positions of the current loops are thus cut.

i.e. the minimum value, because this limits the confinement in radial direction by being linked to the cyclotron radius a . If one just takes two coils to create a cyclotron trap those two criteria are depending on the separation distance and the coil dimensions.

As for this project, using existing coils, the only variable remaining is the distance. Therefore the optimal magnetic field will always be a trade-off in losing positrons axially versus losing them radially. Another criteria for the choice of the minimum field value is that it defines the radius of the out-coming beam, i.e. initial values larger than the values of the experimental region (exp) outside the trap, typically 100 G, will create a large beam spot since it scales as $\sqrt{B_0/B_{\text{exp}}}$.

Different distances, i.e. ratios and fields were tested. A minimum value of $B_{\text{min}} \approx 500$ G has shown to give a good compromise. This lead to a *real* separation of 40 cm and a maximum value of $B_{\text{max}} \approx 2500\text{G} = 5 \cdot B_{\text{min}}$.

Figure 4.8 shows the magnetic field on the z -axis simulated with Matlab. It is to remark that the maximum does not lie at $z = 200$ mm. This is because the magnetic field created by a current loop differs slightly from the one created by a finite coil. The parameters of the current loop and the *real* coils in COMSOL where thus adjusted till the magnetic field values B_{min} and B_{max} were consistent.

The field maps used for the simulations need to represent the magnetic field of the 3D volume. Because the file size of such a map is directly related to the number of points at which the field is calculated, the use of the symmetries of the setup are inevitable to get a field map of sufficient resolution and dimensions within a manageable file size. The cylindrical symmetry makes it a 2D problem greatly reducing the file size. A surface plot of such a 2D field map is shown in Figure 4.9. Using the symmetry in z at the center between the coils further reduces the file size by a factor of two. Maps with a resolution of 0.1 mm and a dimension of

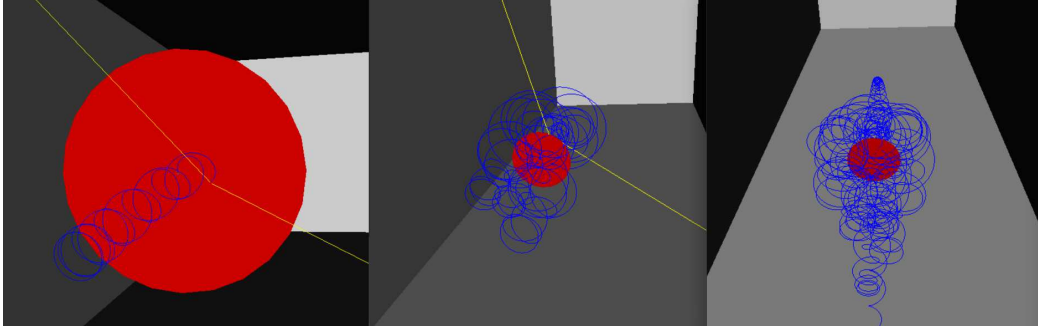


Figure 4.10: Simulated positron trajectories inside the cyclotron trap. The gray box in the background represents the physical world of the Geant4 simulation. The red disc is the thin moderator foil. The blue lines are trajectories from single positrons. The yellow lines are gamma rays created by the annihilation of the positron. The *left* picture shows a positron which gets mirrored not far away from the disc. In the *middle* picture a positron of higher energy being mirroring multiple times before it annihilates. The *right* picture demonstrates a forward scattering event.

$z \in [0, 1000]$ mm and $r \in [0, 200]$ mm have a size of a few GBytes. The field maps are then loaded by Geant4 for the tracking.

During the finite size stepping in the simulations the particle positions will nearly always lie between four points of the field map. The magnetic field values are therefore linearly extrapolated in r and z to get the effective value at the particles position. For tracking a single particle this approach can be somewhat slower and less precise than solving the magnetic field equations of the particle positions on a step by step basis but for a higher amount of events this procedure greatly speeds up the simulations process without losing to much precision.

4.3.5 Trajectories

Examples of trajectories of mirroring events are shown in Figure 4.10. In this section a selection of the properties of the positron trajectories are presented and discussed with histograms or scatter plots, e.g Figure 4.11 shows the positions in z where positrons reversed their perpendicular momentum. Comparing the two wings, one notices a slight asymmetry. The slope when advancing from the center is a little steeper on the right side. This originates from the placement of the foils. The source is centered at $z = 0$ and if there would be no other material the wings should be symmetric but with the moderator foil placed on the $-z$ side, positron (re-)emitted in that direction lose more energy than the ones (re-)emitted in the z direction. This can be understood by linking the mirroring position in z to the energy of a particle. The positrons which make it out of the tungsten foil are generally a bit higher in energy than the ones being (re-)emitted from the source material.

The maximum mirror position $|z| \lesssim 150$ mm is the coil position. Any positron

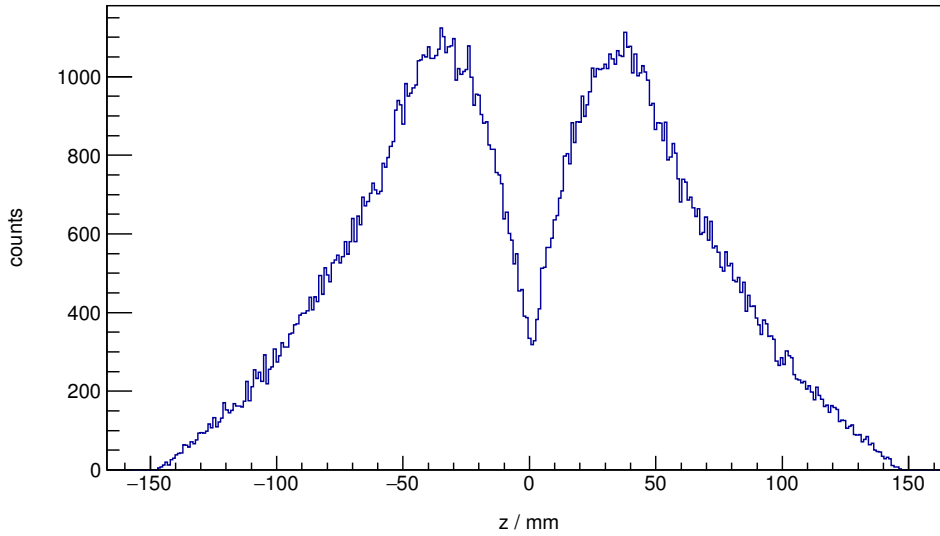


Figure 4.11: z -positions of mirroring of 10^6 simulated positrons. The counts fall to zero at the positions of the current loops.

making it further than that distance will escape. The Figure 4.12 of the energies of the positrons for each mirroring event has, as expected, a similar shape. It is to notice that the number of events drops to basically zero for energies $E \gtrsim 250$ keV, the trap seems not to confine particles with higher energies.

The shape can be qualitatively understood by taking the part of the spectrum of initial energy at creation which should get trapped and accounting that for each of those energies another mirroring count will appear with a lower energy after it has lost energy in the foil and is mirrored again. This leads to the strong increase in counts going from higher to lower energy. At the maximum and lower energies one can indirectly see the energy deposited for a single passage, as shown in Figure 4.13. The counts drop to zero because the probability to lose all the energy and to stop grows with lower energies.

The quantitative values of the deposited energy are of course completely depending on the materials and dimensions of the used foils. Another remark here is that the positrons do not actually pass through the foils on most passages through the trap center, as can be seen for the $E = 0$ bin in the Figure 4.13. This is also dimension related, the radius of the foils is smaller than the cyclotron radius of the positrons so there exists the chance that they spiral around the foils but do not hit it, cf. fig 4.10.

A correlation between the energy lost and the energy when impinging on the moderator can be seen in Figure 4.14. For impinging energies above 70 keV it is very unlikely to stop in the foil and the average deposited energy is about 10 keV. When a positrons has an energy below 70 keV the energy loss is more equally distributed. This explains the effect of the sources choice on the figure of merit.

Even if one would not expect an impact of the different source isotopes when

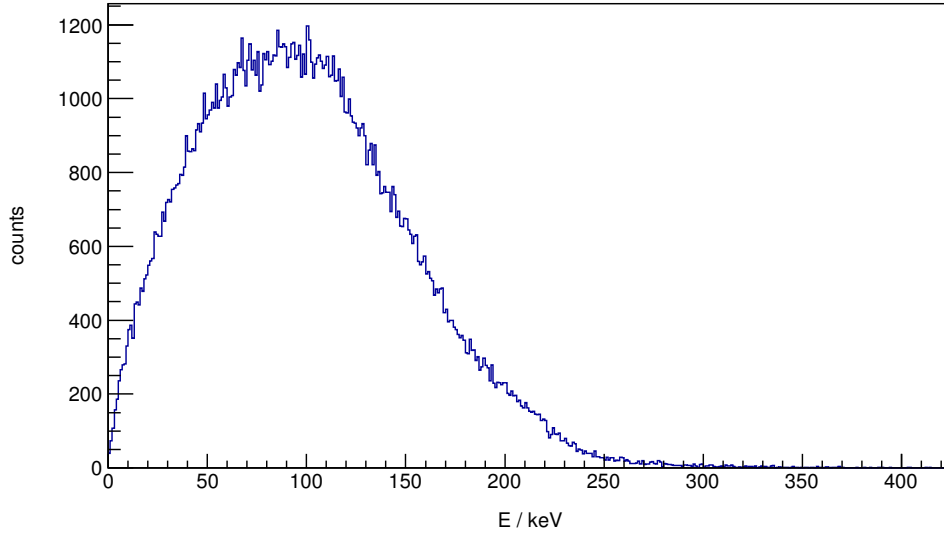


Figure 4.12: Energy E of the positrons when they are mirrored. Positron with energies higher than 250 keV seem not to mirror.

looking at the trapping equations, it does. The higher the endpoint energy, i.e. the whole spectrum, is, the lower is the figure of merit. This relation is on one hand caused by an artificial problem, the magnetic field is not strong enough to confine positrons with large perpendicular momentum, and on the other hand by an effect to be referred as *forward scattering*.

This forward scattering describes the mechanism that particles which were originally trapped, can get scattered into the loss cone when passing through the foils. When the energy lost during each passage is more or less independent of the impinging energy, the average positron from a source with a higher energy spectrum will have to perform more passages, thus the chance that it undergoes the process of forward scattering is more likely. The overall effect of this decreases the performance of the HECTAM⁺ and will be reviewed in section 4.5.

That a mirrored positron will not always imping on the foils can also be seen by comparing Figure 4.16, showing the number of mirroring events versus the initial energy, and Figure 4.17, representing the number of times a positron has passed through the foils versus the initial energy. The fact that some positrons get mirrored and do not pass through the foils actually led to a glitch in the simulations that the tracking of a single particle could take longer than the rest of the run. To prevent memory overflow those particles were artificially stopped when the number of mirroring events reached 999. The number of passages show again that the confinement is only effective for positrons with energies below 200 keV while the number of mirroring events suggests that positrons with energies up to 250 keV can be confined.

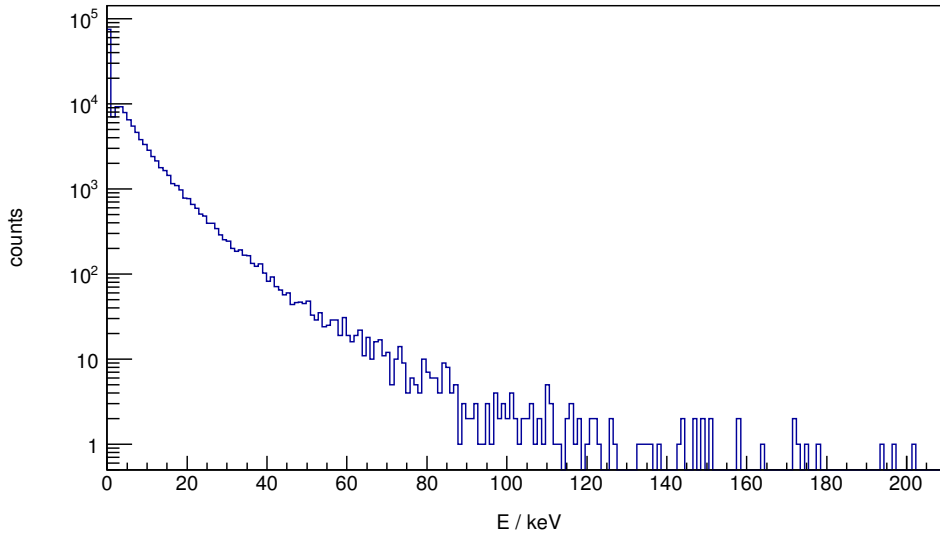


Figure 4.13: Energy deposited in the moderator foil in one passage for each single passage of a positron. An energy of $E = 0$ means that a positron did not pass through the foil on its way from one side of the trap to the other.

4.3.6 The moderator

Figure 4.19 shows the simulated annihilation profile in z dimension. The annihilation of a positron in Geant4 is done when the particle is at rest, i.e. when the particle thermalises. The processes of forming positronium, trapping in volumes or surface states, or moderation is not included in the physics of Geant4.

Consequently the figure of merit (section 4.3.2) was chosen to be the *annihilation* in the 100 nm slice ranging from $z = -1.9$ to $-2 \mu\text{m}$. The Figure 4.19 describes the impact of foil dimensions, i.e. the thickness. In a first approximation the total amount of positrons stopping in the two foils are the same regardless of the thicknesses. Therefore more material, no matter if source or moderator, means less positrons stopping in the 100 nm slice of interest. This also accounts for the other dimensions.

Another factor to consider for the moderator dimensions is that it defines the size of the resulting slow positron beam. Moderated positrons of eV energy have a negligible small cyclotron radius but they originate from all over the moderator surface, therefore, a larger moderator gives a larger beam spot. The relation between the z decay position and the initial energy of positrons is shown in Figure 4.18. The annihilation is with respect to the energy uniform over the solids, except for the low energies which will stop in the source or outer region of the moderator and do not make it up to middle region.

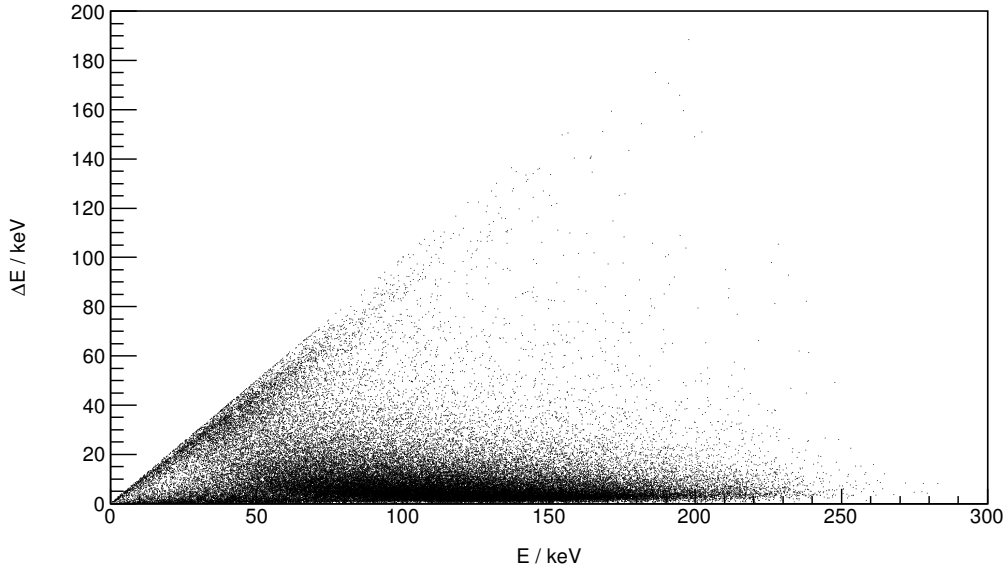


Figure 4.14: Energy deposited in the moderator foil during one passage versus the energy with which they imping for each single passage of the 10^6 positrons.

4.3.7 The vacuum chamber

Because the positrons will rapidly decay if they collide with matter, i.e. gas molecules, the whole setup needs to be kept in an ultra high vacuum (UHV) environment. The critical point is the required volume. Larger volumes usually come with longer evacuation times, worse vacuum and higher costs for the chambers. To get a hold on the volume which is needed for the trapping mechanism Figure 4.20 and 4.18 were taken. Figure 4.20 shows the maximum radii any positron of given energy has taken as a function of its position in z . The cut in the plot shows that high energy positrons with a large perpendicular momentum can escape the trap radially and are lost.

In this sense stronger coils or a higher B_0 would be preferable to get a more efficient radial confinement but for the coils used in this experiment a higher B_0 would lead to a smaller magnetic field ratio and thus a less efficient axial confinement. The simulations suggested that the used magnetic field will yield the best figure of merit for this trade-off.

Furthermore, simulations with stronger magnetic fields showed that the axial loss has a greater impact due to the forward scattering and that high energy positrons are more unlikely to slow down till they moderate. When one considers the characteristics presented in the trajectories section 4.3.5. The conclusion is plotted in Figure 4.18, showing the different fates, stopping in the moderator or the source, or escaping from the trap, of positrons regarding their initial energy. It is evident that for the proposed magnetic field only positrons with energies below 200 keV contribute to the figure of merit. Taking this into account the needed radius of the volume can be read directly from Figure 4.20 as $r \geq 120$ cm.

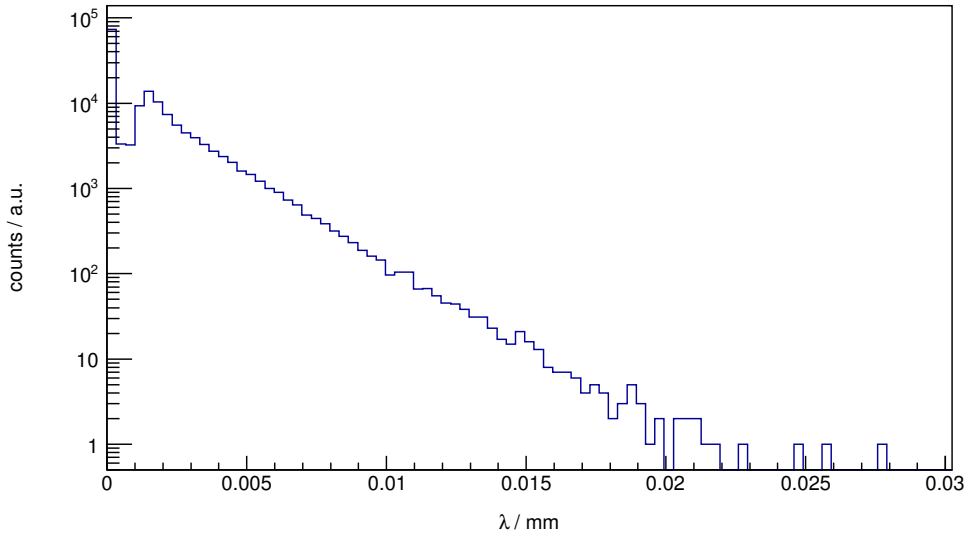


Figure 4.15: Passlength λ of the positrons in the moderator foil of $1\mu\text{m}$ thickness during a single passage. A length of $\lambda = 0$ means that a positron did not pass through the foil on its way from one side of the trap to the other. The flat region next to $\lambda = 0$ matches the thickness of the moderator foil.

4.3.8 Extraction, blocking and guiding

It is of interest to extract the moderated positrons from the trap and guide them to a detector system with a high efficiency. For this purpose the emission of low energetic positrons from the moderator surface were simulated with Geant4 as well. The spread of $p_{\parallel} = 3$ eV is given by a FWHM = 1 eV for a clean tungsten moderator surface. The angle of the loss cone of the cyclotron trap is described by (4.8) and is $\theta \approx 27^\circ$ for the chosen magnetic field ratio of 5. Simulating the extraction efficiency gives a value of about 50%. Applying a potential of +100 V on the source and grounding the extraction grid shown in Figure 4.3 accelerates all moderated positrons into the loss cone and the simulated extraction efficiency increases to 100%.

4.3.9 Detection

The extraction grid does not only support the formation of the slow positron beam but offers the possibility to reverse this effect and provide a tool to measure the moderation efficiency. Originally the positrons escaping the trap would be a mixture of fast positrons with energies in the keV range and the slow, moderated, ones with eV energy. Biasing the extraction grid and source with either +100 V on the source or +100 V on the grid keeping the other one grounded will extract or block all slow positrons. The difference in the number of positrons escaping the trap for these two configuration are the moderated ones.

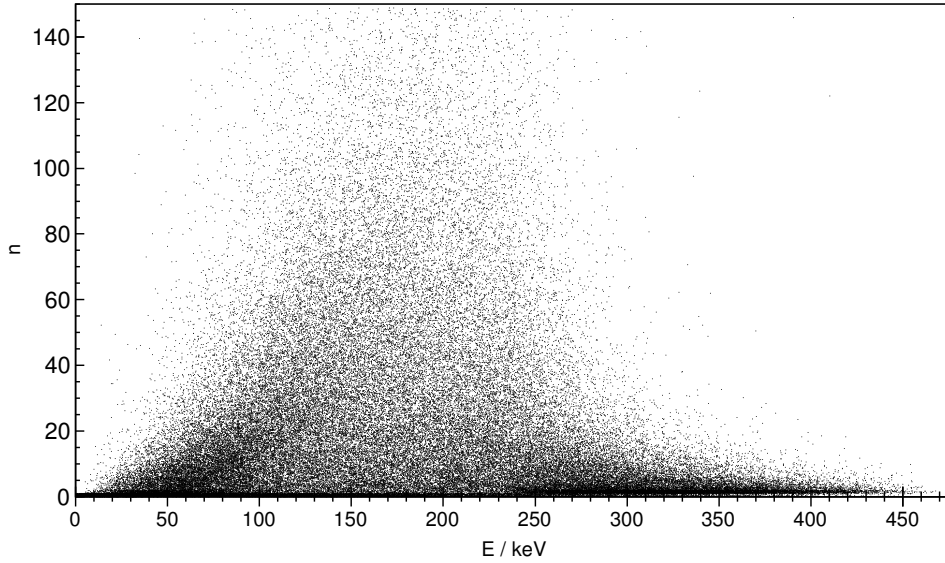


Figure 4.16: Number of mirroring events n of 10^6 positrons versus their initial energy.

To actually detect the extracted slow positrons two setups were implemented. Two large solid angle bismuth germanium oxide (BGO) detector units in coincidence to detect the two 511 keV photons of the positron annihilation or a Electron Multiplier (EM) detector directly detecting the positrons. To reduce the solid angle of γ s emitted by the source hitting the detectors and operating the detectors in a less strong magnetic field a 1 m long 100 G solenoid wound on a tube was added at the end of cyclotron trap to guide the positrons to the detector in the case of the MCP or on a dead end flange as a conversion target for the BGOs. In this geometry only 10^{-5} γ s would add to the background. Additionally most of the fast positrons will annihilate in the guiding tube of 40 mm diameter because their cyclotron radius at 100 G is larger than the tube's. The remaining background of fast positrons is in the order of 10^{-2} and of the same magnitude as the expected moderation efficiency.

4.4 Experimental setup

The final experimental setup is shown in Figure 4.21. The vacuum chamber fabricated at the PSI has a diameter of 250 mm and a length of 40 cm. The top has a 250 mm flange to insert the sample holder. The opening is designed large because the sample holder should cover as little space as possible in the volume of the positron mirroring. On top of the flange on which the sample holder is mounted, is a small flange for the electrical feedthroughs connecting the moderator and the extraction grid.

Below the supporting aluminum plate a turbo and a scroll pump are attached to maintain the UHV. In the back a gaugemeter is added to monitor the pressures.

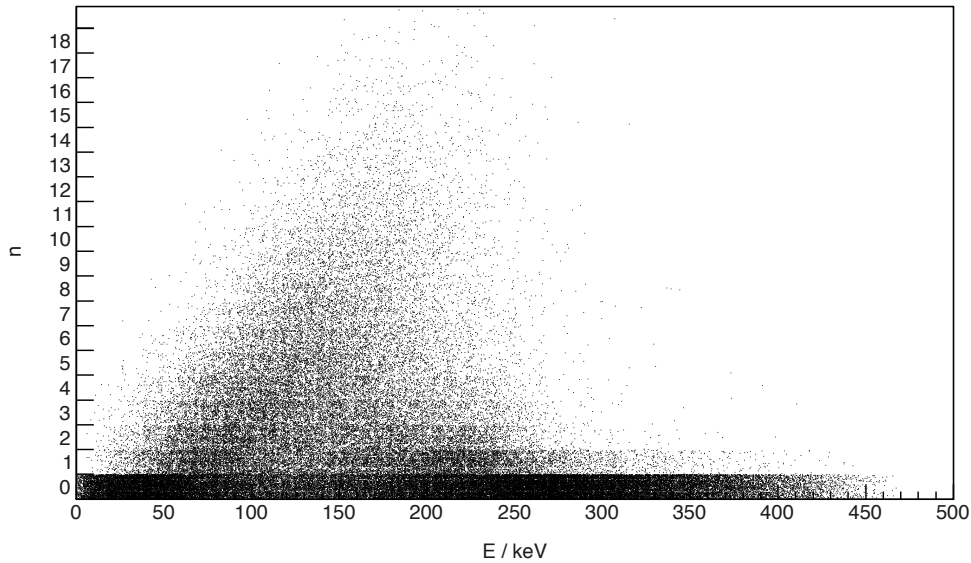


Figure 4.17: Number of passages through the foils n of 10^6 positrons versus their initial energy.

The two coils, their water cooling system and the power cables are fixed on the chamber and framework. To the right, leaving the picture, the 1 m long 100 G guiding coil with 2 turns per mm wound on a 40 mm diameter tube can be seen.

4.4.1 The coils

Refurbished from the WEB-Magnet, an experiment to create a strong highly homogeneous magnetic field, the two coils shown in Figure 4.22 can create fields of up to 2.5 kG in their center. The inner diameter is 16 cm, the width 4 cm and the outer diameter 32 cm. They are wound by a hollow square copper tube which exits the coils every couple turns to attach several lines of water cooling hoses. When run in series with a current of 650 A they use about 100 V and the maximum temperature at the water outlets reaches about 65° C. Higher temperatures would violate the safety precautions of the used materials, e.g. 80° C for the water hoses.

To measure the magnetic an automatized magnetic field analysis probe was build. A LabVIEW script records magnetic field values of a hall bar attached to a lance while piloting the system with a stepper motor. The measurements at different currents are shown in Figure 4.23. Unexpectedly the magnetic field ratios shown in the (*right*) plot declines with current. This effect is assumed to origin from the finite size of the coils. The characteristic field values for a current of $I = 650$ A are $B_{\max} = 2559(2)$ G and $B_0 = 544(2)$ G.

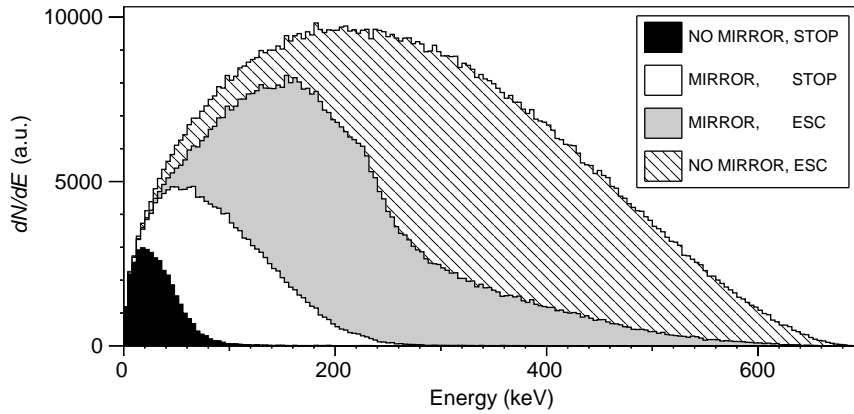


Figure 4.18: Simulated positron energy spectrum of ^{48}V separated into fraction of positrons which were not mirrored and stopped inside the moderator or source foil (black area), mirrored at least once and stopped (white area), mirrored at least once and escaped the trap (grey area) and not mirrored and escaped (hatched area).

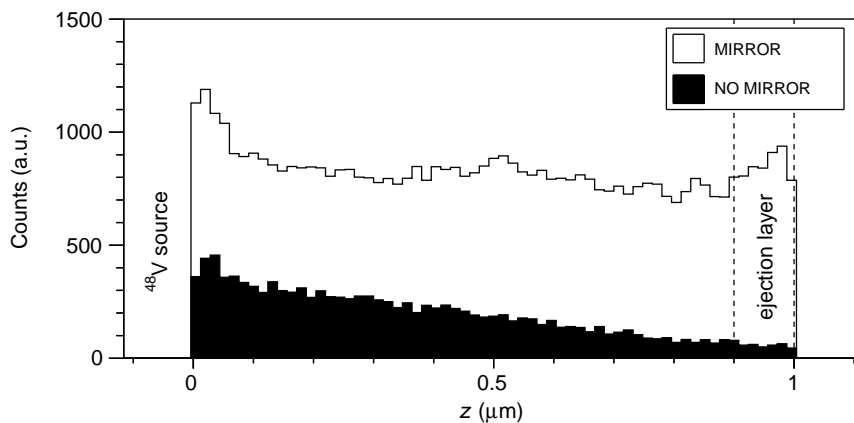


Figure 4.19: Simulated axial stopping position z split into mirrored (white area) and not mirrored (black area) events. The W moderator foil is ranging from 0 to 1 μm . The ^{48}V source sits on the $-z$ side of the moderator. The ejection layer ranging from 0.9 to 1 μm is marked by the dashed lines.

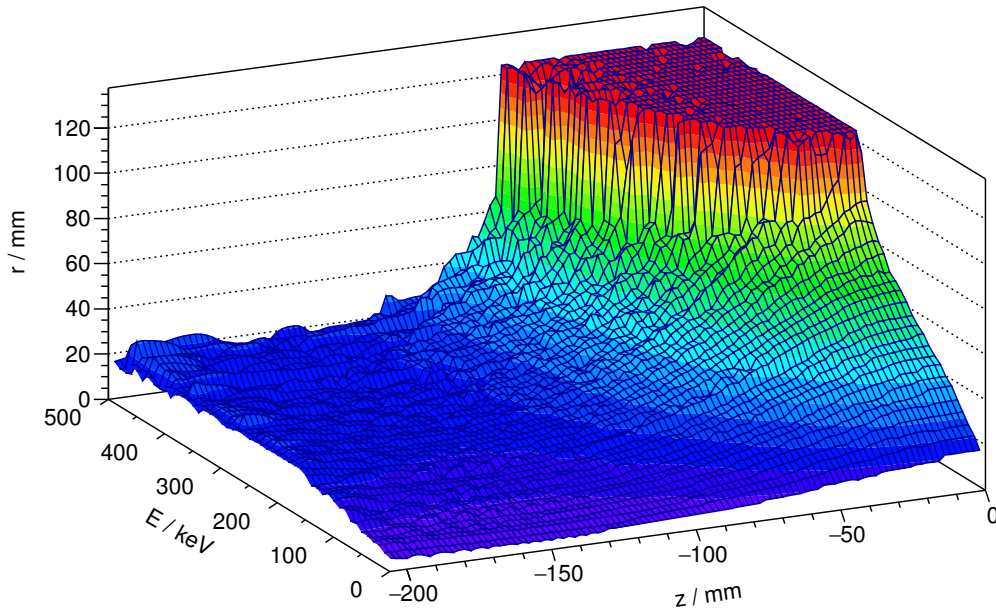


Figure 4.20: Maximum radii $r(E, z)$ positrons of given energy E as a function of z during the simulations. The shown surface represents the volume in which the positrons perform their motion.

4.4.2 Thin film positron sources

The results of the simulations have shown that the radioactive sources should be as small, i.e. thin, as possible. Furthermore they need to be vacuum compatible. The thinnest foils available are around $1 \mu\text{m}$ thickness with sizes up to some cm. The best option would be to bombard such an Al foil with protons to create incorporated atoms of the β^+ emitter ^{22}Na as was done in the past at PSI for the first prototype of the ETHZ slow positron beam. Unfortunately, this facility was not available anymore and no other Institute was found to cooperate in this matter.

The advantage of ^{22}Na , the most common used radioactive source in positron physics, is the long half-life and the high branching for positron emission. Alternatives are ^{58}Co and ^{48}V . The cobalt isotope can be produced via $\text{Ni}(n_{\text{th}}, X)$, has an acceptable half-life and brings the benefit of a lower energy spectrum than sodium but comes with a low branching, see Table 3.1. Vanadium, created by $\text{Ti}(p, X)$, on the other hand has a tolerable branching but a comparably small half-life and has the highest energy spectrum of all.

Activated Thin Metal Foils

Activities A created by irradiation can be calculated as following,

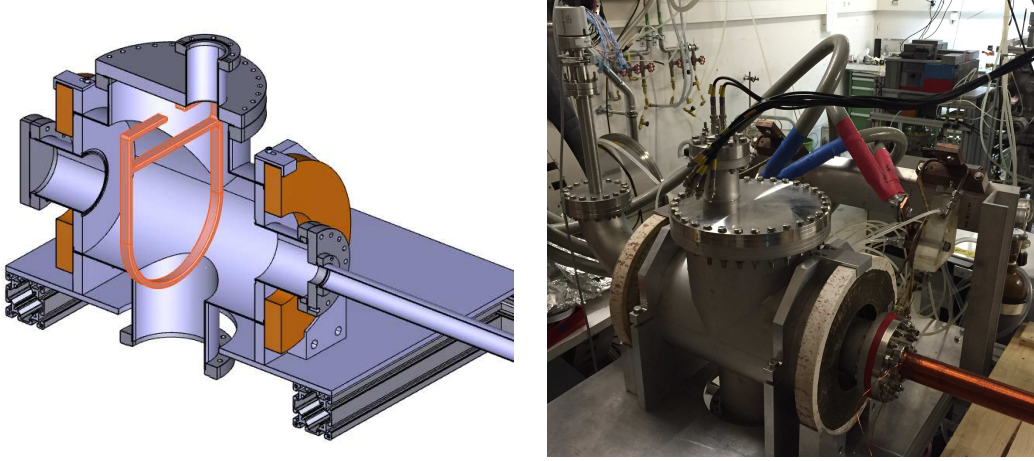


Figure 4.21: Model and picture of the final setup consisting of the CF250 vacuum chamber, the two high current water cooled coils forming the magnetic bottle, the CF40 guiding coil, the source, moderator and extraction grid mount, electrical feedthroughs and the gaugemeter.

$$A = N/\tau = \ln(2) \cdot t_{1/2}^{-1} \cdot Y \cdot I_p \cdot t, \quad (4.14)$$

with the half-life $t_{1/2}$, the projectile current I_p , the irradiation duration t and the yield

$$Y = n_{\text{target}} \cdot \int_0^R \sigma(E) dx, \quad (4.15)$$

with R the stopping range of the projectile in the target, $\sigma(E)$ being the cross-section and the number of atoms per unit volume in the target

$$n_{\text{target}} = \rho/m, \quad (4.16)$$

with the density ρ and atomic mass m . Because the thickness of the target d is much smaller than the stopping range $d \ll R$, the cross section can be seen as a constant $\sigma(E) \approx \text{const}$. In this thin film approximation the yield becomes

$$Y \approx n_{\text{target}} \cdot d \cdot \sigma(E) \quad (4.17)$$

resulting in the end of bombardment (EOB) activity

$$A = \ln(2) \frac{\rho_{\text{target}} \cdot d \cdot \sigma(E) \cdot I_p \cdot t}{t_{1/2} \cdot m_{\text{target}}}. \quad (4.18)$$

An approach to create such an activated Ti foil was to perform an irradiation in-house at the Institute for Particle Physics with the Ion Beam Physics group and their TANDEM accelerator. For this purpose the special copper target mount shown in Figure 4.24 was refurbished from an old experiment. The maximum performance of the TANDEM in the current state is a proton current of $I_p = 1\mu\text{A}$ at about $E = 8 \text{ MeV}$. To improve the yield the foil was mounted in a 45° angle, increasing the thickness seen by the proton beam to $d = \sqrt{2} \cdot 1\mu\text{m}$. Calculating the expected EOB activity with the values listed in table 3.1 gives $A \approx 25 \text{ kBq/hour}$.

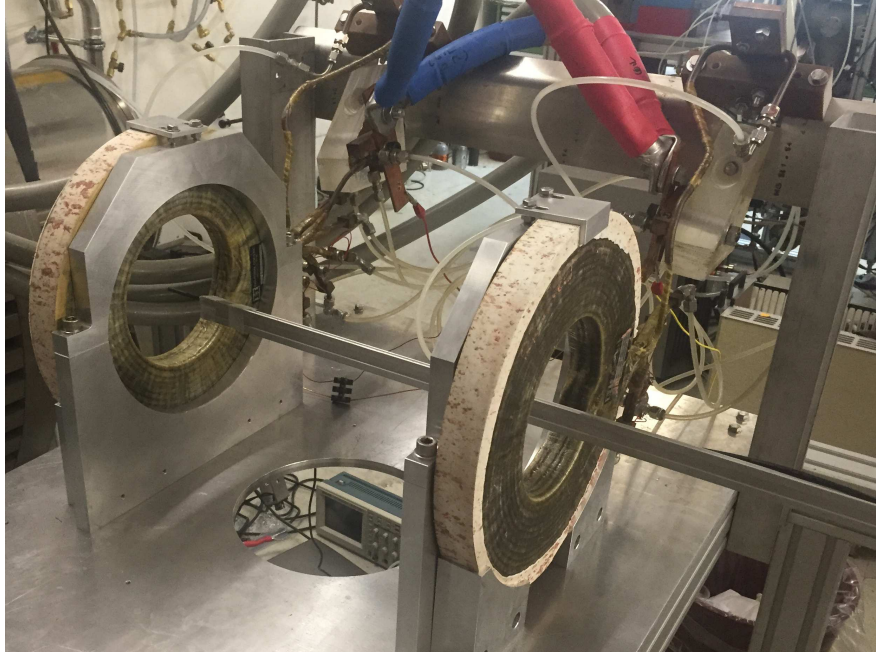


Figure 4.22: Picture of the coils creating the magnetic bottle. In the back the hoses of the water cooling system are connected to the hollow copper windings exiting the coil every couple turns. The red and blue large diameter cables connect the coils in series to the high current power supply.

Because only a small amount of impinging protons will be absorbed by the Ti foil a W beam-dump simulated with the SRIM suite was added. Estimating the heat dissipation through black body radiation of the ~ 8 W deposited in the sample holder shows that the Cu holder of about 300 g should not exceed temperatures of 150° C. It is therefore not expected that the foil sustains any damage from the irradiation.

While this source served the proof-of-concept study the production of larger activities was pursued with the 12 MeV proton external Beam Transfer Line (BTL) of the IBA 18 MeV medical cyclotron located at the Bern University Hospital (Inselspital) [140]. The setup is optimised for the production of highly radioactive samples for Positron Emission Tomography (PET). With a special solid target design [99] an irradiation of a $1 \mu\text{m}$ Ti foil for 1/2h with $20 \mu\text{A}$ yielded 400 kBq. This opens the possibility of producing Ti-V sources at a larger scale.

Concerning a ^{58}Co source a collaboration with the Heavy Elements research group of the Laboratory of Radiochemistry and Environmental Chemistry (LCH) of PSI was engaged. A four week irradiation of a $1 \mu\text{m} \times 4 \text{mm} \times 4 \text{mm}$ Ni foil at the Swiss Spallation Neutron Source (SINQ) at PSI yielded 9.8 kBq ^{58}Co and 1.5 kBq ^{57}Co .

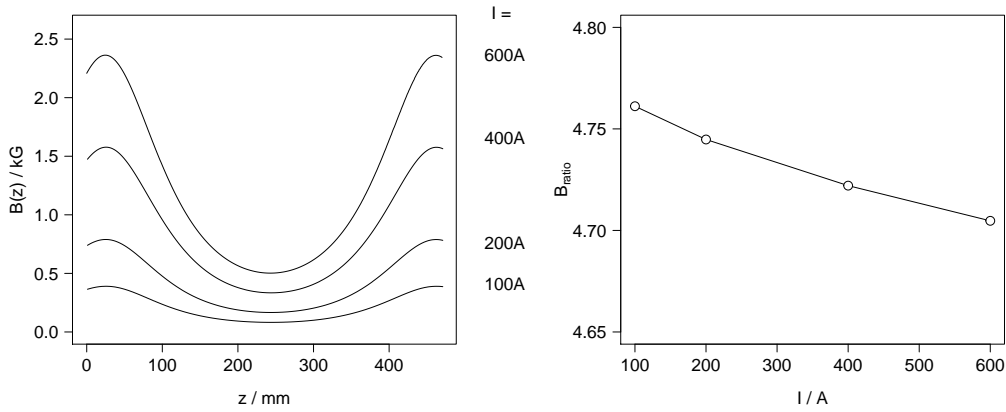


Figure 4.23: Measurement of the magnetic field $B(z)$ of the coils along the z -axis operating at different currents I (*left*) and the corresponding magnetic field ratios B_{ratio} (*right*). The origin in z is arbitrary and the range was limited by the measurement setup.

Implanted ^{22}Na Thin Film

The production of a ^{22}Na source has a higher threshold (see Table 3.1) and to achieve comparable activities requires about 1000 times more protons on target than the ^{48}V production. The production of up to 20 MBq ^{22}Na sources by irradiation of 125 μm aluminium foils with 72 MeV protons has been demonstrated in the past at PSI [24, 141]. With commercial 70 MeV cyclotrons for isotope production [142] 1 MBq sources of stacks of 1 μm foils could be produced in 10 days of irradiation with 80 μA currents.

Another completely new approach is the radioactive ion implantation into thin films or substrates in general. This became only recently possible with the availability of the on-line isotope mass separator ISOLDE at CERN¹⁰. A facility producing high purity ions beams of radionuclides by mass separation of the produce from fixed target proton bombardments. In a proof of concept experiment an annealed 1 μm Ni foil as a target was bombarded for approximately half an hour with 50 keV ^{22}Na ions resulting in an end of bombardment activity $A_{\text{EOB}} = 100 \text{ kBq}$ on 17.05.2019.

The expected mean implantation depth from simulations with the SRIM package [143] is 0.1 μm . Before the shipment of the Ni foil to CERN, the moderation efficiency was characterized in the continuous positron beam to be $\epsilon = 5 \times 10^{-4} \text{ e}^+ \text{ s}^{-1}$. Assuming no degradation of the foil the expected rate of self-moderated positrons is $\Psi_{\text{e}^+} = 10 \text{ e}^+ \text{ s}^{-1}$. An experimental confirmation is planned to be conducted during a scheduled downtime of the continuous positron beam.



Figure 4.24: Picture of thin Ti foil TANDEM proton irradiation mount mainly fabricated out of ~ 300 g copper to ensure a good heat dissipation. The copper parts are protected from irradiation by a 0.3 mm thick W beam dump. The thin Ti foil (black, on the left) is held by another W baffle. A piece of paper on the right is mounted for calibration purposes of the proton beam.

4.4.3 The tungsten moderator

For the moderator the same principle for the dimensions as for the source applies. The less material is present in the trap, the higher the figure of merit. Most important though is a small thickness. The best moderation efficiency for thin film foils are for (110) single crystalline tungsten. Discs of $1 \mu\text{m}$ thickness with diameters up to 1 cm were purchased from the Dept. of Physics and Astronomy of the University of Aarhus from Denmark.

To get the most out of a thin metal moderator their surface needs to be very clean. The best efficiencies for single crystalline foils are achieved by annealing them multiple times in-situ, however, short-term exposure does not degrade the surface dramatically. A common way is, to heat the foil up to about 2000°C by implantation of a bright high energetic electron beam. To apply this technique, a previously used electron gun was mounted on the standalone annealing station shown in Figure 4.25. The tempered foils were kept in vacuum and were only exposed to air for about 1-2 h during the mounting.

4.4.4 Extraction and blocking system

As repeatedly said, it is crucial to have as little material inside the trapping volume as possible. This is especially problematic when it comes to actually placing the source, moderator and extraction grid in the vacuum chamber. The solution is shown in the Figure 4.26. The source and moderator foils are matched between two tungsten high transmission (96%) grids. Those grids are sewed together and suspended with a $100 \mu\text{m}$ thin stainless steel wire which is strung on a U-frame of a radius close to the one of the chamber. The extraction grid is held perpendicular with the same technique.

¹⁰<http://isolde.web.cern.ch/>

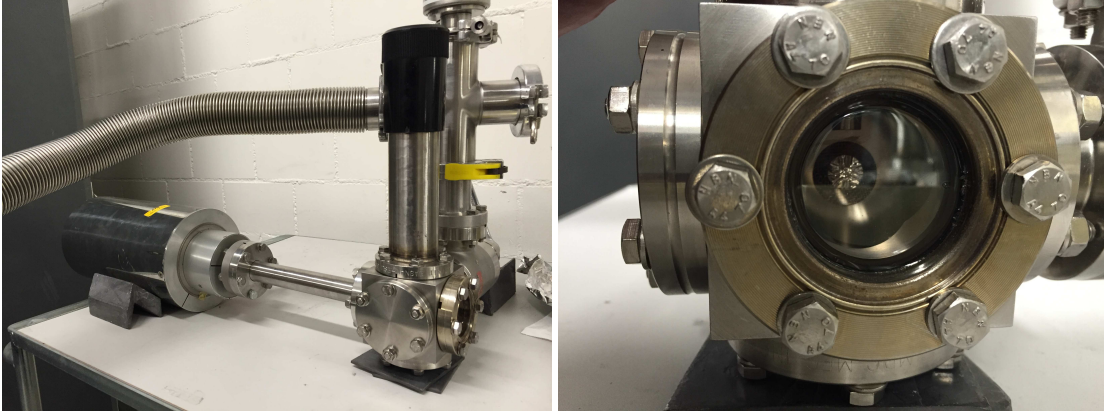


Figure 4.25: The standalone W foil annealing station. The *left* picture shows the setup, the electron gun (big silver cylinder on the left), the foil is mounted between two meshes and can be positioned with a linear shifter (black handlebar). The whole system is connected to a pumping station (flexible tube). *right* picture shows the viewport from where the blackbody radiation spectrum emitted from the W foil (silver disc) can be analyzed to measure the temperature.

Each string is isolated from the large aluminium frame and one string of each unit is connected to an electric feed through. The distance between them is approximately 1 cm to create a well defined electric field along the z -axis when biased thus allowing for extraction or blocking of the moderated positrons.

4.4.5 Detection systems

Two different detection schemes were build to measure the moderation efficiency, an indirect detection by measuring the gamma rays and a direct method with a single particle detector. Figure 4.27 shows a large solid angle BGO detector arrangement consisting of 8 crystals, 4 above and 4 below. The positrons were simply guided on a blind flange as a conversion target. Summing the signals of the 4 crystals in each unit and filtering for coincident events should give a count of positrons reaching the target decaying into two 511 keV γ s convoluted with a background of cosmic radiation and accidentals. The solid angle corrected difference in counts between the extraction and blocking mode should give the number of moderated positrons.

Due to the limited activity of the source available for this experiment an EM to detect the slow positrons was used since it has smaller dark counts (< 1 count/s) compared to MCPs. The drawback is that EMs are very sensitive to magnetic fields and therefore the positrons have to be extracted from the guiding field used for their transport. This was realized by terminating the magnetic field with Mu-metal shielding. Simulations with SIMION and COMSOL were used to optimise the extraction efficiency to values close to 100%.

This was confirmed experimentally by using the ETHZ slow positron beam. As this scheme requires a whole new type of sources more effort to produce thin-film

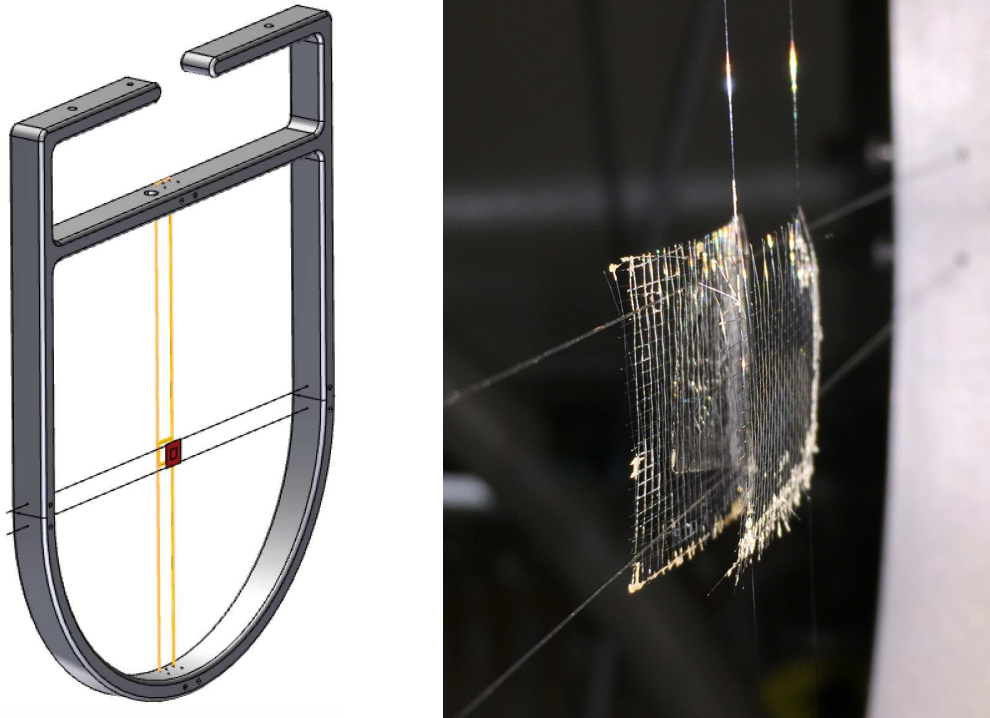


Figure 4.26: Model and picture of the sample, moderator and extraction grid mount.

sources was made. For the proof of concept study of the cyclotron trap assisted moderation a ^{48}V was produced by proton bombardment with the TANDEM ion accelerator at the Laboratory of Ion Beam Physics, ETH. At the time of the experiment the positron activity was $3.2(1)$ kBq, measured with a germanium detector and a calibration source. The division of the counts in the extraction mode by the total positron activity gives a moderation efficiency of $\epsilon = 1.8(2)\%$ is in fair agreement with what has been estimated from the simulation results.

4.5 Discussion

The proposed figure of merit is probably the best way to evaluate the moderation efficiencies of different configurations in the simulation because it is not solely depending on the performance of the trapping but also distinguishes the effect of different dimensions of the foils correctly. For example increasing the thickness of the foils leads to more positrons stopping in them but will not necessarily mean that more positrons will have the chance to be moderated. It was therefore extensively used to assess the best possible configuration for the available parts and led to the design presented in section 4.4.

Nevertheless, the basis of the idea, the iteratively slowing down, will be briefly discussed here for the simulations of the final setup because that is the parameter which at first sight seems to offer the greatest potential for optimization. Especially because the other parts like the foil thicknesses seem to already be the best option

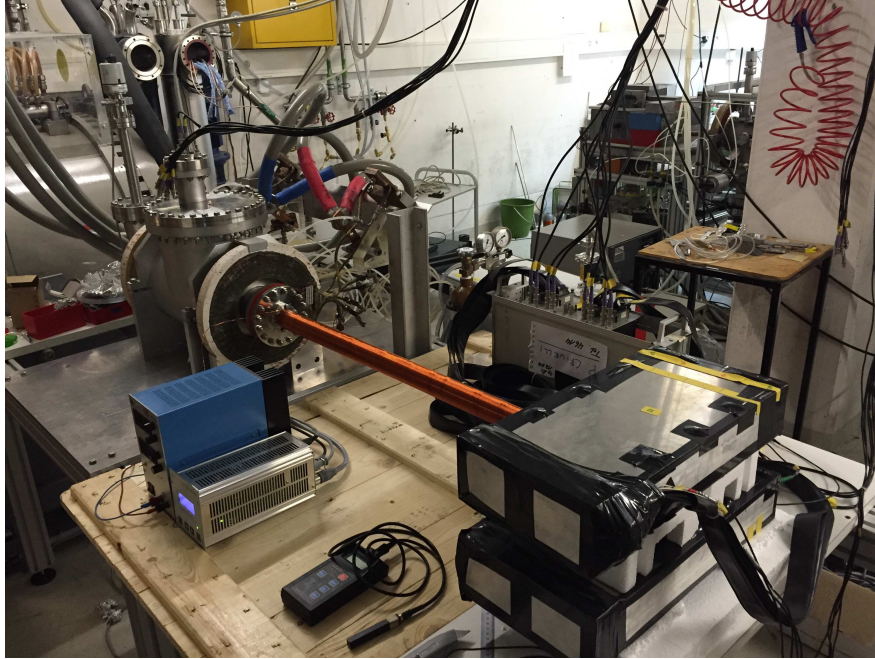


Figure 4.27: Picture of the BGO detection setup placed at the end of the beam line. In the left the cyclotron trap can be seen. The two boxes are each an arrangement of four BGO crystals with attached PMTs. The crystals are positioned to give the largest solid angle possible with the conversion target at their centre.

for what is available of the stock and an increase in the trapping performance will directly lead to a better figure of merit.

The fundamental principle of the cyclotron trap assisted moderator is to pass the positrons through the foils lowering them in energy until they will stop in them. The properties of this, the number of passages, energy lost during a single passage, etc. are shown in the trajectories section 4.3.5. While these describe this process itself and are crucial for understanding it, the raw performance is best seen in the fate in regard to the initial energy with which the positrons were created, Figure 4.18. The total amount of mirrored positrons follows the expectations to be around $2/3$ for a magnetic field radio of about 5. However, that only $1/3$ of the mirrored positrons finally make it to a stop in the foils and $2/3$ escape, even though they were originally trapped, due to forward scattering shows the shortcoming of the constructed proof-of-principle setup.

In this sense, with the limitations of the available parts, e.g. minimal thickness of the foils, the coils, etc., the simulation have shown that moderation efficiencies of 10^{-2} are to be expected for the build setup. Furthermore, some preliminary performed simulations suggest that with stronger coils efficiencies in the order of 10^{-1} are in reach.

In the BGO setup it was impossible to distinguish the counts between the extraction and blocking mode because the expected count rates for the low activity of the nickel source (1.5 kBq of positrons) would have been buried in the large spread of the background and long time measurements were not possible because,

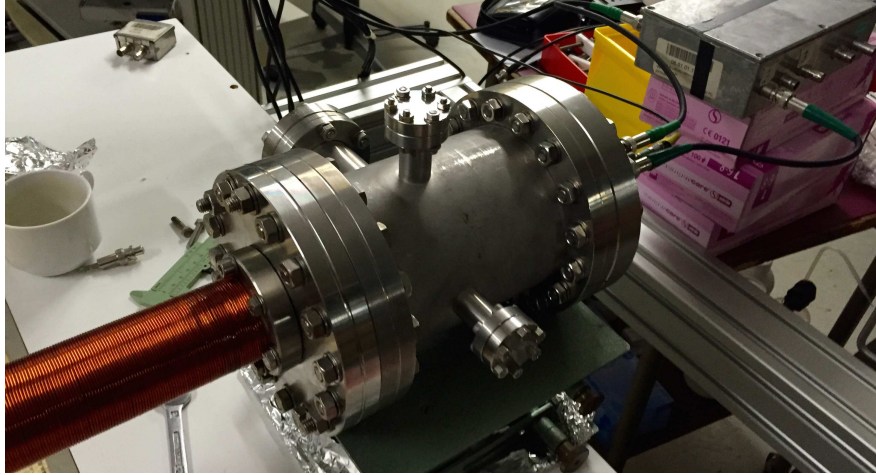


Figure 4.28: Picture of the single particle detection setup placed at the end of the beam line. The solenoid coming from the left guides the positrons directly onto the micro-channel-plate.

on top of it, the signal also had a small drift in time. Furthermore the residual stray magnetic field of the CT of about 5 G in the detector region had a larger impact on the count rate in the BGOs than expected. When the guiding coil is turned off, only 10^{-2} positrons per second should reach the conversion target. Operating the coils at different currents in this case showed that the count rate in the BGOs could drop by half (200 counts/s) for the strongest magnetic fields.

This led to the assumption that the BGOs may have even lost the sensitivity for detecting 511 keV photons when using high magnetic fields. Due to the limited activity of the source available for this experiment an EM to detect the slow positrons was used since it has smaller dark counts (< 1 count/s) compared to MCPs. The drawback is that EMs are very sensitive to magnetic fields and therefore the positrons have to be extracted from the guiding field used for their transport. This was realized by terminating the magnetic field with Mu-metal shielding.

Simulations with SIMION and COMSOL were used to optimise the extraction efficiency to values close to 100%. This was confirmed experimentally by using the ETHZ slow positron beam. As this scheme requires a whole new type of sources more effort to produce thin-film sources was made. The different projects are presented in Section 4.4.2. For the proof of concept study of the cyclotron trap assisted moderation a ^{48}V was produced by proton bombardment with the TANDEM ion accelerator at the Laboratory of Ion Beam Physics, ETH.

At the time of the experiment the positron activity was $3.2(1)$ kBq, measured with a germanium detector and a calibration source. The division of the counts in the extraction mode by the total positron activity gave a moderation efficiency of $\epsilon = 1.8(2)\%$ which is in fair agreement with what has been estimated from the simulation results.

4.6 Conclusions and Outlook

In the course of this thesis two water cooled coils and a high current high voltage (2000 A, 1000 V) power supply were refurbished and aligned to form a cyclotron trap with characteristic magnetic field values of $B_{\max} = 2559(2)$ G and $B_0 = 544(2)$ G. In parallel a Geant4 simulation suite was developed to asses the best possible design of the high efficiency cyclotron trap assisted positron moderation.

To do so, field maps of different cyclotron trap setups were created with COMSOL and Matlab. From the knowledge gained by the simulations the vacuum setup was designed and single parts were ordered and constructed. Before purchasing the moderator and source foils the wire strung mesh mounting scheme was developed and tested. An attempt to produce a thin ^{22}Na source foil did not succeed because the facility used at PSI in the past is not available anymore. However, a collaboration with PSI yielded a Ni foil with incorporated ^{58}Co of 1.5 kBq positron activity. For a second, stronger, source a study for the irradiation of a Ti foil was performed. In cooperation with the Ion Beam Physics laboratory a Ti-V foil with 12.5 kBq / hour was produced for the proof-of-concept test.

Together with Saverio et. al. from the Albert Einstein Center for Fundamental Physics (AEC), Laboratory for High Energy Physics (LHEP), a scheme for higher V activities was tested successful. A special solid target design allows the production of 1 sources with a 1 h irradiation.

During the construction of the framework of the setup an automatized magnetic field analysis probe was build to measure the field of the CT. Simulations of the setup with the realistic magnetic field characteristic suggested moderation efficiencies of 10^{-2} . Some preliminary simulations with optimized parts showed that efficiencies of 10^{-1} should be possible for cyclotron trap assisted positron moderation. For optimizing the efficiency of the moderator foils an annealing station was set up. The tempered tungsten foils where matched with the sources and mounted in the extraction-blocking pattern.

A measurement of with an EM detector ($\epsilon = 1.8(2)\%$) confirmed the simulated moderation efficiency. Because this project was meant to be a proof-of-principle it leaves plenty of room for optimization for which the pioneering of implanted ^{22}Na as a combined moderator-source foil is a perfect starting point. Nevertheless, the realization marks an important step to overcome one of the main limitations of PAS, the lack of availability.

Chapter 5

Positron(ium) Modelling

The existing tools and models to interpret PAS results rely on strong approximations and are only satisfyingly applicable for simple materials and structures. For example, the lifetime and void size analysis via the Tao-Eldrup approach presented in Section 2.2.1 is assuming localizing oPs in closed geometries with a infinite potential well approximation. The model cannot cope with highly symmetric arrangements favouring de-localization, confining elements with open faces or tunnel barriers. The approximation of a potential well of a certain size that is related to a *pore size* can be ambiguous. Especially on the smaller scale, a large relative uncertainty remains.

Another often ignored aspect is the size dependence and hierarchy of the sample. When arguing about the porous properties and how much oPs diffuses out of the probed volume it becomes eminent to consider the underlying geometry. The case of a standard thin film, i.e., a single surface, the Makhovian profile, see Section 2.1, provides the positron stopping distribution. This can be used to estimate which part of the sample is probed and how the diffusion properties of positronium are affected.

When considering samples made out of substructures of sizes comparable to the mean implantation depth of positrons it becomes more complex. The positron may completely penetrate one crystal and stop in another, resulting in a distance to a surface different to the 1D implantation depth. While this effect needs to be accounted for when wanting to understand the PAS response of a sample, it becomes even more important for the comparison of sample sets where a difference in size may mask other effects.

In this chapter a new implantation profile model which takes into account all the dimensions and all possible impact energies as also scattering through smaller sub-units of materials is introduced. This convolution of the Makhovian profile with a rectangular cuboid for a 3D distribution is qualitatively confirmed using the data of two differently sized zeolite crystals. Moreover, with new approaches on modelling the Ps confining potential in porous materials, via a 1D Kronig-Penny approximation and a 3D approach, more general applicable annihilation rate simulation models are presented. Those allow to extend the application of PAS

to more complex systems as it will be shown in Section 5.2.2 for Metal-Organic Framework (MOF)s as a model material.

5.1 Positron Implantation Profiles

To get a better understanding of the dynamics of the PALS response it is uttermost to understand the impact of the initial positronium distribution in the sample. Even though the origin of this, the positron implantation profile, is established in the literature by using the Makhovian profile

$$P_{1D}(z) = \frac{mz^{-1}}{z_0^-} \cos \left[- \left(\frac{z}{z_0} \right)^{-1} \right] \quad (5.1)$$

where P is the probability of stopping at distance z , m is a dimensionless material dependent parameter, and z_0 is a mean implantation depth that depends on the effective mass density (e.g. 1.7 g/cm³ for MFI zeolite) and positron implantation energy [47]. In most PAS studies the implantation is only treated for the case of positrons impinging perpendicular on an infinitely large plane resulting such 1D implantation profile. In realistic measurement conditions, the sample orientation and size does not justify this approximation, the angle of impact is largely randomized and positrons passing through multiple crystals before annihilating or forming positronium is not a negligible effect. Furthermore, the different pore topology along the crystallographic axis, the diffusion of positronium linked to those, and the crystal's dimensions along those will impact the PALS response heavily, i.e., a smaller crystal will naturally lead to more out-diffusion. To highlight the complexity of these effects the sample of the acidity study (Section 6.3) were modelled with 3D implantation profile. The description of this study in the following section is adapted with permission from [65].

Specific crystal sizes are treated as discrete matrices with $n_x \times n_y \times n_z$ elements where $n_i = L_i/\Delta$, L_i is the crystal length in direction i , and Δ is the step size. Assuming the Makhovian profile is equivalent for the spatial coordinates, the three-dimensional case will be

$$P_{3D}(x, y, z) = P_{1D} \left(x^2 + y^2 + z^2 \right) \quad (5.2)$$

To account for positrons penetrating through the sample, the points (x, y, z) which lie outside the crystal, i.e., $x > L_x$ or $y > L_y$ or $z > L_z$, the distribution is folded back onto the surface from which it exited. The generated three-dimensional profile is then convoluted along the crystal boundary to account for every possible incoming angle at every point of the crystal surface.

The resulting profile describes the positron and thus the approximate initial positronium distribution averaged over all crystals. The simulations indicate that for the large coffin-shaped crystals of 20 μ m \times 5 μ m \times 0.5 μ m, the only appreciable differences in implantation occur along the shorter axis. Thus, we reduce the

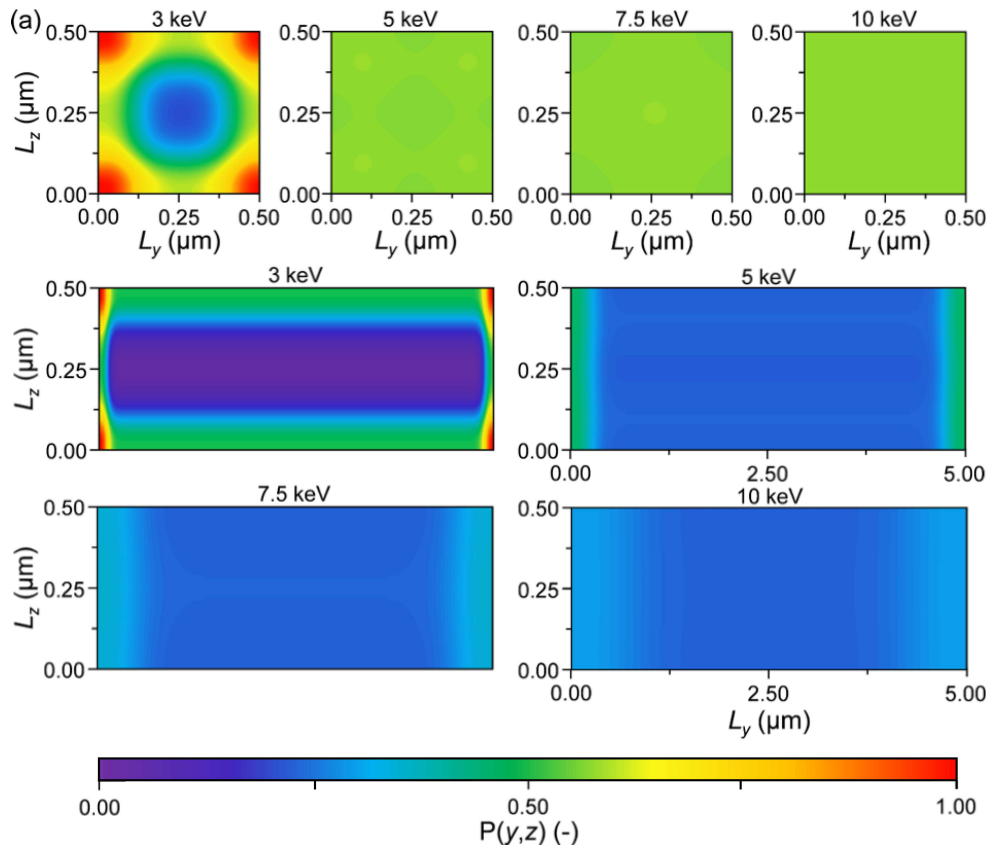


Figure 5.1: Three-dimensional positron implantation profiles estimated for the (a) small and (b) large crystal samples at 3 keV, 5 keV, 7.5 keV and 10 keV. Note the profiles have been averaged along one dimension (L_x) to produce two-dimensional representations. $P(y,z)$ has been normalized in each case to the equivalent 3 keV profile in the series. Adapted with permission from [65]. Copyright 2018 American Chemical Society.

three-dimensional distribution to two dimensions by averaging along the long axis to get $P(y,z)$. This is illustrated in Figure 5.1 which considers the modelled three-dimensional positron implantation profiles for crystals of different sizes at 3 keV, 5 keV, 7.5 keV and 10 keV incident positron energy.

In contrast to typical one-dimensional models where positron implantation occurs perpendicular to an infinitely large plane (see Figure 2.4), in the presented model positrons are implanted across all of the surface at each point and every angle, which is a better representation of the randomly orientated distribution of crystals that will be measured experimentally. At 5 keV, a homogeneous positron distribution is observed for small crystals ($0.5 \mu\text{m} \times 0.5 \mu\text{m}$ in diameter). This results in a reduced intensity of oPs annihilation in the zeolite micropore and an increased intensity of out-diffused oPs (>10 ns) as confirmed in Section 6.3.

Comparatively, with dimensions similar to those of the large crystals studied ($20 \mu\text{m} \times 5 \mu\text{m} \times 0.5 \mu\text{m}$), a higher density of positrons is observed close to the surface at low implantation energies, but the distribution becomes more uniform

upon deeper positron implantation at 10 keV. Using these profiles as a basis for modelling the out-diffusion process of positronium would allow studying the interconnectivity of a porous framework in an additional dimension [7].

Furthermore, the response of different frameworks could be compared when being able to correct for the crystal size. A successful prediction of positronium behaviour during diffusion would further enable the study of more complex systems. Therefore, helping in guiding the design of novel materials with advanced functionalities. For this purpose, a study of a well-controlled sample set with only varying crystal sizes is proposed. From a morphological point of view, the cubic structure of MOFs presented in the next section would qualify as an ideal candidate.

5.2 Quantum Mechanical Confinement of Positronium

How does one define a *surface* of a void made of a layer of atoms, nuclei surrounded by electrons, in a quantum mechanical approach confining a particle? The example of electron orbitals and the corresponding probability density is a good analogy. For 3D illustrations the orbital is often shown as the volume encompassing the electron with an e.g. 95 % probability.

In the classic analysis like shown in Figure 6.2 atoms are hard spheres with the radii as the Van der Waals radius (distance of closest approach of two unbound atoms) or covalent radius (half of a covalent bond length). It is then analysed what is the largest hard-sphere or other geometrical objects which fit into a framework of such atoms for the case of a void or intersection or what is the largest sphere which might be rolled through the structure to asses a channel size.

Undoubtedly positronium with a size in vacuum, i.e., mean distance, a_{Ps} of two times the Bohr radius $a_{Ps} = 2a_0 = 0.106$ nm and a de Broglie wavelength of similar magnitude for meV to eV energies will probe a structure differently. In the search for a more general approach two advanced models are presented here, a 1D approximation based on the separation of variables in a finite potential well and the Bloch theorem, and an extension to a full scope 3D description based on a reduced parameter space. The methods are then evaluated on PAS data of MOFs.

5.2.1 Calibration Material - Metal-Organic Frameworks

MOFs with their variety in size and shapes but highly symmetric porous structure are the ideal basis to study positronium behaviour in highly porous materials. One of the main applications of MOFs, the adsorption of gases like CO₂, H₂, as electrical and optical applications are still under research. For an industrial breakthrough, the main obstacle currently is the stability in ambient air [144].

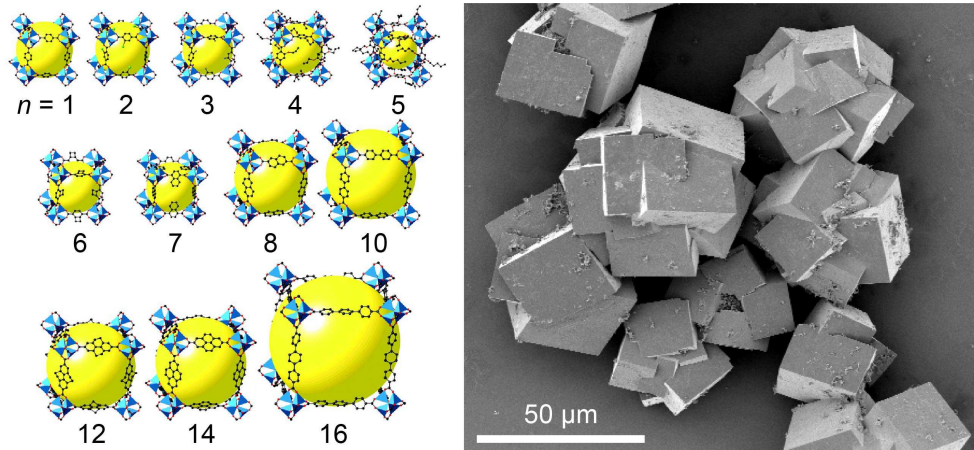


Figure 5.2: Unit cell structures of IRMOF- n structures and a micrograph of MOF crystals [146]. Each IRMOF cluster is formed by a node, a $[\text{Zn}_4\text{O}]_6^+$ metal complex, and a linker consisting of C and H (not shown) atoms. The large yellow spheres represent the largest spheres that would fit in the cavities without touching the frameworks. (left) Reprinted with permission from [147]. Copyright 2002, the American Association for the Advancement of Science.

The MOF structure is composed of a coordination network of organic ligands (linkers) evolving from metal ions or clusters (nodes).

While there are existing more than 1×10^5 different structures already there is virtually no upper limit. From the chemical perspective of known potential organic linkers of more than 1 million the combination possibilities for functionalisation sparked the strong interest in these materials for a multitude of applications [145]. This large number enables a vast number of unit cell structures. The most common ones are still of high symmetry, i.e., rectangular cuboids, or even cubes.

Different to most other porous materials, MOF unit cells have open faces without any material blocking, see Figure 5.2 for unit cells of the group of IsoReticular Metal-Organic Framework (IRMOF)s. The confinement of Ps in such cages is different from those in closed pores as modelled by the Tao-Eldrup model described in Section 2.2.1. Moreover, the high symmetry over large scales ($\sim \mu\text{m}$) leads to de-localisation effects which exhibits itself with Ps being in Bloch states [54]. To model this, new approaches are necessary as shown by Crivelli et al. [53] where a Kronig-Penney model was used to successfully predict the confinement energy in four different frameworks. The solution relies on the separation of variables which was justified by the authors based of the cubic geometry of the confining geometry. This applicability of this approximation was confirmed with the full three dimensional solution of a cubic square linker model shown in Figure 5.4 presented in the next section. The wavefunctions of the two approaches have a root-mean-square deviation of less than 1%.

Table 5.1: Overview of properties of the set of studied MOF frameworks. The cluster to cluster side length L , aperture size a and confinement energy E used in [53]. Measured lifetime for the ground state τ_{meas} , electron density scaling factor Z_{eff} and framework electron number density n .

Name	L (nm)	a (nm)	E (meV)	τ_{meas} (ns)	τ_{sim}	n (e^-/nm^3)
MOF-FMA	1.082	0.91	162	8.9	6	238
IRMOF-1	1.290	1.08	125	13.4	9	176
IRMOF-8	1.505	1.15	138	18.9	17	134
IRMOF-20	1.469	1.17	120	20.0	26	192

5.2.2 Modelling of Open Pore Geometries

The research which led to the confirmation of Ps occupying Bloch states in highly symmetric MOF crystals [53] did so by analysing the confinement energy. As a continuation of the associated modelling, the goal was set to find a proper descriptor of the Ps lifetimes as well.

Starting from a simplistic model multiple iteratively more complex models were developed and tested. The models were tested against a set of data presented in Table 5.1. The presented measurement values were performed with a bulk PALS setup at the University of Michigan and represent a clearer set of data compared to the one taken with the ETHZ slow positron beam presented in [53]. Data collected with the positron beam showed an inconsistent lifetime value which could origin from poor sample coverage, effectively hitting the holder, and backscattered positrons which are known to distort the spectra in the low lifetime region. The studied frameworks are MOF-FMA, and IRMOF-1 (a.k.a. MOF-5), IRMOF-8 and IRMOF-20. All structures consist of the same $[\text{Zn}_4\text{O}]_6^+$ metal complex as the nodes but with differently long hydrocarbyls as linkers, i.e., functional groups only consisting of hydrogen and carbon.

The simple model tested by I. Petrides assumes a separation of variables in the orthogonal crystal axis. In a single particle approximation the Kronig Penney Model, describing the repeating 3D finite dimension wells shown in Figure 5.3, is solved. The finite potential V_0 between the MOF cages confining a Ps atom are calculated by assuming an optical potential of the square aperture a^2 with on-axis width b

$$V_0 = \frac{\hbar^2 \pi^2}{ma^2}. \quad (5.3)$$

A Ps tunnelling from one cage to another would need to, figuratively speaking, *squeeze* through the aperture to overcome the confining potential step defined by the 2D infinite potential well. To estimate a lifetime from the wave function a

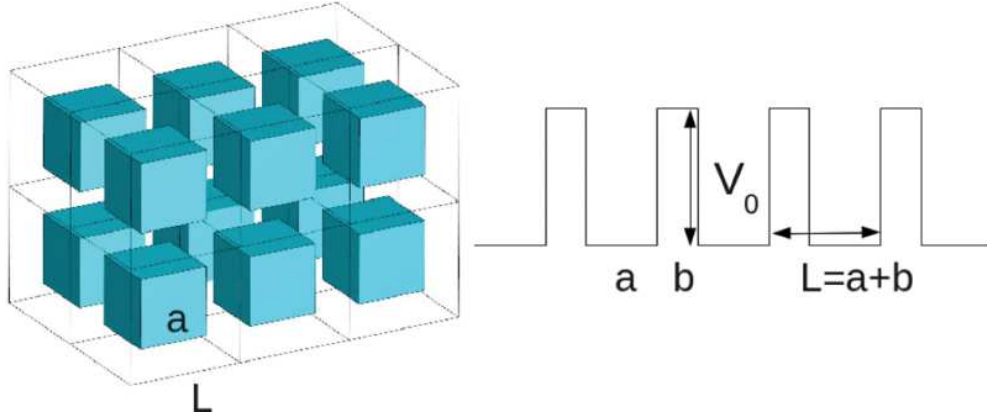


Figure 5.3: Cubic muffin tin geometry of the MOFs and Kronig-Penney potential. Reprinted with permission from [53]. Copyright 2014 by the American Physical Society (right).

weighted overlap with the barrier is calculated

$$\Gamma = \tau^{-1} = 4\pi cr_0^2 n Z_{\text{eff}} \int_L^{L-a} |\Psi(x)^2| dx \quad (5.4)$$

$$\tau_{\text{sim}} = \left(4\pi cr_0^2 n Z_{\text{eff}} \int_L^{L-a} |\Psi(x)^2| dx \right)^{-1}. \quad (5.5)$$

The annihilation rate is scaled by the respective MOF framework electron density n , the integrated probability distribution $|\Psi(x)^2|$ of the Ps atom, the cross section for direct annihilation with a free electron $4\pi cr_0^2$, with r_0 being the classical electron radius, and a scaling factor Z_{eff} to take electron screening effects into account. This simplistic model matches the observed confinement energies very well with a common set of parameters.

The calculated lifetimes τ_{sim} , see Equation 5.5, are presented in Table 5.1. The model is an improvement to the commonly applied RTE-model (Eq. 2.16) presented in Section 2.2.1. The mean absolute percentage error

$$M = n^{-1} \sum_{i=1}^n \left| 1 - \frac{\tau_{\text{sim},i}}{\tau_{\text{meas},i}} \right| \quad (5.6)$$

of the 1D Kronig Penney model is 0.2. In comparison with the RTE-model ($M = 0.6$) it is an improvement by a factor 3.

To further improve the lifetime estimations efforts were made towards a more generally applicable and more realistic description with a 3D model. A way is to solve the 3D muffin tin geometry shown in Figure 5.4 and calculate the lifetime by adding an electron layer around the square rods. Because this would not differentiate enough on the linker types the model was advanced further. In a second step, each atom was modelled as a hard-sphere of a fixed radii creating a volume of an infinite potential to get a more precise description of the linkers. The positions can be obtained from electron scattering which are available as structure files (Crystallographic Information File - CIF [148]) listing the atom

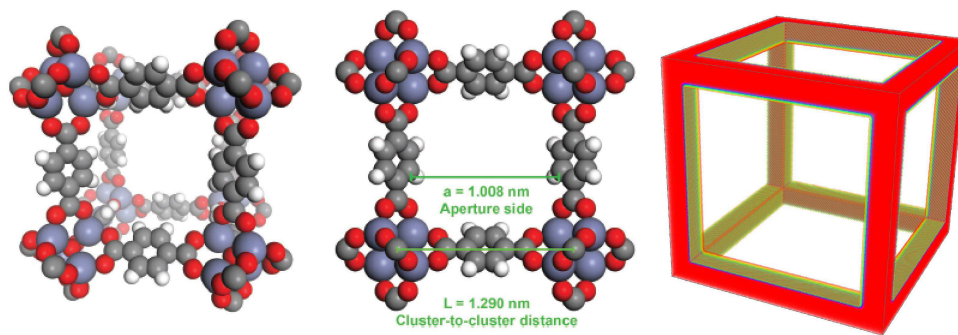


Figure 5.4: Detailed structure of IRMOF-1 [53] and 3D square linker model. Reprinted with permission. Copyright 2014 by the American Physical Society.

positions and their bonds published for several IRMOF frameworks by Eddaoudi et al. [147].

Similarly, it was investigated for a group of zeolite frameworks in [149]. The main issue of this approach is the number of free parameters, the radii of all the atomic species present in a structure. While the zeolite study [149] aimed to compare frameworks with partly exclusive atoms not present in the other materials, all studied MOFs are composed of the same elements. This should have made it more reliable to find a common set of radii for all samples rather than having a free parameter per framework to tweak. Furthermore, instead of a Density Functional Theory (DFT) approach a brute force solving of the Schrödinger Equation with a discretized potential by diagonalizing the Hamiltonian was chosen. It was planned that the lifetime could then be calculated in a Tao-Eldrup approach. In this case, first, the wave function is found by solving for the energy and then a common parameter to match the lifetime is searched. The radii used for creating the potential would be increased by a little δ to mimic the electron layer. Weighting this layer with the Ps wave function overlap and a cross-section a lifetime could have been calculated. However, during the study of the necessary discretisation n of the unit cell into voxels of side lengths $\Delta = L/(n - 1)$ for the energy solution to converge, the *resolution* of the Ps atom was considered more deeply. The de Broglie wavelength of ~ 1 eV Ps is around 1 nm. Therefore, it is to expect that the Ps will never resolve the atomic details of the framework.

To create a smoother potential the CIF file visualization program VESTA [150] was used to calculate actual electron densities by a Fourier transform of electron scattering structure factors [151]. Using the electron density rather than atoms or other simplistic bodies as input for the potential is considered to be far superior.

Positronium sitting in a void interact almost only with the electrons since they shield the positively charged nuclei. The electron density is a very smooth scalar field as can be seen in the isosurface representation shown in Figure 5.5. Ideally, the potential would be calculated using this density and a first principle approach. However, for a precise description, a difficulty arises from including positronium as a two-particle bound state interacting with this electron density. Figure 5.6

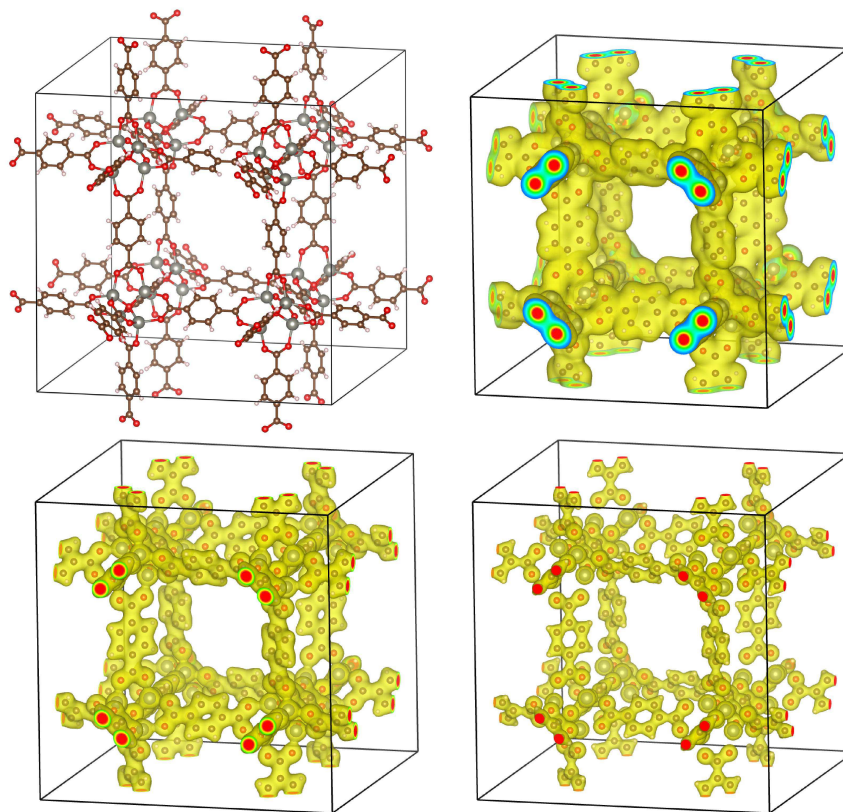


Figure 5.5: Unit cell ball and stick model and isosurface visualization of electron number densities (600, 800, 1000 e^-/nm^3) of IRMOF-1 from left to right, top to bottom.

shows an illustrative comparison of different Ps potentials for a 1D case. The electron density is a projection onto one dimension from a central slice through the IRMOF-1.

A physically correct description would be based on the polarizability of the Ps atom. This will result in a dynamic dipole, dynamic because its strength will be depending on its position and the electron density. The interaction of the Ps atom with the electrons will, therefore, have a repulsive and attractive part. A short-ranged but strong Pauli repulsion of the positronium's electron and the comparatively weaker but longer-ranged electrostatic attraction of the positron. Unlike most potential well models this results with minima close to the sides rather than in the centre.

This full description has never been calculated because the precise mathematical dependence of the repulsion is not known. The standard approximation, like in the Tao Eldrup or Kronig Penney models, is to use a square potential calibrated by comparison to measured values like shown with the dashed blue line in Figure 5.6. When comparing both models a deviation in the wave function close to the electron density is expected. Therefore, depending on which quantity, i.e., energy or lifetime, is used to adjust the model parameters the respective other might be mismatched.

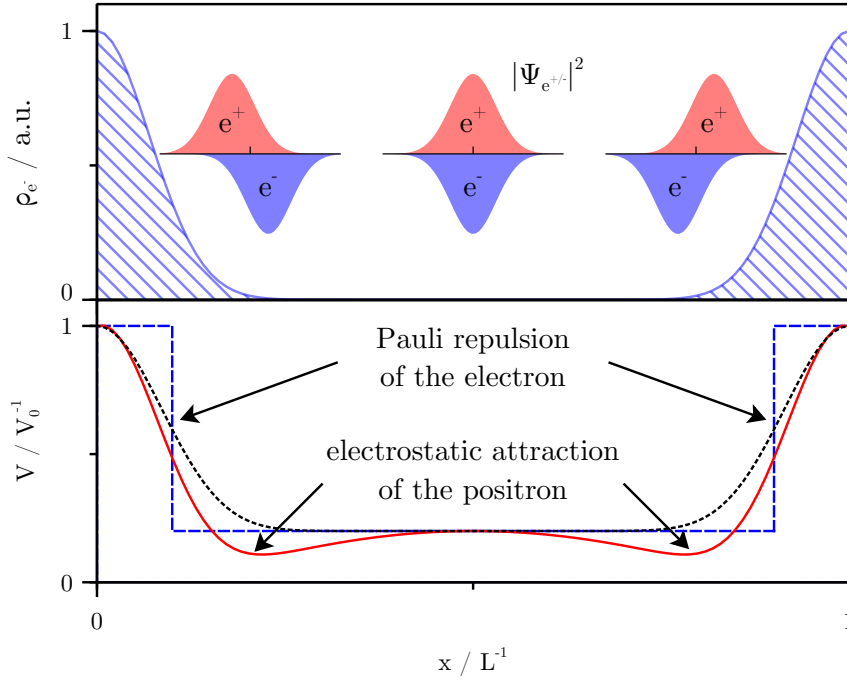


Figure 5.6: *Top*, pore defining electron density ρ_{e-} (hatched light blue) and induced Ps polarization, i.e., charge distribution inside Ps. *Bottom*, related illustrative 1D Ps potentials V (finite potential well, dashed blue; smooth potential, dotted black; true potential, solid red).

Nevertheless, in pursue of a model with parameters common for a multitude of structures an infinite squared potential based on electron density levels, i.e., isosurfaces like in Figure 5.5, was investigated. The first step is to solve the time-independent Schrödinger equation

$$H\Psi = (T + V)\Psi = E_{\text{sim}}\Psi \quad (5.7)$$

with the kinetic energy operator T and the potential V . This was done with an adapted version of the algorithm designed by I. Petrides. The employed potential is a square potential defined by a critical electron density isosurface level,

$$V(\vec{x}) = \begin{cases} \infty, & \rho_e(\vec{x}) \geq \rho_{e,\text{iso}} \\ 0, & \rho_e(\vec{x}) < \rho_{e,\text{iso}} \end{cases} \quad (5.8)$$

By tuning the isosurface for each framework to match the measured energy E_{exp} from Table 5.1 the respective wavefunction can be found. In the second step this calibrated probability density $|\Psi|^2$ can be used together with the electron density ρ_e to calculate a decay rate

$$\begin{aligned} \Gamma &= \lambda \int \rho_e |\Psi|^2 dV \\ &= \lambda \sum_{i,j,k=0}^n \rho_e^{i,j,k} |\Psi_{i,j,k}|^2. \end{aligned} \quad (5.9)$$

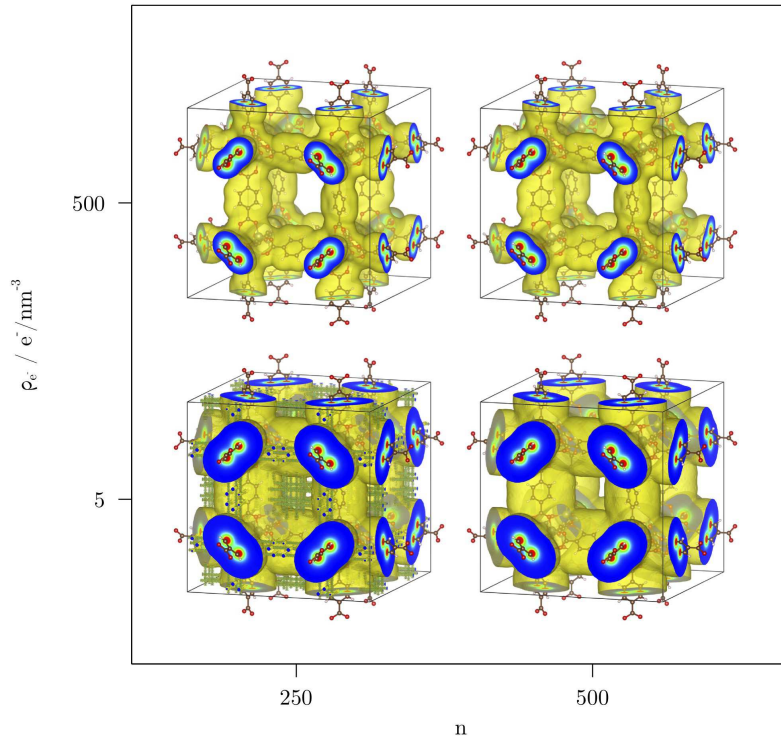


Figure 5.7: Electron densities isosurfaces for IRMOF-1 from VESTA export showing resolution depended discretisation artefacts visible only in the low electron density region.

A scaling factor λ multiplied with the Ps and framework electrons overlap, the integrated electron density times the Ps probability density, i.e., the sum for the discretized case. With the VESTA suite the electron density of the unit cell ($2.583 \text{ nm} \times 2.583 \text{ nm} \times 2.583 \text{ nm}$) was calculated for a Cartesian grid with a resolution of $\Delta = 5 \text{ pm}$ resulting in a discretisation of $m = 517$. Such a fine tessellation is necessary to reduce artefacts in low-density regions happening on export as can be seen in Figure 5.7.

With a 3D potential matrix V of size $n \times n \times n = n^3$ the Hamiltonian matrix H will be $(n^3)^2 = n^6$ large. In the implementation of the Schrödinger equation, the discretisation was limited to $n \leq 56$ because of computational storage limitations. In the binary format using 16 byte sized long doubles necessary for the solving algorithm the H matrix has the size of 493 GByte for $n = 56$. The model was simulated with discretisations of $n = 40..1..56$ and isosurface values of $\rho_{e,\text{iso}} = 100..100..1000$ to see if the results would converge and are not subject to finite element size errors. Contour plots of the simulation output E_{sim} in terms of relative deviation to the experimental value E_{exp} from Table 5.1 are presented in Figure 5.8.

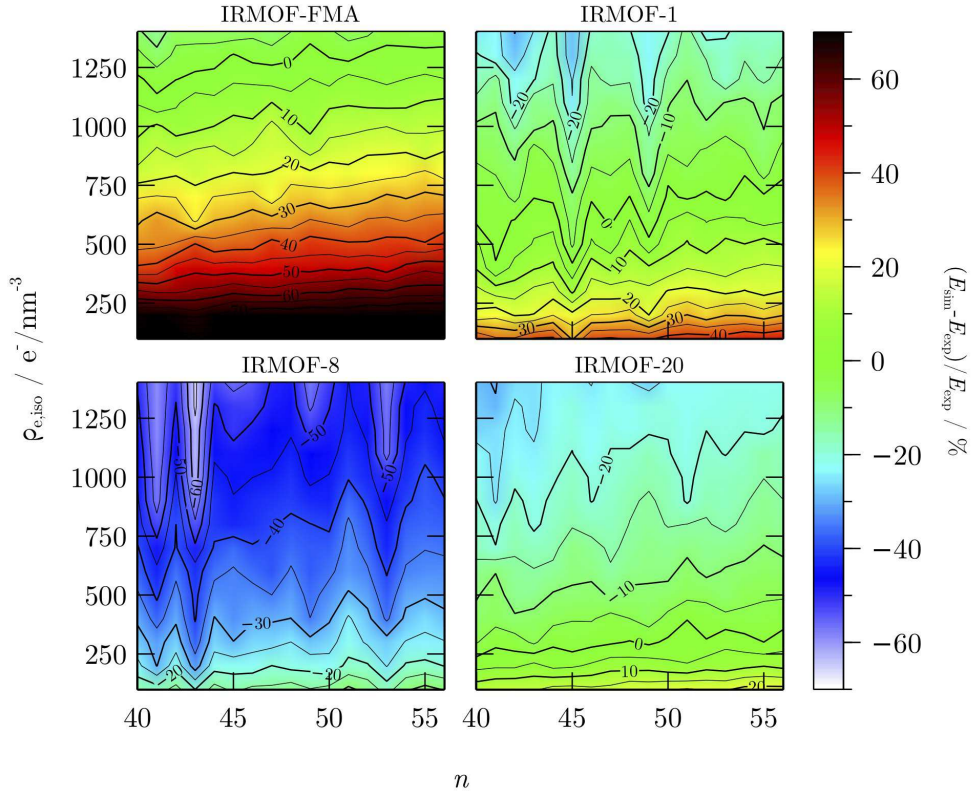


Figure 5.8: Results of the isosurface square potential model depending on discretization n and electron density isosurface value $\rho_{e,iso}$ for different IRMOF frameworks.

It is evident at first glance that there is no common isosurface level providing the correct solutions, the confinement energies E_{sim} , for all frameworks. The best $\rho_{e,iso}$ values for the IRMOF frameworks FMA, 1, 8 and 20 at $n = 58$ are 1350, 600, 50 and 350 e^-/nm^3 respectively. Even though the expectations of a common parameter was not met the following stands out:

- The discretisation has not fully converged, an overall slight upwards trend is observable.
- IRMOF-1 and 8 show distinct discretisation effects as sharp trenches.
- Remarkably, there seems to be a dependence on the unit cell size L , see Table 5.1.

Prospects to overcome this limitations is to move to an all-electron full-potential Linearised Augmented-Plane Wave solver (LAPW) which allows higher discretisations and to calculate the oPs confining potential from first principle with repulsive and attractive forces between oPs as a two-particle system and the electron density. A successful prediction of positronium behaviour in such pores would enable the study of highly complex systems. Therefore, helping in guiding the design of novel materials with advanced functionalities.

Chapter 6

Studies on Zeolites

In collaboration with the group of ACE from the Institute for Chemistry and Bioengineering, D-CHAB, ETH, the characterization of hierarchical zeolites, as advanced functional materials, was pioneered [51]. In fact, it was demonstrated in an early proof-of-concept study that there is a direct correlation between the pore connectivity and the catalytic performance of a novel class of zeolites with hierarchical pore structures and PAS parameters as shown in figure ?? [16]. Up to now, PAS is the only method that conveys such a relationship [17].

These findings triggered multiple studies on the behaviour of positronium in microporous crystalline networks [62], impact of acidity [65], positronium modelling [149], studies on other materials as layered hydroxides [64] and ongoing research on the formation of mesoporosity.

This chapter gives an introduction to the material zeolite and presents two studies of the class of ZSM-5, also known as MFI. The description of the material is presented to complement the positron(ium) related analysis used to explain the observed of data two applied studies.

- The study on the way on how the zeolite pore structure is formed [62] which important to understand how to functionalise the material.
- An investigation on the effect of acidity on the PAS response [65] motivated by the acidity related observations in [17] to be able to better entangle the PAS response regarding all material properties.

6.1 The material class of zeolites

Zeolites are intrinsically micro- and/or modified mesoporous¹ aluminosilicate minerals of different unique frameworks. The term zeolite was created by the mineralogist A. F. Cronstedt. In an early study, he found that upon heating the material stilbite emits large amounts of water vapour that had been previously adsorbed

¹IUPAC definition: pore diameter < 2 nm for micropore, between 2 and 50 nm for mesopore [39]

from the atmosphere by the material [152]. Inspired by this observation he gave it name from the Greek ζέω (*zéō*), meaning 'to boil' and λίθος (*lithos*), meaning 'stone'. Because of the different porosity and high controllability zeolites are used as catalysts and sorbents in various industrial applications from petrochemical molecule cracking up to radioactive waste trapping.

The unit cell as presented in Figure 6.1 is hosting microporous channels or cages in the Å up to nm range, is composed of hundreds of atoms and has a side length of a couple of nm [153]. They are mostly synthesized as crystals with sizes from a tenth of nm up to several μm. Multiple crystals often form agglomerates from interconnected growth but with different seed orientations. The number per agglomerate strongly depends on the crystal sizes. Several agglomerates together form the next biggest instance, a particle. The powder in which zeolites are usually present are simply numerous of such particles. An overview of the scales is shown in pictures and scanning electron and transmission electron micrographs in Figure 6.2.

With the many applications zeolites have already in industry, there is a clear focus on the improvement of the material by additional functionalising or tailoring to the specific needs as also research into new areas. The insights gained by PAS are of great potential as an additional descriptor of the porous network and its modifications for this goal. The here most studied zeolite type is the ZSM-5, also known as MFI, framework, an industrial relevant catalyst for chemical reactions, e.g. oil refinery.

The highly porous material made out of H, Si, O, and Al hosts an intrinsic microporous network. The unit cell of side lengths $a = 2.009 \text{ \AA}$, $b = 1.974 \text{ \AA}$ and $c = 1.31 \text{ \AA}$ is penetrated by two kinds of cylindrical channels with cages at their intersections, straight channels in one direction, zig-zag channels in another, see Figure 6.1. Both have a diameter of 0.55 nm. The largest cages of the framework have a diameter of 0.7 nm.

6.2 Zeolite Detemplation

The following section presents the study on detemplation of MFI-type zeolites, see Section 6.1, and is adapted with permission from [62]. Copyright 2016 American Chemical Society. Template agent are used as structure-directing material during the synthesis. The reactants, i.e., constituents or atoms, of the final product assemble in a predefined structure around the template. With subsequent treatment, detemplation, the agent can be removed to yield the final product. The goal of the study was to gain insight into the removal process of the industrial relevant templating agent tetrapropylammonium (TPA+).

Templating strategies continue to play an important role in zeolite synthesis, where the application of structure-directing agents (SDA) such as amines and alkyl ammonium cations has enabled the crystallization of a large proportion of the over 200 different framework types and related structures discovered to

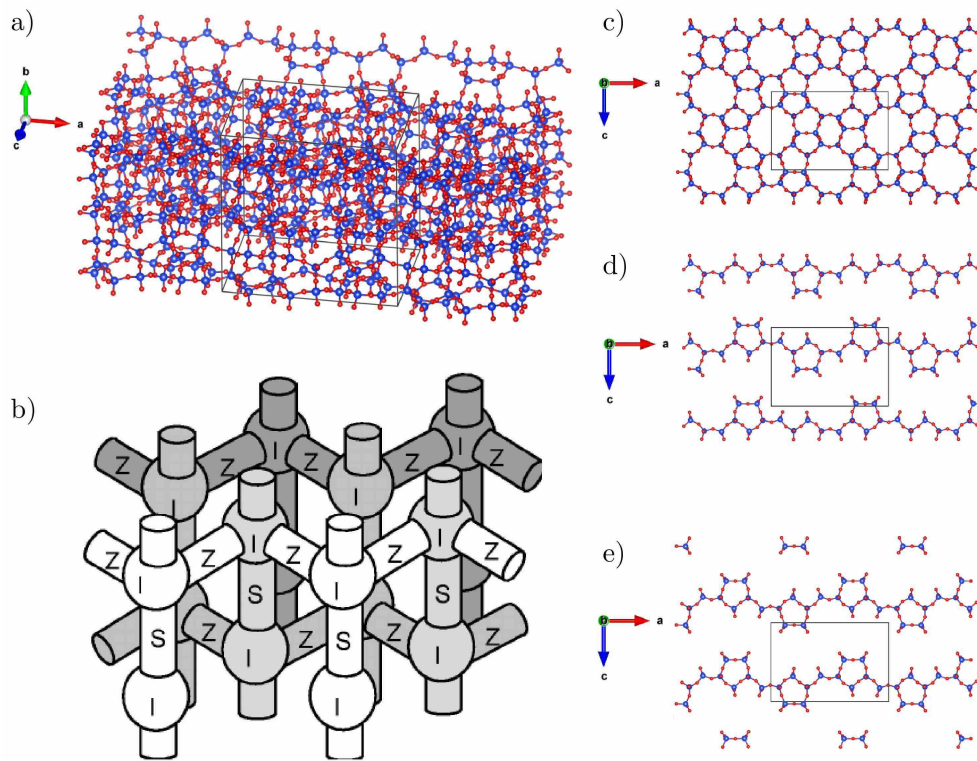


Figure 6.1: Atomic net and illustration of the pore network. a) A ball-and-stick model of the structure showing the same volume as b), a sketch of the pore network (S/Z are straight/zig-zag channels, I is intersection). c), d) and e) show a top view of the framework (perpendicular to the b-axis). c) shows the straight channels. d) and e) are a cut-through to visualize the upper and lower plane of zig-zag channels. The solid black lined box shows the unit cell. a), c), d) and e) are visualization of the MFI structure file from the International Zeolite Association's Database of Zeolite Structures [154]. b) is reprinted with permission from [155]. Copyright 2003, AIP Publishing.

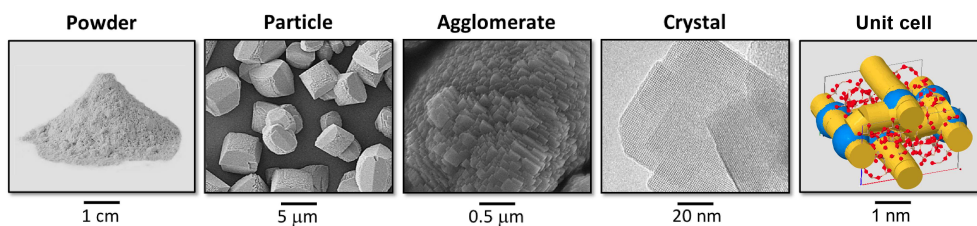


Figure 6.2: Overview over the different hierarchies found in typical zeolites. Reproduced with permission. Copyright 2019, John Wiley and Sons.

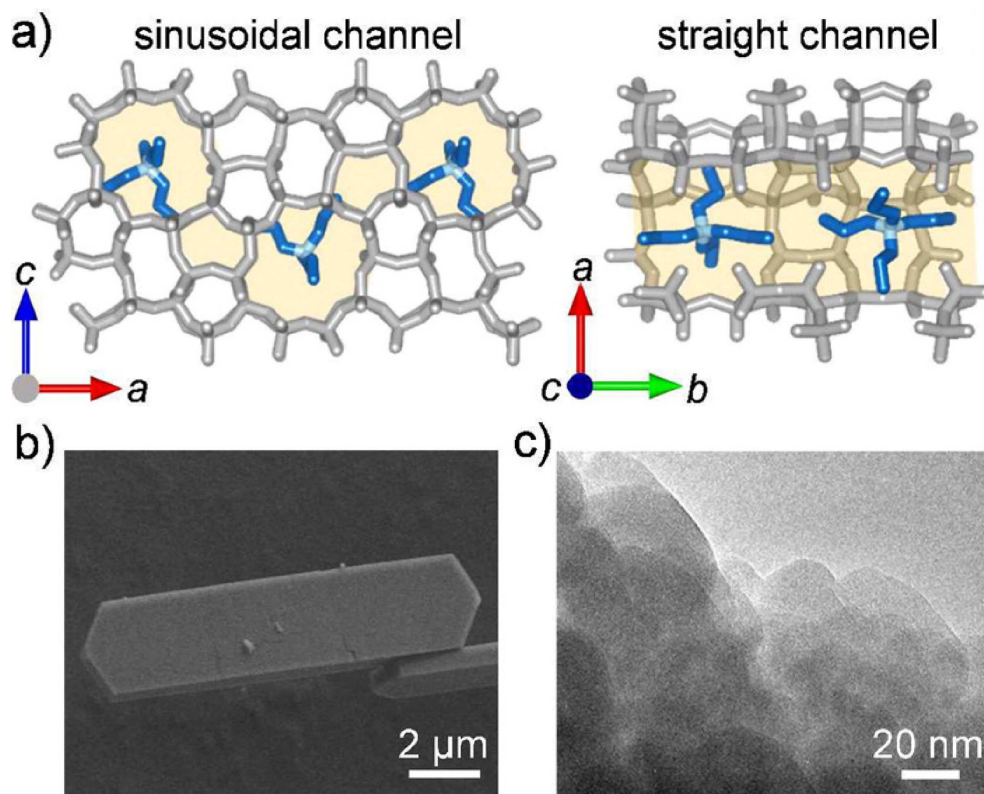


Figure 6.3: a) Location and optimized geometry of template agent TPA+ within the sinusoidal and straight channels (shaded yellow) of the MFI framework. b) Scanning electron micrograph of ZM-1.00 and c) transmission electron micrograph of ZN-1.00. Reprinted with permission from [62]. Copyright 2016 American Chemical Society.

date [154, 156–159]. In commercial applications, MFI is commonly synthesized using tetrapropylammonium cations (TPA+) as SDA, with the ammonium ion occupying the intersection volume and the propyl arms oriented along the straight and sinusoidal channels (Figure 6.3) [160]. As is the case for most templating strategies, TPA+ needs to be removed to vacate the micropore network for other functions, which is typically achieved by calcining the zeolite at high temperatures. However, such procedures can profoundly impact the structural integrity of the microporous framework [161]. Milder alternatives such as the removal by chemical means [162, 163] and ozonation [164] have been explored in attempts to address this issue. The location and distribution of TPA+ in MFI has also been correlated to the presence of silanol defects [165–167].

Therefore a thorough understanding of the detemplation process is important to gauge the possible effects on the resulting pore network. The detemplation in MFI-type zeolites has been studied by NMR [165, 166, 168], XRD [169], thermoanalytical methods [170, 171] and fluorescence microspectroscopy [172, 173]. However, the development of the micropore network upon SDA removal has not been spatially resolved.

This study characterises the porosity evolution upon SDA removal in MFI-type

zeolites by PALS coupling measurements with simulation and modelling on the behaviour of oPs within the micropores.

Methods

A series of partially detemplated samples were prepared by R. Warringham (ACE, D-CHAB, ETHZ) from a well-characterized micron-sized ZSM-5. Two MFI-type ZSM-5 zeolites with micron- (coded ZM) or nanosized (coded ZN) crystals were prepared via hydrothermal synthesis using tetrapropylammonium bromide as a structure-directing agent (SDA). Partial detemplation was achieved by isothermal calcination at 693 K for varying durations (0.25–16 h) with complete template removal reached after 16 h for both samples. The fraction of detemplation was hereby calibrated by thermogravimetric analysis, the assessment of the weight loss during the process. The samples are coded ZM- x or ZN- x , where x refers to the fraction of detemplation (0.00 to 1.00). A more detailed description of the production procedure and chemical quality control can be found in [62].

PALS measurements were performed using the ETHZ continuous slow positron beam. Powdered samples (ca. 0.1 mg) were degassed in situ under vacuum ($<2 \times 10^{-7}$ mbar) at 365 K for 2 h. Monoenergetic positrons were accelerated into the sample at 7.5 keV, resulting in a mean implantation depth of 300 nm. Comparatively, the sample covers a much larger area (ca. 3 cm²) than the beam spot size, which has been measured to be approx. 0.8 cm².

The PALS spectra were best fitted by five or six exponential lifetime components corresponding to the annihilation of para-positronium (pPs, <1 ns), direct annihilation of positron with free electrons (e^+ , $\tau_{e^+} <1$ ns), ortho positronium (oPs, τ_{mic} (1–15 ns), τ_{mes} (15–100 ns), and τ_{vac} (>100 ns). The time resolution of the ETHZ slow positron beam is optimized for the measurement of oPs above 1 ns and is insufficient to measure accurately the lifetime of pPs and e^+ (<1 ns). However, the accurate determination of the pPs and e^+ are not required for the assessment of the longer oPs components.

The oPs lifetime ranges ($P_{\text{S}_{\text{mic}}}$ and $P_{\text{S}_{\text{mes}}}$) were estimated with the Rectangular extension of the Tao-Eldrup (RTE) model [5] presented in Section 2.2.1 using a spherical geometry, cubic and square channel geometries according to the IUPAC defined ranges for a micropore (<2 nm in diameter) and mesopores (2–50 nm in diameter) [39]. Their relative fractions were extracted using a fitting method based on Markov chain Monte-Carlo Bayesian inference calculations in the PAScual data suite [174] after subtraction of the background due to uncorrelated start-stop signals. Intensities attributed to oPs components I_{xyz}^{\oplus} are normalized by the total amount of oPs measured (I_{oPs}), where I_{oPs} represents all components with lifetimes greater than 1 ns. In addition, the total amount oPs annihilating outside of the micropore network, i.e., out-diffused (I_{out}) is defined as the sum of I_{mes} and I_{vac} .

Results

Figure 6.3 shows the expected location of the SDA tetrapropylammonium (TPA+) cation within the micropore framework of ZSM-5 based on X-ray crystallographic data [160]. The molecule occupies the intersection between the straight and sinusoidal channels dangling along each of the channel sections. Several studies have examined the variation of $P_{S_{mic}}$ with the inclusion of water and counterions within zeolite frameworks [10, 175, 176] but studies exploring the systematic blocking of the micropore structure have not been reported.

To study the detemplation mechanism, a zeolite was prepared with micron-sized coffin-shaped crystals (ZM- x , Si:Al = 87, average crystal length ca. 20 μm), where x indicates the fraction of SDA removed. The crystal size and well-defined morphology is visible upon examination by scanning electron microscopy (Figure 6.3b). X-ray diffraction of the fully templated (ZM-0.00) and detemplated (ZM-1.00) ZM- x samples confirms the single-phase crystalline MFI structure. Analysis by N_2 sorption confirmed the virtual absence of porosity in the ZM-0.00 sample consistent with the occupation of the pore network with the TPA+ cations. Comparatively, ZM-1.00 exhibits the expected characteristic of a microporous material with minimal hysteresis. More details on the chemical analysis and confirmation on the successful control of the detemplation can be found in [62] and its SI.

The ZM- x samples were studied by PALS to gain further insight into the evolution of the pore network upon detemplation. The lifetime spectra acquired are a summation of all the lifetimes (pPs, direct e^+ and oPs annihilation) detected during the measurement. A comparison of selected spectra is presented in Figure 6.4. An increase in the intensity of longer lifetime components (>30 ns) can be seen as a function of SDA removal. Interestingly, however, the lifetimes of the short-lived components (<30 ns) initially increase (ZM-0.00 to ZM 0.40) before levelling and subsequently dropping at higher levels of SDA removal (ZM-0.65 to ZM-1.00).

This observation would suggest during the detemplation procedure there is a marked intensity shift in oPs distribution from shorter lifetimes to longer lifetimes. The derived intensity and lifetime values are presented in Table 6.1. Intensities of oPs are normalized by the total amount of oPs measured (I_{tot}) to facilitate comparison of the data. Analysis of the fully templated ZM 0.00 sample identifies a considerable amount of oPs formation ($I_{tot} = \text{ca. } 36\%$) with a majority of the oPs annihilating between 1 to 10 ns (96.6% after normalization), indicative of annihilation in micropores.

From gas sorption analysis, negligible micropore volume was observed within the ZM-0.00 sample as the presence of the TPA+ blocked access to the micropores as shown in Figure 6.5. However, this blocking behaviour appears to have little effect on oPs localization within the micropore domain (Figure 6.5b) with the majority components being $I_{mic,1}$ and $I_{mic,2}$.

Upon SDA-removal, $I_{mic,1}$ drops sharply whilst $I_{mic,2}$ is sustained up to a fraction of 0.75 SDA removal. During this final stage the intensity of $I_{mic,2}$ sharp decline with a correlated increase in longer-lived I_{vac} . This behaviour contrasts with the linear dependency observed with V_{mic} (Figure 6.5a) and suggests the presence of

Table 6.1: The contributions derived from PALS measurements of the ZM sample. Lifetimes and intensities associated with pPs, e^+ and oPs decaying in micropores(mic 1,2), mesopores (mes), and vacuum (vac), total oPs fraction $I_{\text{oPs}} = I_{\text{mic},1} + I_{\text{mic},2} + I_{\text{mes}} + I_{\text{vac}}$ and normalized oPs components I_{oPs} , i.e., $I_{\text{mic},1}^{\ominus} = I_{\text{mic},1}/I_{\text{oPs}}$. Reprinted with permission from [62]. Copyright 2016 American Chemical Society.

Sample	I_{oPs} (%)	$I_{\text{mic},1}^{\ominus}$ (%)	$I_{\text{mic},2}^{\ominus}$ (%)	I_{mes}^{\ominus} (%)	I_{vac}^{\ominus} (%)
I_{pPs} (%)	I_{e^+} (%)	$I_{\text{mic},1}$ (%)	$I_{\text{mic},2}$ (%)	I_{mes} (%)	I_{vac} (%)
τ_{pPs} (ns)	τ_{e^+} (ns)	$\tau_{\text{mic},1}$ (ns)	$\tau_{\text{mic},2}$ (ns)	τ_{mes} (ns)	τ_{vac} (ns)
ZM-0.00	35.8(39)	92.4(90)	4.2(11)	1.1(2)	2.2(0)
	12.1(20)	51.9(2)	33.1(38)	1.5(4)	0.4(1)
	0.127(3)	0.798(36)	1.43(3)	3.31(28)	16.4(50)
ZM-0.23	38.8(12)	47.4(26)	51.0(16)	-	1.6(8)
-	61.1(8)	18.4(10)	19.8(6)	-	0.6(3)
-	0.712(5)	1.53(4)	3.11(3)	-	107(3)
ZM-0.40	31.6(25)	-	92.7(56)	-	7.3(0)
	15.1(2)	53.2(2)	-	29.2(18)	-
	0.125(0)	0.799(0)	-	2.91(2)	-
ZM-0.47	33.5(12)	-	87.8(15)	-	12.2(0)
-	66.2(6)	-	29.4(5)	-	4.1(0)
-	0.812(7)	-	2.87(8)	-	121(1)
ZM-0.65	34.4(4)	-	88.4(11)	-	11.6(0)
	12.9(4)	52.6(2)	-	30.4(4)	-
	0.125(0)	0.858(8)	-	2.84(2)	-
ZM-0.74	30.3(1)	-	87.4(3)	-	12.6(3)
	9.4(3)	60.3(3)	-	26.5(1)	-
	0.125(0)	0.896(2)	-	2.88(9)	-
ZM-1.00	32.6(7)	36.2(22)	6.2(3)	14.4(3)	43.2(3)
-	67.4(7)	11.8(7)	2.0(1)	4.7(1)	14.1(1)
-	0.831(6)	1.98(6)	7.00(0)	81.3(33)	141(1)

TPA+ confines the oPs within the micropore network.

As the lifetime (τ) of oPs can be correlated with the size of the volume in which it annihilates, it is interesting to assess the variation in micropore lifetimes observed the ZM-x samples (Figure 6.5 c)). Two micropore components are seen in ZM-0.00 at $\tau_{\text{mic},1} = 1.43$ ns and $\tau_{\text{mic},2} = 3.31$ ns. Application of the RTE model [14] permits estimation of the equivalent pore diameter for a particular oPs lifetime. The effect of different geometries on the calculated pore diameter have been explored previously [177].

For the MFI zeolite, one could expect the square channel geometry to best represent the straight channels of the pore system. However, due to the occupation of the intersections with the SDA interrupting the continuous straight channel volume, the square channel geometry would be a poor representation. Indeed considering the diameter of the channel and intersection volumes derived from the

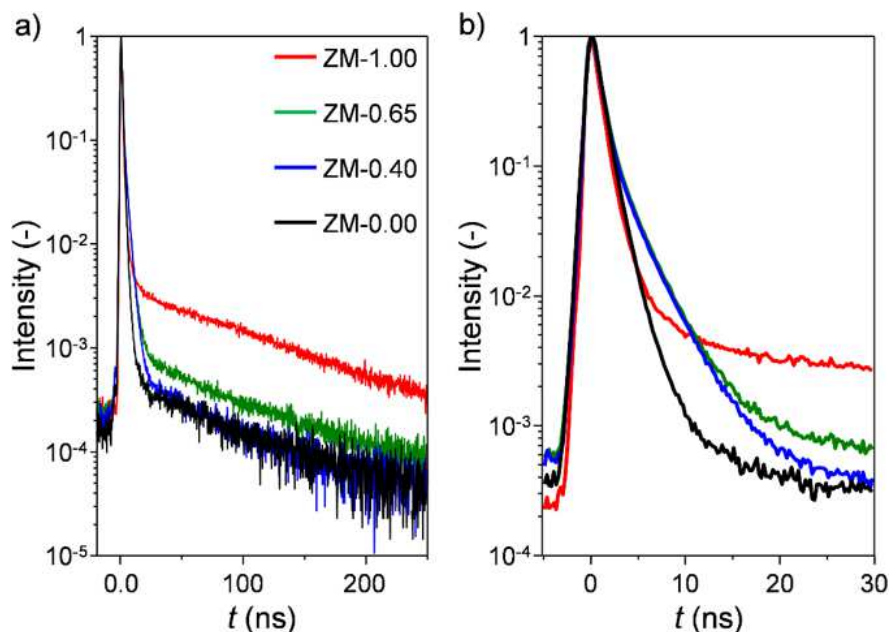


Figure 6.4: Positron annihilation lifetime spectra of selected ZM samples collected with the BaF2 detector. Part b) shows a zoom-in of the prompt peak in a). Reprinted with permission from [62]. Copyright 2016 American Chemical Society.

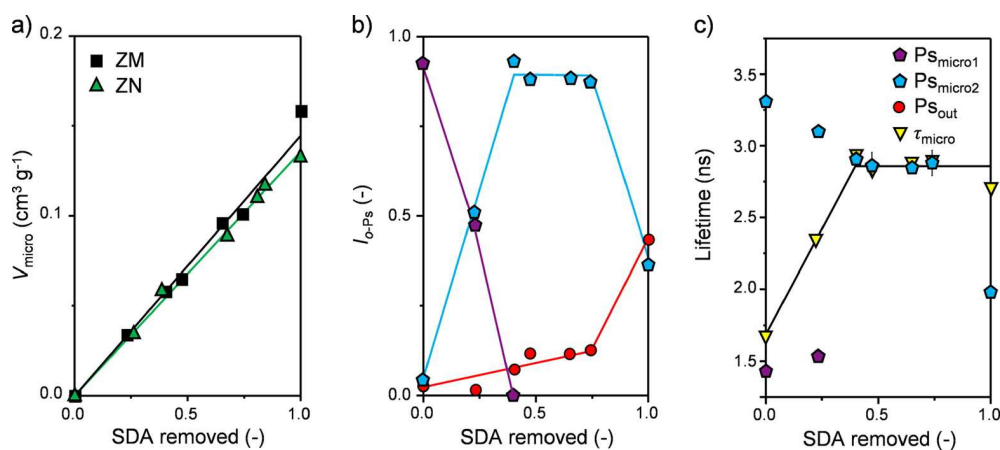


Figure 6.5: a) Variation of V_{mic} with detemplation in the ZM-x and ZN-x zeolites measured by gas sorption. b) The relative fraction of oPs annihilating in the micropores ($P_{\text{S}_{\text{mic},1}}$ and $P_{\text{S}_{\text{mic},2}}$) and in vacuum ($P_{\text{S}_{\text{vac}}}$), and c) $P_{\text{S}_{\text{mic},1}}$, $P_{\text{S}_{\text{mic},2}}$, and τ_{mic} (the weighted micropore mean oPs lifetime) versus the SDA content of the ZM-x zeolites. Reprinted with permission from [62]. Copyright 2016 American Chemical Society.

crystallographic structure (0.55 nm and 0.80 nm, respectively) [154] the square channel geometry estimates pore sizes of $d_{\text{mic},1} = 0.37$ nm and $d_{\text{mic},2} = 0.65$ nm. Due to the presence of the SDA, the free volumes available for Ps localization will be small, likely between the terminal ends of adjacent SDA molecules and in a few discrete intersections containing no SDA.

Estimations based on the spherical ($d_{\text{mic},1} = 0.52$ nm, $d_{\text{mic},2} = 0.84$ nm) and cubic geometries ($a_{\text{mic},1} = 0.47$ nm, $a_{\text{mic},2} = 0.80$ nm) provide closer agreement with the crystallographic data, with the spherical model providing a best match. As $I_{\text{mic},1}$ has substantially higher intensity in the fully templated sample (92.4% versus 4.2% for $I_{\text{mic},2}$) and considering the near-complete occupation of the intersection volumes with the SDA molecule, it is proposed that oPs annihilation predominately occurs in the interconnecting channels with a very minor fraction annihilating in the few vacant intersection volumes.

Upon detemplation $\tau_{\text{mic},1}$ and $\tau_{\text{mic},2}$ converge at ca. 2.8 ns (0.78 nm from RTE), identified as $\text{Ps}_{\text{mic},2}$ in Figure 6.5c. This lifetime remains stable until a fraction of 0.75 detemplation where two lifetimes at 1.98 ns (0.64 nm) and 7.00 ns (1.23 nm) appear. The origins of these components coincides with the increased intensity of I_{mes} and I_{vac} , indicative of oPs out-diffusion, and consistently a decreased intensity of $I_{\text{mic},2}$.

The reverse intensity trend was observed in the study of MFI-type zeolites whose external surface was capped with an organic molecule, essentially confining oPs within the micropores and preventing out-diffusion from the crystal [51]. Additionally, capping strategies for porous materials have been suggested previously as a method to obtain an average lifetime representative of the pore network [7]. The presence of the SDA appears to have a confining effect on oPs until a detemplation fraction of 0.75, where the 2.8 ns lifetime is an average lifetime of the pore network. After this fraction, there is a reduction in lifetime to 1.98 ns and a substantial drop in intensity (87.4 to 11.8%), which could be attributed to increased out-diffusion of oPs from the micropore network to vacuum [59]. The low-intensity component at 7.00 ns is ascribed to small defects (<2 nm) in the sample, e.g., grain boundaries.

By considering the experimentally derived mean micropore lifetime (all components between 1 to 10 ns, $\overline{\tau_{\text{mic}}}$) weighted by intensity (Figure 6.5c) the observed trends in oPs lifetime for the ZM-x zeolites can be rationalized. ZM-0.00 exhibits a mean lifetime at 1.7 ns, which increases to a value of 2.8 ns upon partial detemplation. Interestingly, the lifetime remains at 2.8 ns, suggesting that above a certain point the amount of detemplated volume does not affect the micropore lifetime.

At full detemplation, the weighted mean value remains at 2.8 ns. This suggests that more than one factor contributes to the micropore lifetime. Considering the relative intensity of $I_{\text{mic}} = I_{\text{mic},1} + I_{\text{mic},2}$ and I_{out} , out-diffusion, which also impacts the measured lifetime, only increases significantly when the fraction of SDA removed is > 0.75 . This would indicate the number of these detemplated volumes connected to the surface are limited until a majority of the SDA has been removed. Thus, the drop in I_{mic} for ZM-1.00 most likely relates to the increased

out-diffusion of oPs in this sample.

Modelling

To qualitatively understand the detemplation process, different mechanisms of removal were simulated utilizing percolation theory and compared to the PALS observations (Figure 6.6). Similar approaches have been made previously considering the kinetics of template removal in silicalite-1 [178]. Within this model the three-dimensionality of the ZSM-5 pore network has been translated to an array of nodes, i , j , and k , and interpreted as a matrix M of size $n_x \times n_y \times n_z$.

Channels within the pore network are represented by connections between these different points (black lines, Figure 6.6a-c) with sinusoidal channels contained within the xz -plane and the straight channels positioned on along the y -axis. Assuming every intersection within the fully templated material is occupied by the SDA ($p = 0$), the corresponding matrix, $M(p = 0)$, is filled with zeros. If an intersection becomes SDA-free, the corresponding element in M is set to 1.

Different states of detemplation p can thus be simulated as flipping the $N_p = n_x \cdot n_y \cdot n_z \cdot p$ elements of the matrix M . By selecting how these N sites are generated, four different models of detemplation were simulated (Figure 6.6d-g). These models can be considered by differing degrees of ordered detemplation:

1. Shrinking core model (SC, Figure 6.6d). Highly ordered detemplation from the exterior of the crystallite toward the centre. The templated elements ($M(i, k, k)$) with the largest distance

$$r = (i - n_x/2)^2 + (j - n_y/2)^2 + (k - n_z/2)^2 \quad (6.1)$$

are set to 1 until the desired detemplation ratio

$$p = \frac{\sum_{i,j,k} M_{i,j,k}}{n_x n_y n_z} \quad (6.2)$$

is attained.

2. Isolated volume model (IV, Figure 6.6e). An arrangement of randomly chosen sites become increasingly detemplated to form discrete, isolated volumes. A $M(p = 0)$ matrix is evolved with a Markov Chain Monte Carlo method favouring the detemplation of randomly chosen elements if their nearest neighbours are already detemplated. The weighting is applied using Glauber-Dynamics [179] by defining the acceptance probability for a flip from $p = 0$ to $p = 1$ as

$$p = \frac{\exp(\beta N)}{1 + \exp(\beta N_{\max})} \quad (6.3)$$

with N being the number of free nearest neighbours, $N_{\max} = n_x n_y n_z$ and β a temperature-like scaling parameter.

3. Non isolated volume model (NV, Figure 6.6f). Detemplation occurs randomly throughout the framework with no restriction on the formation of

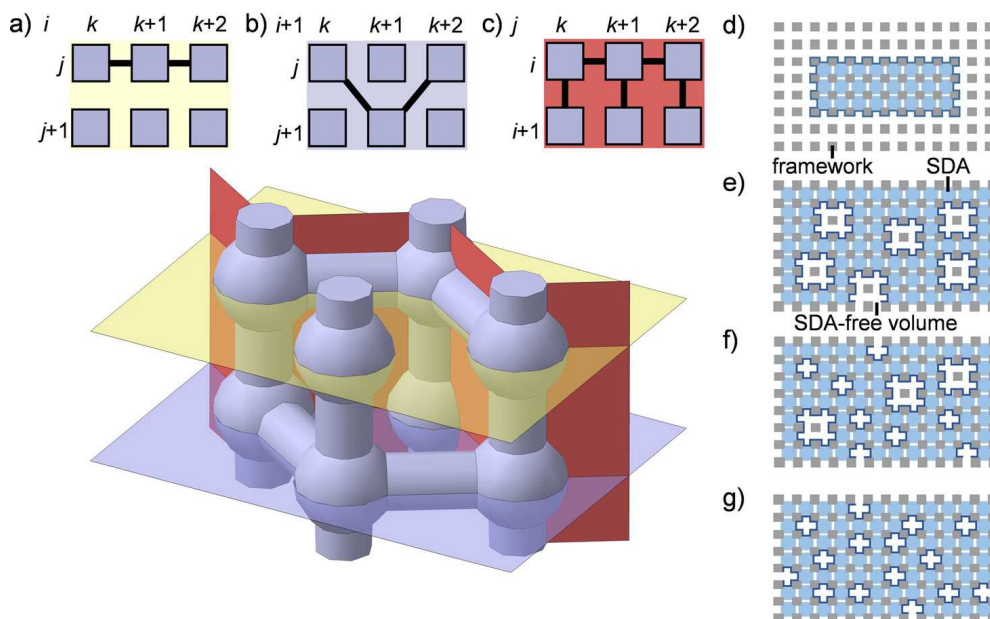


Figure 6.6: a)–c) Diagrams representing the translation of the MFI framework to the matrix utilized for the percolation theory modeling. Schematics of the various detemplation mechanisms modeled by the percolation theory, d) shrinking core (SC), e) isolated volume (IV), f) nonisolated volume (NV), and g) isotropic detemplation (ID) models. Reprinted with permission from [62]. Copyright 2016 American Chemical Society.

new detemplated sites or expanding existing detemplated sites. The matrices are created by filling with random numbers, $\epsilon(0, 1)$, and setting the elements to 1 if $M(i, j, k) < p$ and 0 otherwise. This is equivalent to $\beta = 0$ but computationally faster because the matrix does not need to be evolved as done in the Markov Chain.

4. Isotropic detemplation model (ID, Figure 6.6g). As with the NV model, detemplation occurs randomly. However, the formation of larger voids as found in both the IV and NV models is suppressed to enforce a distribution of small volume sites. Application of the acceptance probability defined for model 2, but setting β to be negative ensures a higher probability to form a new site rather than expand an existing one.

The parameter β is applied to scale the probability of freeing a randomly chosen intersection with a particular number of template-free neighbours and can be varied to control the *strength* of the particular detemplation process. For instance, by increasing $\beta (> 0)$ for the IV model, the probability of detemplation is increased to sites where detemplation has already occurred, creating larger open volumes. By decreasing $\beta (< 0)$, detemplation of sites with no near detemplated neighbours is more probable.

The matrices for a set of p values are then analysed individually with the Hoshen-Kopelman algorithm [180] to get a list of all volumes, i.e., the number of connected intersections, channels, and connections to the crystal surfaces.

These volumes are categorized based on the number of neighbouring SDA-free intersections; a single channel, i.e., no free intersections (τ_{ch}), a single intersection (τ_{si}), and two or more neighbouring intersections (τ_{mi}). The latter are grouped as the number of possible configurations of neighbouring intersections increases sharply once two neighbouring SDA molecules are removed.

Figure 6.8a compares the variation in the number of discrete τ_{si} and τ_{mi} volumes with detemplation for each of the models. Considering the oPs lifetime values for the ZM-0.00 and ZM-1.00 as typical of a single channel (ZM-0.00, $\tau_{\text{mic},1} = 1.7$ ns), a single intersection (ZM-0.00, $\tau_{\text{mic},2} = 3.3$ ns) and of a SDA-free sample (ZM-1.00, $\tau_{\text{mic}} = 2.9$ ns), one can estimate τ_{ch} , τ_{si} , and τ_{mi} . Thus, the mean lifetime of oPs in the micropores, τ_{mean} , can be extracted from the proposed models by applying the equation

$$\tau_{\text{mean}} = \tau_{\text{ch}}I_{\text{ch}} + \tau_{\text{si}}I_{\text{si}} + \tau_{\text{mi}}I_{\text{mi}} \quad (6.4)$$

where the intensities I_{ch} , I_{si} , and I_{mi} are the normalized volume ratios in the simulated model. Typical intensity plots derived from the simulations are provided in Figure 6.7, where the distribution of the different volumes can be summed to yield the total simulated pore volume upon detemplation. From the previously outlined calculations, it is possible to follow the variation of τ_{mean} with detemplation for the SC, IV, NV, and ID models using the measured values from the ZM-x samples (Figure 6.8b).

Interestingly the best fit with the experimental data is found in cases where the formation of large detemplated volumes are suppressed ($\beta < 0$, ID model) as indicated by the blue shaded area in Figure 6.8b. Conversely, the fit is worse in cases where $\beta > 0$ (green area, SC and IV model). These trends indicate that the detemplation mechanism of the ZM zeolite is highly random and occurs throughout the micropore structure, rather than forming large SDA-free volumes.

To assess the generality of the trends observed for the ZM zeolite, a sample more typical of commercial materials comprised of aggregated nano-sized crystals (ZN, Si:Al = 29, average crystallite diameter ca. 20 nm, Figure 6.3c) was synthesized with TPA+ as the SDA. Quality analysis confirmed the MFI crystallinity of the material and a comparable detemplation mechanism [62]. Analysis of the porosity development upon controlled SDA removal by gas sorption also revealed equivalent trends in V_{mic} as for the ZM zeolite (Figure 6.5a).

PALS analysis of ZN-0.00 identifies a similar distribution of components as for ZM-0.00 (τ_{mic} , τ_{mes} , and τ_{vac}), but with significantly higher intensity for the longer lived I_{mes} and I_{vac} components (14.7 versus 3.3%, Table 6.2). Upon SDA removal an almost inverse linear correlation is observed between I_{mic} and $I_{\text{out}} = I_{\text{mes}} + I_{\text{vac}}$, Figure 6.9a). This suggests that the confinement effect observed for the ZM-x samples (Figure 6.5) is weaker in the ZN-x series, which is reflected in the variation of the micropore lifetime (increasing from 2.1 to 5.5 ns) during detemplation (Figure 6.9b). Estimation of the pore diameter from RTE places this range of lifetimes between 0.66 to 1.00 nm.

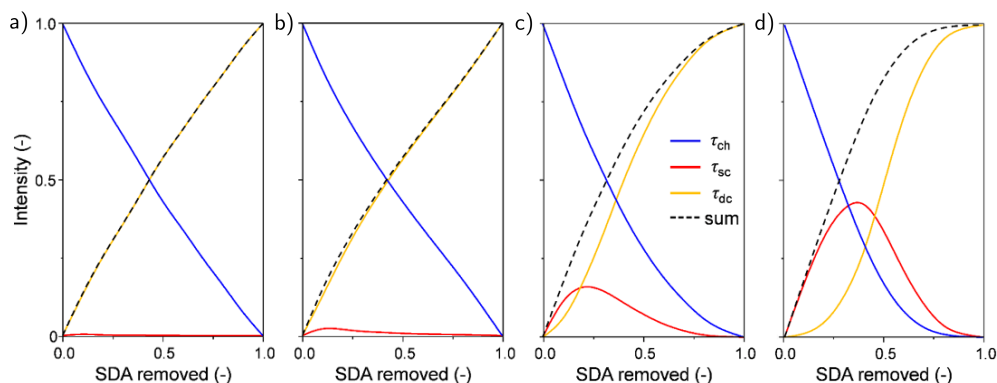


Figure 6.7: Normalized intensity of the distinct components contributing towards the lifetime of oPs in the micropores of ZSM-5 predicted by the a) shrinking core, b) isolated volume, c) non-isolated volume and d) isotropic detemplation percolation models as a function of the SDA content. The codes denote a single channel (τ_{ch}), single intersection (τ_{si}) and SDA-free units comprising two or more intersections (τ_{mi}) while the dashed line indicates the sum of the micropore components. Adapted with permission from [62]. Copyright 2016 American Chemical Society.

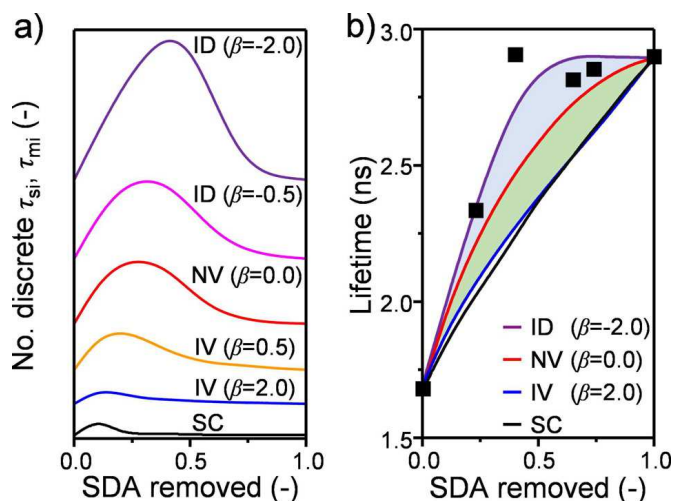


Figure 6.8: a) Comparison of the total number of discrete τ_{si} and τ_{mi} volumes derived from the SC, IV, NV, and ID models with detemplation. Note each plot has been offset for clarity. b) Comparison of the calculated τ_{mean} value for the SC, IV, NV, and ID models for the ZM-x zeolites. The black markers indicate the weighted mean τ_{mic} values for the ZM-x samples. Reprinted with permission from [62]. Copyright 2016 American Chemical Society.

Table 6.2: The contributions derived from PALS measurements of the ZN sample. Lifetimes and intensities associated with pPs, e^+ and oPs decaying in micropores (mic 1,2), mesopores (mes), and vacuum (vac), total oPs fraction $I_{\text{oPs}} = I_{\text{mic},1} + I_{\text{mic},2} + I_{\text{mes}} + I_{\text{vac}}$ and normalized oPs components I_{oPs} , i.e., $I_{\text{mic},1}^{\ominus} = I_{\text{mic},1}/I_{\text{oPs}}$ are presented.

Sample	I_{oPs} (%)	$I_{\text{mic},1}^{\ominus}$ (%)	$I_{\text{mic},2}^{\ominus}$ (%)	I_{mes}^{\ominus} (%)	I_{vac}^{\ominus} (%)
I_{pPs} (%)	I_{e^+} (%)	$I_{\text{mic},1}$ (%)	$I_{\text{mic},2}$ (%)	I_{mes} (%)	I_{vac} (%)
τ_{pPs} (ns)	τ_{e^+} (ns)	$\tau_{\text{mic},1}$ (ns)	$\tau_{\text{mic},2}$ (ns)	τ_{mes} (ns)	τ_{vac} (ns)
ZN-0.00	25.8(12)	72.9 (27)	12.4 (39)	5.0 (4)	9.7 (4)
-	74.2 (19)	18.8 (7)	3.2 (10)	1.3 (1)	2.5 (1)
-	0.592 (13)	2.12 (19)	7.21 (122)	34.0 (45)	120 (4)
ZN-0.26	26.6(4)	71.1 (4)	10.5 (8)	5.3 (8)	13.2 (8)
-	73.3 (2)	18.9 (1)	2.8 (2)	1.4 (2)	3.5 (2)
-	0.612 (2)	2.83 (4)	13.3 (10)	44.3 (63)	114 (4)
ZN-0.39	26.7(1)	59.9 (4)	-	21.3 (4)	Ⓡ18.7 (0)
-	73.2 (2)	16.0 (1)	-	5.7 (1)	5.0 (0)
-	0.629 (2)	3.42 (5)	-	16.8 (4)	99 (0)
ZN-0.67	30.1(7)	43.5 (10)	22.6 (13)	13.0 (10)	20.9 (13)
-	70.0 (6)	13.1 (3)	6.8 (4)	3.9 (3)	6.3 (4)
-	0.669 (7)	3.39 (20)	13.2 (13)	44.3 (70)	125 (4)
ZN-0.81	25.6(2)	46.5 (8)	-	28.1 (4)	25.4 (4)
39.1 (4)	35.2 (5)	11.9 (2)	-	7.2 (1)	6.5 (1)
0.498 (1)	0.899 (0)	4.59 (9)	-	19.6 (6)	105 (1)
ZN-1.00	22.8(6)	38.2 (18)	-	29.4 (18)	32.5 (9)
19.6 (10)	57.6 (12)	8.7 (4)	-	6.7 (4)	7.4 (2).
0.465 (17)	0.899 (0)	5.5 (4)	-	20.6 (16)	113 (2)

Besides, the sum of components between 13 ns and 45 ns (1.64 to 3.96 nm, respectively) increases in intensity during detemplation, further evidencing the increased amount of oPs localizing in isolated mesopores within the sample. Such an effect is absent for the large crystal ZM sample due to the more regular crystal morphology giving rise to fewer intragranular voids (Figure 6.3). As the latter will be random in size and shape, the corresponding lifetimes will cover a broad range of values. Therefore, fitting oPs with a single lifetime component will lead to inaccuracies, highlighting a limitation of the fitting strategy employed here. Although this restricts the application of the percolation theory described for the ZM samples in terms of lifetime analysis, the measured intensity trends are still a useful indicator toward the amount of oPs contained within the micropores versus the amount of out-diffusion.

Exploiting the fact that the average crystallite size of ZN is comparable to the dimensions of the simulated model, it is possible to calculate the discrete volumes within the micropore structure which become connected to the external surface of the crystallite during SDA removal. The occurrence of these volumes can be considered as out-diffusion routes for oPs, and so the total sum of these surface-connected volumes can be scaled to match the measured out-diffusion in the fully

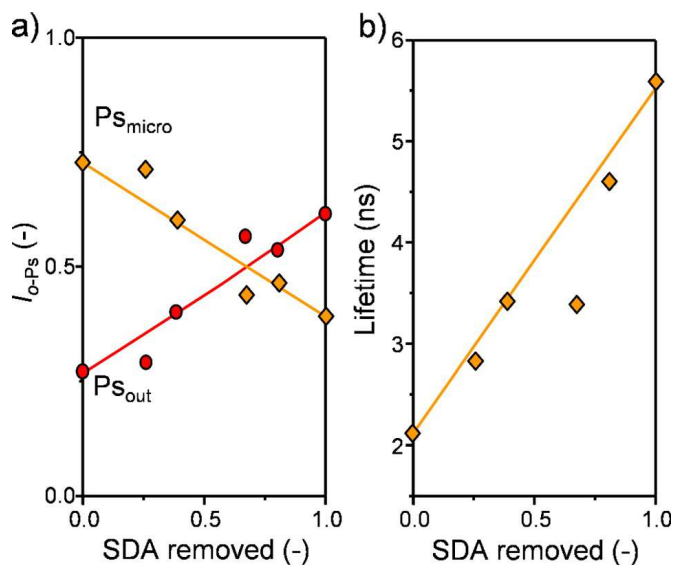


Figure 6.9: Variation of a) Ps_{mic} and Ps_{out} intensities and b) Ps_{mic} lifetime with detemplation for the ZN-x zeolites. Reprinted with permission from [62]. Copyright 2016 American Chemical Society.

detemplated sample (Figure 6.10). Note that a similar assessment of the ZM-x samples would not be informative as the out-diffusion of oPs will be affected by the larger crystallite size of those samples. Interestingly, as with the ZM sample, the SC model provides the poorest correlation (Figure 6.10a). However, when comparing the IV, NV, and ID models (Figure 6.10b–d), the best correlations appear when β is parametrized close to zero ($-0.5 > \beta < 0.5$) suggesting that the mechanism of detemplation is random and non-discriminatory in terms of the number of detemplated neighbouring intersections in this case.

Summary

Based on observations by Confocal Fluorescence Microscopy (CFM) [62] and the models studied by the percolation theory, the mechanism of SDA removal within the ZSM-5 zeolite is believed to proceed via a site-independent process occurring homogeneously throughout the crystal (Figure 6.11). For the ZM-x samples, this results in a small number of surface connected micropore volumes with respect to the total crystallite volume, explaining the low fraction of oPs out-diffusion until the later stages of detemplation (ca. 75% SDA removed). However, for the ZN-x samples, this oPs confinement is less noticeable due to the smaller crystallite size, which reduces the diffusion path for oPs from the micropore domain to the crystallite surface.

For both sets of samples and particularly ZM-x, the models best simulated the data when the formation of large SDA-free volumes was suppressed ($\beta < 0.5$, NV and ID models). This was confirmed by CFM analysis where there was a lack of distinct SDA-free micropore regions, further evidencing the isotropic manner of the detemplation process.

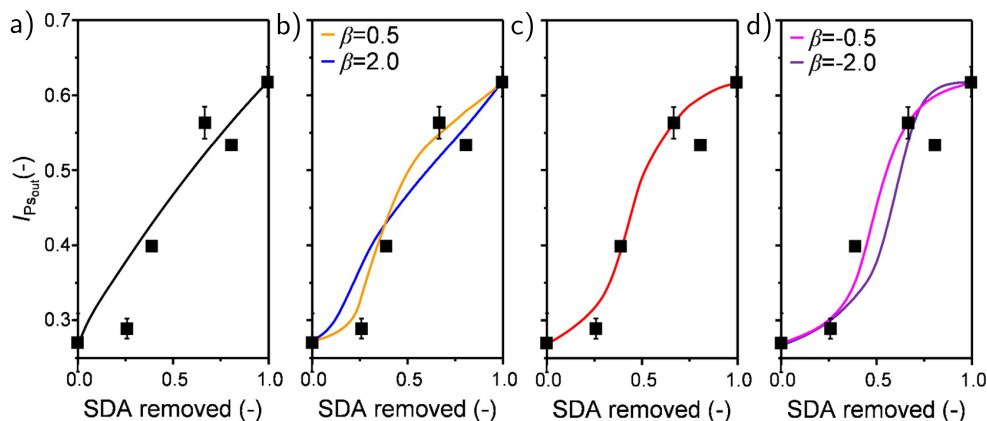


Figure 6.10: Comparison of the calculated intensity of out-diffusion for the a) SC, b) IV, c) NV, and d) ID models for the ZN-x zeolites. The black squares indicate the experimentally obtained values. Reprinted with permission from [62]. Copyright 2016 American Chemical Society.

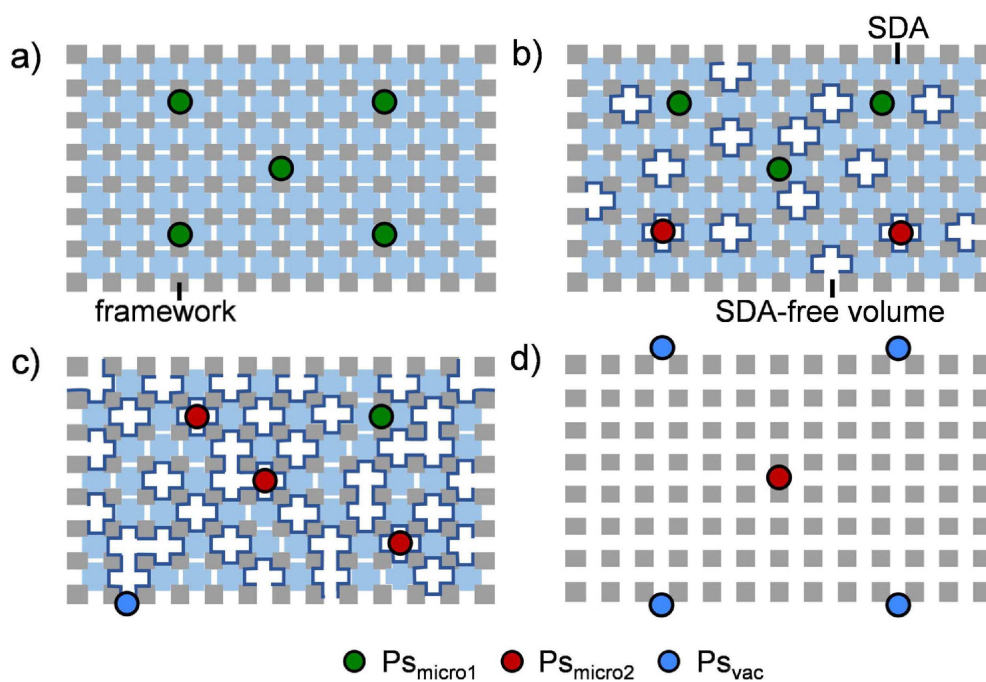


Figure 6.11: Illustration of the observed mechanism of SDA removal in ZSM-5 zeolites and the effect on oPs diffusion, from a) fully templated to d) fully detemplated. Adapted with permission from [62]. Copyright 2016 American Chemical Society.

In this regard, it was shown that PALS can provide a unique level of insight into the evolution of the micropore network of zeolites. Due to the diffusional nature of the ortho-positronium probe within the MFI framework, it was possible to differentiate between ortho-positronium confined in sinusoidal channels by SDA molecules and SDA-free intersections. Trends in the diffusional behaviour of ortho-positronium occurred upon SDA removal, which was modelled using percolation theory. The best correlations with the experimental data suggests SDA removal in ZSM-5 zeolite occurs isotropically throughout the micropore structure, with the absence of large discrete detemplated volumes. These results highlight the unique spatial sensitivity positron annihilation lifetime spectroscopy can provide in zeolite materials, from the single intersection to the detemplation process of a single crystal. The approaches adopted here could easily be adapted to study other porous systems where the micropore structure is disrupted in some capacity by the presence of guest species.

6.3 Acidity in Zeolites

The following section presents the study on the impact of acidity in MFI-type zeolites on PALS, see Section 6.1, and is adapted with permission from [65]. Copyright 2018 American Chemical Society.

An interesting but less explored facet of PALS is the sensitivity of oPs to acid sites present in zeolites, which could have significant implications for porosity assessment using this technique [18, 181–184]. Early works by Goldanskii and co-workers reported a chemical quenching effect, correlating the concentration of exposed Brønsted acid sites in partially hydrated amorphous silica-alumina catalysts with the lifetime of oPs [185, 186]. Specifically, it was proposed that oPs could be oxidized by the following reaction:



A later study of FAU-type zeolites by Nakanishi and co-workers, using a combination of PALS and DBS, related variations in the lifetime and intensity of oPs contributions upon thermal treatment to the exposure of Brønsted acid sites upon dehydration [187]. The presence of the latter was postulated to have two possible effects, either to inhibit the formation of oPs or, if formed, to catalyze their oxidation. Similar findings were also reported by Gao and co-workers for a series of FAU-type zeolites [188]. Huang and co-workers published a series of studies on various zeolite frameworks utilizing different positron spectroscopy methods, including PALS, DBS, and angular correlation of annihilation radiation (ACAR) [189–193]. The authors concluded that the strength of the Brønsted acidity determined the rate of oPs oxidation and proposed a mechanistic cycle involving the decomposition and subsequent regeneration of the acid site [189]. The role of Lewis acidity has rarely been addressed. Huang and co-workers reported that Lewis acid sites formed upon thermal treatment of zeolites played no role in the oxidation of oPs [189]. In contrast, later calculations indicated that a

higher rate of oPs oxidation should be expected to occur at Lewis rather than at Brønsted acid centres [194].

The limited understanding of the effects of acidity on the PALS response is exacerbated by the fact that many previous studies focused on a narrow range of the lifetime spectra. Furthermore, the studies often failed to provide sufficient characterization data (e.g. type and concentration of acid sites present, crystal size, morphology, etc.) to enable proper rationalization. In this study, well-crystallized MFI-type zeolites with tailored Brønsted (varying Si/Al ratio) and Lewis (lattice substitution of tin or sodium exchange) acidity were prepared to decouple the effects of the pore and acid-site structure on the PALS measurement. Zeolites with MFI-type framework were chosen due to the possibility of varying the acidic properties over a wide range while preserving the crystal size and morphology. A variable-energy slow positron beam was utilized to differentiate annihilation in the micropore. A mechanistic discussion is developed based on the results.

Methods

A series of ZSM-5 zeolites comprised of coffin-shaped single crystals of ca. $20\ \mu\text{m} \times 5\ \mu\text{m} \times 0.5\ \mu\text{m}$ with varying silicon-to-aluminium (purely siliceous, Si:Al = 80 and 50, coded Si1, Z80, and Z50) and silicon-to-tin (Si:Sn = 96, Sn-MFI) ratios were synthesized by the group of Advanced Catalysts Engineering, D-CHAB, ETHZ. Commercial ZSM-5 zeolites of varying Si:Al ratios were obtained for comparative analysis: ZC1000 (HSZ-890HOA, H⁺ form, Si:Al = 1060, TOSOH), ZC40 (CBV8014, NH₄-form, Si:Al = 40, Zeolyst International), and ZC15 (CBV302-E, NH₄ form, Si:Al = 15, Zeolyst International). These samples exhibited crystal aggregates with a particle size range of 0.5–2.0 μm in diameter. A tin-containing sample of similar morphology was also obtained through a treatment of ZC1000 (ZC-Sn) following a previously described protocol [195]. Partially (ZC40-Na-0.5) and fully (ZC40-Na-1) sodium-exchanged samples were obtained by three consecutive treatments of the as-received ZC40. A more detailed description of the preparation of these samples can be found in [65].

PALS measurements were performed using the ETHZ slow positron beam. Powdered samples (ca. 100 mg) were suspended in acetone ($50\ \text{cm}^3/\text{g}$) and deposited on the sample stage, resulting in a uniform ca. 1 mm thick layer which was degassed in situ under vacuum ($<2 \times 10^{-7}$ mbar) at 365 K for 2 h. Once vacuum conditions were attained, monoenergetic positrons were accelerated into the sample at the desired energy (3–15 keV), resulting in mean implantation depths varying from approximately 0.2 to 1.6 μm . Spectra were obtained with at least 3×10^7 counts. The acquired lifetime spectra were fitted with multiple exponential lifetime components with their relative fractions (lifetime, τ , and intensity, I) extracted using the PASCual data suite after subtraction of the background due to uncorrelated start-stop signals [174]. One to two short lifetime components (<1 ns), corresponding to the annihilation of para-positronium (τ_{pPs} , I_{pPs}) or positrons (τ_{e^+} , I_{e^+}) and two to four longer-lived components (>1 ns) attributed to ortho-positronium, with the summed intensity referred to as I_{oPs} , were identified in all cases. It was not

always possible to resolve the pPs and e^+ contributions due to the time resolution of the beam instrumentation utilized (<1 ns).

Studies of large crystal MFI-type silicalite-1 crystals reported a similar distribution of oPs components [196], and considering the expected relationship between the lifetime and the pore size, the annihilation was assigned to occur in the crystalline micropore framework ($\tau_{\text{mic}} = 1\text{--}10$ ns, I_{mic}), outside of the crystalline micropore framework, i.e., in small defects or intercrystalline voids ($\tau_{\text{inc}} = 10\text{--}80$ ns, I_{def}) or in vacuum ($\tau_{\text{vac}} > 80$ ns, I_{vac}). In some cases several components could be fitted within the defined lifetime ranges and are identified by consecutive numbering, e.g. $\tau_{\text{def},1}$, $\tau_{\text{def},2}$. The intensity of oPs able to out-diffuse from the micropores of the crystalline zeolite framework to larger volumes or into a vacuum (I_{out}) corresponds to the sum of I_{def} and I_{vac} .

Results

To quantify the impact of the acidic properties on the PALS response, a series of large coffin-shaped ZSM-5 zeolite crystals of varying Si:Al ratios (Sil, Z80, and Z50) and a tin-containing MFI sample of similar morphology (Sn-MFI) were synthesized (6.3). Substitution of Si by Al or Sn could be expected to impact the number of electrons available to form positronium, therefore distorting the PALS comparison between Sil and the aluminium/tin-containing samples. However, the variation in electron numbers is relatively small, with the percentage increase from Sil to Z50 being 0.07% and to Sn-MFI being 1.25%. In terms of the expected effect on positronium formation, the variation in electron numbers would be negligible.

The study of large crystals is important for minimizing kinetic effects due to the out-diffusion of oPs from the zeolite which can shorten the lifetime and reduce the amount of oPs sampling the micropore network [51]. It also ensures greater control over the positron stopping profile, since the mean implantation depth is smaller than the crystal size, as discussed in Section 5.1. The isomorphous substitution of aluminium into the MFI-type framework leads to the formation of Brønsted acid sites when the zeolite is in protonic form, while the introduction of tin gives rise to Lewis acid sites. A more detailed description of the chemical analysis to assess the proper quality of the samples can be found in [62].

PALS measurements of Sil, Z80, and Z50 were performed to assess the impact of varying Brønsted acidity on the annihilation behaviour of oPs. Additional information can be obtained upon varying the incident positron energy, thereby controlling the depth of positron implantation to assess different volumes within the zeolite crystal. The contour plot in Figure 6.12 show the correlation between I_{oPs} (i.e., the total measured amount of oPs), Brønsted acid site concentration ($c_{\text{Brønsted}}$) and implantation depth. No significant variation in I_{oPs} was observed for Sil, consistent with the high structural uniformity and absence of acid centres in these samples. However, increases in $c_{\text{Brønsted}}$ lead to a significant drop in I_{oPs} , which is more pronounced at higher positron implantation depths. This is consistent with previous reports of the oxidative effect of Brønsted acidity on positronium [18, 182–193].

Table 6.3: Composition, porosity, and acidity of the zeolites studied. Si:X determined by inductively coupled plasma optical emission spectrometry and x-ray photoelectron spectroscopy. Porosity parameters from N₂ gas sorption. Concentrations of Brønsted and Lewis acid sites determined from IR spectroscopy of adsorbed pyridine. Characterization performed by R. Warringham or members of the ACE group, D-CHAB, ETH. Adapted with permission from [65]. Copyright 2018 American Chemical Society.

Sample	Si:X $\left(\frac{\text{mol}}{\text{mol}}\right)$	V_{ads} $\left(\frac{\text{cm}^3}{\text{g}}\right)$	V_{mic} $\left(\frac{\text{cm}^3}{\text{g}}\right)$	V_{mes} $\left(\frac{\text{cm}^3}{\text{g}}\right)$	S_{mes} $\left(\frac{\text{m}^2}{\text{g}}\right)$	$c_{\text{Brønsted}}$ $\left(\frac{\text{mol}}{\text{g}}\right)$	c_{Lewis} $\left(\frac{\text{mol}}{\text{g}}\right)$
Sil	-	0.18	0.16	0.02	24	0	0
Z80	81	0.18	0.16	0.02	25	74	6
Z50	50	0.17	0.15	0.02	29	144	14
Sn-MFI	95	0.18	0.16	0.02	17	0	46
Z50-Na	-	0.17	0.14	0.03	24	0	160
ZC1000	961	0.19	0.14	0.05	59	19	10
ZC40	39	0.25	0.17	0.08	68	168	18
ZC15	15	0.29	0.14	0.15	76	305	43
ZC-Sn	94	0.29	0.08	0.21	98	15	58
ZC40-Na-0.5	-	0.24	0.16	0.08	67	102	66
ZC40-Na-1	-	0.23	0.14	0.09	70	0	168

Interestingly, comparison of the absolute intensities of the different components reveals a stronger effect of the presence of Brønsted acid sites on I_{mic} (the intensity of oPs annihilation in the zeolite micropores) compared to I_{out} (the combined intensity of annihilation components >10 ns) (Figure 6.13a), revealing a non-uniform impact on oPs species. In particular, these observations indicate that the presence of Brønsted acid centers does not affect the diffusion of oPs out of the crystal, which is consistent with the comparable oPs lifetimes (τ_{oPs}) evidenced within each of the samples (Figure 6.13b, Tables 6.4, 6.56.6).

To generalize the observations for the Sil, Z80, and Z50, a series of commercially available samples with differing acidity were studied (ZC1000, ZC40, and ZC15, Table 6.3). The morphology of these samples consists of smaller crystals (ca. 2 μm for ZC1000 and 0.5 μm for ZC40 and ZC15) arranged in larger crystal aggregates of >2 μm average diameter.

The effect of these types of morphologies and the incident positron energy on the PALS response are discussed in Section 5.1. In general, larger kinetic effects are expected due to the increased out-diffusion of oPs [51]. Comparing the fits (Table 6.7), an additional component between 30–60 ns appears, consistent with the annihilation of oPs in the intercrystalline voids present in these samples. Additionally, the intensity of the longest component, I_{vac} , is much higher due to the reduced diffusion path out of the crystals.

Nonetheless, as for the large crystal samples, a reduction in the measured amount

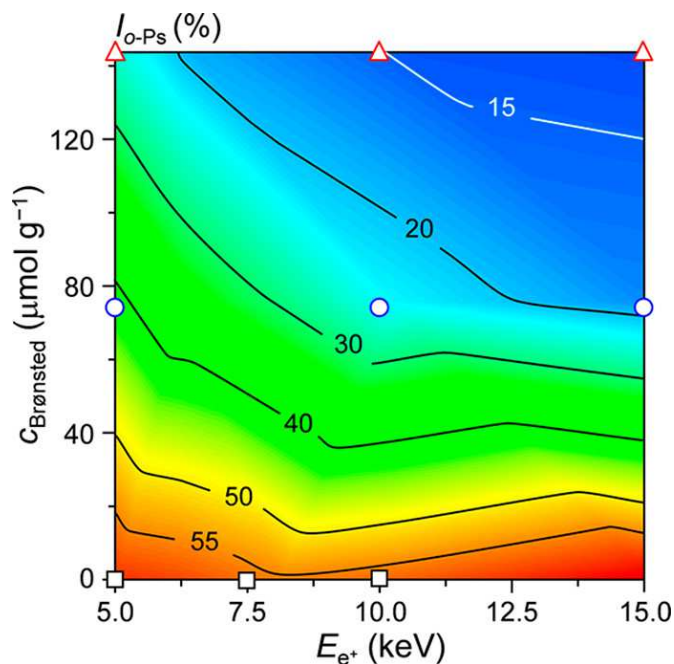


Figure 6.12: Contour representation of the variation of the total measured intensity of oPs with the concentration of Brønsted acid sites and positron implantation energy E_{e^+} . Adapted with permission from [65]. Copyright 2018 American Chemical Society.

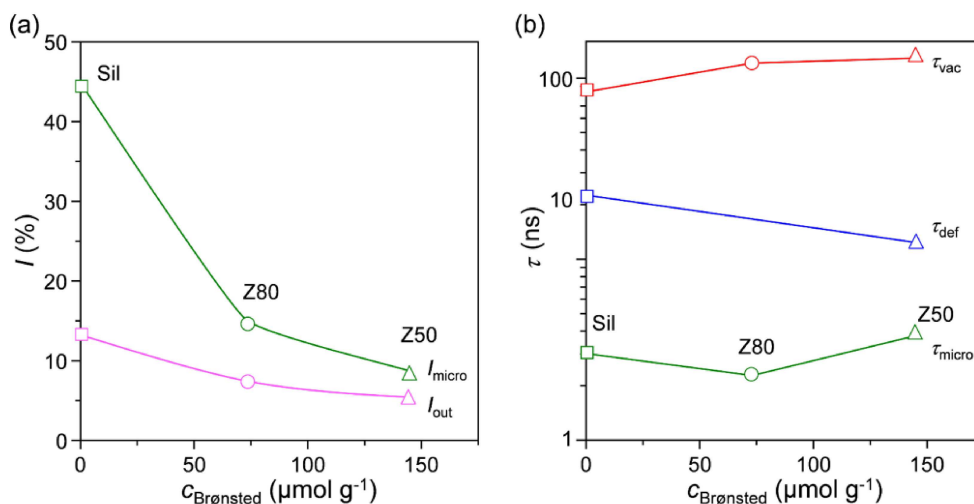


Figure 6.13: The variation in oPs (a) intensity and (b) lifetime values with the concentration of Brønsted acid sites for Sil, Z80 and Z50, obtained at 10 keV. I_{out} represents the sum total of I_{def} and I_{vac} . Adapted with permission from [65]. Copyright 2018 American Chemical Society.

Table 6.4: PALS results of acidity study Sil zeolite at different implantation energies E_{e^+} . Lifetimes and intensities associated with pPs and e^+ are grouped under *not oPs* annihilation ($\circ\mathcal{P}\overline{s}$), oPs is divided into micropores (mic), mesopores (mes) and vacuum (vac), total oPs fraction $I_{\text{oPs}} = I_{\text{mic}} + I_{\text{mes}} + I_{\text{vac}} = 1 - I_{\circ\mathcal{P}\overline{s}}$ and normalized oPs components I_{oPs} , i.e., $I_{\text{mic}}^{\ominus} = I_{\text{mic}}/I_{\text{oPs}}$. Adapted with permission from [65]. Copyright 2018 American Chemical Society.

E_{e^+} (keV)	$\tau_{\circ\mathcal{P}\overline{s}}$ (ns)	τ_{mic} (ns)	τ_{mes} (ns)	τ_{vac} (ns)
	$I_{\circ\mathcal{P}\overline{s}}$ (%)	I_{mic} (%)	I_{mes} (%)	I_{vac} (%)
	I_{oPs} (%)	I_{mic}^{\ominus} (%)	I_{mes}^{\ominus} (%)	I_{vac}^{\ominus} (%)
3	0.6(1)	2.9(0)	21.0(3)	96.6(14)
	39.8(2)	44.8(2)	10.1(1)	5.3(1)
	60.2(2)	74.4(3)	16.8(1)	8.8(2)
5	0.6(1)	2.9(1)	19.1(3)	84.2(14)
	40.6(2)	44.3(2)	10.1(1)	5.0(1)
	59.4(2)	74.6(3)	17.0(2)	8.4(2)
7.5	0.5(1)	3.1(1)	23.3(3)	97.6(20)
	43.8(2)	42.7(1)	10.0(1)	3.5(1)
	56.2(2)	76.0(2)	17.8(2)	6.2(2)
10	0.6(1)	3.0(1)	21.9(7)	85.0(41)
	42.1(3)	44.7(3)	9.2(2)	4.0(2)
	57.9(4)	77.2(5)	15.9(3)	6.9(4)

Table 6.5: PALS results of acidity study Z80 zeolite at different implantation energies E_{e^+} . Lifetimes and intensities associated with pPs and e^+ are grouped under *not oPs* ($\circ\mathcal{P}\overline{s}$) annihilation, oPs is divided into micropores (mic), mesopores (mes) and vacuum (vac), total oPs fraction $I_{\text{oPs}} = I_{\text{mic}} + I_{\text{mes}} + I_{\text{vac}} = 1 - I_{\circ\mathcal{P}\overline{s}}$ and normalized oPs components I_{oPs} , i.e., $I_{\text{mic}}^{\ominus} = I_{\text{mic}}/I_{\text{oPs}}$. Adapted with permission from [65]. Copyright 2018 American Chemical Society.

E_{e^+} (keV)	$\tau_{\circ\mathcal{P}\overline{s}}$ (ns)	τ_{mic} (ns)	τ_{mes} (ns)	τ_{vac} (ns)
	$I_{\circ\mathcal{P}\overline{s}}$ (%)	I_{mic} (%)	I_{mes} (%)	I_{vac} (%)
	I_{oPs} (%)	I_{mic}^{\ominus} (%)	I_{mes}^{\ominus} (%)	I_{vac}^{\ominus} (%)
5	0.8(1)	2.5(1)	-	128(1)
	64.9(14)	26.2(14)	-	8.9(1)
	35.1(14)	74.6(40)	-	25.4(3)
10	0.9(1)	2.3(1)	-	117(1)
	77.4(8)	14.9(6)	-	7.7(0)
	22.6(6)	65.9(29)	-	34.1(0)
15	0.9(1)	2.9(1)	-	127(1)
	83.0(8)	9.5(1)	-	7.5(1)
	17.0(7)	55.9(38)	-	44.1(6)

Table 6.6: PALS results of acidity study Z50 zeolite at different implantation energies E_{e^+} . Lifetimes and intensities associated with pPs and e^+ are grouped under *not oPs* ($\circ\text{Ps}$) annihilation, oPs is divided into micropores (mic), mesopores (mes) and vacuum (vac), total oPs fraction $I_{\text{oPs}} = I_{\text{mic}} + I_{\text{mes}} + I_{\text{vac}} = 1 - I_{\circ\text{Ps}}$ and normalized oPs components I_{oPs} , i.e., $I_{\text{mic}}^{\ominus} = I_{\text{mic}}/I_{\text{oPs}}$. Adapted with permission from [65]. Copyright 2018 American Chemical Society.

E_{e^+} (keV)	$\tau_{\circ\text{Ps}}$ (ns)	τ_{mic} (ns)	τ_{mes} (ns)	τ_{vac} (ns)
	$I_{\circ\text{Ps}}$ (%)	I_{mic} (%)	I_{mes} (%)	I_{vac} (%)
	I_{oPs} (%)	I_{mic}^{\ominus} (%)	I_{mes}^{\ominus} (%)	I_{vac}^{\ominus} (%)
3	0.9(1)	2.8(1)	10.0(0)	102(1)
	75.7(7)	12.5(6)	8.1(1)	3.7(1)
	24.3(6)	51.4(25)	33.4(4)	15.2(5)
5	0.9(1)	3.5(2)	12.4(6)	115(1)
	81.4(4)	10.6(2)	5.0(3)	3.0(1)
	18.6(4)	57.0(11)	26.9(16)	16.1(7)
10	0.9(1)	3.8(1)	11.8(4)	131(4)
	85.7(3)	8.5(1)	3.8(1)	2.0(1)
	14.3(5)	59.4(15)	26.6(15)	14.0(25)
15	0.8(1)	3.3(1)	10.7(4)	119(1)
	86.3(3)	8.0(1)	3.9(1)	1.8(0)
	13.7(3)	58.4(16)	28.5(16)	13.1(0)

of oPs (from 40.8% to 22.5%) was observed with increasing $c_{\text{Brønsted}}$ (Figure 6.14, Table 6.7). Another comparable trend is the substantial drop in I_{mic} , from 9.5% in ZC1000 to 1.6% in ZC15, indicating that the general response of oPs with $c_{\text{Brønsted}}$ occurs irrespective of crystal size. More notable discrepancies between the large crystal and commercial samples occur in the lifetime values for oPs. However, the fitting procedure of these components can be influenced by the corresponding low intensity and a higher level of out diffusion [51, 197].

The impact of Lewis Acid Centers alters from the Brønsted analogue. Lewis acidity can be introduced in zeolites in different ways. A major factor limiting the understanding of the effect of Lewis acidity from previous studies is that the majority of samples studied contained both Brønsted and Lewis acid sites, and the latter were primarily related to extra framework aluminium species the structure of which was poorly characterized.

A more elegant approach to quantify the potential influence of Lewis acid sites is to prepare a purely Lewis acidic material, which in MFI can be readily achieved through the introduction of tin into the framework while preserving a similar crystal size and coffin-shaped morphology (Sn-MFI, Table 6.3, Figure 6.15). Comparison with Sil as a non-acidic reference, a substantial drop in intensity was observed in the PALS spectra acquired for Sn-MFI (Figure 6.16). This observation is reflected in the fitted I_{oPs} values with ca. 42% loss compared to Sil (Table 6.8). Remarkably, inspection of the lifetime and intensity values of the

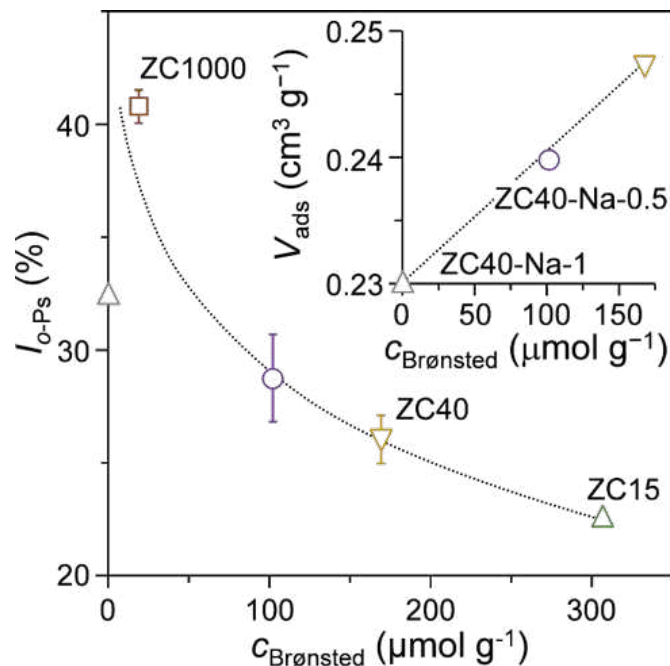
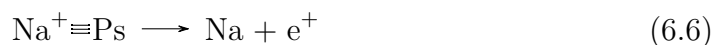


Figure 6.14: Total measured intensity of oPs as a function of the concentration of Brønsted acid centers for the commercial samples. The inset shows the correlation of V_{ads} with $c_{Brønsted}$ for ZC40, ZC40-Na-0.5, and ZC40-Na-1. Reprinted with permission from [65]. Copyright 2018 American Chemical Society.

individual components show negligible variation across the energies studied, suggesting that the presence of tin in the framework has a uniform effect on oPs annihilation. This indicates a difference in the mechanism of interaction with Brønsted and Lewis acid centres.

Possible hypotheses for this behaviour are discussed later in this paper. The influence of Lewis acid centres was extended to the commercial materials by introducing tin centres into ZC1000 via alkaline-assisted stannation (ZC-Sn), leading to an observable increase in c_{Lewis} (Table 6.3) [195]. Unlike Sn-MFI, ZC-Sn also exhibits a low concentration of Brønsted acid sites due to the presence of a small amount of aluminium. From the PALS analysis (Table 6.9), the introduction of Lewis acidity considerably reduces the amount of oPs detected compared to ZC1000 (ca. 49% at 5 keV). The observed drop is comparable to that evidenced between Sil and Sn MFI at 5 keV (ca. 42%), further confirming the strong effect of Lewis acid centres on the PALS response.

A common strategy for the elimination of Brønsted acid centres in zeolites is the exchange of acidic protons with cationic species such as Na^+ . Goldanskii et al. proposed that, in terms of positron measurements, the reaction;



in silica and alumina gels is endothermic and therefore plays no role in the oxidation of oPs [183].

Similar findings have also been reported from the study of different forms of a

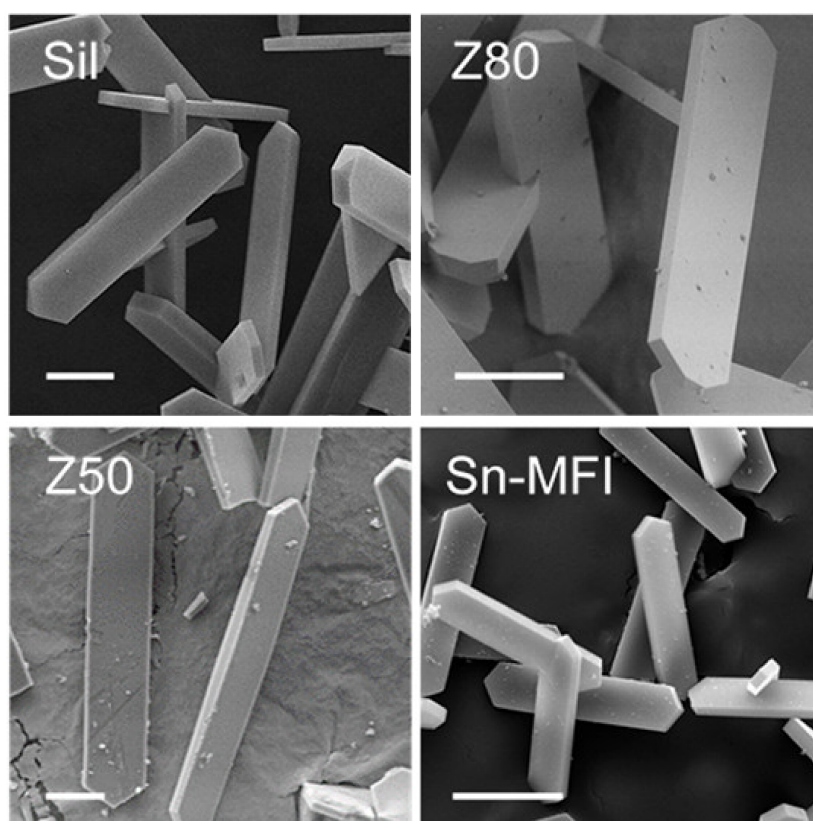


Figure 6.15: Scanning electron micrographs of selected zeolites and acidity characterization. The scale bar in all micrographs represents 5 μm . Adapted with permission from [65]. Copyright 2018 American Chemical Society.

Table 6.7: PALS results of acidity study on commercial and ion exchanged zeolites at $E_{e^+} = 5$ keV implantation energy. Lifetimes and intensities associated with pPs and e^+ are grouped under *not oPs* (\overline{oPs}) annihilation, oPs is divided into micropores (mic), mesopores (mes), inter crystalline (inc) and vacuum (vac), total oPs fraction $I_{oPs} = I_{mic} + I_{mes} + I_{vac} = 1 - I_{\overline{oPs}}$ and normalized oPs components I_{oPs}^e , i.e., $I_{mic}^e = I_{mic}/I_{oPs}$. Adapted with permission from [65]. Copyright 2018 American Chemical Society.

Sample	$\tau_{\overline{oPs}}$ (ns)	τ_{mic} (ns)	τ_{mes} (ns)	τ_{inc} (ns)	τ_{vac} (ns)
	$I_{\overline{oPs}}$ (%)	I_{mic} (%)	I_{mes} (%)	I_{vac} (%)	
	I_{oPs} (%)	I_{mic}^e (%)	I_{mes}^e (%)	I_{inc}^e (%)	I_{vac}^e (%)
ZC1000	0.8(1)	2.4(1)	7.3(2)	54.5(38)	133(1)
	59.2(4)	9.5(1)	6.4(3)	3.8(4)	21.1(3)
	40.8(7)	23.3(7)	15.7(7)	9.3(10)	51.7(7)
ZC40	0.8(1)	5.0(3)	17.0(22)	34.3(32)	120(4)
	73.9(2)	6.3(4)	6.0(5)	7.2(8)	6.6(4)
	26.1(10)	24.1(15)	23.0(18)	27.6(29)	25.3(15)
ZC15	0.8(1)	6.5(2)	-	56.4(31)	133(1)
	77.5(11)	1.6(0)	-	2.5(2)	18.4(2)
	22.5(3)	7.1(0)	-	11.1(9)	81.8(9)
ZC40-Na-0.5	0.9(1)	4.3(4)	12.7(9)	53.9(88)	132(8)
	71.9(2)	6.5(5)	6.5(7)	6.8(9)	9.3(13)
	29.1(18)	22.3(17)	22.3(24)	23.4(31)	32.0(45)
ZC40-Na-1	0.7(1)	3.0(1)	10.5(5)	40.5(2)	104(1)
	67.7(1)	9.0(1)	2.4(1)	14.6(1)	6.4(0)
	32.4(2)	27.8(3)	7.4(29)	45.1(3)	19.8(0)

FAU-type zeolite Y (Na^+ , NH_4^+ , and H^+), where it was proposed that Brønsted acid centres favour the formation and annihilation of oPs at the pore surface of the zeolite, leading to shortening of the lifetime [188]. A considerable increase in the intensity of oPs annihilation has also been reported upon sodium exchange of a zeolite Y sample [198]. The preceding studies primarily focused on the chemical reaction between oPs and an acid centre and therefore the discussion often did not consider the effects on oPs out-diffusion and the implications for porosity assessment by PALS.

To address this, the Z50 sample was fully exchanged with sodium (Z50-Na, Table 6.3). The absence of Brønsted acidity was confirmed by IR spectroscopy of adsorbed pyridine (Table 6.3). PALS analysis of the exchanged sample indicates a similar distribution of components as in the Brønsted acidic Z50 (Table 6.10). As expected, the removal of Brønsted acid centres led to an increase in I_{oPs} across all the studied energies. Nonetheless, the values remain substantially lower than Sil suggesting that the removal of Brønsted acid centres by ion exchange does not fully recover the acid-site free values. Interestingly, the measured I_{oPs} are comparable to those observed for Sn-MFI pointing towards a similar influence of the distinct Lewis acid centre (Na^+ vs. framework Sn). Considering the individ-

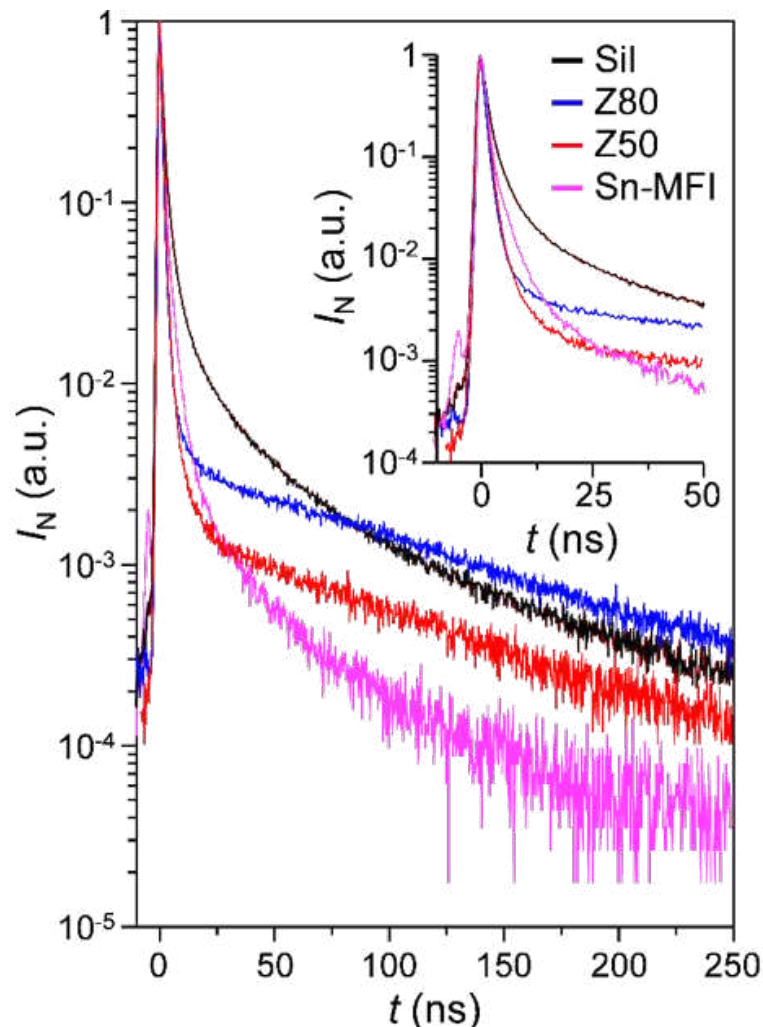


Figure 6.16: Positron annihilation lifetime spectra of Sil, Z80, Z50, and Sn-MFI collected with the BaF₂ detector at 5 keV incident positron energy, normalized to the intensity of the prompt peak at 0 ns. The inset shows a zoom of the prompt peak. Reprinted with permission from [65]. Copyright 2018 American Chemical Society.

ual components, Z50-Na displays a marked increase in I_{mic} , which constitutes ca. 83 % of the total oPs measured compared to ca. 57 % for Z50. Comparatively, the increase in I_{mic} for Z50-Na (19.1 % at 3 keV to 29.7 % at 10 keV) is more significant than that observed for Sn-MFI, which is steady at ca. 27 % from 5 keV upwards.

This could suggest the presence of sodium in the micropore volume impedes the diffusion of positronium, increasing the extent of oPs annihilation in the micropore. A series of sodium-exchanged ZC40 samples were also prepared where the Brønsted acid centres were partially (ZC40-Na-0.5) or fully (ZC40-Na-1) exchanged (Table 6.3). Consistent with the progressive incorporation of the larger sodium cations, a linear correlation was observed between V_{ads} and $c_{\text{Brønsted}}$ (Figure 5). As with the Z50-Na sample, the partial or full exchange of Brønsted acid centres led to an overall increase in I_{oPs} , but the values remained lower than ZC1000 (Figure 6.14, Table 6.7). However, τ_{mic} dropped from ca. 5 ns in ZC40

Table 6.8: PALS results of acidity study Sn-MFI zeolite at different implantation energies E_{e^+} . Lifetimes and intensities associated with pPs and e^+ are grouped under *not oPs* ($\circ\mathcal{P}s$) annihilation, oPs is divided into micropores (mic), mesopores (mes) and vacuum (vac), total oPs fraction $I_{\text{oPs}} = I_{\text{mic}} + I_{\text{mes}} + I_{\text{vac}} = 1 - I_{\circ\mathcal{P}s}$ and normalized oPs components I_{oPs} , i.e., $I_{\text{mic}}^{\ominus} = I_{\text{mic}}/I_{\text{oPs}}$. Adapted with permission from [65]. Copyright 2018 American Chemical Society.

E_{e^+} (keV)	$\tau_{\circ\mathcal{P}s}$ (ns)	τ_{mic} (ns)	τ_{mes} (ns)	τ_{vac} (ns)
	$I_{\circ\mathcal{P}s}$ (%)	I_{mic} (%)	I_{mes} (%)	I_{vac} (%)
	I_{oPs} (%)	I_{mic}^{\ominus} (%)	I_{mes}^{\ominus} (%)	I_{vac}^{\ominus} (%)
3	0.9(1)	2.8(1)	10.0(0)	102(1)
	75.7(7)	12.5(6)	8.1(1)	3.7(1)
	24.3(6)	51.4(25)	33.4(4)	15.2(5)
5	0.9(1)	3.5(2)	12.4(6)	115(1)
	81.4(4)	10.6(2)	5.0(3)	3.0(1)
	18.6(4)	57.0(11)	26.9(16)	16.1(7)
10	0.9(1)	3.8(1)	11.8(4)	131(4)
	85.7(3)	8.5(1)	3.8(1)	2.0(1)
	14.3(5)	59.4(15)	26.6(15)	14.0(25)
15	0.8(1)	3.3(1)	10.7(4)	119(1)
	86.3(3)	8.0(1)	3.9(1)	1.8(0)
	13.7(3)	58.4(16)	28.5(16)	13.1(0)

to 3 ns for ZC40 Na-1, which is closer to the micropore value observed in the larger crystal, further suggesting that the presence of sodium may impede out-diffusion of oPs and slightly mitigate the larger kinetic effects observed for the small crystals.

Discussion

An overview of the relative effects of Brønsted and Lewis acidity can be obtained by comparing the trends in oPs intensity of the large crystal zeolites with implantation depth after normalization to the values measured at 5 keV ($I_{\text{oPs},N} = I_{\text{oPs}}/I_{\text{oPs},5\text{keV}}$, $I_{\text{mic},N} = I_{\text{mic}}/I_{\text{mic},5\text{keV}}$, $I_{\text{out},N} = I_{\text{out}}/I_{\text{out},5\text{keV}}$). Note that the values measured at 3 keV are not used due to the non-negligible contribution of backscattered positrons and positronium at this energy.

Consistent with its non acidic character, minor variation in $I_{\text{oPs},N}$ is observed for Sil (Figure 6.17a). Comparatively $I_{\text{mic},N}$ also stays fairly constant (Figure 6.17b), while $I_{\text{out},N}$ exhibits a slight drop (Figure 6.17c). The variation in $I_{\text{out},N}$ confirms that some oPs are confined within and diffusing through the micropores, and thus the probability of escape from the crystal decreases with increasing implantation depth. An associated increase in I_{mic} is not obvious from the normalized trends due to the significantly higher absolute values with respect to I_{out} . Considering Z80 and Z50 i.e., the samples with high Brønsted acidity, a marked drop in $I_{\text{mic},N}$

Table 6.9: PALS results of acidity study ZC-Sn zeolite at different implantation energies E_{e^+} . Lifetimes and intensities associated with pPs and e^+ are grouped under *not oPs* (\cancel{oPs}) annihilation, oPs is divided into micropores (mic), mesopores (mes), inter crystalline (inc) and vacuum (vac), total oPs fraction $I_{oPs} = I_{mic} + I_{mes} + I_{vac} = 1 - I_{\cancel{oPs}}$ and normalized oPs components I_{oPs} , i.e., $I_{mic}^{\ominus} = I_{mic}/I_{oPs}$. Adapted with permission from [65]. Copyright 2018 American Chemical Society.

E_{e^+} (keV)	$\tau_{\cancel{oPs}}$ (ns)	τ_{mic} (ns)	τ_{mes} (ns)	τ_{inc} (ns)	τ_{vac} (ns)
	$I_{\cancel{oPs}}$ (%)	I_{mic} (%)	I_{mes} (%)	I_{vac} (%)	
	I_{oPs} (%)	I_{mic}^{\ominus} (%)	I_{mes}^{\ominus} (%)	I_{inc}^{\ominus} (%)	I_{vac}^{\ominus} (%)
3	0.7(1)	5.1(4)	19.7(18)	68.0(53)	142(0)
	77.4(209)	4.3(2)	6.3(4)	10.8(9)	1.3(4)
	22.7(11)	18.9(10)	27.8(19)	47.6(42)	5.7(2)
5	0.7(1)	6.2(1)	-	45.9(7)	100(1)
	79.0(0)	6.0(1)	-	11.3(2)	3.7(1)
	21.0(2)	28.6(4)	-	53.8(7)	17.6(6)
7.5	0.6(1)	4.9(2)	18.2(8)	45.7(25)	101(1)
	78.9(1)	4.9(1)	5.9(3)	6.9(4)	3.4(3)
	21.1(6)	23.2(7)	28.0(14)	32.7(18)	16.1(13)
10	0.6(1)	4.0(4)	15.2(11)	50.3(8)	132(14)
	79.6(2)	3.7(3)	6.8(2)	8.5(7)	1.4(1)
	20.4(12)	18.1(14)	33.3(9)	41.7(37)	6.9(44)

is observed with respect to Sil (Figure 6.17b). This trend is less exaggerated for Z50 due to the already low absolute value of I_{mic} at 5 keV. Interestingly, the trend of $I_{out,N}$ is comparable to Sil (Figure 6.17c).

In the case of the Lewis acidic samples, Sn-MFI and Z50-Na are found to display very similar behavioural trends, despite the significant distinctions in absolute intensity values. A slight increase in I_{mic} with incident energy for Z50-Na likely relates to the impeded diffusion of oPs in the micropore due to the presence of sodium cations but would require further investigation to confirm.

To explain the observed trends, it is necessary to consider the mechanisms of oPs formation, thermalization, and diffusion. As illustrated in Figure 6.18, the formation of positronium in materials is described by the Spur model [48, 49], which proposes that high energy positrons implanted into the material collide with atoms in the framework, ionizing electrons along its path. The generation of positronium can be defined as;



where A represents an atom in the solid. The energy required to form positronium will be dependent on the ionization potential of A and the binding energy of positronium. Thus, a fraction of the positrons are unable to form positronium and annihilate with a lifetime < 1 ns. The remaining positrons can capture an ionized electron at a *terminal spur* and form pPs or oPs, which will dissociate

Table 6.10: PALS results of acidity study Z50-Na zeolite at different implantation energies E_{e^+} . Lifetimes and intensities associated with pPs and e^+ are grouped under *not oPs* (\overline{oPs}) annihilation, oPs is divided into micropores (mic), mesopores (mes) and vacuum (vac), total oPs fraction $I_{oPs} = I_{mic} + I_{mes} + I_{vac} = 1 - I_{\overline{oPs}}$ and normalized oPs components I_{oPs} , i.e., $I_{mic}^{\ominus} = I_{mic}/I_{oPs}$. Adapted with permission from [65]. Copyright 2018 American Chemical Society.

E_{e^+} (keV)	$\tau_{\overline{oPs}}$ (ns)	τ_{mic} (ns)	τ_{mes} (ns)	τ_{vac} (ns)
	$I_{\overline{oPs}}$ (%)	I_{mic} (%)	I_{mes} (%)	I_{vac} (%)
	I_{oPs} (%)	I_{mic}^{\ominus} (%)	I_{mes}^{\ominus} (%)	I_{vac}^{\ominus} (%)
3	1.1(0)	3.1(1)	25.1(6)	127(0)
	74.9(2)	19.1(2)	1.6(0)	4.4(10)
	25.1(2)	76.1(8)	6.4(0)	17.5(5)
5	0.8(1)	2.7(1)	16.2(5)	126(1)
	71.8(2)	23.8(2)	1.3(1)	3.1(1)
	28.2(2)	84.4(7)	4.6(1)	11.0(4)
7.5	0.8(1)	2.6(1)	15.2(7)	126(1)
	70.8(4)	25.3(3)	1.4(1)	2.5(1)
	29.2(3)	86.6(10)	4.8(2)	8.6(5)
10	0.7(1)	2.6(1)	12.3(2)	100(1)
	64.8(28)	29.7(16)	3.1(10)	2.4(2)
	35.2(53)	84.4(45)	8.8(28)	6.8(6)

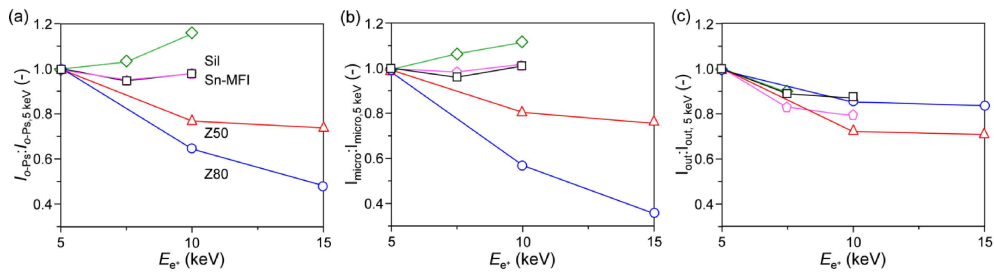


Figure 6.17: Variation in (a) I_{oPs} , (b) I_{mic} , and (c) I_{out} with the energy of the incident positrons for Sil, Z80, Z50, and Sn-MFI. Each intensity set is normalized to the intensity value obtained at 5 keV. Reprinted with permission from [65]. Copyright 2018 American Chemical Society.

following the expression;



$$\Delta H_{\text{dis}} > 0 \quad (6.9)$$

where H_{dis} is the enthalpy of positronium dissociation. For this study, pPs is considered to be <1 ns and is included in a single fitted component along with positron direct annihilation. Ortho-positronium may be formed in two different populations, namely high energy oPs that is localized within the pores (I_{local}), and low energy delocalized (Bloch State) oPs in the ground state (I_{delocal}) [149]. The latter has very long diffusion lengths with respect to the point of formation [53, 149] and is the main contributor to the out-diffused component (I_{out}), but may also annihilate within the micropore ($\tau_{\text{micro}} = \text{ca. } 3 \text{ ns}$) [149]. High-energy localized oPs will thermalize in the pore and a majority will annihilate within the micropore. The oxidation of positronium (pPs and oPs) by a Brønsted acid center has been previously defined in Equation 6.5 and the enthalpy of positronium oxidation ($\Delta H_{\text{B,ox}}$) is defined as;

$$\Delta H_{\text{B,ox}} = \Delta H_{\text{dis}} + \Delta H_{\text{red}} \quad (6.10)$$

where ΔH_{red} is the enthalpy of acid reduction. If the energy required to reduce the Brønsted acid centre is greater than for the dissociation of positronium ($\Delta H_{\text{B,ox}} < 0$) then Equation 7 is favourable and positronium is readily oxidized. However, if $\Delta H_{\text{B,ox}} > 0$ then positronium will require a certain kinetic energy (E_{Ps}) to overcome this threshold of interaction. Additionally, if this process can happen after many collisions, at a time consistent with the expected lifetime within the MFI framework (ca. 2.5–3 ns), then the observed τ_{mic} would be expected to decrease with increasing acid concentration. However, no such dependence is observed (Table 6.46.66.5).

A proposed explanation is that localized oPs enter the pore with a few eV of energy [12] and quenching occurs before it makes many collisions. The following relation can be drawn;

$$E_{\text{out}} \leq \Delta H_{\text{B,ox}} \leq E_{\text{mic}} \quad (6.11)$$

It is also possible that high-energy localized positronium is able to sufficiently thermalize below the energy threshold, introducing additional paths for annihilation within the micropore and out diffusion (Figure 6.18). However, as the trends in I_{out} are similar for all samples (Figure 6.17c), these fractions are considered to be small. An equivalent expression to Equation 6.11 for a Lewis acid centre is more difficult to propose as all positronium intensities are diminished. This suggests a direct impact on the positronium formation process either by scavenging spur electrons that would normally be available for the positron to interact or by scavenging positrons themselves (Figure 6.18).

For a comprehensive understanding of zeolite assessment, it will be inevitable to decouple porosity and acidity effects. The previous application of PALS to probe pore connectivity in zeolites was primarily based on the assessment of the normalized fraction of out diffused oPs ($C_{\text{pore}} = I_{\text{out}}/I_{\text{oPs}}$) [17]. Considering the identified impacts, correction for the effects of Brønsted and Lewis acidity will be essential for the precise quantification of pore architecture.

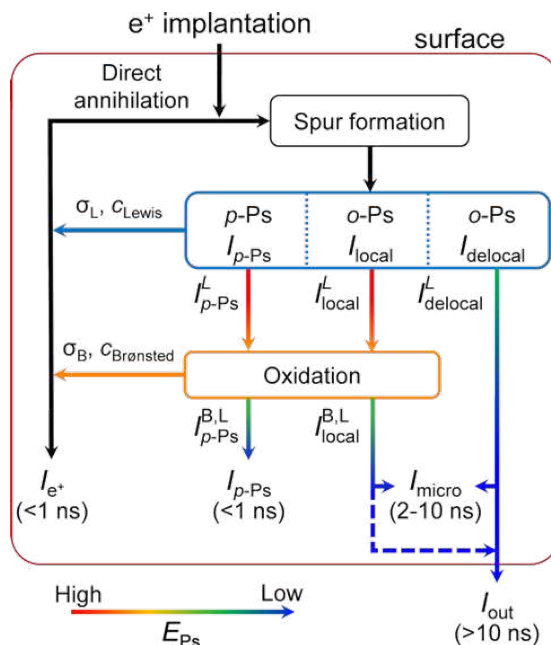


Figure 6.18: Schematic representation of positronium formation and the various annihilation paths in zeolites. After thermalization, most positrons directly annihilate with the solid, but a small fraction form positronium in para- or ortho- spin states. The presence of Brønsted and Lewis acid sites have distinct impacts. The former reduces the amount of oPs by oxidation of high energy localized positronium (I_{local}) in the micropores, while the latter suppresses the formation of positronium. The colour scale indicates the estimated kinetic energy of positronium. Reprinted with permission from [65]. Copyright 2018 American Chemical Society.

In the presence of Brønsted acid sites, the fact that the oxidation only impacts localized high-energy oPs is advantageous as it means that the diffusion through and sampling of the micropore network is unaltered. However, the differing effects on I_{mic} and I_{out} cause variations in C_{pore} unrelated to pore structure.

Fortuitously, in the case of purely Lewis acidic materials, assuming that the acid centres are homogeneously distributed and therefore suppress oPs formation uniformly throughout the sample, they should not affect the determination of C_{pore} . However, as outlined below, accounting for the reduced formation of oPs may be necessary if mixed with Brønsted acid sites.

In this regard, cation exchange with small alkali metals such as sodium can be a good strategy to avoid the need for correcting for Brønsted acidity, but the species introduced should not significantly impede oPs diffusion and therefore the effectiveness will be greater for large and medium-pore zeolites. Looking towards correcting for the effects of Brønsted and Lewis acidity, models have been proposed for the effect of electrons scavengers in other materials on oPs formation [199, 200]. As Lewis acidity was seen to effect both I_{mic} and I_{out} equally (Figure 6.17), the following expressions are proposed:

$$\begin{aligned}
 I_{\text{out}}^{\text{L}} &= I_{\text{out}}^0 / \left(1 + (\sigma_{\text{L}} c_{\text{Lewis}})^{\alpha}\right) \\
 I_{\text{mic}}^{\text{L}} &= I_{\text{mic}}^0 / \left(1 + (\sigma_{\text{L}} c_{\text{Lewis}})^{\alpha}\right)
 \end{aligned}
 \tag{6.12}$$

where $I_{\text{out}}^{\text{L}}$ and $I_{\text{mic}}^{\text{L}}$ are the intensities of the out-diffused and micropore oPs respectively in the presence of Lewis acidity, I_{out}^0 and I_{mic}^0 are the intensities without acid sites, σ_{L} is the electron scavenging co-efficient, and α is a fitting parameter.

From Figure 6.18, the oxidation of high energy positronium by Brønsted acidity is described by the coefficient σ_{B} . Provided that the quenching of positronium in the micropore depends on the probability of interacting and annihilating with a Brønsted acid site, it is expected that I_{mic} will depend exponentially on σ_{B} and $c_{\text{Brønsted}}$:

$$I_{\text{mic}}^{\text{B,L}} = I_{\text{mic}}^0 / \left(1 + (\sigma_{\text{L}} c_{\text{Lewis}})^{\alpha}\right) \times e^{-\sigma_{\text{B}} c_{\text{Brønsted}}} + I_{\text{B}}
 \tag{6.13}$$

where $I_{\text{mic}}^{\text{B,L}}$ is the intensity of oPs after interacting with the acid sites and I_{B} is the asymptotic intensity observed at high $c_{\text{Brønsted}}$. Given that the majority of out-diffused positronium is thought to originate from the delocalized Bloch state, which has a too low energy to interact with the Brønsted acidity, the impact on $I_{\text{out}}^{\text{L}}$ is negligible and can be ignored. Thus, the measured out diffused intensity $I_{\text{out}}^{\text{L}} = I_{\text{out}}^{\text{L}}$ and the micropore intensity $I_{\text{mic}} = I_{\text{mic}}^{\text{B,L}}$ (Equation 6.12).

As a preliminary assessment, the data for the large-crystal Sil, Z80, Z50, Sn-MFI, and Z50-Na obtained at 5 keV and 10 keV have been fitted simultaneously using a least-squares fitting routine obtaining correlations between I_{out} and c_{Lewis} (Figure 6.19a) and I_{mic} with $c_{\text{Brønsted}}$ and c_{Lewis} (Figure 6.19b and Figure 6.20). Considering the different trends observed for I_{out} and I_{mic} (Figure 6.17), σ_{B} has been fitted independently at different incident positron energies, whereas σ_{L} has been kept constant. Additionally, fitting of the α parameter obtained a value of 0.5, which is consistent with previous literature [199, 200]. Due to the limited data set the fits have large 90% confidence bands and so interpretation remains qualitative.

In general the experimental and the estimated trends show good agreement and similar profiles are observed at both energies. The proposed model stresses the possible implications of acidity in interpreting PALS results in zeolites. A larger sample series is required to further parametrize the multiple system variables that can influence the PALS response with sufficient confidence. For example, it was not possible to unite the trends for the large-crystal and commercial samples. An improved description of kinetic effects requires a better understanding of the impacts of crystal size and morphology [51]. Although attaining reasonable quantitative trends, the broad definition of Brønsted and Lewis acidity in the current study does not consider variations in strength relating to the specific origin or possible heterogeneity in their distribution. It was also not yet possible to discriminate the relative fractions of localized and delocalized oPs.

Finally, it is noted that this study was possible due to the flexibility of synthesizing MFI-type zeolites with model acidity and equivalent porosity. While similar

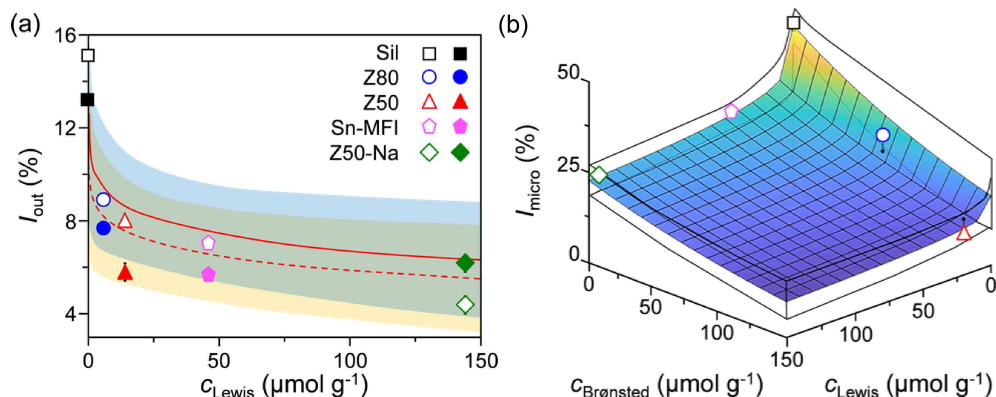


Figure 6.19: Application of the proposed numerical model to estimate the effect of (a) Lewis acidity on I_{out} at 5 keV (blank symbols), 10 keV (solid symbols), and (b) Brønsted and Lewis acidity on I_{mic} at 5 keV. The red lines in (a) indicate the average value from the model (solid = 5 keV, dashed = 10 keV) with the colored shaded regions representing the calculated error (blue = 5 keV, yellow = 10 keV) whilst the black frame in (b) indicate the estimated error. Reprinted with permission from [65]. Copyright 2018 American Chemical Society.

behaviour is expected for zeolites of different framework type, knowledge of the influence of the former factors (i.e., kinetic effects, acid strength, distribution etc.) and an improved understanding of topology effects on the delocalized state of oPs will be critical to fully interpret PALS measurements.

Summary

This study has quantified the relative effects of Brønsted and Lewis acidity on the analysis of zeolites by PALS. A series of MFI-type samples with controlled Brønsted and Lewis acidity were prepared with large crystal sizes to minimize the kinetic effects associated with oPs out-diffusion. The total amount of measured oPs was found to decrease with increasing acidity, irrespective of the nature of the acid sites. Deconvolution of the distinct annihilation events revealed that Brønsted acidity diminishes the amount of oPs annihilating in the micropore more than the number of longer-lived out-diffused components. This observation was attributed to the selective oxidation of high-energy positronium species in localized states within the micropore.

The study of tin-containing samples demonstrated that Lewis acid centres exhibit a stronger effect on the PALS response than Brønsted acid centres. However, the equivalent impact on all oPs components revealed that this resulted from suppressed positronium formation, likely due to either scavenging spur electrons from the positron thermalization process or scavenging positrons. The results were generalized by studying a series of commercial MFI type zeolites, where compatible trends were observed. Sodium exchange of the zeolites led to an increase in observed oPs but did not recover the values of the non-acidic sample due to the presence of Lewis acidity in this sample.

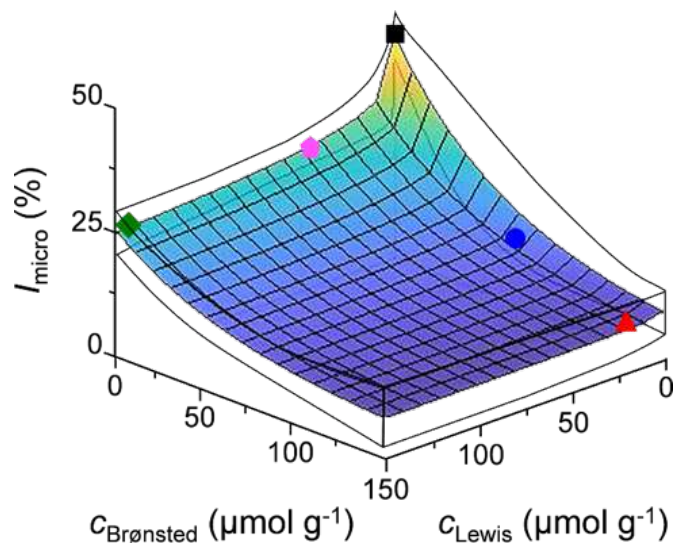


Figure 6.20: Application of the proposed numerical model to estimate the effect of Brønsted and Lewis acidity on I_{mic} at 10 keV. The black frame indicates the estimated error. Reprinted with permission from [65]. Copyright 2018 American Chemical Society.

The observed effects have direct implications for porosity analysis and require the development of a correction model. A first empirical attempt to account for the distinct impacts of Brønsted and Lewis acid centres considering the relative concentrations and interaction cross-sections with oPs obtained a reasonable description for the large-crystal samples but requires further parametrization to become generally applicable. In particular, the impacts of kinetic effects, acid strength, and zeolite framework type still need to be addressed. The ability to evaluate both the porosity and acidity of zeolites using positrons will widen the scope of the technique for the analysis of functional materials.

Chapter 7

Other Material Studies

In this chapter, studies to explore the potential of positronium annihilation on other materials with nano-porous networks are presented.

The specific class of SURface anchored Metal-Organic Framework (SURMOF)s could envisage the long-sought goal of a monoenergetic highly efficient Ps transmission formation target useful in fundamental Ps studies [201]. All state-of-the-art Ps converters operate in a reflection geometry. This puts constraints on the design of the experimental settings as the preparation of the positrons, which often requires electromagnetic fields, and the final experimental stage, e.g. laser spectroscopy of Ps in a preferably field-free region. A transmission geometry itself would allow to spacially separate the parts crucially simplifying detection schemes.

Another type of materials where PAS might give novel insights are nanocrystals [202]. Behaviours different from bulk, small individual building units with unique properties, high scalability and controllability makes it a very interesting topic [203–205]. Single site defects in a crystal, which is made of only some thousands of atoms, can have a huge impact on its properties. The interaction of crystals as a colloid or depending on the packing can give the ensemble novel characteristics [206]. The nm size-regime naturally calls for the potential application of PAS.

Moreover, in the wake of a metal annealing effort with the Laboratory for Nanometallurgy from the Institute of Metals Research, D-MATL, ETH, a small pilot project of defect assessment within thin metal films defect engineered for optoelectronic applications was launched.

At last, the known efficient positronium into vacuum productions of zeolites and MOFs applicable in fundamental research, e.g. spectroscopy study, and the correlation between positronium and muonium production into vacuum [207] lead to the study of carbon nanotubes as positronium and muonium conversion targets.

Specifically, studying the confinement and out-diffusion of Ps to asses the properties of . Therefore, multiple materials exhibiting pores, defects and voids in the nm-scale have been investigated through measurement and simulations.

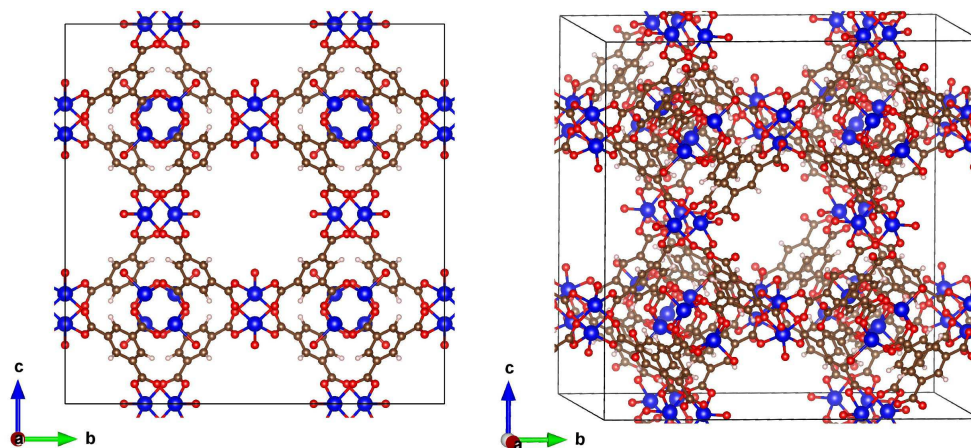


Figure 7.1: Unit cell structures of HKUST-1. Ball and stick model based on a cif file from Crystallography Open Database (COD) [211]

7.1 Surface Anchored Metal-Organic Frameworks

The material of SURMOFs is a controlled growth of MOFs (Section 5.2.1) on two dimensional surfaces. Specifically the layer-by-layer selective growth of thin-film SURMOFsheterostructures with functionalised components are receiving increasing attention as a novel form of nanotechnology [208]. While these highly ordered crystals have great potential as positron to positronium converters for fundamental physics [209], PAS could also help to tackle the current challenges of quantifying the role of defects in SURMOFs [145] and simplify the determination of porous heterostructures [210]. The different sized MOF cages should be visible as an implantation energy dependence on the oPs lifetime, i.e. different decay constants attributed to the geometries will appear with different intensities in the PALS spectra.

The most common structure is hereby the HKUST-1, a $\text{Cu}_2(\text{BDC})_2$ complex. Two copper ions form a metal cluster from where two benzenedicarboxylate (BDC) organic linker molecules form the bonds. A ball and stick depiction of the structure is shown in Figure 7.1

To investigate the application of PAS to the class of SURMOFstwo different structures were measured with the PALS spectrometer, a HKUST-1 and a heterostructure (Cu-NDC-SURMOF-2 on Cu-BDC-SURMOF-2). The samples were prepared by the Karlsruhe Institute of Technology (KIT). Because MOFs, in general, tend to be very hygroscopic a glove bag¹ was used to unpack and mount the samples in the beam. The bag was sheathed over the beam port and exposed to a constant flow of N_2 throughout the experimental chamber to keep the bag inflated and to drive away any air leaking through the seals. Each SURMOF was received on a Si substrate bonded through a layer of gold. The substrates were fixed on the sample mount with a drop of silver glue to ensure conductivity.

¹AtmosBag, four-hand, non-sterile, size L, closure type, Zipper-lock, Sigma-Aldrich

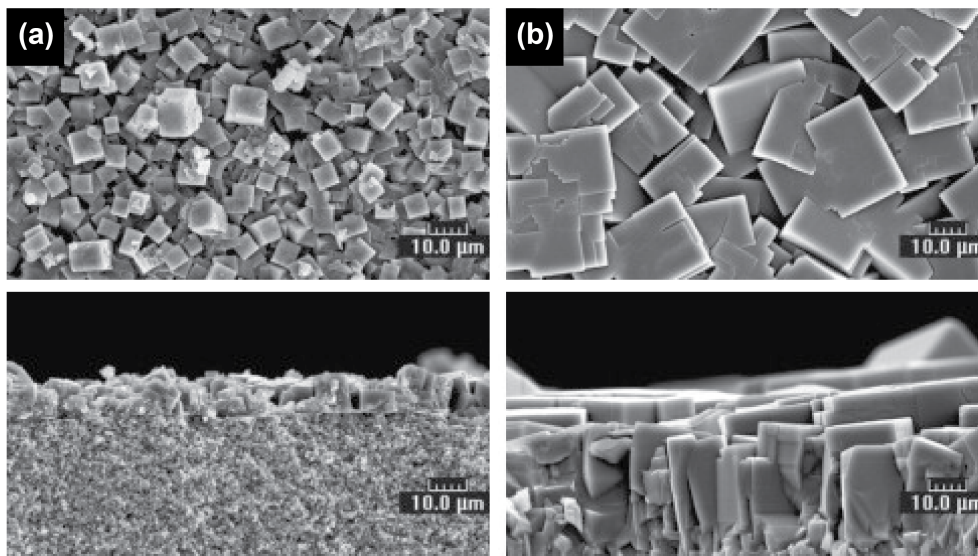


Figure 7.2: SEM images of top views (upper) and cross-sections (lower) of (a) a MOF-5 seed layer and (b) a continuous MOF-5 membrane during secondary growth for 9 h. Reprinted with permission from [212]. Copyright 2009, Elsevier.

As observed for several nanocrystals, the SURMOF samples had a similar high uncorrelated spontaneous electron background. It is believed that the edges of the substrates used to mount the samples exhibit high field gradients under high voltage and tend to emit electrons. From the experience with other MOFs, the IRMOF dataset studied at ETH in 2013 [53], it was expected to see a considerable fraction of oPs in delocalized states and emission into vacuum. Furthermore, positronium occupying Bloch states which exit into vacuum is thought to be primarily emitted perpendicular to the surface [53, 54]. In fact, the Ps emission distribution should resemble the more populated high symmetry points of the band structure, having preferred momenta. Grainy samples with a wild mix of crystallographic orientations will smear this into a cosine distribution [53]. The resulting emission of oPs with only thermal energy spread can e.g. help to reduce systematics in spectroscopy coming from a moving atom interacting with the laser beam.

However, a perfectly large crystal with a single surface should reveal such behaviour. SURMOFs are usually patches of large crystals on the $\sim\mu\text{m}$ scale with one crystallographic axis perpendicular to the substrate surface. The discrete emission patterns expected from each single surface are therefore randomly rotated around the surface normal. Provided the positron beam spot is small enough the emission into vacuum should, therefore, exhibit a multi cone distribution. The narrow energy spread expected for each such cone could be potentially very interesting for fundamental research using positronium, i.e., anti hydrogen based experiments or spectroscopy studies.

Unexpectedly the PALS data did not show large amounts of oPs, a total fraction of less than 5% was measured. Reconsidering the unit cell structure shown in Figure 7.1 and comparing it to the IRMOF, Figure 5.2, one difference is salient.

While the electron-rich atoms known for increased oPs pick-off and quenching like the metals and oxygen are focused in the nodes hidden behind the linkers in IRMOFs, they are heavily exposed in HKUST-1. Even though a classic pore size approach would have suggested large voids for positronium confinement with ns lifetimes, it is the more detailed view of the pore-forming atoms that define the observable lifetime. With the availability of the IRMOF-1 framework grown as a SURMOF structure [212, 213] a study based on the known high oPs production from bulk samples [53] is envisaged.

7.2 Nanocrystals

The compositional tunability of multicomponent chalcogenide thin films and the ordering of atoms enables novel functionality, leading to successful photovoltaic [205], piezoelectric [206], thermoelectric [214] and resistive phase-change memory applications [215]. PAS results are hereby employed for the fundamental characterization of the existence and impact of small defects in a Cu-(Zn)-In-Se system. Moreover, the precise packing of NanoCrystals (NC) is still an ambiguity.

Nanocrystals are usually suspended in a shell of organic linkers making them appear as fuzzy balls. Novel types of linkers and the exchange from one type to another has lead to some disambiguity on the resulting packing. With a study of two different sized Pb-S samples, the effect of linker exchange on the PALS response is looked at. After a proof of concept study with two Ge-Te samples, it is planned to assess the temperature-dependent packing by looking at the void sizes created during a phase transition with PAS.

7.2.1 Cu-Zn-In-Se Nanocrystals

The subjects of investigation are colloidal nanoparticles, crystallites about 3.3 nm in size (about 800 atoms in total) that have a chalcopyrite crystal structure with a certain amount of atomic vacancies in the cationic sublattice prepared by the MAterials Device Engineering group (MADE) led by Prof. Vanessa Woods (ETH). The composition of nanoparticles is Cu-Zn-In-Se. The vacancy concentration varies between 1 and 10 at.% as a function of composition (ratio between Cu, Zn, and In). Each colloidal nanoparticle is surrounded by a layer of organic surfactant (trioctylphosphine, coverage density of 1-4 molecules per nm² of nanoparticle surface). This *ligand shell* enables colloidal stability of material so concentrated solutions look like a dense coffee.

A typical PAS sample is prepared by drop-casting of concentrated colloidal solutions of Cu-Zn-In-Se nanoparticles from highly-volatile non-coordinating solvent, such as hexane. As a host substrate, a 20 × 20mm conductive Al sheet was covered with an NC thin film with a typical thickness of the order of 1-5 μm. The film consists of space-separated nanoparticles and organic ligands in between. A certain porosity within the film of nanoparticles is expected. These free spaces can be filled with either organics or can become a void. Also, the ordering of such

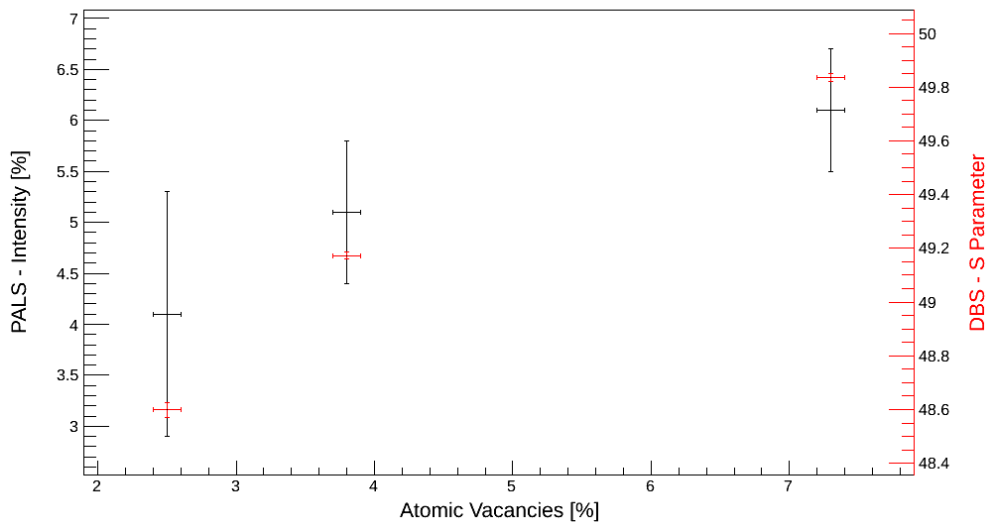


Figure 7.3: Cu-Zn-In-Se NC DBS and PALS results, presented in comparison. Reprinted with permission from [100].

film of nanoparticles is not perfect so there could be missing nanoparticles and larger voids as well.

PAS results for three Cu-Zn-In-Se nanocrystal samples with different expected vacancy concentrations (2.5 at.%, 3.8 at.%, and 7.3 at.%, shown in Figure 7.3, suggest that the vacancies consist of single missing atoms in the expected concentrations. From positron annihilation lifetime spectroscopy data, Table 7.1, shows a constant positronium lifetime of approximately 3 ns for all samples, indicative that the size of the void is the same for all compositions. Assuming a spherical shape, the estimated radius of the void to be approximately 3.8 Å, which is comparable to the size of a single missing atom [5]. The intensity of this lifetime increases proportionally with the expected concentration of cationic vacancies in the Cu-Zn-In-Se nanocrystals.

Accordingly, positron annihilation Doppler Broadening Spectroscopy conducted by Dr. Carlos Vigo, Figure 7.3, reveals an increasing shape parameter, S , (i.e., a narrowing of the annihilation peak) with increasing expected vacancy concentration (as explained in Section 2.2.3, a narrower annihilation peak corresponds to more vacancies). Table 7.1 shows the set of (I, τ) components for all samples. The first component can be identified as pPs annihilation, usually 125 ps, but since the time resolution of the system is of the order of 1 ns FWHM, the detector is not sensitive to such short lifetimes and 16 ps gave the best fit. The second component around 700–900 ps is assumed to be direct annihilation.

The lifetime τ_3 is for oPs pickoff annihilation in the defect volumes, and τ_4 is an oPs pickoff annihilation, associated with the interparticle volume. Figure 7.3 shows τ_3 intensity (which is related to oPs pick-off annihilation in defect volumes) dependency with expected atomic vacancies. Despite large errors due to low statistics, a correlation is visible. Comparing the DBS parameter and PALS intensities, a similar trend with expected atomic vacancies is found.

Table 7.1: PALS spectra fitting results of Cu-Zn-In-Se NC with different atomic vacancy concentrations, N_{vac} (atomic %).

Sample	N_{vac} (at. %)	τ_1 (ns) I_1 (%)	τ_2 (ns) I_2 (%)	τ_3 (ns) I_3 (%)	τ_4 (ns) I_4 (%)
m2130	7.3	0.016(1) 35(3)	0.770(12) 59(6)	2.42(4) 6.1(6)	40.7(19) 0.77(22)
m2215(1)	3.8	0.016(1) 50(13)	0.814(19) 44(10)	3.17(4) 4.9(13)	63(3) 0.77(17)
m2215(2)	3.8	0.016(1) 46.6(10)	0.769(14) 47(3)	3.08(3) 5.35(14)	50.6(12) 0.7(4)
m2215(mean)	3.8	0.016(1) 49(7)	0.791(12) 46(5)	3.13(3) 5.1(7)	57.0(17) 0.74(23)
Reference	2.5	0.015(0) 35(11)	0.692(12) 58(12)	2.64(4) 4.1(12)	141.9(3) 1.6(5)

While the results point towards a successful defect concentration assessment an ambiguity still to investigate is the contribution from the organic ligands. A possible scenario to explain the observed trends could also stem from a more efficient oPs production depending on a higher defect concentration on the surface of the NCs. With more surface oPs formed, a larger fraction of e^+ annihilate with the NCs surface and the space-filling organic ligands. The momentum from the electrons associated with this pickoff are on average lower than the ones inside the NC. Therefore, the S parameter would also increase, mimicking a higher defect concentration.

A study to address these issues is planned by using a PALS spectrometer with superior performance. If the existence of defects will be confirmed, this would prove that the underlying cationic ordering and vacancy engineering can be controlled in nanocrystals and would imply an immense emergence of opportunities for the tailorability of NCs.

7.2.2 Pb-S Nanocrystals

Nanocrystals are usually embedded in a matrix of organic linker molecules. In reality, they do not resemble a hard *sphere* but do actually look more like a *fuzzy ball*. Depending on the linker the packing and therefore properties of a nanocrystal ensemble may vary. In recent developments, not only novel nanocrystals but also ligand exchange was studied [216, 217]. For the Pb-S nanocrystals, the typical oleic acid was replaced with 1,2-Ethanedithiol as linker molecules as sketched in Figure 7.4. The structural change of the film properties is interesting for the application as solar cells. To make solar cells one would evaporate lithium fluoride and then aluminium on top. This electrode forms a Schottky junction with semiconducting PbS enabling the extraction of the charge carriers. The samples were prepared by W. Lin of the MADE group.

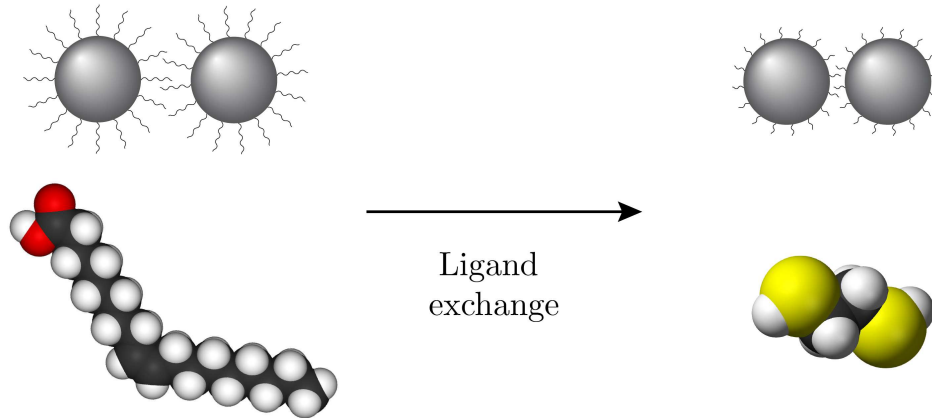


Figure 7.4: Sketch of the linker exchange from oelic acid to 1,2-Ethanedithiol molecules for colloidal Pb-S nanocrystals. In the chemical atomic models of the linkers white represents hydrogen, black carbon, red oxygen and yellow sulphur.

The goal of the conducted PAS study was to investigate the packing, i.e., the free volume between the NCs. For this purpose, two different nanocrystal sizes were measured. The data analysis was performed conjointly with visiting Prof. Rich Vallery, Grand Valley State University. A summary of the results is shown in Table 7.2. The best fits were achieved with four components using PAScual. Using more or less components lead to a much worse χ^2 . The for PAScual mostly typical small errors are the output of the Bayesian Inference algorithm but do, from experience, underestimate the true error. The lifetime τ_1 are the pPs (125 ps) and direct annihilation (< 1 ns) which merge into one component because the time resolution of the system is ~ 1 ns. Only using one component here gave the best fit. The second, third and fourth component are originating from oPs with different pick-off contribution.

Correlating the lifetimes with the extended Tao Eldrup model for a sphere geometry the diameters are 0.7 nm, 1.6–2.0 nm and 25–75 nm respectively. Compared to the previously discussed Cu-Zn-In-Se nanocrystals no defects are expected. The high intensity of the ~ 2 ns component either suggests otherwise or different phenomena are responsible for this decay channel. Since the linkers are different, one would not suspect the component originating from oPs trapped in the polymer forest of linkers. Another possibility might be that it is coming from copious formation on the surface of the NCs on which oPs can be trapped like observed for semiconductors [218].

The lifetime τ_3 and the corresponding 1.2–1.8 nm voids are believed to be empty spaces in the packing of NCs, i.e., missing crystals in the lattice. With a similar low intensity like I_3 , the longest component τ_4 , which is significantly lower than the oPs vacuum lifetime (142 ns), is addressed to a distribution of larger voids in the packing of the NC agglomerates and a very little fraction of actual vacuum oPs.

Looking at the trends with higher implantation energies some puzzling dependen-

Table 7.2: Fitting results τ_i and I_i of Pb-S NC PALS spectra of sample S1 and S2 at different positron implantation energies E_{e^+} .

Sample & NC radius	E_{e^+} (keV)	τ_1 (ns) I_1 (%)	τ_2 (ns) I_2 (%)	τ_3 (ns) I_3 (%)	τ_4 (ns) I_4 (%)
LW27-S1, 3 nm	5.0	0.318(6)	2.43(1)	17.2(3)	119(1)
		88.2(2)	9.9(2)	0.66(21)	1.2(2)
	7.5	0.568(3)	2.12(2)	19.1(11)	120(4)
		88.6(1)	10.2(1)	0.50(33)	0.75(2.9)
10.0	0.586(2)	1.84(1)	12.1(4)	115(2)	
	88.1(3)	11.0(1)	0.40(22)	0.50(1.0)	
LW27-S2, 1.2 nm	5.0	0.612(1)	2.29(2)	18.7(8)	121(3)
		89.6(1)	8.9(1)	0.56(13)	0.7(2.6)
	7.5	0.661(1)	2.34(1)	19.7(6)	132(4)
		93.0(2)	6.2(1)	0.39(21)	0.4(1.5)
10.0	0.641(2)	2.12(3)	14.1(1.0)	117(7)	
	93.6(1)	5.8(2)	0.30(20)	0.3(2.1)	

cies become eminent. For example, the I_2 is slightly increasing with higher energy for the S1 sample while it is decreasing for the S2. Because a clear correlation between the sizes of the two samples and the PALS response was not seen a more in-depth study of simpler systems was envisaged but not executed. Instead, a different nanocrystal species, Ge-Te, which should exhibit a more pronounced inter crystal space phase transition was favoured.

7.2.3 Ge-Te Nanocrystals

The class of Ge-Te nanocrystals have attracted widespread interest as candidates for a novel type of non-volatile information storage devices, high-k dielectrics, and other applications [219, 220]. For this purpose, the temperature properties regarding a phase shift are of particular interest. While the unit cell changes it is also expected that the NCs start to agglomerate or even merge effectively changing the intercrystalline volume. A proof of concept study with two samples was conducted. The samples were prepared by Weyde Lin of the MADE group by drop-casting them on a substrate and then subsequently heating one to 100 °C to remove all linker material and the other to 200 °C to induce the phase shift.

The PALS results at different energies are summarized in Table 7.3. On this dataset a different error analysis was used, which was shown by comparison with simulated data to have a better correlation to the limits of resolvability defined by the time resolution. This had a rather large impact on the uncertainty of the intensities I of the lower lifetimes, i.e., up to 50% for I_1 .

With this large errors at hand it is impossible to conclude a difference in the inter crystalline volume from the 100 °C sample to the 200 °C as also only the 3 keV data would suggest such, 1.5 ns versus 3.0 ns. Another point to raise is that no

Table 7.3: Fitting results of Ge-Te NC PALS spectra.

Sample	E_{e^+} (keV)	τ_1 (ns) I_1 (%)	τ_2 (ns) I_2 (%)	τ_3 (ns) I_3 (%)
100 °C	3.0	1.50(10)	9.3(7)	49(3)
		39(14)	13.3(10)	2.1(8)
	5.0	1.50(10)	11.0(15)	57(5)
		37(15)	0.97(21)	1.87(9)
	7.5	1.70(20)	12.0(25)	56(5)
34(18)		0.6(3)	1.76(9)	
10.0	1.4(10)	13.0(5)	66(5)	
200 °C	3.0	28(12)	1.03(13)	1.61(8)
		3.0(4)	12.5(15)	65(5)
	8(6)	1.6(6)	2.12(14)	
	5.0	1.50(10)	10.5(10)	58(6)
		34(13)	1.08(21)	1.83(9)
7.5	1.60(10)	9.0(5)	50(5)	
	15(5)	0.92(25)	1.84(12)	
10.0	1.50(10)	9.0(5)	54(4)	
		19(8)	0.90(21)	1.79(9)

vacuum component was observed. While the other nanocrystals showed at least a very weak one, the Ge-Te did not. The samples were particularly prominent in emitting uncorrelated spontaneous electrons through all energies resulting in a bad SNR, especially for low-intensity long lifetime components.

In that perspective, this sample would also benefit from a bunched beam elevated to the implantation energy rather than having to float the sample itself at the necessary potential. From that aspect, it was concluded to repeat the measurement on the secondary beamline on the buffer gas trap (see Section 3.4.2) or after installation of an elevator in the epic beam.

7.3 Defect Engineered Thin Copper Films

The group of Prof. R. Spolenak, the Laboratory for Nanometallurgy, is focussing with their research on size effects in materials. They deem to study how materials properties change as a function of the external length scale. The goal is to identify the size that optimizes material properties, such as yield or fracture strength, toughness, and also electronic properties. One established method for the characterization is to do resistance measurements. However, the interpretation is based on multiple assumptions, i.e. defect types and concentrations, which have not been experimentally confirmed.

Thin copper films were manufactured by Physical Vapor Deposition (PVD) with and without Ion Beam Assisted Deposition (IBAD) from the Laboratory for Nanometallurgy. The resulting thin films with different defects and defect dis-

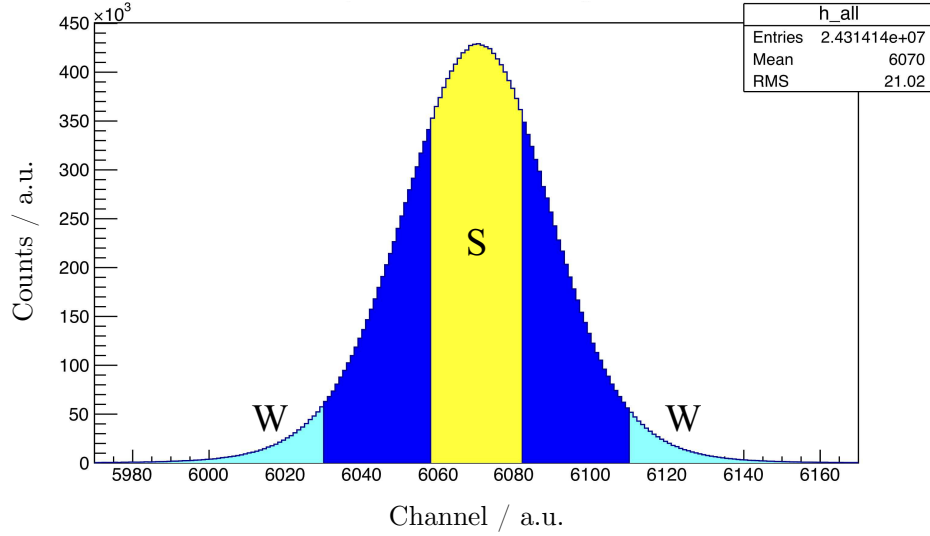


Figure 7.5: A DBS spectrum of the IBAD Cu thin film.

Table 7.4: Summary of the DBS measurements of the Cu thin film with and without IBAD.

Name	S-parameter	N	η (%)
Cu	49.880 ± 0.019	1.5×10^6	1.5
Cu IBAD	51.707 ± 0.015	1×10^6	1.4

tributions can have vastly different properties [221]. The samples are the basis for research into a new class of optoelectronic devices. Engineering these defects from the IBAD growth play a major role in the successful functionalising. In the perspective of positron based defect assessment via DBS a pilot study was conducted. The aim was to test the DBS sensitivity.

Figure 7.5 shows the 511 peak of the Cu sample DBS spectra highlighting the areas used to calculate the S parameter. It was not clear beforehand that positrons would reveal defects induced by the ion bombardment. PVD grown samples consist of many grains where a strong positron response to the boundaries was expected. However, the summary shown in Table 7.4 proves that PAS can assess a difference in the two samples.

Based on this a more elaborated study of a heterostructure with a depth profiling was planned but could not be conducted because of instrument failure at the positron beam.

7.4 Carbon Nanotubes

The highly specific tube structure solely made from carbon with nanometer-sized diameters called CNTs is a vibrant field of research since their discovery in the 1990s [222]. One can imagine the structure being a rolled-up graphene sheet

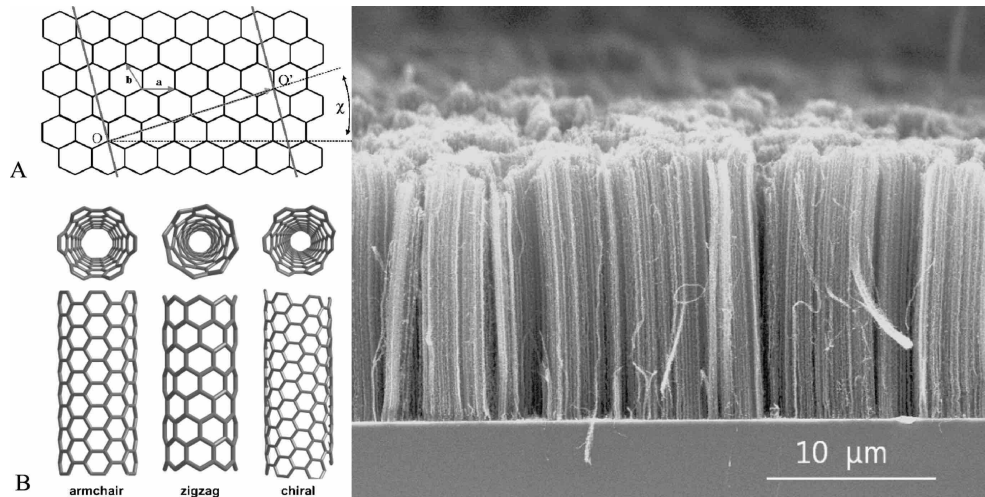


Figure 7.6: Schematic of different structures of carbon nanotubes [171] and a micrograph of a carbon nanotube forest [223]. Reprinted with permission. Copyright 2001 by Annual Reviews (left). Copyright 2012 by the American Physical Society (right).

(hexagonal 2D carbon sheet), see Figure 7.6. The properties of graphene can thereby vary from being metallic to small or moderate bandgap semiconductors. This stems from the different structures, i.e., the ways one could potentially connect the sides of a cut-out of a graphene sheet when rolling it to a seamless cylinder while preserving the honeycomb structure.

While this material is heavily studied for nanoelectronics, membranes and coatings and such, it has also potential application for fundamental particle physics experiments which require low energetic muonium production into vacuum, like Mu-MASS [224] and the study of gravity on antimatter [225]. A specific growth process of CNTs is hereby of particular interest. Under the correct conditions, they form a carbon nanotube forest. A nearly parallel arrangement of CNTs grown perpendicular to a substrate surface. From the correlation of positronium and muonium emitted into vacuum as seen from porous silica [207] a proof of concept measurement for CNT oPs production was made. Such a large collection of mostly perfect arranged voids in the nanometer scale are suspected to be ideal as a conversion target. The high surface to volume ratio allows muonium to form and diffuse into one of the tubes. The muonium which can be too heavy to be quantum mechanically confined in the tubes can then be treated classically. Undergoing multiple collisions will reduce the energy as seen in porous silicas [207], but the more directed tubes should lead more directed emission of muonium into vacuum.

The here studied carbon nanotubes samples were prepared by M. De Volder and C. Valentine from Cambridge University and received from A. Soter (PSI) for characterization with positrons. It was planned to do a small study of the fraction of oPs produced into vacuum at several energies. The CNT forest was grown on a Si substrate which was mounted with silver glue on the sample stage of the positron beam. After a degassing period of around 2h a high voltage was

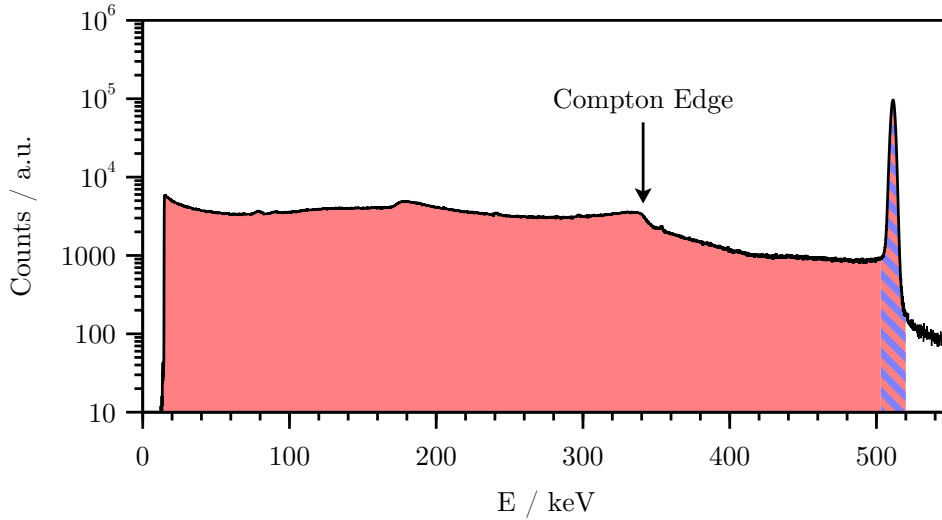


Figure 7.7: Gamma spectrum of a CNT forest taken with a HPGe. The marked regions are the peak (hatched blue) and total spectrum area (full & hatched red) used for the $3\gamma/2\gamma$ technique. The Compton Edge of the 511 keV 2γ annihilation is shown at 341 keV.

applied to define the positron implantation energy as described in Section 3.

The sample immediately started emitting a high number of spontaneous electrons, uncorrelated with any positron flux. Already at low energies the MCP tagging detector was swamped with strong electron flux, e.g. $3 \times 10^4 \text{ e}^- \text{ s}^{-1}$ at 1 keV. Increasing the energy leads to an exponential rise. A PALS measurement at acceptable implantation energies of 2 keV or more, utilizing the MCP tagging detector, was therefore unfeasible. The high electron flux would potentially damage the detector which upper limit is around $1 \times 10^6 \text{ Hz}$. Moreover, such a bad signal to noise ratio would require a long measurement time to acquire the necessary statistics. At higher energies, the increased current density per single CNT would potentially evaporate it.

Therefore, the sample is a perfect example of an application of a bunched and elevated beam. Positrons accelerated to the implantation energy before the sample and bunches with small enough time spread to make a tagging detector redundant would have made the envisaged measurement possible. However, with the tools at hand a different, less precise, method was employed, three gamma two gamma spectroscopy. With the use of the HPGe detector energy spectra of the gamma radiation of the CNT sample and two reference samples were taken.

An example spectra of the CNT-2.1 sample is shown in Figure 7.7. As references, the blank aluminium sample holder is known to not produce any oPs and a standard porous silica target with 30% oPs into vacuum were used. Annihilation in 2 photons results in a peak at 511 keV and Compton scattered events in the region between 0 keV and the Compton edge at 341 keV. Any oPs decay into three gammas, from free oPs and partly from oPs in pores, produce an energy spectrum from 0 to 511 keV. Taking the ratio R of the area up to the peak $T - P$ and the

Table 7.5: Summary of the $3\gamma/2\gamma$ measurements of the carbon nanotube and reference samples. $3\gamma/2\gamma$ ratio R , oPs into vacuum f , number of events in spectrum N , dead time ratio $\eta = (t_{\text{real}} - t_{\text{life}})/t_{\text{real}}$ and comments.

Name	f (%)	Ω	R	N	η (%)	Comment
Al	0	0	3.23	130×10^6	2.0	0 oPs ref.
Silica	30	1.5	4.72	93×10^6	2.1	max. oPs ref.
CNT-1	1	0.058	3.30	48×10^6	1.3	burned from HV
CNT-2.0	4	0.22	3.45	78×10^6	1.2	beam not optimized
CNT-2.1	16	0.78	4.01	21×10^6	0.8	after venting
CNT-2.2	2	0.083	3.31	0.2×10^6	1.7	burned from HV

peak P subtracted by the same ratio of a purely 2γ reference sample $R_{2\gamma}$ gives the $3\gamma/2\gamma$ -ratio

$$\Omega = R - R_{2\gamma} \text{ with} \quad (7.1)$$

$$R = \frac{T - P}{P} , \quad (7.2)$$

$$T = \int_0^{511+9} S(E)dE , \quad (7.3)$$

$$P = \int_{511-9}^{511+9} S(E)dE . \quad (7.4)$$

$$(7.5)$$

The integral T is of the full spectrum, P only the 511 peak region. A shortcoming of this technique is, that with a measurement at only a single energy one can not distinguish between free oPs annihilation in vacuum versus oPs partly annihilating into 3γ inside a pore. Measurements at multiple energies can reveal the diffusion behaviour and entangle the two components. As this was not feasible a simple scaling by an oPs rich sample, porous silica, was made. The oPs fraction into vacuum f was therefore approximated as

$$f_{\text{CNT}} = \frac{R_{\text{CNT}}}{R_{\text{sil}}} f_{\text{sil}} . \quad (7.6)$$

The results and properties of data collected at 2 keV implantation energy to limit the damage to the CNTs are summarized in Table 7.5. Two CNT samples were used. The first one was subjected to a high voltages exceeding 2 keV in the initial trial run for PALS. As expected the oPs into vacuum was rather low (1%) after potentially a lot of damage was dealt. The second sample showed a slightly higher oPs fraction of 4% on the start. An increase to $f_{\text{CNT}} = 15\%$ was seen after two improvements were made. A new beam optimization and steering at 2 keV through gamma detector counts rather than the usual secondary electron transportation efficiency for the MCP tagging detector. Additionally, the sample chamber was

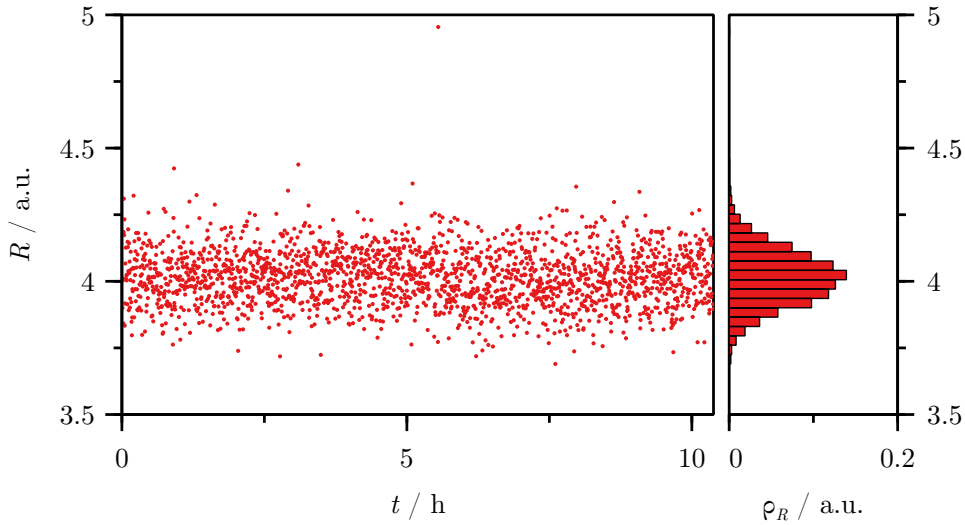


Figure 7.8: Time series scatter plot and histogram of the CNT-2.1 511 peak to spectrum ratio R . The standard errorbars of $\sigma_R \approx 0.1$ are omitted for visibility reasons.

vented with nitrogen to negate any charging effects which might have occurred during the optimization procedure.

The stability of the run is shown in Figure 7.8. A total of 2077 spectra of 1×10^4 counts each were taken. The ratio R was constant for more than 10 h. After a trial to increase the energy, which led to sparking, Ω dropped before the CNT-2.2 measurement

As mentioned before, the resulting $f_{\text{CNT}} = 15\%$ is not necessarily only oPs emitted into vacuum. The scaling from the 30% of porous silica to the $3\gamma/2\gamma$ ratio Ω is subject to multiple errors. Any trapped oPs is annihilating in 2γ via pick-off annihilation as into 3γ by self-annihilation. The fraction of each is strongly depending on the confining pore, i.e., the lifetime, as can be seen from the Tao-Edlrup model, see Equation 2.16 which uses a weighting of the two annihilation channels to get a pore lifetime. If the CNTs and the silica do not have exactly the same oPs components, diffusion etc., i.e., are identical from the oPs response, the scaling will not be linear. A rigorous systematic study would be necessary to assess the resulting uncertainty. Nevertheless, the very nature of the strongly aligned CNT forest suggests, that most oPs which is created has a substantial chance of leaving the nanotubes. The oPs into vacuum has by far the largest contribution to the 3γ fraction in porous silica. Therefore, it is to be expected that the emission into vacuum is in the range of the approximated 15%. This result motivated the study of CNTs as potential muon to muonium converters. The production of muonium was later confirmed during beamtime at PSI conducted during the PhD of N. Ritjoho [226].

Chapter 8

Conclusion

The goal of this thesis was to study and advance the application of PAS for the characterization of novel materials with advanced functionalities. Positrons and positronium, have a unique sensitivity to their immediate electron density. The presence of electrons distinctly alters the annihilation characteristics. Analysing the annihilation of positrons implanted into a material can, therefore, give insights into their inherent structure. It is the property of the positron(ium) acting as a dynamic local probe which makes this method unique and complementary to other techniques.

The research conducted in this thesis spans over all fields related to PAS, instrumentation, theoretical modelling, and applied material studies. Most of the work hereby evolved around the previously existing ETHZ slow positron beam.

One important aspect was the development of new solutions and continuous improvements to the instruments and positron beams. A focus was hereby set on improving the availability of positron beams. With a new scheme, placing a thin radioactive source inside a magnetic bottle unprecedented moderation efficiencies of 1% were shown with a proof-of-concept setup. Already at this level, it is a factor 100 improvement compared to standard laboratory beams utilizing the same solid metal moderators. This advancement allows to operate beams with sources of low activity (~ 1 MBq) but comparable overall flux ($\sim 10^4 e^+ / s$) without needing to fulfil strict radio-safety guidelines.

Preliminary simulation results suggest that with an improved setup up to 10% could be achievable. This allows operating a positron beam with fluxes comparable to state-of-the-art laboratory beams with radioactive sources of activities below the legal regulation threshold. An important step to overcome one of the main limitations of PAS, the lack of availability. An added benefit comes from the approach of ion implantation of 100 kBq of ^{22}Na into a $1 \mu\text{m}$ Ni foil at ISOLDE, CERN. With the use of such ^{22}Na source and its long lifetime directly combined with a positron moderation material, a rigorous characterization and optimization of the novel moderation approach can now be conducted.

Furthermore, the use of proton cyclotrons for medical applications for the productions of lower lifetime but on average more radioactive positron sources was

studied. The interesting cases of ^{68}Ga , ^{44}Sc , ^{86}Y , ^{89}Zr and ^{48}V were proposed to be further investigated because of their good yield of positron activity per irradiation and low threshold energies.

In collaboration with the Advanced Catalyst Engineering Group (ETH), the development of a special sample stage was pursued. The design of an in-operando cell, a heatable container with gas throughput to reproduce the operating conditions of catalysts under reaction. A large challenge hereby is how positrons can be brought to the sample environment with temperatures and pressures of up to 500 °C and 1 bar. A special welding techniques to create a vacuum tight positron to reaction environment interface is currently being done at PSI. On success, this would revolutionize the understanding of catalytic materials and other functional solids by enabling the time-resolved monitoring of pore network evolution under reaction conditions.

In parallel, the second positron beam of the laboratory is modified to have a PAS beam port. A code created to simulated the performance of this beam show that it has superior timing capabilities with time resolutions of 0.24 ns or less. This provides a better sensitivity for faster positron annihilation channels, allowing to disentangle the disambiguities which occurred for a set of samples. Moreover, the usage of this beam-line would not only imply an improved spectrometer, but also lift some design constraints on the operando cell.

The scope of the applied material characterization ranged from proof of concept work to explore the general sensitivity of PAS, over applications to investigate novel materials, up to the determination of specific effects. A summary of the different materials studied, their current or foreseen main industrial application, the research goals, used techniques and the expected impact is shown in Table 8.1. The findings have shown new successful applications of PAS helping to disentangle the effect of voids on the materials properties where established methods do not have access.

In terms of modelling, a strong effort was made for the development of tools to simulate oPs lifetimes and confinement energies in open-pore geometries. The established models are based on infinite square well approximations and do only provide reliable descriptions for closed pore geometries. However, novel functionalized porous materials are often highly interconnected with open-pore structures. For example, the MFI type zeolite has an intrinsic highly symmetric micropore network of channels and cages. With additional treatments, amorphous mesopores can be added to form a hierarchical framework which can further increase the catalytic performance. A successful prediction by simulations would help to better understand these materials and to deconvolute the performance relevant parameters.

The first step was the study of a 1D approximation including confining volumes with open faces. The used solution was based on the in solid state well established Kronig Penney model. The predicted lifetimes associated with the trapping of oPs were calibrated with a set of IRMOFs PALS data. Compared with the established RTE method the presented model shows an improvement of a factor three in terms of mean absolute percentage deviation.

Table 8.1: Summary of the results of applied material PAS studies for zeolites type ZSM-5 (MFI), different kind of nanocrystals (NC), Surface Anchored Metal-Organic Framework (SURMOF) type HKUST-1, functional thin copper films, and Carbon Nanotube (CNTs) Forests.

Material	Main current/foreseen industrial application
Used techniques	Research goal of conducted study Summary of results Impact
ZSM-5 Zeolite	catalysis, sorption
PALS	Characterization of pore network evolution
	The unique sensitivity of PALS to the presence of guest species within a porous network was shown. A set of differently evolved samples were measured and the data was successfully modelled with percolation theory. The specific process of detemplation was found to be isotropic. These findings prove that complex questions of the evolution of porous materials can be assessed with PAS by developing an appropriate model.
ZSM-5 Zeolite	catalysis, sorption
PALS	Sensitivity of PAS to chemical properties
	A series of MFI-type samples with controlled Brønsted and Lewis acidity were used to calibrate the impact on the PALS response. An empirical model to correct for these effects was developed. The ability to evaluate both the porosity and acidity of zeolites using positrons widens the scope of the technique for the analysis of functional materials.
SURMOF	sorption, opto-, and nanoelectronics
PALS	Highly directed mono energetic Ps emission into vacuum
	The studied SURMOF, HKUST-1, showed only little oPs formation (<5%) and no emission into vacuum. The unit-cell structure of HKUST-1 highlighted the sensitivity of Ps to the incorporated metal ions. Different SURMOF structures were proposed as Ps converters.
NC Cu-Zn-In-Se	optoelectronics, i.e. light emitting quantum dots
PALS, DBS	Confirmation of controlled incorporation of defects in NCs
	Samples with different expected vacancy concentrations were characterized with DBS and PALS. Both techniques point towards the existence of defects. The proof that vacancies can exist in nanocrystals would imply an immense emergence of opportunities for the tailorability of NCs.
NC Pb-S	optoelectronics, i.e. photovoltaic
PALS	Distances in drop-cast NCs with different linker molecules
	No quantitative supported conclusion could be drawn from the proof of concept study of two different sized nanocrystal samples. The use of the proposed buffer gas trap beam PAS setup with improved time resolution is expected to provide the sought after insights. The positioning of NCs in a colloid defines their interaction as individual quantum dots. A control over the packing is therefore of high interest to tailor the assembly towards the desired electronic bulk properties.

NC Ge-Te Non-volatile information storage devices
PALS Phase transition and fusing of NCs with temperature
Two samples subjected to temperatures at 100 °C and 200 °C were measured. No clear PALS response showing fusion was seen because of the limitations of the cw positron beam. The use of the proposed buffer gas trap beam PAS setup with improved time resolution is expected to provide the sought after insights. Phase transitions are crucial for memory applications. A non-reversal fusion of the building blocks would prohibit the usage as a storage medium.

Cu Films optoelectronics
DBS Assessment of Ion bombarded induced defects
The sensitivity of PAS was shown by comparing the response in a defect rich sample to an untreated pre-courser. PAS was added to characterization tool-set of these material class to assess the uncharted territory of defect effects.

CNTs forests nanoelectronics, membranes and coatings
 $3\gamma/2\gamma$ Study Ps emission into vacuum as an indicator for muonium production
The previously correlation between positronium and muonium into vacuum production from porous silica was affirmed. The oPs fraction was approximated to be about 15%. The production of muonium was subsequently verified during beam-time at PSI. Confirming the correlation enables the study of potential muonium converters with positrons. The fundamental experiments on the muon beamlines at PSI with more limited beam time clearly benefit from this pre-selection.

To further improve the annihilation rate predictions also for more generic frameworks, an a priori approach was pursued. A method to use the electron density in the unit cell of the materials to create a confining potential was established. Modelling a full 3D solution, it was envisaged that the interaction, i.e., overlap, of the positronium with the electrons of the material defining the oPs lifetimes is better approximated. It was shown, that using an infinite potential well based on electron density isosurfaces does not describe experimental values of confinement energies and lifetimes.

Another important factor for PAS analysis is the consideration of the sample dimensionality, i.e. granularity. A first step was made towards the inclusion of rate equations in the data analysis to have a grip on the diffusion dynamics in the porous systems of differently sized crystals. The commonly used 1D-model describing the implantation profile of positrons was advanced to a 3D case. This highlighted the impact of implantation energy and sample subunit sizes of e.g. crystals on the studied volume. Using these profiles as a basis for modelling the out-diffusion process of positronium allows studying the interconnectivity of a porous framework in an additional dimension.

Inspired by nature's elegant examples and proclaimed as the next frontier in advanced materials design, hierarchical organization has become a truly inter-

disciplinary phenomenon in the development of numerous advanced technologies. There is growing awareness that the additional level of complexity introduced in these materials requires the development of new characterization strategies to guide the design. The development of a new technique for materials characterization would constitute a breakthrough for the characterization of advanced technologies. The work presented in this thesis contributed to the successful application of PAS to these novel kinds of materials. In other parts, limits were shown and prospects were discussed.

Chapter 9

Outlook

While there is still a set of problems to be solved towards a wide-spread use of PAS, it is to be expected that the remaining challenges will be successfully tackled in the coming years. The number of studies conducted in this thesis, which provided novel insights, can be seen as a small sample of the plentiful of possible applications. This motivates that the work should also be expanded to other fields not presented here. Many other hot topics employing nano-porosity could potentially profit, e.g. pharmaceuticals, fuel cell and battery technology. Therefore, a focus for the future should be a strong dissemination of the technique.

As important as the growing number of applications for a wide-spread use of PAS, is the development of better theoretical models and improved instrumentation. For example, the finalisation of the operando cell, this could pioneer the understanding of catalytic materials and other functional solids by enabling the time-resolved monitoring of pore network evolution under reaction conditions. The last crucial steps on how to vacuum seal the positron to sample interface, a 30 nm SiN membrane, are currently explored. The use of novel detectors and detector geometries could allow to combine more annihilation parameters to obtain a complete picture.

The proof-of-concept of the cyclotron trap assisted moderator is an important step towards smaller scale table-top positron beams for applied research laboratories. The simplicity of the setup compared to state-of-the-art laboratory beams with cryogenic equipment makes it easier to use. Merely the availability of the positron source needs further attention. One possible solution is the use of long lived sources created by irradiation or implantation. A scalability of both production methods is a question that has to be addressed in the future. Therefore, the existing medical proton cyclotron infrastructures could be a great opportunity for the positron beam community to benefit from these existing infrastructures, with sources in both the multi GBq level and highly available thin film source for table-top devices.

Prospects to improve the modelling is to include an all-electron full-potential Linearised Augmented-Plane Wave solver (LAPW) which allows higher discretisation and to calculate the oPs confining potential from first principle with repulsive

and attractive forces between oPs as a two-particle system and the electron density. Furthermore, effort to take the kinematics of the positronium annihilation channels into accounts by employing rate equations should be made.

Acronyms

ACE Advanced Catalysis Engineering.

AFM Atomic Force Microscopy.

AWG Arbitrary Waveform Generator.

BaF₂ Barium Fluoride.

BGO Bismuth Germanium Oxide.

CDBS Coincidence Doppler Broadening Spectroscopy.

CNT Carbon NanoTube.

CT Cyclotron Trap.

DBS Doppler Broadening Spectroscopy.

EM Electron Multiplier.

HECTAM⁺ High Efficiency Cyclotron Trap Assisted Moderator.

HPGe High Purity Germanium.

IBAD Ion Beam Assisted Deposition.

IRMOF IsoReticular Metal-Organic Framework.

LAPW Linearised Augmented-Plane Wave solver.

MCP MicroChannel Plate.

ME MEchanical techniques.

MOF Metal-Organic Framework.

N Neutron scattering.

NC NanoCrystals.

OM optical Microscopy.

oPs Ortho-PoSitronium.

PALS Positronium Annihilation Lifetime Spectroscopy.

PAS Positron Annihilation Spectroscopy.

PET Positron Emission Tomography.

pPs Para-PoSitronium.

Ps PoSitronium.

PSI Paul Scherrer Institute.

PVD Physical Vapor Deposition.

SE Secondary Electrons.

SM Standard Model.

SNR Signal to Noise Ratio.

STM Scanning Tunneling Microscopy.

SURMOF SURface anchored Metal-Organic Framework.

TEM Transmission Electron Microscopy.

TOF Time-Of-Flight.

Bibliography

- [1] P. A. M. Dirac, *Proc. R. Soc. London Ser. A* **1928**, *117*, 610–624, DOI [10.1098/rspa.1928.0023](https://doi.org/10.1098/rspa.1928.0023).
- [2] C. D. Anderson, *Phys. Rev.* **1933**, *43*, 491–494, DOI [10.1103/PhysRev.43.491](https://doi.org/10.1103/PhysRev.43.491).
- [3] S. Mitchell, L. Gerchow, R. Warringham, P. Crivelli, J. Pérez-Ramírez, *Small Methods* **2018**, *2*, 1800268, DOI [10.1002/smt.201800268](https://doi.org/10.1002/smt.201800268).
- [4] P. J. Schultz, K. G. Lynn, *Rev. Mod. Phys.* **1988**, *60*, 701–779, DOI [10.1103/RevModPhys.60.701](https://doi.org/10.1103/RevModPhys.60.701).
- [5] D. W. Gidley, W. E. Frieze, T. L. Dull, A. F. Yee, E. T. Ryan, H.-M. Ho, *Phys. Rev. B* **1999**, *60*, R5157–R5160, DOI [10.1103/PhysRevB.60.R5157](https://doi.org/10.1103/PhysRevB.60.R5157).
- [6] J. N. Sun, Y. F. Hu, W. E. Frieze, D. W. Gidley, *Radiat. Phys. Chem.* **2003**, *68*, Proceedings of the 7th International Conference on Positron and Positronium Chemistry, 345–349, DOI [10.1016/S0969-806X\(03\)00182-8](https://doi.org/10.1016/S0969-806X(03)00182-8).
- [7] J.-N. Sun, D. W. Gidley, T. L. Dull, W. E. Frieze, A. F. Yee, E. T. Ryan, S. Lin, J. Wetzel, *J. Appl. Phys.* **2001**, *89*, 5138–5144, DOI [10.1063/1.1360704](https://doi.org/10.1063/1.1360704).
- [8] H.-G. Peng, W. E. Frieze, R. S. Vallery, D. W. Gidley, D. L. Moore, R. J. Carter, *Appl. Phys. Lett.* **2005**, *86*, 121904, DOI [10.1063/1.1886905](https://doi.org/10.1063/1.1886905).
- [9] K. S. Sing, *Colloids and Surf.* **1989**, *38*, 6th International Conference on Surface and Colloid Science, 113–124, DOI [10.1016/0166-6622\(89\)80148-9](https://doi.org/10.1016/0166-6622(89)80148-9).
- [10] D. W. Gidley, H.-G. Peng, R. S. Vallery, *Annu. Rev. Mater. Res.* **2006**, *36*, 49–79, DOI [10.1146/annurev.matsci.36.111904.135144](https://doi.org/10.1146/annurev.matsci.36.111904.135144).
- [11] F. Tuomisto, I. Makkonen, *Rev. Mod. Phys.* **2013**, *85*, 1583–1631, DOI [10.1103/RevModPhys.85.1583](https://doi.org/10.1103/RevModPhys.85.1583).
- [12] S. J. Tao, *J. Chem. Phys.* **1972**, *56*, 5499–5510, DOI [10.1063/1.1677067](https://doi.org/10.1063/1.1677067).

-
- [13] M. Eldrup, D. Lightbody, J. Sherwood, *Chem. Phys.* **1981**, *63*, 51–58, DOI [10.1016/0301-0104\(81\)80307-2](https://doi.org/10.1016/0301-0104(81)80307-2).
- [14] T. L. Dull, W. E. Frieze, D. W. Gidley, J. N. Sun, A. F. Yee, *J. Phys. Chem. B* **2001**, *105*, 4657–4662, DOI [10.1021/jp004182v](https://doi.org/10.1021/jp004182v).
- [15] Y. C. Jean, J. D. Van Horn, W.-S. Hung, K.-R. Lee, *Macromolecules (Washington DC U. S.)* **2013**, *46*, 7133–7145, DOI [10.1021/ma401309x](https://doi.org/10.1021/ma401309x).
- [16] M. Milina, S. Mitchell, P. Crivelli, D. Cooke, J. Pérez-Ramírez, *Nat. Commun.* **2014**, *5*, 3922, DOI [10.1038/ncomms4922](https://doi.org/10.1038/ncomms4922).
- [17] M. Milina, S. Mitchell, D. Cooke, P. Crivelli, J. Pérez-Ramírez, *Angew. Chem. Int. Ed.* **2015**, *54*, 1591–1594, DOI [10.1002/anie.201410016](https://doi.org/10.1002/anie.201410016).
- [18] Y. Kobayashi, K. Ito, T. Oka, K. Hirata, *Radiat. Phys. Chem.* **2007**, *76*, Proceedings of the 8th International Workshop on Positron and Positronium Chemistry, 224–230, DOI [10.1016/j.radphyschem.2006.03.042](https://doi.org/10.1016/j.radphyschem.2006.03.042).
- [19] R. Krause-Rehberg, H. S. Leipner, *Positron Annihilation in Semiconductors: Defect Studies*, 1st ed., Springer-Verlag Berlin Heidelberg, New York, **1999**.
- [20] P. Coleman, *Positron Beams and Their Applications*, Singapore: World Sci. Publ. Co., **2000**, DOI [10.1142/3719](https://doi.org/10.1142/3719).
- [21] L. Michel, *Il Nuovo Cimento (1943-1954)* **2008**, *10*, 319, DOI [10.1007/BF02786202](https://doi.org/10.1007/BF02786202).
- [22] A. Ore, J. L. Powell, *Phys. Rev.* **1949**, *75*, 1696–1699, DOI [10.1103/PhysRev.75.1696](https://doi.org/10.1103/PhysRev.75.1696).
- [23] G. S. Atoyan, S. N. Gninenko, V. I. Razin, Y. V. Ryabov, *Phys. Lett. B* **1989**, *220*, 317–320, DOI [10.1016/0370-2693\(89\)90059-2](https://doi.org/10.1016/0370-2693(89)90059-2).
- [24] N. Alberola, T. Anthonioz, A. Badertscher, C. Bas, A. Belov, P. Crivelli, S. Gninenko, N. Golubev, M. Kirsanov, A. Rubbia, D. Sillou, *Nucl. Instrum. Methods Phys. Res. Sect. A* **2006**, *560*, 224–232, DOI <http://dx.doi.org/10.1016/j.nima.2006.01.025>.
- [25] A. Badertscher, P. Crivelli, W. Fetscher, U. Gendotti, S. Gninenko, et al., *Phys. Rev. D* **2007**, *75*, 032004, DOI [10.1103/PhysRevD.75.032004](https://doi.org/10.1103/PhysRevD.75.032004).
- [26] P. Crivelli, A. Belov, U. Gendotti, S. Gninenko, A. Rubbia, *JINST* **2010**, *5*, P08001, DOI [10.1088/1748-0221/5/08/P08001](https://doi.org/10.1088/1748-0221/5/08/P08001).
- [27] C. Vigo, L. Gerchow, L. Liskay, A. Rubbia, P. Crivelli, *Phys. Rev. D* **2018**, *97*, 092008, DOI [10.1103/PhysRevD.97.092008](https://doi.org/10.1103/PhysRevD.97.092008).

- [28] G. S. Adkins, N. M. McGovern, R. N. Fell, J. Sapirstein, *Phys. Rev.* **2003**, *A68*, 032512, DOI [10.1103/PhysRevA.68.032512](https://doi.org/10.1103/PhysRevA.68.032512).
- [29] W. E. Caswell, G. P. Lepage, *Phys. Rev. A* **1979**, *20*, 36–43, DOI [10.1103/PhysRevA.20.36](https://doi.org/10.1103/PhysRevA.20.36).
- [30] S. G. Karshenboim, *J. Exp. Theor. Phys.* **1993**, *76*, 541–546.
- [31] G. S. Adkins, *Phys. Rev. Lett.* **1996**, *76*, 4903–4906, DOI [10.1103/PhysRevLett.76.4903](https://doi.org/10.1103/PhysRevLett.76.4903).
- [32] G. S. Adkins, R. N. Fell, J. Sapirstein, *Phys. Rev. Lett.* **2000**, *84*, 5086–5089, DOI [10.1103/PhysRevLett.84.5086](https://doi.org/10.1103/PhysRevLett.84.5086).
- [33] K. Melnikov, A. Yelkhovsky, *Phys. Rev. D* **2000**, *62*, 116003, DOI [10.1103/PhysRevD.62.116003](https://doi.org/10.1103/PhysRevD.62.116003).
- [34] A. H. Al-Ramadhan, D. W. Gidley, *Phys. Rev. Lett.* **1994**, *72*, 1632–1635, DOI [10.1103/PhysRevLett.72.1632](https://doi.org/10.1103/PhysRevLett.72.1632).
- [35] R. S. Vallery, P. W. Zitzewitz, D. W. Gidley, *Phys. Rev. Lett.* **2003**, *90*, 203402, DOI [10.1103/PhysRevLett.90.203402](https://doi.org/10.1103/PhysRevLett.90.203402).
- [36] S. G. Karshenboim, *Int. J. Mod. Phys.* **2004**, *A19*, 3879–3896, DOI [10.1142/S0217751X04020142](https://doi.org/10.1142/S0217751X04020142).
- [37] M. Deutsch, *Phys. Rev.* **1951**, *82*, 455–456, DOI [10.1103/PhysRev.82.455](https://doi.org/10.1103/PhysRev.82.455).
- [38] F. F. Heymann, P. E. Osmon, J. J. Veit, W. F. Williams, *Proceedings of the Physical Society* **1961**, *78*, 1038–1047, DOI [10.1088/0370-1328/78/5/351](https://doi.org/10.1088/0370-1328/78/5/351).
- [39] R. L. Burwell, *Pure & Appl. Chem.* **1976**, *46*, (Eds.: H. Burrows, J. Stohner), 79, DOI [10.1351/pac197646010071](https://doi.org/10.1351/pac197646010071).
- [40] R. Mayer, A. Weiss, *Phys. Rev. B* **1988**, *38*, 11927–11930, DOI [10.1103/PhysRevB.38.11927](https://doi.org/10.1103/PhysRevB.38.11927).
- [41] D. W. Gidley, D. N. McKinsey, P. W. Zitzewitz, *J. Appl. Phys.* **1995**, *78*, 1406–1410, DOI [10.1063/1.360296](https://doi.org/10.1063/1.360296).
- [42] C. Hugenschmidt, *Surf. Sci. Rep.* **2016**, *71*, 547–594, DOI [10.1016/j.surfrep.2016.09.002](https://doi.org/10.1016/j.surfrep.2016.09.002).
- [43] H. Marinov, N. Djourelou, P. Nédélec, L. Petrov, *Nuclear Instruments and Methods in Physics Research Section A: Accelerators Spectrometers Detectors and Associated Equipment* **2013**, *729*, 569–575, DOI [10.1016/j.nima.2013.08.045](https://doi.org/10.1016/j.nima.2013.08.045).

-
- [44] P. Asoka-Kumar, K. G. Lynn, *Appl. Phys. Lett.* **1990**, *57*, 1634–1636, DOI [10.1063/1.104071](https://doi.org/10.1063/1.104071).
- [45] K. G. Lynn, H. Lutz, *Phys. Rev. B* **1980**, *22*, 4143–4160, DOI [10.1103/PhysRevB.22.4143](https://doi.org/10.1103/PhysRevB.22.4143).
- [46] A. P. Mills, R. J. Wilson, *Phys. Rev. A* **1982**, *26*, 490–500, DOI [10.1103/PhysRevA.26.490](https://doi.org/10.1103/PhysRevA.26.490).
- [47] J. A. Baker, N. B. Chilton, K. O. Jensen, A. B. Walker, P. G. Coleman, *Appl. Phys. Lett.* **1991**, *59*, 2962–2964, DOI [10.1063/1.105812](https://doi.org/10.1063/1.105812).
- [48] O. E. Mogensen, *J. Chem. Phys.* **1974**, *60*, 998–1004, DOI [10.1063/1.1681180](https://doi.org/10.1063/1.1681180).
- [49] S. V. Stepanov, V. M. Byakov, D. S. Zvezhinskiy, G. Duplâtre, R. R. Nurmukhametov, P. S. Stepanov, *Advances in Physical Chemistry* **2012**, *2012*, DOI [10.1155/2012/431962](https://doi.org/10.1155/2012/431962).
- [50] O. E. Mogensen in *Positron Annihilation in Chemistry*, Springer Berlin Heidelberg, Berlin, Heidelberg, **1995**, pp. 66–87, DOI [10.1007/978-3-642-85123-0_5](https://doi.org/10.1007/978-3-642-85123-0_5).
- [51] A. Zubiaga, R. Warringham, M. Boltz, D. Cooke, P. Crivelli, D. Gidley, J. Pérez-Ramírez, S. Mitchell, *Phys. Chem. Chem. Phys.* **2016**, *18*, 9211–9219, DOI [10.1039/C6CP00408C](https://doi.org/10.1039/C6CP00408C).
- [52] D. B. Cassidy, P. Crivelli, T. H. Hisakado, L. Liskay, V. E. Meline, P. Perez, H. W. K. Tom, A. P. Mills, *Phys. Rev. A* **2010**, *81*, 012715, DOI [10.1103/PhysRevA.81.012715](https://doi.org/10.1103/PhysRevA.81.012715).
- [53] P. Crivelli, D. Cooke, B. Barbiellini, B. L. Brown, J. I. Feldblyum, P. Guo, D. W. Gidley, L. Gerchow, A. J. Matzger, *Phys. Rev. B* **2014**, *89*, 241103, DOI [10.1103/PhysRevB.89.241103](https://doi.org/10.1103/PhysRevB.89.241103).
- [54] A. C. L. Jones, H. J. Goldman, Q. Zhai, P. Feng, H. W. K. Tom, A. P. Mills, *Phys. Rev. Lett.* **2015**, *114*, 153201, DOI [10.1103/PhysRevLett.114.153201](https://doi.org/10.1103/PhysRevLett.114.153201).
- [55] T. Goworek, K. Ciesielski, B. Jasińska, J. Wawryszczuk, *Chem. Phys. Lett.* **1997**, *272*, 91–95, DOI [10.1016/S0009-2614\(97\)00504-6](https://doi.org/10.1016/S0009-2614(97)00504-6).
- [56] T. Goworek, K. Ciesielski, B. Jasińska, J. Wawryszczuk, *Radiat. Phys. Chem.* **2000**, *58*, 719–722, DOI [http://dx.doi.org/10.1016/S0969-806X\(00\)00246-2](http://dx.doi.org/10.1016/S0969-806X(00)00246-2).
- [57] L. Liskay, C. Corbel, P. Perez, P. Desgardin, M.-F. Barthe, T. Ohdaira, R. Suzuki, P. Crivelli, U. Gendotti, A. Rubbia, M. Etienne, A. Walcarus, *Appl. Phys. Lett.* **2008**, *92*, 063114, DOI [10.1063/1.2844888](https://doi.org/10.1063/1.2844888).

- [58] R. Golovchak, S. Wang, H. Jain, A. Ingram, *J. Mater. Res.* **2012**, *27*, 2561–2567, DOI [10.1557/jmr.2012.252](https://doi.org/10.1557/jmr.2012.252).
- [59] L. Liskay, F. Guillemot, C. Corbel, J.-P. Boilot, T. Gacoïn, E. Barthel, P. Pérez, M.-F. Barthe, P. Desgardin, P. Crivelli, U. Gendotti, A. Rubbia, *New J. Phys.* **2012**, *14*, 065009, DOI [10.1088/1367-2630/14/6/065009](https://doi.org/10.1088/1367-2630/14/6/065009).
- [60] C. He, B. Xiong, W. Mao, Y. Kobayashi, T. Oka, N. Oshima, R. Suzuki, *Chem. Phys. Lett.* **2013**, *590*, 97–100, DOI [10.1016/j.cplett.2013.10.042](https://doi.org/10.1016/j.cplett.2013.10.042).
- [61] C. Li, N. Qi, Z. Liu, B. Zhou, Z. Chen, Z. Wang, *Appl. Surf. Sci.* **2016**, *363*, 445–450, DOI [10.1016/j.apsusc.2015.12.055](https://doi.org/10.1016/j.apsusc.2015.12.055).
- [62] R. Warringham, L. Gerchow, A. Zubiaga, D. Cooke, P. Crivelli, S. Mitchell, J. Pérez-Ramírez, *J. Phys. Chem. C* **2016**, *120*, 25451–25461, DOI [10.1021/acs.jpcc.6b08931](https://doi.org/10.1021/acs.jpcc.6b08931).
- [63] A. Uedono, S. Armini, Y. Zhang, T. Kakizaki, R. Krause-Rehberg, W. Anwand, A. Wagner, *Appl. Surf. Sci.* **2016**, *368*, 272–276, DOI [10.1016/j.apsusc.2016.01.267](https://doi.org/10.1016/j.apsusc.2016.01.267).
- [64] R. Warringham, S. Mitchell, R. Murty, R. Schäublin, P. Crivelli, J. Kenvin, J. Pérez-Ramírez, *Chem. Mater.* **2017**, *29*, 4052–4062, DOI [10.1021/acs.chemmater.7b00734](https://doi.org/10.1021/acs.chemmater.7b00734).
- [65] R. Warringham, L. Gerchow, D. Cooke, P. Crivelli, R. S. Vallery, S. Mitchell, J. Pérez-Ramírez, *J. Phys. Chem. C* **2018**, *122*, 3443–3453, DOI [10.1021/acs.jpcc.7b11336](https://doi.org/10.1021/acs.jpcc.7b11336).
- [66] P. Crivelli, U. Gendotti, A. Rubbia, L. Liskay, P. Perez, C. Corbel, *Phys. Rev.* **2010**, *A81*, 052703, DOI [10.1103/PhysRevA.81.052703](https://doi.org/10.1103/PhysRevA.81.052703).
- [67] P. Asoka-Kumar, K. G. Lynn, D. O. Welch, *Jour. of Applied Physics* **1994**, *76*, 4935–4982, DOI [10.1063/1.357207](https://doi.org/10.1063/1.357207).
- [68] S. Szpala, P. Asoka-Kumar, B. Nielsen, J. P. Peng, S. Hayakawa, K. G. Lynn, H.-J. Gossmann, *Phys. Rev. B* **1996**, *54*, 4722–4731, DOI [10.1103/PhysRevB.54.4722](https://doi.org/10.1103/PhysRevB.54.4722).
- [69] L. P. Chan, K. G. Lynn, D. R. Harshman, *Mod. Phys. Lett. B* **1992**, *06*, 617–635, DOI [10.1142/S0217984992000715](https://doi.org/10.1142/S0217984992000715).
- [70] H. Stoll, P. Wesolowski, M. Koch, K. Maier, A. Seeger, J. Major in Positron Annihilation - ICPA-9, Trans Tech Publications Ltd, **1992**, pp. 1989–1992, DOI [10.4028/www.scientific.net/MSF.105-110.1989](https://doi.org/10.4028/www.scientific.net/MSF.105-110.1989).
- [71] U. Ackermann, B. Löwe, M. Dickmann, J. Mitteneder, P. Sperr, W. Egger, M. Reiner, G. Dollinger, *New J. Phys.* **2016**, *18*, 113030, DOI [10.1088/1367-2630/18/11/113030](https://doi.org/10.1088/1367-2630/18/11/113030).

- [72] A. Weiss, N. Fazleev, M. Nadesalingam, S. Mukherjee, S. Xie, J. Zhu, B. Davis, *Radiat. Phys. Chem.* **2007**, *76*, Proceedings of the 8th International Workshop on Positron and Positronium Chemistry, 285–290, DOI [10.1016/j.radphyschem.2006.03.053](https://doi.org/10.1016/j.radphyschem.2006.03.053).
- [73] T. J. Murphy, C. M. Surko, *Phys. Rev. A* **1992**, *46*, 5696–5705, DOI [10.1103/PhysRevA.46.5696](https://doi.org/10.1103/PhysRevA.46.5696).
- [74] J. R. Danielson, D. H. E. Dubin, R. G. Greaves, C. M. Surko, *Rev. Mod. Phys.* **2015**, *87*, 247–306, DOI [10.1103/RevModPhys.87.247](https://doi.org/10.1103/RevModPhys.87.247).
- [75] D. B. Cassidy, S. H. M. Deng, H. K. M. Tanaka, A. P. Mills, *Appl. Phys. Lett.* **2006**, *88*, 194105, DOI [10.1063/1.2203336](https://doi.org/10.1063/1.2203336).
- [76] B. S. Cooper, A. M. Alonso, A. Deller, T. E. Wall, D. B. Cassidy, *Rev. Sci. Instrum.* **2015**, *86*, 103101, DOI [10.1063/1.4931690](https://doi.org/10.1063/1.4931690).
- [77] B. S. Cooper, J.-P. Boilot, C. Corbel, F. Guillemot, L. Gurung, L. Liskay, D. B. Cassidy, *Phys. Rev. B* **2018**, *97*, 205302, DOI [10.1103/PhysRevB.97.205302](https://doi.org/10.1103/PhysRevB.97.205302).
- [78] C. Hugenschmidt, G. Kögel, R. Repper, K. Schreckenbach, P. Sperr, B. Straßer, W. Triftshäuser, *Nuclear Instruments and Methods in Physics Research Section B: Beam Interactions with Materials and Atoms* **2004**, *221*, Proceedings of the XII International Workshop on Positron and Positronium Physics, 160–164, DOI [10.1016/j.nimb.2004.03.048](https://doi.org/10.1016/j.nimb.2004.03.048).
- [79] R. Krause-Rehberg, S. Sachert, G. Brauer, A. Rogov, K. Noack, *Appl. Surf. Sci.* **2006**, *252*, Proceedings of the Tenth International Workshop on Slow Positron Beam Techniques for Solids and Surfaces, 3106–3110, DOI [10.1016/j.apsusc.2005.08.109](https://doi.org/10.1016/j.apsusc.2005.08.109).
- [80] R. Howell, I. Rosenberg, M. Fluss, *Appl. Phys. A: Solids Surf.* **1987**, *43*, cited By 41, 247–255, DOI [10.1007/BF00635179](https://doi.org/10.1007/BF00635179).
- [81] F. T. Tárkányi, A. V. Ignatyuk, A. Hermanne, R. Capote, B. V. Carlson, J. W. Engle, M. A. Kellett, T. Kibédi, G. N. Kim, F. G. Kondev, M. Hussain, O. Lebeda, A. Luca, Y. Nagai, H. Naik, A. L. Nichols, F. M. Nortier, S. V. Suryanarayana, S. Takács, M. Verpelli, *J. Radioanal. Nucl. Chem.* **2019**, *319*, 533–666, DOI [10.1007/s10967-018-6380-5](https://doi.org/10.1007/s10967-018-6380-5).
- [82] J. Hubbell, *Radiat. Phys. Chem.* **2006**, *75*, Pair Production, 614–623, DOI [10.1016/j.radphyschem.2005.10.008](https://doi.org/10.1016/j.radphyschem.2005.10.008).
- [83] M. Jungmann, R. Krause-Rehberg, A. Müller, A. Krille, G. Brauer, *Appl. Surf. Sci.* **2008**, *255*, Proceedings of the Eleventh International Workshop on Slow Positron Beam Techniques for Solids and Surfaces, 42–45, DOI [10.1016/j.apsusc.2008.05.176](https://doi.org/10.1016/j.apsusc.2008.05.176).

- [84] R. Krause-Rehberg, G. Brauer, M. Jungmann, A. Krille, A. Rogov, K. Noack, *Appl. Surf. Sci.* **2008**, *255*, Proceedings of the Eleventh International Workshop on Slow Positron Beam Techniques for Solids and Surfaces, 22–24, DOI [10.1016/j.apsusc.2008.05.283](https://doi.org/10.1016/j.apsusc.2008.05.283).
- [85] N. Oshima, R. Suzuki, T. Ohdaira, A. Kinomura, T. Narumi, A. Uedono, M. Fujinami in Positron and Positronium Chemistry, Trans Tech Publications Ltd, **2009**, pp. 238–242, DOI [10.4028/www.scientific.net/MSF.607.238](https://doi.org/10.4028/www.scientific.net/MSF.607.238).
- [86] P. Pérez, L. Liskay, J.-M. Rey, V. Blideanu, M. Carty, A. Curtoni, O. Delferrière, P. Dupré, T. Muranaka, N. Ruiz, Y. Sacquin, *Phys. Status Solidi C* **2009**, *6*, 2462–2464, DOI [10.1002/pssc.200982123](https://doi.org/10.1002/pssc.200982123).
- [87] C. Falub, S. Eijt, P. Mijnders, H. Schut, A. van Veen, *Nucl. Instrum. Methods Phys. Res. Sect. A* **2002**, *488*, 478–492, DOI [10.1016/S0168-9002\(02\)00566-1](https://doi.org/10.1016/S0168-9002(02)00566-1).
- [88] A. I. Hawari, D. W. Gidley, J. Moxom, A. G. Hathaway, S. Mukherjee, *J. Phys.: Conf. Ser.* **2011**, *262*, 012024, DOI [10.1088/1742-6596/262/1/012024](https://doi.org/10.1088/1742-6596/262/1/012024).
- [89] C. Hugenschmidt, H. Ceeh, T. Gigl, F. Lippert, C. Piochacz, M. Reiner, K. Schreckenbach, S. Vohburger, J. Weber, S. Zimmik, *J. Phys.: Conf. Ser.* **2014**, *505*, 012029, DOI [10.1088/1742-6596/505/1/012029](https://doi.org/10.1088/1742-6596/505/1/012029).
- [90] H. Chen, S. C. Wilks, J. D. Bonlie, E. P. Liang, J. Myatt, D. F. Price, D. D. Meyerhofer, P. Beiersdorfer, *Phys. Rev. Lett.* **2009**, *102*, 105001, DOI [10.1103/PhysRevLett.102.105001](https://doi.org/10.1103/PhysRevLett.102.105001).
- [91] H. Chen, G. Fiksel, D. Barnak, P.-Y. Chang, R. F. Heeter, A. Link, D. D. Meyerhofer, *Physics of Plasmas* **2014**, *21*, 040703, DOI [10.1063/1.4873711](https://doi.org/10.1063/1.4873711).
- [92] X. Ribeyre, E. d’Humières, O. Jansen, S. Jequier, V. T. Tikhonchuk, M. Lobet, *Phys. Rev. E* **2016**, *93*, 013201, DOI [10.1103/PhysRevE.93.013201](https://doi.org/10.1103/PhysRevE.93.013201).
- [93] M. Berger, J. Hubbell, S. Seltzer, J. Chang, J. Coursey, R. Sukumar, D. Zucker, K. Olsen, *XCOM: Photon Cross Sections Database*, (Ed.: N. S. R. D. 8. (XGAM)), NIST, PML, Radiation Physics Division, **2010**, DOI [10.18434/T48G6X](https://doi.org/10.18434/T48G6X).
- [94] L. Madansky, F. Rasetti, *Phys. Rev.* **1950**, *79*, 397–397, DOI [10.1103/PhysRev.79.397](https://doi.org/10.1103/PhysRev.79.397).
- [95] A. I. Williams, D. J. Murtagh, S. E. Fayer, S. L. Andersen, J. Chevallier, Á. Kövér, P. V. Reeth, J. W. Humberston, G. Laricchia, *J. Appl. Phys.* **2015**, *118*, 105302, DOI [10.1063/1.4930033](https://doi.org/10.1063/1.4930033).

-
- [96] A. P. M. Jr., E. M. Gullikson, *Appl. Phys. Lett.* **1986**, *49*, 1121–1123, DOI [10.1063/1.97441](https://doi.org/10.1063/1.97441).
- [97] K. G. Lynn, B. Nielsen, J. H. Quateman, *Appl/ Phys. Lett.* **1985**, *47*, 239–240, DOI [10.1063/1.96231](https://doi.org/10.1063/1.96231).
- [98] F. Saito, Y. Nagashima, L. Wei, Y. Itoh, A. Goto, T. Hyodo, *Appl. Surf. Sci.* **2002**, *194*, 9th International Workshop on Slow Positron Beam Techniques for Solids and Surfaces, 13–15, DOI [10.1016/S0169-4332\(02\)00103-4](https://doi.org/10.1016/S0169-4332(02)00103-4).
- [99] L. Gerchow, S. Braccini, T. S. Carzaniga, D. Cooke, M. Döbeli, K. Kirch, U. Köster, A. Müller, N. P. Van der Meulen, C. Vermeulen, A. Rubbia, P. Crivelli, *Instruments* **2018**, *2*, DOI [10.3390/instruments2030010](https://doi.org/10.3390/instruments2030010).
- [100] C. Vigo, PhD thesis, ETH Zurich, Zurich, **2017-12-15**, DOI [10.3929/ethz-b-000245118](https://doi.org/10.3929/ethz-b-000245118).
- [101] X.-P. Huang, F. Anderegg, E. M. Hollmann, C. F. Driscoll, T. M. O’Neil, *Phys. Rev. Lett.* **1997**, *78*, 875–878, DOI [10.1103/PhysRevLett.78.875](https://doi.org/10.1103/PhysRevLett.78.875).
- [102] J. L. Wiza, *Nucl. Instrum. Methods* **1979**, *162*, 587–601, DOI [10.1016/0029-554X\(79\)90734-1](https://doi.org/10.1016/0029-554X(79)90734-1).
- [103] Nikob7, Discrete_and_Continuous_Dynode_Systems, licensed under CC BY-SA 4.0, https://commons.wikimedia.org/wiki/File:Discrete_and_Continuous_Dynode_Systems.jpg (visited on 10/09/2019).
- [104] W. Yi, T. Jeong, S. Jin, S. Yu, J. Lee, J. Heo, J. Yoo, J. M. Kim, *J. Vac. Sci. Technol. B: Microelectron. Nanometer Struct.–Process. Meas. Phenom.* **2001**, *19*, 2247–2251, DOI [10.1116/1.1420206](https://doi.org/10.1116/1.1420206).
- [105] P. Crivelli, C. L. Cesar, U. Gendotti, *Canadian Journal of Physics* **2011**, *89*, This paper was presented at the International Conference on Precision Physics of Simple Atomic Systems, held at École de Physique, les Houches, France, 30 May – 4 June, 2010., 29–35, DOI [10.1139/P10-101](https://doi.org/10.1139/P10-101).
- [106] D. A. Cooke, P. Crivelli, A. Alnis, J. and Antognini, B. Brown, S. Friedreich, A. Gabard, T. W. Haensch, K. Kirch, A. Rubbia, V. Vrankovic, *Hyperfine Interactions* **2015**, *233*, 67–73, DOI [10.1007/s10751-015-1158-4](https://doi.org/10.1007/s10751-015-1158-4).
- [107] D. A. Cooke, G. Barandun, S. Vergani, B. Brown, A. Rubbia, P. Crivelli, *J. Phys. B: At. Mol. Opt. Phys.* **2015**, *49*, 014001, DOI [10.1088/0953-4075/49/1/014001](https://doi.org/10.1088/0953-4075/49/1/014001).
- [108] W. Zhou, Z. Chen, N. Oshima, K. Ito, B. E. O’Rourke, R. Kuroda, R. Suzuki, H. Yanagishita, T. Tsutsui, A. Uedono, N. Hayashizaki, *Applied Physics Letters* **2012**, *101*, 014102, DOI [10.1063/1.4729425](https://doi.org/10.1063/1.4729425).

- [109] B. E. O'Rourke, W. Zhou, N. Oshima, K. Ito, R. Suzuki, *J. Phys.: Conf. Ser.* **2013**, *443*, 012069, DOI [10.1088/1742-6596/443/1/012069](https://doi.org/10.1088/1742-6596/443/1/012069).
- [110] A. P. Mills, *Appl. Phys.* **1980**, *22*, 273–276, DOI [10.1007/BF00899876](https://doi.org/10.1007/BF00899876).
- [111] D. A. Dahl, *International Journal of Mass Spectrometry* **2000**, *200*, Volume 200: The state of the field as we move into a new millenium, 3–25, DOI [http://dx.doi.org/10.1016/S1387-3806\(00\)00305-5](http://dx.doi.org/10.1016/S1387-3806(00)00305-5).
- [112] J. A. Nelder, R. Mead, *The Computer Journal* **1965**, *7*, 308–313, DOI [10.1093/comjnl/7.4.308](https://doi.org/10.1093/comjnl/7.4.308).
- [113] P.-A. Hervieux, A. Chakraborty, H. Chakraborty, *Phys. Rev. A* **2017**, *95*, 020701 (R), DOI [10.1103/PhysRevA.95.020701](https://doi.org/10.1103/PhysRevA.95.020701).
- [114] G. Wichmann, PhD thesis, ETH Zurich, Zurich, **2018-04**, DOI [10.3929/ethz-b-000266482](https://doi.org/10.3929/ethz-b-000266482).
- [115] C. Giffin, H. Boettger, D. Norris, *Int. J. Mass Spectrom. Ion Phys.* **1974**, *15*, 437–449, DOI [10.1016/0020-7381\(74\)80041-0](https://doi.org/10.1016/0020-7381(74)80041-0).
- [116] J. H. D. Eland, *Meas. Sci. Technol.* **1994**, *5*, 1501–1504, DOI [10.1088/0957-0233/5/12/011](https://doi.org/10.1088/0957-0233/5/12/011).
- [117] C. Martin, P. Jelinsky, M. Lampton, R. F. Malina, H. O. Anger, *Rev. Sci. Instrum.* **1981**, *52*, 1067–1074, DOI [10.1063/1.1136710](https://doi.org/10.1063/1.1136710).
- [118] M. Lampton, C. W. Carlson, *Rev. Sci. Instrum.* **1979**, *50*, 1093–1097, DOI [10.1063/1.1135990](https://doi.org/10.1063/1.1135990).
- [119] X.-D. Ju, M.-Y. Dong, Y.-C. Zhao, C.-X. Zhou, O.-Y. Qun, *Chin. Phys. C* **2016**, *40*, 086004, DOI [10.1088/1674-1137/40/8/086004](https://doi.org/10.1088/1674-1137/40/8/086004).
- [120] S. Braccini, C. Belver-Aguilar, T. Carzaniga, G. Dellepiane, P. Häffner, P. Scampori in 22st Int. Conf. on Cyclotrons and their Applications - Cyclotrons2019, Cape Town, South Africa, JACoW Publishing, **2019**, DOI [10.18429/JACoW-Cyclotrons2019-TUA02](https://doi.org/10.18429/JACoW-Cyclotrons2019-TUA02).
- [121] IBA, Cyclone® 11 - 18 - 30, licensed under CC BY-SA 4.0, <https://www.iba-radiopharmasolutions.com/products/cyclotrons#modal-map> (visited on 11/21/2019).
- [122] M. Maekawa, Y. Fukaya, A. Yabuuchi, I. Mochizuki, A. Kawasuso, *Nucl. Instrum. Methods Phys. Res. Sect. B* **2013**, *308*, 9–14, DOI [10.1016/j.nimb.2013.04.015](https://doi.org/10.1016/j.nimb.2013.04.015).
- [123] G. B. Andresen, M. D. Ashkezari, M. Baquero-Ruiz, W. Bertsche, P. D. Bowe, E. Butler, C. L. Cesar, S. Chapman, M. Charlton, J. Fajans, T. Friesen, M. C. Fujiwara, D. R. Gill, J. S. Hangst, W. N. Hardy, R. S. Hayano, M. E. Hayden, A. Humphries, R. Hydomako, S. Jonsell, L. Kur-

- chaninov, R. Lambo, N. Madsen, S. Menary, P. Nolan, K. Olchanski, A. Olin, A. Povilus, P. Pusa, F. Robicheaux, E. Sarid, D. M. Silveira, C. So, J. W. Storey, R. I. Thompson, D. P. van der Werf, D. Wilding, J. S. Wurtele, Y. Yamazaki, *Phys. Rev. Lett.* **2010**, *105*, 013003, DOI [10.1103/PhysRevLett.105.013003](https://doi.org/10.1103/PhysRevLett.105.013003).
- [124] D. Gidley, A. Köymen, T. Capehart, *Phys. Rev. Lett.* **1982**, *49*, 1779–1783, DOI [10.1103/PhysRevLett.49.1779](https://doi.org/10.1103/PhysRevLett.49.1779).
- [125] M.-M. Bé, V. Chisté, C. Dulieu, M. Kellett, X. Mougeot, A. Arinc, V. Chechev, N. Kuzmenko, T. Kibédi, A. Luca, A. Nichols, *Table of Radionuclides*, Bureau International des Poids et Mesures, Pavillon de Breteuil, F-92310 Sévres, France, **2016**.
- [126] J. R. Rumble, *CRC Handbook of Chemistry and Physics*, 100th Edition (Internet Version 2019), CRC Press/Taylor & Francis, Boca Raton, FL, **2019**.
- [127] J. D. Jackson, *Classical electrodynamics*, Wiley, New York, **1999**.
- [128] L. M. Simons, *Physica Scripta* **1988**, *T22*, 90–95, DOI [10.1088/0031-8949/1988/t22/013](https://doi.org/10.1088/0031-8949/1988/t22/013).
- [129] J. Eades, L. M. Simons, *Nucl. Instrum. Meth.* **1989**, *A278*, 368–374, DOI [10.1016/0168-9002\(89\)90851-6](https://doi.org/10.1016/0168-9002(89)90851-6).
- [130] L. Simons, *Hyperfine Interactions* **1993**, *81*, 253–262, DOI [10.1007/BF00567270](https://doi.org/10.1007/BF00567270).
- [131] M. Shi, W. Waeber, D. Gerola, U. Zimmermann, D. Taqqu, *Nucl. Instrum. Methods Phys. Res. Sect. A* **1994**, *349*, 8–14, DOI [10.1016/0168-9002\(94\)90601-7](https://doi.org/10.1016/0168-9002(94)90601-7).
- [132] D. Gerola, W. Waeber, M. Shi, S. Wang, *Rev. Sci. Instrum.* **1995**, *66*, 3819–3825, DOI [10.1063/1.1145443](https://doi.org/10.1063/1.1145443).
- [133] D. Gerola, W. Waeber, M. Shi, *Nucl. Instrum. Methods Phys. Res. Sect. A* **1995**, *364*, 33–43, DOI [10.1016/0168-9002\(95\)00392-4](https://doi.org/10.1016/0168-9002(95)00392-4).
- [134] W. B. Waeber, M. Shi, *Appl. Surf. Sci.* **1997**, *116*, 7th International Workshop on Slow-Positron Beam Techniques for Solids and Surfaces, Unterageri, Switzerland, Jun 02-07, 1996, 91–97, DOI [10.1016/S0169-4332\(96\)01035-5](https://doi.org/10.1016/S0169-4332(96)01035-5).
- [135] A. Antognini, PhD thesis, **2005**.
- [136] R. Schill, *Magnetics IEEE Transactions on* **2003**, *39*, 961–967, DOI [10.1109/TMAG.2003.808597](https://doi.org/10.1109/TMAG.2003.808597).

- [137] J. Dryzek, P. Horodek, *Nucl. Instrum. Methods Phys. Res. Sect. B* **2008**, *266*, 4000–4009, DOI [10.1016/j.nimb.2008.06.033](https://doi.org/10.1016/j.nimb.2008.06.033).
- [138] A. P. Mills, *Hyperfine Interact.* **1989**, *44*, 105–123, DOI [10.1007/BF02398662](https://doi.org/10.1007/BF02398662).
- [139] E. Fermi, *Zeitschrift für Physik* **1934**, *88*, 161–177, DOI [10.1007/BF01351864](https://doi.org/10.1007/BF01351864).
- [140] S. Braccini in Application Of Accelerators In Research And Industry, (Ed.: McDaniel, FD and Doyle, BL and Glass, GA and Wang, Y), 22nd International Conference on the Application of Accelerators in Research and Industry (CAARI), Fort Worth, TX, AUG 05-10, 2012, Sandia Natl Labs; Univ N Texas; Los Alamos Natl Lab; Pacific NW Natl Lab; High Voltage Engn Europa B V; Kurt J Lester Co; Natl Electrostat Corp (NEC), **2013**, 144–150, DOI [10.1063/1.4802308](https://doi.org/10.1063/1.4802308).
- [141] U. Gendotti, PhD thesis, ETH Zurich, **2010**, DOI [10.3929/ethz-a-006250397](https://doi.org/10.3929/ethz-a-006250397).
- [142] P. Schmor in Cyclotrons 2010 – Lanzhou, China, (Eds.: Y. Youjin, S. Lina, M. Lijun, V. Schaa), Cyclotrons 2010 - 19th International Conference on Cyclotrons and Their Applications, Institute of Modern Physics (IMP), Chinese Academy of Sciences in Lanzhou, P.R.China, **2010**, pp. 419–424.
- [143] J. F. Ziegler, M. Ziegler, J. Biersack, *Nuclear Instruments and Methods in Physics Research Section B: Beam Interactions with Materials and Atoms* **2010**, *268*, 19th International Conference on Ion Beam Analysis, 1818–1823, DOI [10.1016/j.nimb.2010.02.091](https://doi.org/10.1016/j.nimb.2010.02.091).
- [144] A. U. Czaja, N. Trukhan, U. Müller, *Chem. Soc. Rev.* **2009**, *38*, 1284–1293, DOI [10.1039/B804680H](https://doi.org/10.1039/B804680H).
- [145] J. Liu, C. Wöll, *Chem. Soc. Rev.* **2017**, *46*, 5730–5770, DOI [10.1039/C7CS00315C](https://doi.org/10.1039/C7CS00315C).
- [146] D. P. Falcaro, D. D. Buso, scanning-electron-microscope-image-of-the-seed-inside-the-mof-crystals, licensed under CC BY-SA 3.0, <https://www.scienceimage.csiro.au/image/11684/scanning-electron-microscope-image-of-the-seed-inside-the-mof-crystals> (visited on 01/13/2020).
- [147] M. Eddaoudi, J. Kim, N. Rosi, D. Vodak, J. Wachter, M. O’Keeffe, O. M. Yaghi, *Science* **2002**, *295*, 469–472, DOI [10.1126/science.1067208](https://doi.org/10.1126/science.1067208).
- [148] I. D. Brown, B. McMahon, *Acta Crystallogr. Sect. B: Struct. Sci.* **2002**, *58*, 317–324, DOI [10.1107/S0108768102003464](https://doi.org/10.1107/S0108768102003464).
- [149] A. Zubiaga, R. Warringham, S. Mitchell, L. Gerchow, D. Cooke, P. Crivelli, J. Pérez-Ramírez, *ChemPhysChem* **2017**, *18*, 470–479, DOI [10.1002/cphc.201601258](https://doi.org/10.1002/cphc.201601258).

- [150] K. Momma, F. Izumi, *J. Appl. Crystallogr.* **2011**, *44*, 1272–1276, DOI [10.1107/S0021889811038970](https://doi.org/10.1107/S0021889811038970).
- [151] D. Waasmaier, A. Kirfel, *Acta Crystallogr. Sect. A* **1995**, *51*, 416–431, DOI [10.1107/S0108767394013292](https://doi.org/10.1107/S0108767394013292).
- [152] A. Cronstedt, *Svenska Vetenskaps Akademiens Handlingar Stockholm* **1756**, *17*, 120.
- [153] G. T. Kokotailo, S. L. Lawton, D. H. Olson, W. M. Meier, *Nature* **1978**, *272*, 437–438, DOI [10.1038/272437a0](https://doi.org/10.1038/272437a0).
- [154] C. Baerlocher, L. McCusker, Database of Zeolite Structures, licensed under CC BY-SA 3.0, <http://www.iza-structure.org/databases/> (visited on 02/02/2020).
- [155] S. C. Turaga, S. M. Auerbach, *The Journal of Chemical Physics* **2003**, *118*, 6512–6517, DOI [10.1063/1.1558033](https://doi.org/10.1063/1.1558033).
- [156] C. S. Cundy, P. A. Cox, *Microporous and Mesoporous Mater.* **2005**, *82*, 1–78, DOI [10.1016/j.micromeso.2005.02.016](https://doi.org/10.1016/j.micromeso.2005.02.016).
- [157] M. Moliner, F. Rey, A. Corma, *Angew. Chem. Int. Ed.* **2013**, *52*, 13880–13889, DOI [10.1002/anie.201304713](https://doi.org/10.1002/anie.201304713).
- [158] Z. Wang, J. Yu, R. Xu, *Chem. Soc. Rev.* **2012**, *41*, 1729–1741, DOI [10.1039/C1CS15150A](https://doi.org/10.1039/C1CS15150A).
- [159] J. Li, A. Corma, J. Yu, *Chem. Soc. Rev.* **2015**, *44*, 7112–7127, DOI [10.1039/C5CS00023H](https://doi.org/10.1039/C5CS00023H).
- [160] H. van Koningsveld, H. van Bekkum, J. C. Jansen, *Acta Crystallogr. Sect. B* **1987**, *43*, 127–132, DOI [10.1107/S0108768187098173](https://doi.org/10.1107/S0108768187098173).
- [161] V. Valtchev, G. Majano, S. Mintova, J. Pérez-Ramírez, *Chem. Soc. Rev.* **2013**, *42*, 263–290, DOI [10.1039/C2CS35196J](https://doi.org/10.1039/C2CS35196J).
- [162] I. Melián-Cabrera, F. Kapteijn, J. A. Moulijn, *Chem. Commun.* **2005**, 2744–2746, DOI [10.1039/B502167G](https://doi.org/10.1039/B502167G).
- [163] M. J. Ortiz-Iniesta, I. Melián-Cabrera, *Microporous Mesoporous Mater.* **2015**, *206*, 58–66, DOI [10.1016/j.micromeso.2014.12.019](https://doi.org/10.1016/j.micromeso.2014.12.019).
- [164] J. Kuhn, M. Motegh, J. Gross, F. Kapteijn, *Microporous and Mesoporous Mater.* **2009**, *120*, NoE INSIDE-POReS 2007 – Alicante, 35–38, DOI [10.1016/j.micromeso.2008.08.061](https://doi.org/10.1016/j.micromeso.2008.08.061).
- [165] J. Chezeau, L. Delmotte, J. Guth, Z. Gabelica, *Zeolites* **1991**, *11*, 598–606, DOI [10.1016/S0144-2449\(05\)80011-9](https://doi.org/10.1016/S0144-2449(05)80011-9).

- [166] E. Dib, J. Grand, S. Mintova, C. Fernandez, *Chem. Mater.* **2015**, *27*, 7577–7579, DOI [10.1021/acs.chemmater.5b03668](https://doi.org/10.1021/acs.chemmater.5b03668).
- [167] E. Geus, H. van Bekkum, *Zeolites* **1995**, *15*, 333–341, DOI [10.1016/0144-2449\(94\)00034-P](https://doi.org/10.1016/0144-2449(94)00034-P).
- [168] J. B. Nagy, Z. Gabelica, E. G. Derouane, *Zeolites* **1983**, *3*, 43–49, DOI [10.1016/0144-2449\(83\)90084-2](https://doi.org/10.1016/0144-2449(83)90084-2).
- [169] G. M. Lassinantti, G. A. F., H. Jonas, *Microporous Mesoporous Mater.* **2006**, *89*, 1–8, DOI [10.1016/j.micromeso.2005.09.022](https://doi.org/10.1016/j.micromeso.2005.09.022).
- [170] L. Parker, D. Bibby, J. Patterson, *Zeolites* **1984**, *4*, 168–174, DOI [10.1016/0144-2449\(84\)90056-3](https://doi.org/10.1016/0144-2449(84)90056-3).
- [171] X. Gao, C. Y. Yeh, P. Angevine, *Microporous Mesoporous Mater.* **2004**, *70*, 27–35, DOI [10.1016/j.micromeso.2004.02.014](https://doi.org/10.1016/j.micromeso.2004.02.014).
- [172] L. Karwacki, E. Stavitski, M. H. F. Kox, J. Kornatowski, B. M. Weckhuysen, *Angew. Chem. Int. Ed.* **2007**, *46*, 7228–7231, DOI [10.1002/anie.200702012](https://doi.org/10.1002/anie.200702012).
- [173] L. Karwacki, B. M. Weckhuysen, *Phys. Chem. Chem. Phys.* **2011**, *13*, 3681–3685, DOI [10.1039/C0CP02220A](https://doi.org/10.1039/C0CP02220A).
- [174] C. Pascual-Izarra, A. W. Dong, S. J. Pas, A. J. Hill, B. J. Boyd, C. J. Drummond, *Nucl. Instrum. Methods Phys. Res. Sect. A* **2009**, *603*, 456–466, DOI [10.1016/j.nima.2009.01.205](https://doi.org/10.1016/j.nima.2009.01.205).
- [175] A. Cabral-Prieto, I. García-Sosa, J. Jiménez-Becerril, M. Solache-Ríos, S. Bulbulian, *Microporous Mesoporous Mater.* **2004**, *69*, 109–118, DOI [10.1016/j.micromeso.2004.01.008](https://doi.org/10.1016/j.micromeso.2004.01.008).
- [176] S. Bosnar, D. Bosnar, N. Ren, N. Rajić, B. Gržeta, B. Subotić, *J. Porous Mater.* **2013**, *20*, 1329–1336, DOI [10.1007/s10934-013-9718-y](https://doi.org/10.1007/s10934-013-9718-y).
- [177] R. Zaleski, J. Wawryszczuk, T. Goworek, *Radiat. Phys. Chem.* **2007**, *76*, Proceedings of the 8th International Workshop on Positron and Positronium Chemistry, 243–247, DOI [10.1016/j.radphyschem.2006.03.044](https://doi.org/10.1016/j.radphyschem.2006.03.044).
- [178] O. Prokopova, B. Bernauer, M. Frycova, P. Hrabanek, A. Zikanova, M. Kocirik, *The Journal of Physical Chemistry C* **2013**, *117*, 1468–1476, DOI [10.1021/jp3090364](https://doi.org/10.1021/jp3090364).
- [179] R. J. Glauber, *J. Math. Phys.* **1963**, *4*, 294–307, DOI [10.1063/1.1703954](https://doi.org/10.1063/1.1703954).
- [180] J. Hoshen, R. Kopelman, *Phys. Rev. B* **1976**, *14*, 3438–3445, DOI [10.1103/PhysRevB.14.3438](https://doi.org/10.1103/PhysRevB.14.3438).

- [181] W. Schmidt in *Handbook of Porous Solids*, John Wiley & Sons, Ltd, **2008**, Chapter 2.13, pp. 506–532, DOI [10.1002/9783527618286.ch15](https://doi.org/10.1002/9783527618286.ch15).
- [182] B. Levin, V. Shantarovich, D. Agievskii, M. Landau, G. Chukin, *Kinetics And Catalysis* **1977**, *18*, 1260–1265.
- [183] V. I. Goldanskii, V. G. Firsov, *Annu. Rev. Phys. Chem.* **1971**, *22*, 209–258, DOI [10.1146/annurev.pc.22.100171.001233](https://doi.org/10.1146/annurev.pc.22.100171.001233).
- [184] H. J. Ache, *Angew. Chem. Int. Ed.* **1972**, *11*, 179–199, DOI [10.1002/anie.197201791](https://doi.org/10.1002/anie.197201791).
- [185] V. Goldanskii, B. Levin, A. Mokrushin, M. Kaliko, M. Pervushina in *Dokl. Akad. Nauk. SSSR*, Vol. *191*, **1970**, pp. 855–858.
- [186] V. Goldanskii, B. Levin, V. Pazderskij, V. Shantarovich, *Doklady Akademii Nauk SSSR* **1976**, *228*, 1372–1375.
- [187] H. Nakanishi, Y. Ujihira, *The Journal of Physical Chemistry* **1982**, *86*, 4446–4450, DOI [10.1021/j100219a035](https://doi.org/10.1021/j100219a035).
- [188] Z. Gao, X. Yang, J. Cui, Y. Wang, *Zeolites* **1991**, *11*, 607–611, DOI [10.1016/S0144-2449\(05\)80012-0](https://doi.org/10.1016/S0144-2449(05)80012-0).
- [189] W. Huang, R. Ochoa, R. Miranda, *Phys. Let. A* **1991**, *158*, 417–424, DOI [10.1016/0375-9601\(91\)90684-Z](https://doi.org/10.1016/0375-9601(91)90684-Z).
- [190] W. F. Huang, D. C. Huang, P. K. Tseng, *Catalysis Letters* **1994**, *26*, 269–275, DOI [10.1007/BF00810599](https://doi.org/10.1007/BF00810599).
- [191] W. F. Huang, D. C. Huang, K. J. Hung, P. K. Tseng, *Catalysis Letters* **1996**, *40*, 31–34, DOI [10.1007/BF00807452](https://doi.org/10.1007/BF00807452).
- [192] W. F. Huang, K. J. Hung, D. C. Huang, C. C. Huang, P. K. Tseng, *Catalysis Letters* **1999**, *59*, 213–216, DOI [10.1023/A:1019060219073](https://doi.org/10.1023/A:1019060219073).
- [193] W. Huang, K. Hung, D. Huang in *Positron Annihilation - ICPA-12*, Trans Tech Publications Ltd, **2001**, pp. 263–265, DOI [10.4028/www.scientific.net/MSF.363-365.263](https://doi.org/10.4028/www.scientific.net/MSF.363-365.263).
- [194] A. Paiziev, *Radiat. Phys. Chem.* **2000**, *58*, 787–790, DOI [10.1016/S0969-806X\(00\)00260-7](https://doi.org/10.1016/S0969-806X(00)00260-7).
- [195] G. M. Lari, P. Y. Dapsens, D. Scholz, S. Mitchell, C. Mondelli, J. Pérez-Ramírez, *Green Chem.* **2016**, *18*, 1249–1260, DOI [10.1039/C5GC02147B](https://doi.org/10.1039/C5GC02147B).
- [196] Z. Kajcsos, G. Duplâtre, L. Liskay, I. Billard, A. Bonnenfant, E. Azenha, K. Lázár, G. Pál-Borbély, P. Caulet, J. Patarin, L. Lohonyai, *Radiat. Phys. Chem.* **2000**, *58*, 709–714, DOI [10.1016/S0969-806X\(00\)00244-9](https://doi.org/10.1016/S0969-806X(00)00244-9).

- [197] L. Liskay, C. Corbel, P. Perez, P. Desgardin, M. F. Barthe, T. Ohdaira, R. Suzuki, P. Crivelli, U. Gendotti, A. Rubbia, M. Etienne, A. Walcarius, *Materials Science Forum* **2009**, *607*, 30–33, DOI [10.4028/www.scientific.net/MSF.607.30](https://doi.org/10.4028/www.scientific.net/MSF.607.30).
- [198] J. Zhu, L. Ma, S.-J. Wang, X.-H. Luo, *Chin. Phys. Lett.* **2000**, *17*, 134–136, DOI [10.1088/0256-307x/17/2/021](https://doi.org/10.1088/0256-307x/17/2/021).
- [199] B. Levay, O. E. Mogensen, *The Journal of Physical Chemistry* **1977**, *81*, 373–377, DOI [10.1021/j100520a001](https://doi.org/10.1021/j100520a001).
- [200] Y. Nagashima, Y. Morinaka, T. Kurihara, Y. Nagai, T. Hyodo, T. Shidara, K. Nakahara, *Phys. Rev. B* **1998**, *58*, 12676–12679, DOI [10.1103/PhysRevB.58.12676](https://doi.org/10.1103/PhysRevB.58.12676).
- [201] S. L. Andersen, D. B. Cassidy, J. Chevallier, B. S. Cooper, A. Deller, T. E. Wall, U. I. Uggerhøj, *J. Phys. B: At. Mol. Opt. Phys.* **2015**, *48*, 204003, DOI [10.1088/0953-4075/48/20/204003](https://doi.org/10.1088/0953-4075/48/20/204003).
- [202] P. Moriarty, *Rep. Prog. Phys.* **2001**, *64*, 297–381, DOI [10.1088/0034-4885/64/3/201](https://doi.org/10.1088/0034-4885/64/3/201).
- [203] W. Parak, D. Gerion, T. Pellegrino, D. Zanchet, C. Micheel, S. Williams, R. Boudreau, M. Le Gros, C. Larabell, A. Alivisatos, *Nanotechnology* **2003**, *14*, R15–R27, DOI [10.1088/0957-4484/14/7/201](https://doi.org/10.1088/0957-4484/14/7/201).
- [204] J.-U. A. H. Junghanns, R. H. Mueller, *Int. J. Nanomed.* **2008**, *3*, 295–309.
- [205] P. V. Kamat, *J. Phys. Chem. C* **2008**, *112*, 18737–18753, DOI [10.1021/jp806791s](https://doi.org/10.1021/jp806791s).
- [206] A. M. Smith, S. Nie, *Acc. Chem. Res.* **2010**, *43*, 190–200, DOI [10.1021/ar9001069](https://doi.org/10.1021/ar9001069).
- [207] A. Antognini, P. Crivelli, T. Prokscha, K. S. Khaw, B. Barbiellini, L. Liskay, K. Kirch, K. Kwuida, E. Morenzoni, F. M. Piegsa, Z. Salman, A. Suter, *Phys. Rev. Lett.* **2012**, *108*, 143401, DOI [10.1103/PhysRevLett.108.143401](https://doi.org/10.1103/PhysRevLett.108.143401).
- [208] Z. Wang, C. Wöll, *Adv. Mater. Technol.* **2019**, *4*, 1800413, DOI [10.1002/admt.201800413](https://doi.org/10.1002/admt.201800413).
- [209] D. Cassidy, *Eur. Phys. J. D* **2018**, *72*, DOI [10.1140/epjd/e2018-80721-y](https://doi.org/10.1140/epjd/e2018-80721-y).
- [210] S. Grosjean, Z. Hassan, C. Wöll, S. Bräse, *Eur. J. Org. Chem.* **2019**, *7*, 1446–1460, DOI [10.1002/ejoc.201801232](https://doi.org/10.1002/ejoc.201801232).

- [211] S. Gražulis, D. Chateigner, R. T. Downs, A. F. T. Yokochi, M. Quirós, L. Lutterotti, E. Manakova, J. Butkus, P. Moeck, A. Le Bail, *J. Appl. Crystallogr.* **2009**, *42*, 726–729, DOI [10.1107/S0021889809016690](https://doi.org/10.1107/S0021889809016690).
- [212] Y. Yoo, Z. Lai, H.-K. Jeong, *Microporous and Mesoporous Mater.* **2009**, *123*, 100–106, DOI [10.1016/j.micromeso.2009.03.036](https://doi.org/10.1016/j.micromeso.2009.03.036).
- [213] O. Shekhah, J. Liu, R. A. Fischer, C. Wöll, *Chem. Soc. Rev.* **2011**, *40*, 1081–1106, DOI [10.1039/C0CS00147C](https://doi.org/10.1039/C0CS00147C).
- [214] G. J. Snyder, E. S. Toberer, *Nat. Mater.* **2008**, *7*, 105–114, DOI [10.1038/nmat2090](https://doi.org/10.1038/nmat2090).
- [215] M. Wuttig, N. Yamada, *Nat. mater.* **2007**, *6*, 824–832.
- [216] R. A. Sperling, W. J. Parak, *Philos. Trans. R. Soc. A* **2010**, *368*, 1333–1383, DOI [10.1098/rsta.2009.0273](https://doi.org/10.1098/rsta.2009.0273).
- [217] M. C. Weidman, K. G. Yager, W. A. Tisdale, *Chem. Mater.* **2015**, *27*, 474–482, DOI [10.1021/cm503626s](https://doi.org/10.1021/cm503626s).
- [218] A. Kawasuso, M. Maekawa, A. Miyashita, K. Wada, T. Kaiwa, Y. Nagashima, *Phys. Rev. B* **2018**, *97*, 245303, DOI [10.1103/PhysRevB.97.245303](https://doi.org/10.1103/PhysRevB.97.245303).
- [219] J. F. Scott, C. A. Paz de Araujo, *Science* **1989**, *246*, 1400–1405, DOI [10.1126/science.246.4936.1400](https://doi.org/10.1126/science.246.4936.1400).
- [220] J. F. Scott, *Science* **2007**, *315*, 954–959, DOI [10.1126/science.1129564](https://doi.org/10.1126/science.1129564).
- [221] Y. Gotoh, H. Yoshii, T. Amioka, K. Kameyama, H. Tsuji, J. Ishikawa, *Thin Solid Films* **1996**, *288*, 300–308, DOI [10.1016/S0040-6090\(96\)08828-1](https://doi.org/10.1016/S0040-6090(96)08828-1).
- [222] R. Baughman, A. Zakhidov, W. de Heer, *Science* **2002**, *297*, 787–792, DOI [10.1126/science.1060928](https://doi.org/10.1126/science.1060928).
- [223] O. Dyatlova, J. Gomis-Bresco, E. Malic, H. Telg, J. Maultzsch, G. Zhong, J. Geng, U. Woggon, *Phys. Rev. B* **2012**, *85*, DOI [10.1103/PhysRevB.85.245449](https://doi.org/10.1103/PhysRevB.85.245449).
- [224] P. Crivelli, *Hyperfine Interact.* **2018**, *239*, 49, DOI [10.1007/s10751-018-1525-z](https://doi.org/10.1007/s10751-018-1525-z).
- [225] A. Antognini, D. M. Kaplan, K. Kirch, A. Knecht, D. C. Mancini, J. D. Phillips, T. J. Phillips, R. D. Reasenberg, T. J. Roberts, A. Soter, *Atoms* **2018**, *6*, DOI [10.3390/atoms6020017](https://doi.org/10.3390/atoms6020017).
- [226] N. Ritjoho, PhD thesis, ETH Zurich, Zurich, **2020**.

Curriculum Vitae

Personal Information

Name Lars Frieder Gerchow
Date of birth 30th January, 1989
Nationality Germany

Education

Jan. 2016 – May 2020 Doctor of Sciences
 ETH Zurich, Switzerland
Jan. 2014 – Dez. 2015 MSc ETH
 ETH Zurich, Switzerland
Sep. 2010 – Dez. 2013 BSc ETH
 ETH Zurich, Switzerland

